Structure and kinematics of the milky way as seen from barred galactic model

José Fernandez Trincado

THESE DE DOCTORAT DE L'ETABLISSEMENT UNIVERSITE BOURGOGNE FRANCHE-COMTE

PREPAREE A l'UNIVERSITE DE FRANCHE-COMTE

Ecole doctorale n°554

Ecole doctorale Carnot pasteur

Discipline : Astrophysique

Par

José Gregorio FERNANDEZ TRINCADO

Structure and kinematics of the Milky Way as seen from barred Galactic model

Structure et cinématique de la Voie Lactée dans un modèle de Galaxie barrée

Thèse présentée et soutenue à Besançon le 29 mars 2017

Composition du Jury :

Françoise COMBES	Astronome, Observatoire de Paris	Président
Benoît, FAMAEY	Professeur des Universités, Université de Strasbourg	Rapporteur
Caroline, SOUBIRAN	Professeur des Universités, Université de Bordeaux	Rapporteur
Francesca, FIGUERAS-SINOL	Professeur des Universités, Université de Barcelone	Examinateur
Jean-Marc, PETIT	Professeur des Universités, Université de Bourgogne Franche-Comté	Examinatrice
Annie, ROBIN	Professeur des Universités, Université de Bourgogne Franche-Comté	Directeur de thèse
Céline, REYLE	Astronome, Université de Bourgogne Franche-Comté	Codirecteur de thèse

UBFC
UNIVERSITÉ
BOURGOGNE FRANCHE-COMTÉ

Titre : Structure et cinématique de la Voie Lactée dans un modèle de Galaxie barrée

Mots clés : Voie Lactée, Dynamique, Cinématique

Résumé : Cette thèse consiste en l'étude détaillée de la structure, de la cinématique et de la dynamique de la Voie Lactée, avec un accent particulier sur la région du bulbe et le halo. Le but principal de ce travail est d'établir des contraintes dynamiques sur les paramètres physiques de la barre galactique afin de construire une carte cinématique détaillée des régions internes de notre galaxie. Cette carte peut être un ingrédient pour le modéle de synthèse de populations stellaires de Besançon, permettant de simuler la cinématique précise dans les régions internes du disque et dans la barre elle-même.
Dans cette thèse, je présente plusieurs potentiels analytiques et semi-analytiques afin de reproduire le modèle de potentiel gravitationnel 3D de la Voie Lactée, où les perturbations produites par la barre Galactique correspondent assez bien à la cinématique globale observée dans les régions internes.
J'ai développé une méthode de calcul des orbites stellaires déduites des profils de densité et du potentiel gravitationnel de plusieurs populations stellaires. Le logiciel que j'ai produit dans ce cadre, GravPot16, qui permet l'intégration des orbites, est disponible pour la communauté scientifique.
J'ai également utilisé les données de haute qualité publiées dans la première version de la mission Gaia (TGAS), associées à des informations chimiques précises issues des données APOGEE, pour étudier les propriétés chimiques et dynamiques de la Voie Lactée. Je présente les premiers résultats de cette étude.
J'ai par ailleurs effectué des simulations par particules-test. En utilisant environ 10 millions de particules sans masse comme traceurs de la cinématique stellaire, je présente une étude complète des variations de structures dans le halo stellaire liées à la formation des barres. En particulier, j'ai étudié les orbites typiques de la barre et les effets non-stationaires de la barre sur le disque et le halo
Enfin, j'ai étudié les orbites des étoiles de composition chimique particulière prèsentes dans le disque et le bulbe et leur relation avec les étoiles des amas globulaires. Ces résultats confirment des affirmations antérieures selon lesquelles une petite fraction du halo galactique comporte des étoiles dont l'abondance en éléments légers est normalement ob- servée uniquement dans les environnements d'amas globulaires. Ils fournissent un soutien crucial au scénario de fusion dans la région du bulbe de Voie Lactée aussi bien que dans le halo.

Title : Structure and kinematics of the Milky Way as seen from barred Galactic model

Keywords : Milky Way, Dynamics, Kinematics

Abstract : This work of thesis concerns an in detailed study of the structure, kinematics and dynamics of the Milky Way, with a particular emphasis on the bulge region and the halo. The main goal of this work is to establish dynamical constraints on the physical parameters of the Galactic bar in order to construct a detailed kinematic maps of the inner regions of the our Galaxy. Such map can be used as an ingredient for the Besançon stellar populations synthesis model, allowing to provide accurate kinematic simulations in the inner regions of the disk and in the bar itself.
In this thesis I present several analytic and semi-analytic potentials to approximate the 3D gravitational potential model of the Milky Way, observationally and dynamically constrained, where the perturbations produced by the Galactic bar fit fairly well the global kinematic trends in the Galactic bulge.
Using ~10 millions massless particles as tracers of stellar kinematics, we present a full study of the orbits in the bar, and non-stationary effects of the bar on the disks and the halo.
In particular we trace the kinematic imprints of disk particles trapped/scattered in the Galactic bar.
Finally, we analyse the orbits of chemically peculiar stars in the Milky Way field and its relation with globular cluster stars from the analysis of spectroscopic data. These results confirm previous claims that a small fraction of the Galactic halo is made up of light-element abundance patterns observed only in the globular clusters environments. They provide a crucial observational support to the "merging" scenario of the Milky Way bulge region as well as in the halo.
We develop a method to compute the stellar kinematics and orbits inferred from the density profiles and the gravitational potential for several stellar populations. As a by product of this thesis, we provide the GravPot16 package, a software designed for Galactic dynamics, and orbit integration. Also taking advantage of high quality data produced by the first data release of the mission Gaia (TGAS) combined with accurate chemical information from the APOGEE datasets, I present preliminary results of the Chemo-orbital properties of the Milky Way.

Université Bourgogne Franche-Comté
32, avenue de l'Observatoire
25000 Besançon

A mis padres.

Acknowledgements

I would like to express my deepest sense of gratitude to Dr. Edmundo Moreno, Dr. Angeles Pérez Villegas, Dr. Barbara Pichardo, and Dr. Annie C. Robin who have put his valuable experience, and generous guidance to make part of this work possible, and Dr. Céline Reylé for insightful comments that helped to improve this manuscript and for your support during my PhD program.

Thank you Dr. Caroline Soubiran, Dr. Benoit Famaey, Dr. Francesca Figueras, Dr. Françoise Combes, and Dr. Jean Marc Petit for agreeing to serve on my committee.

I am very grateful to all the people I have met along the way and have contributed to the development of my research. In particular I would like to express my special appreciation to Dr. Katherine Vieira Villarreal, Dr. Anna Katherina Vivas Maldonado, Dr. Jesús Hernández, Dr. France Allard, Dr. Houri Ziaeepour, Dr. Julien Montillaud, Dr. Jaime Forero Romero, Gonzalez, Dr. Octavio Valenzuela, Dr. Olga Zamora, Dr. Katia Cunha, Dr. Chris Sneden, Dr. Anibal Garcia Hernández, Dr. Mercé Romero Gómez, Dr. Olivier Bienaymé, Dr. Matthew Shetrone, Dr. Lagarde Nadège, Dr. Mathias Schultheis, Dr. Ricardo P. Schiavon, Dr. Baitian Tang, Dr. Doug Geisler, Friedrich Anders, Diogo Souto, Sten Hasselquist, and others SDSS/APOGEE members for the helpful and stimulating discussions during my career.

I am also very grateful with truly friends that I am lucky enough to meet, especially Erika Antiche ("Naguará", gracias por todo tu apoyo incondicional), Tomas Verdugo, Ivan Cabrera Ziri Castro, José Serra, Daniele Fantin (tutto l'amore), Alexis Benigni (tio, tac, tac), Daniel Baguet (qu'est-ce que tu dis?), Guillaume Nasello (merci pour tout, "parlare quando sei ubriaco"), Timote Acadia, Andrés Martins ("gracias por tu orientación y las buenas vivencias que tuvimos en Besançon: Eu sempre serei grato a você"), Gaelle Laporte, Silvia Vidal, and many others.

I am also very grateful with Carole Heritier, Eliane Soudagne, Stéphanie Djerioui, Françoise Gazelle, Sylvain Picaud for their constant support.

I am also very grateful with Sékou Diakité for providing support in Mésocentre.

This thesis made use of a number of programs provided by the **Astropy** software community (Astropy Collaboration et al., 2013; Muna et al., 2016), the **AstroML** software community (Ivezić et al., 2014), and **TOPCAT** (Taylor, 2005).

Simulations have been executed on computers from the Utinam Institute of the Université de Franche-Comté, supported by the RÃľgion de Franche-Comté and Institut des Sciences de l'Univers (INSU), and on the supercomputer facilities of the Mésocentre de calcul de Franche-Comté (∼400,000 hours CPUTIME).

The work was supported by Centre National d'Etudes Spatiales (CNES) through PhD grant 0101973 and the Région de Franche-Comté and by the French Programme Na-

tional de Cosmologie et Galaxies (PNCG). I also appreciate the support received from different institutions and groups: European Astronomical Society (EWASS), Institute for Astro- and Particle Physics (MIAPP), Gaia Research for European Astronomy Training (GREAT), Indo-French Astronomy School for Optical Spectroscopy, La Société française d'astronomie et d'astrophysique (SF2A), GALHIS group (Galaxy History), Dark Matter Distribution in the Era of Gaia Workshop.

Last but not the least, I would like to thank my family for supporting me emotionally with this work and my life in general.

Résumé

Cette thèse consiste en l'étude détaillée de la structure, de la cinématique et de la dynamique de la Voie Lactée, avec un accent particulier sur la région du bulbe et le halo. Le but principal de ce travail est d'établir des contraintes dynamiques sur les paramètres physiques de la barre galactique afin de construire une carte cinématique détaillée des régions internes de notre galaxie. Cette carte peut être un ingrédient pour le modéle de synthèse de populations stellaires de Besançon, permettant de simuler la cinématique précise dans les régions internes du disque et dans la barre elle-même.

Dans cette thèse, je présente plusieurs potentiels analytiques et semi-analytiques afin de reproduire le modèle de potentiel gravitationnel 3D de la Voie Lactée, où les perturbations produites par la barre Galactique correspondent assez bien à la cinématique globale observée dans les régions internes.

J'ai développé une méthode de calcul des orbites stellaires déduites des profils de densité et du potentiel gravitationnel de plusieurs populations stellaires. Le logiciel que j'ai produit dans ce cadre, GravPot16, qui permet l'intégration des orbites, est disponible pour la communauté scientifique. J'ai également utilisé les données de haute qualité publiées dans la première version de la mission Gaia (TGAS), associées à des informations chimiques précises issues des données APOGEE, pour étudier les propriétés chimiques et dynamiques de la Voie Lactée. Je présente les premiers résultats de cette étude.

J'ai par ailleurs effectué des simulations par particules-test. En utilisant environ 10 millions de particules sans masse comme traceurs de la cinématique stellaire, je présente une étude complète des variations de structures dans le halo stellaire liées à la formation des barres. En particulier, j'ai étudié les orbites typiques de la barre et les effets non-stationaires de la barre sur le disque et le halo

Enfin, j'ai étudié les orbites des étoiles de composition chimique particulière prèsentes dans le disque et le bulbe et leur relation avec les étoiles des amas globulaires. Ces résultats confirment des affirmations antérieures selon lesquelles une petite fraction du halo galactique comporte des étoiles dont l'abondance en éléments légers est normalement observée uniquement dans les environnements d'amas globulaires. Ils fournissent un soutien crucial au scénario de fusion dans la région du bulbe de Voie Lactée aussi bien que dans le halo.

Abstract

This work of thesis concerns an in detailed study of the structure, kinematics and dynamics of the Milky Way, with a particular emphasis on the bulge region and the halo. The main goal of this work is to establish dynamical constraints on the physical parameters of the Galactic bar in order to construct a detailed kinematic maps of the inner regions of the our Galaxy. Such map can be used as an ingredient for the Besançon stellar populations synthesis model, allowing to provide accurate kinematic simulations in the inner regions of the disk and in the bar itself.

In this thesis I present several analytic and semi-analytic potentials to approximate the 3D gravitational potential model of the Milky Way, observationally and dynamically constrained, where the perturbations produced by the Galactic bar fit fairly well the global kinematic trends in the Galactic bulge.

We develop a method to compute the stellar kinematics and orbits inferred from the density profiles and the gravitational potential for several stellar populations. As a by product of this thesis, we provide the GravPot16 package, a software designed for Galactic dynamics, and orbit integration. Also taking advantage of high quality data produced by the first data release of the mission *Gaia* (TGAS) combined with accurate chemical information from the APOGEE datasets, I present preliminary results of the *Chemo-orbital* properties of the Milky Way.

Using ~ 10 millions massless particles as tracers of stellar kinematics, we present a full study of the orbits in the bar, and non-stationary effects of the bar on the disks and the halo. In particular we trace the kinematic imprints of disk particles trapped/scattered in the Galactic bar.

Finally, we analyse the orbits of chemically peculiar stars in the Milky Way field and its relation with globular cluster stars from the analysis of spectroscopic data. These results confirm previous claims that a small fraction of the Galactic halo is made up of light-element abundance patterns observed only in the globular clusters environments. They provide a crucial observational support to the "merging" scenario of the Milky Way bulge region as well as in the halo.

Contents

List of Figures

List of Tables

Statement of originality

This statement on research interest describes work carried out within the Sloan Digital Sky Survey (SDSS-III/SDSS-IV) consortium, l'Institut UTINAM et de l'Observatoire des Sciences de l'Univers THETA Franche-Comté Bourgogne, Université Bourgogne Franche-Comté (UBFC), between March 2014 to January 2017. The work presented in this statement is, to the best of my knowledge and belief, original. I hereby declare that I have not submitted this material, either in full or in part, for a degree at this or any other institution.

Chapter 1

Introduction

In the last years, a number of observational evidence have been accumulated showing a Milky Way (MW) dominated by many composite structures belonging to the bulge[1], the interstellar matter, one or more Galactic disks with different scale parameters, surrounded by a stellar component of the halo with different chemistry and kinematics properties (see Carollo et al., 2007; Fernández-Alvar et al., 2017), and one more extended component the so-called "dark matter". These components represent the basics of any Milky Way model (see e.g., Freeman & Bland-Hawthorn, 2002; Robin et al., 2003; Pichardo et al., 2003, 2004; Hawkins et al., 2015; Pasetto et al., 2016, and references therein). To understand how these structures have been formed it is necessary to investigate the properties of the stellar content (stellar populations) of the Milky Way and in particular the dynamical properties of each component, including orbital properties and resonnance traping. For such studies realistic models of the Milky Way are required. Here we attempt to assemble such models, that satisfy observational constraints as far as possible.

More generally, most of the photometric and kinematics studies of the formation process and evolution of the MW have unveiled in unprecedented detail the existence of peculiar structures in the primary "internal" components of the MW. For instance, within the inner few kpc, the Galactic bulge appears to be dominated by a "boxy/peanut" morphology or X-shape structure made-up of old (∼10 Gyr) and metal rich stars (Blitz & Spergel, 1991; Binney et al., 1991; Rich, 1992; Whitelock, 1992; Weiland et al., 1994; Dwek et al., 1995; Picaud & Robin, 2004; Benjamin et al., 2005; López-Corredoira et al., 2005; Howard et al., 2009; Churchwell et al., 2009; Nataf et al., 2010; McWilliam & Zoccali, 2010; Saito et al., 2011; Robin et al., 2012; Ness et al., 2012; Gonzalez et al., 2012; Wegg & Gerhard, 2013; Gonzalez et al., 2015; Nataf et al., 2015; Wegg et al., 2015; Ness & Lang, 2016; Zoccali & Valenti, 2016; Ness & Freeman, 2016; Shen & Li, 2016; Schultheis et al., 2017, and references therein), while a more spheroidal and metal poor structure (e.g., Babusiaux et al., 2010; Hill et al., 2011; Soszyński et al., 2014; Kunder et al., 2016) seems to coexist as a separate population from the so-called "3D bar-like structure".

Additionally it has been suggested that the Galactic bulge is also made-up of multiple components with different chemistry and kinematic features, uncovering the composite nature of the bulge (see e.g., Gonzalez et al., 2013; Ness et al., 2013a,b; Rojas-Arriagada

[1]Throughout this work we call "bulge" the full structure that is present within the central regions, $r_{gal} < 4.5$ kpc, independently of its origin.

et al., 2014; Di Matteo et al., 2015; Schultheis et al., 2015; Kunder et al., 2015; Williams et al., 2016; Babusiaux, 2016; McWilliam, 2016; Zasowski et al., 2016; Bland-Hawthorn & Gerhard, 2016). Recently, Schiavon et al. (2017b) claimed to have found evidence for a new population in the Galactic bulge with chemical abundance patterns strikingly similar to those observed in globular cluster stars. Similar abundance variations have been observed in other field stars, i.e., Fernández-Trincado et al. (2017, submitted) and Recio-Blanco et al. (2017) discovered signature of *second-generation* globular cluster stars in metal poor stars with α element deficiencies in bulge fields. Understanding this complex chemical mixture towards the Milky Way bulge can help to answer questions about the formation of the bulge itself.

Different scenarios have been put forward to account for many of these observed features. Essentially the main concept is that the bulge was formed via: i) *dissipative collapse of a protogalactic gas cloud*; ii) *hierarchical merging of primordial substructures*; and iii) *formation via instability of the inner disk*. For more details on the formation scenarios, see Eggen et al. (1962); Combes & Sanders (1981); Raha et al. (1991); Bureau & Freeman (1999); Scannapieco & Tissera (2003); Immeli et al. (2004); Kormendy & Kennicutt (2004); Athanassoula (2005); Ballero et al. (2007); Carollo et al. (2007); McWilliam et al. (2008); Elmegreen et al. (2008); Saha & Gerhard (2013); Martinez-Valpuesta & Gerhard (2013); Di Matteo et al. (2014); Joo et al. (2017); Laurikainen & Salo (2016); Ferraro et al. (2016).

The presence of a triaxial structure in the inner bulge plus the so-called "spiral arms" along the Galactic disk produces non-axisymmetries in the Galactic disk, causing stellar orbital variations and consequently chemical mixtures in the Galaxy. In fact, Moreno et al. (2015) have recently analyzed the intrinsic properties of these non-axisymmetries in the Milky Way, and it has been suggested that the same underlying mechanism producing the resonant trapping regions in the Galactic disk and Galactic halo could as well apply to explain the origin of the so-called *moving groups*.

The present work has similarities with several work in the literature, proposing different techniques and methods attempting to construct a detailed steady-state gravitational potential of the Milky Way (e.g., Bienaymé et al., 1987; Allen & Santillan, 1991; Pichardo et al., 2003, 2004; Binney, 2012; Bienaymé et al., 2015; Bovy, 2015; Smith et al., 2015; Pasetto et al., 2016; McMillan, 2017; Rojas-Niño et al., 2016; Pouliasis et al., 2017, and references therein), observationally and dynamically constrained. Among the main similarities we can mention that the bases of these models is the adoption of one and/or several stellar disk(s) surrounded by a dark matter component, and provide a reasonable shape of the Galactic rotation curve beyond of the bulge regions, as well as predicting a circular velocity at the solar radius of $\sim 220\pm30$ km s^{-1}, whereas the inner Galactic "rotation curve" for mostly of present Milky Way models still suffers of severe uncertainties probably generated by asymmetries like the stellar bar. So far, we are presently working on more detailed simulations, incorporing the structural properties of the present-day Galactic bulge as inferred from star-count techniques (e.g., Robin et al., 2012).

As a first objective of the present thesis, we added a non-axisymmetric Gravitational potential to the classical axisymmetric Gravitational potential model of the BGM. For this purpose, we include the contribution of the Galactic boxy/peanut bar presented by Robin et al. (2012). In this model, some modifications are made on the non-axisymmetric

Galactic potential of Pichardo et al. (see model of superposition in 2004) to mimic the BGM profiles. On the other hands, the Einasto spheroids that define the thin disk structure are mapped according to the density stratification methodology– see Pichardo et al. (2004) for details. The Gravitational potential from these structures are combined consistently with the mass model of all components including the Interstellar medium (ISM), the thick disk, the stellar halo, and an isothermal dark matter component, in order to reproduce the Gravitational potential of the updated version of the BGM.

This thesis has been based on different aspects of the Milky Way, aims to shed some light in the comprehension of its structure, stellar content, and some kinematics behaviour, particularly associated with the Galactic bulge.

The outline of the present work is as follows. After this general introductory chapter, in §2 we briefly summarize the origin of the observational data used in this work. In §3, the properties and construction of the gravitational potential model employed in this thesis to compute stellar orbits and massless particle simulations are presented. In §4 a detailed description of the method employed to generate and to compute test particle simulations, and the relevant results concerning the vertical and radial velocity dispersions are provided. The chapter ends with a qualitative comparison of the distance and the line-of-sight velocity (V_{los}) as predicted by the Besançon Galaxy model (Robin et al., 2003, 2012, 2014), our test particles simulations, and the APOGEE dataset towards the Milky Way bulge. In §5 we present the main physical constrains of the Galactic bar, and the predicted velocity maps (V_{los}), and velocity dispersion profiles of our best-fit model to BRAVA dataset, the chapter ends with relevant conclusions and discussion of the limitations of our model. In §6 we discuss the effect of the "boxy/peanut" bar on the shape and kinematics of the stellar halo. In §7 we introduce for the first time a new approach to identify, characterize and quantify particles captured by the bar potential and its relation with the Jacobi energy, and limit our result to the general understanding of the observed kinematic behaviour towards the Galactic bulge. In §8 we present a first application of our Galactic potential and orbital elements are analysed with focus on the eccentricity and orbital Jacobi energy. The chapter ends with relevant discovery, a chemically anomalous giant star in the Milky Way field and its relation with globular clusters. The conclusions and perspectives of the present work are presented in §9.

Chapter 2

Observational data

This chapter briefly describes the origin of the observational data used throughout this work.

2.1 APOGEE

Through this work we make use of data (Data Release 13, DR13) acquired in the **A**pache **P**oint **O**bservatory **G**alactic **E**volution **E**xperiment (APOGEE; Majewski et al., 2015) with the APOGEE multi-object fiber spectrograph (Wilson et al., 2010) of $\sim$ 300 fibers mounted at the Sloan Digital Sky Survey 2.5-m telescope (Gunn et al., 2006), covering a field of view of $\sim$ 3 sq. degree and observing in the spectral regime of $1.51 - 1.70$ μm ($H-$band). APOGEE is a near-infrared and high resolution ($R \sim 22,000$) spectroscopic survey, part of the SDSS III (Eisenstein et al., 2011, SDSSIII), mapping $\sim$100,000 red giant stars (Holtzman et al., 2015) around all components of the Milky Way (bulge, halo, and disk). Figure 2.1 display the aitoff projection in Galactic coordinates of the DR12 APOGEE survey.

The APOGEE target information is widely described in Zasowski et al. (2013), and this includes globular cluster stars, open cluster stars, moving groups candidates, among others. The reduction of each APOGEE spectrum, as well as the determination of radial velocities with typical uncertainties better than 1 km s^{-1}, and derivation of elemental abundances and stellar atmospheric parameters are based on the ASPCAP[1] pipeline (a software developed for the automated analysis of APOGEE spectra) (Nidever et al., 2015; Holtzman et al., 2015; García Pérez et al., 2016). The ASPCAP pipeline interpolates in a grid of synthetic spectra (Zamora et al., 2015) to find the best fit, through χ^2 minimization, to the observed spectrum by varying $T_{\rm eff}$, [M/H], log g, ϵ, [C/M], [N/M], and [α/M].

The APOGEE distances are computed from spectro-photometric bayesian methods, with a typical random distance error of $\sim$30% for giants (see e.g., Santiago et al., 2016). APOGEE is the only near-infrared spectrocopic survey able to provide accurate information for many atomic (C, N, O, Na, Mg, Al, Si, S, K, Ca, Ti, V, Mn, Fe, Ni, P, Cl, Ti, V, Cr, Cu, etc) and molecular (CO, CN, OH) species, and also with the ability to identify neutron-capture element abundances including Neodymium, Nd II ($Z = 60$) (see

[1]The acronym ASPCAP means: The APOGEE Stellar Parameter and Chemical Abundances Pipeline

e.g., Hasselquist et al., 2016), and Cerium Ce II (private communication from Cunha, 2017) (these elements will be available in the forthcoming APOGEE DR14), many of these elements are now available in the APOGEE DR13 catalogue (SDSS Collaboration et al., 2016).

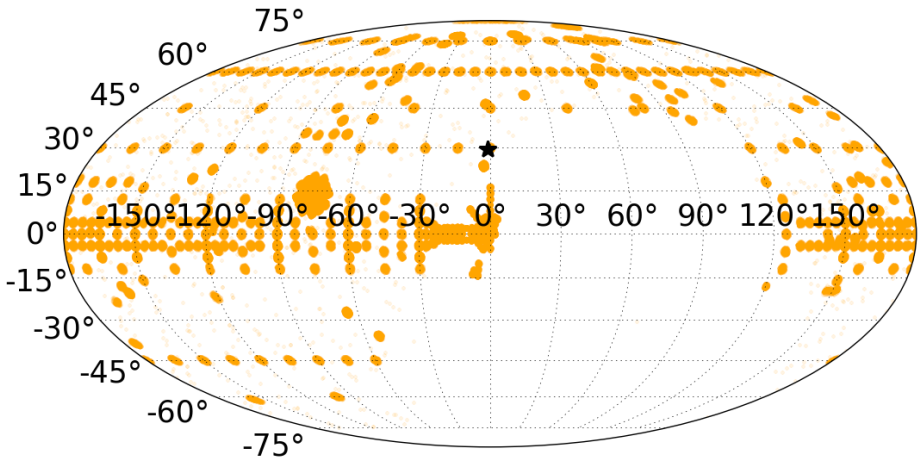

Figure 2.1: Aitoff projection in Galactic coordinates of the DR12 APOGEE survey. The black "star" symbol denote the galactocentric localization of the field giant star 2M16011638-1201525, which have unusual abundance pattern in the "light" elements (Al, N, Mg, C) and also enhanced in the $s-$process elements (Nd II, Ce II) found in the APOGEE survey by Fernández-Trincado et al. (2016a); Hasselquist et al. (2016); Cunha (2017), see §8.

2.2 SEGUE

In §3 we use the same datasets listed in Table 3 in Bovy & Rix (2013) in order to compare the measures of the vertical force with the predictions of our barred Milky Way model, around the galactocentric radius between 4 kpc to 9 kpc, and at heights above the Galactic plane of 1.1 kpc. These measurements come essentially from a sample of G-type dwarfs stars (see Bovy et al., 2012) (along the galactocentric radius, $5 < r_{gal} < 12$ kpc, and height above the plane $0.3 < Z < 3$ kpc), selected from the **S**loan **E**xtension for **G**alactic **U**nderstanding and **E**xploration (SDSS/SEGUE) survey (Yanny et al., 2009), and available as part of the SDSS-II Data Release 7 (DR7) (Abazajian et al., 2009). SEGUE is a imaging and low-resolution (R ∼1,800) spectrocopic survey around of the Milky Way targeting ∼ 240,000 stars in the spectral regime of 3900Å to 9000Å and in the magnitude range $14 < g <$20.3 (see Yanny et al., 2009). Additionally, SEGUE also provides multicolor imaging in five photometric bands $ugriz$ for ∼ 3500 sq. degree of the Milky Way at low Galactic latitudes ($b < 35°$). In §8 we also compare the eccentricity distribution for a sample of ∼ 34,223 G-dwarfs stars from the SEGUE DR7 datasets (see Dierickx et al., 2010) with distances and velocities available, with the eccentricity distribution as predicted from our barred Milky Way model.

2.3 BRAVA

The **B**ulge **RA**dial **V**elocity **A**ssay survey (BRAVA; Howard et al., 2008; Kunder et al., 2012) is a large scale spectroscopic survey to obtain radial velocity for over ∼ 10,000 M-type giants samping the Galactic bulge, covering the Galactic latitudes b =-4°, -6°, and -8°, and Galactic longitudes $-10° < l < +10°$, and using the Hydra multifiber bench spectrograph (with a effective resolving power of R∼4,200 central $\lambda \sim 7900$ Å, in order to retain the TiO band at ∼ 7050 Å, and three CaT lines between ∼ 8500 - 8750 Å) at the Cassegrain focus of the Cerro Tololo Inter-American Observatory (CTIO) Blanco 4-m telescope (for details, see Howard et al., 2008). Figure 2.2 display the observed BRAVA fields towards the Milky Way bulge. The main result of the BRAVA survey shows that the Galactic boxy bulge rotates cylindrically (Howard et al., 2009; Kunder et al., 2012) and the N-body models including a boxy/peanut bar fit fairly well the BRAVA kinematics (Shen et al., 2010; Gardner et al., 2014; Portail et al., 2017, and reference therein), these results have been recently confirmed from medium resolution spectroscopic survey ARGOS (Abundances and Radial velocity Galactic Origins Survey Freeman et al., 2013; Ness et al., 2013b), surveying ∼ 28,000 stars towards the Galactic bulge and the inner disk; and from APOGEE data including the bulge region (Ness et al., 2016).

2.4 TGAS

In §8 we make use of a sub-sample of giant stars from the APOGEE DR12 combined with accurate astrometric information from the Gaia Data Release 1 **T**ycho-**G**aia **A**strometric **S**olution (TGAS) data (Gaia Collaboration et al., 2016a), recently compiled by Allende Prieto et al. (2016).

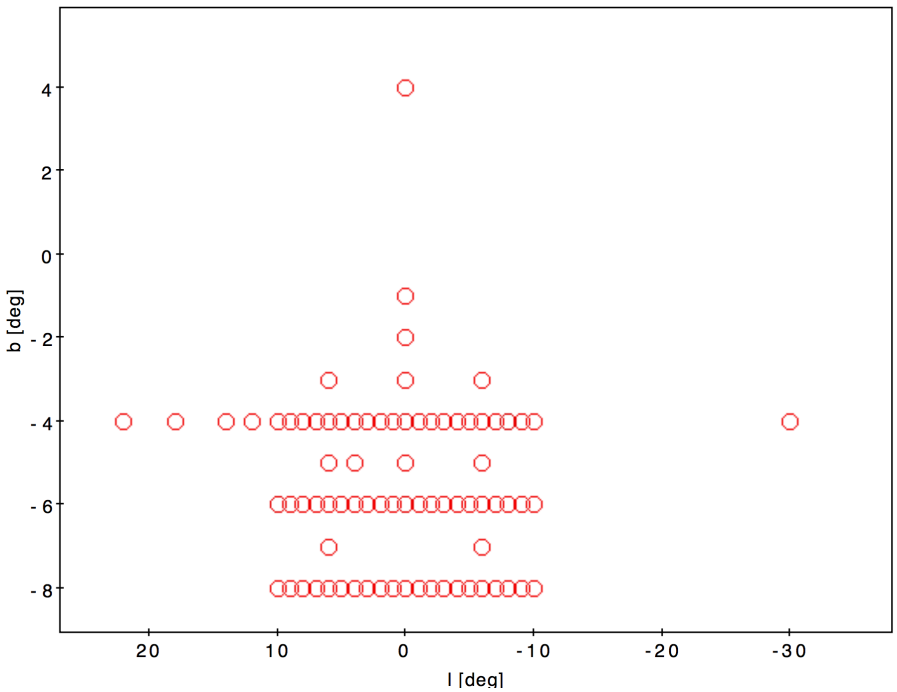

Figure 2.2: Galactocentric distribution of the BRAVA fields.

The TGAS datasets contains the Tycho-Gaia astrometric solutions (Michalik et al., 2015; Lindegren et al., 2016), and provides the astrometric information, parallaxes, proper motions and positions for $\sim 2 \times 10^6$ stars (with magnitudes below V ~11.0) in common with the Tycho-2 catalogue (Høg et al., 2000). Figure 2.3 shows the aitoff projection in Galactic coordinates of the whole sky from the Gaia Data Release 1 TGAS sources.

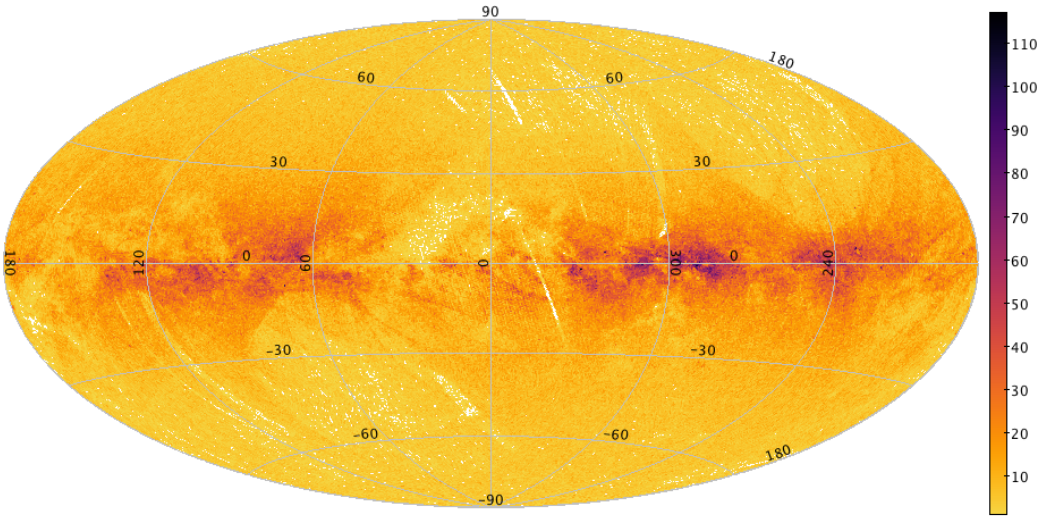

Figure 2.3: Aitoff projection in Galactic coordinates of the Gaia Data Release 1 TGAS dataset. The colours indicate the kernel density estimate per bin.

2.5 RAVE

The **R**adial **V**elocity **E**xperiment (RAVE) (Steinmetz et al., 2006; Zwitter et al., 2008; Siebert et al., 2011) Data Release 4(Kordopatis et al., 2013) is a large multi-fiber (six degree field) spectroscopic survey (medium resolution, $R \sim 7,000$) mapping $\sim$ 483,330 stars around ~20,000 sq. degree of sky towards the southern hemisphere with the 1.2-m UK Schmidt Telescope of the Australian Astronomical Observatory (AAO), and observing in the spectral regime of 8410Å−8794Å around Ca II triplet for stars in the magnitude range $8 < I < 12$. The RAVE DR4 catalogue provides radial velocity information with uncertainties better than 2 km s^{-1}, stellar parameters and distances with uncertainties around 20%, and chemical abundances for six elements (Al, Si, Fe, Ti, Ni, Mg) with a mean error of ~0.2 dex (Boeche et al., 2008). Figure 2.4 shows the aitoff projection in Galactic coordinates of the RAVE DR4 survey.

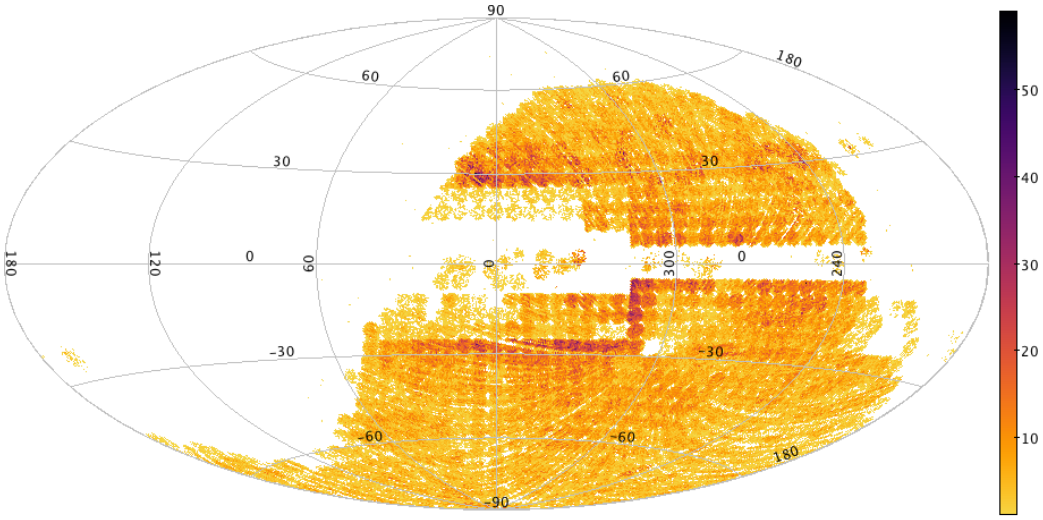

Figure 2.4: Aitoff projection in Galactic coordinates of the RAVE DR4 dataset. The colours indicate the kernel density estimate per bin.

Chapter 3

The Milky Way potential

The main purpose of this chapter, is to present and discuss the numerical scheme of the Gravitational potential model of the Milky Way, hereafter called "GravPot16" model, combining the 3D mass density distribution of the Milky Way predicted by the Besançon synthetic model (Robin et al., 2003, 2012, 2014). We have also performed 3D test particle simulations aiming to set the kinematics of the Besançon Galaxy model and to explore the dynamical properties of a barred bulge. The results will be presented in the next chapters.

To carry out this research we focus on the framework of the Besançon model of stellar populations synthesis of the Galaxy (e.g., Robin et al., 2003, 2012, 2014), which reproduces fairly well the stellar content of the Milky Way. The model was originally built by Robin & Crézé (1986a,b) to compare the prediction of synthetic stellar populations in parts of the parameter space (i.e., colours, luminosity, etc) along each line of signal in the sky with observed stars, aiming to understand the link between observations and Galactic components.

3.1 Overview of the Besançon Galaxy model

As already mentioned, the density profiles of the Besançon Galaxy model (BGM) introduced originally by Robin et al. (2003) constitutes the backbone of the GravPot16 model in terms of the mass density distribution. Here, we outline briefly the basics of the BGM model:

The Besançon Galaxy model is a semi-empirical and self-consistent dynamical model, built to reproduce different stellar populations of the Milky Way. In this sense, the originality of the model is based on computations of self-consistent numerical solutions of the Poisson equation, the first moment of the Boltzmann equation, and the age-vertical velocity dispersion (e.g., Bienaymé et al., 1987) at the solar position, in order to constrain the axis ratios (ϵ) of the thin disk. A set of density laws are generated in the process of self-consistency that are directly translated in terms of general star count predictions, used to constrain stellar populations models. Over time, the classical scheme of self-consistency dynamics introduced for first time by Bienaymé et al. (1987) has remained in many versions of the model, while the global Gravitational potential has been inferred from axisymmetric components (see Bienaymé et al., 1987; Bienaymé et al., 2015).

Since 2003, the BGM has been updated several times. Nevertheless, from the point of view of dynamics, non-axisymmetric components have not been added. Here, we describe briefly the more relevant changes during the last two decades:

- A 3D extinction model was added by Marshall et al. (2006).
- The fit of the warp and flare parameters in the outer disk was performed by Reylé et al. (2009). In this work, we assumed negligible effects of this component on the Gravitational potential, because we are interested in a kinematics study of the inner regions of the Milky Way.
- In Robin et al. (2012) a new density law was presented, finding a boxy/peanut (B/P) morphology (the *boxy bar*) in the inner regions of the Milky Way, inferred from star counts in the 2MASS and SDSS surveys. The authors showed that the boxy bulge is oriented at $\sim 13^{\circ}$ (at positive longitudes), and the total mass contained in the so-called bar is estimated to be $\sim 0.63 \times 10^{10}$ $M_{\odot}$. Anticipating the results presented in §5, we note that their results do not provide a good fit to the global kinematics trends of the Milky Way bulge, leading to the hypothesis that incompleteness in the dataset could potentially bias the determination of the main physical parameters of the Galactic bar (angle orientation, mass, length scales, etc).
- Binary stars, and other parameters, such as the Initial Mass Function and Star Formation History, and new evolutionary tracks have been recently revised in Czekaj et al. (2014), still acccounting for the classical scheme of dynamical self-consistency
- An improved fit of the thick disc and stellar halo populations was performed by Robin et al. (2014).

These modifications are needed to be accounted in the computation of the Gravitational potential to accurately evaluate the kinematics response to several different potential models.

3.2 Updating the potential model

In the following, we describe the assembly of the overall global gravitational potential It consists of seven thin disks, two thick disks, a Hernquist stellar halo, the presence of the interstellar matter also contributes to the global potential, a bulge dominated by a boxy/peanut shaped structure, and a spherical distribution of dark matter surrounding the baryonic matter. These components constitutes the backbone of our Milky Way gravitational potential model. We also consider the functional form of other galactic contributions, i.e., a super massive black hole, and a stellar and central mass distribution, which do not participate in our Milky Way's model, unless otherwise noted. The whole model is described as follows:

$$\Phi(r_{gal}, z_{gal}) = \Phi_{axi}(r_{gal}, z_{gal}) + \Phi_{non-axi}(r_{gal}, z_{gal}) + \Phi_{opc}(r_{gal}, z_{gal}) \tag{3.1}$$

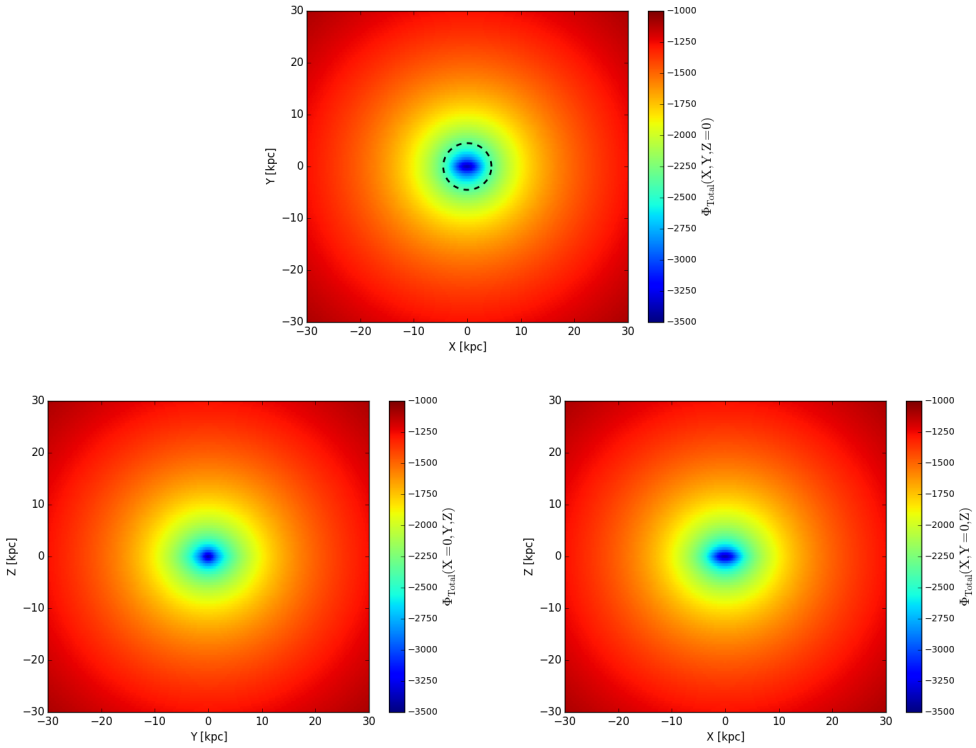

Figure 3.1: 3D map of the gravitational potential resulting from the GravPot16 model (axisymmetric plus non-axisymmetric model) in the Galactic non-inertial frame where the bar is at rest. The black dashed line refers to the co-rotation radius about ∼6.5 kpc (see text). Φ_{Total}(X,Y,Z) are in units of 100 km^2 s^{-2}.

where, $\Phi_{axi}(r_{gal}, z_{gal})$ is the gravitational potential of the axisymmetric model; $\Phi_{non-axi}(r_{gal}, z_{gal})$ is the gravitational potential of the non-axisymmetric model (the boxy/peanut bulge structure), and $\Phi_{opc}(r_{gal}, z_{gal})$ the optional gravitational potential associated with a super massive black hole and/or a spherically symmetric potential of the form Miyamoto, with the functional forms as given in Eq. 3.2 and Eq. 3.3, respectively:

$$\Phi_{SBH}(r_{gal}, z_{gal}) = -\frac{M_{BH}}{(r_{gal}^2 + z^2)^{1/2}} \tag{3.2}$$

where $M_{BH} = 4 \times 10^{10}$ $M_\odot$ is the mass of the super massive black hole (SBH) at the center of the Milky Way (e.g., Gillessen et al., 2009)

$$\Phi_{CM}(r_{gal}, z_{gal}) = -\frac{M_{CM}}{(r_{gal}^2 + z^2 + r_{core}^2)^{1/2}} \tag{3.3}$$

where M_{CM} is the mass of the spherically symmetric potential, and r_{core} is the core radius. Each set of parameters, M_{CM}, and r_{core} are adopted to follow the mass and major axis of the bulge presented in Robin et al. (2012). The role of this component will be the subject of further chapter, see §4. For this component, the potential is computed from the spherically symetric distribution function given by Miyamoto & Nagai (1975).

The structural parameters of the density profiles of the Galactic components used in this work, are summarized in Appendix A, and are essentially the same as in Robin et al. (2003, 2012, 2014).

Figure 3.1 illustrates the 3D map of the potential energy resulting from our model (seven thin disks, two thick disks, the ISM, the Hernquist stellar halo, the Galactic bar, and the dark matter halo), in the non-inertial frame where the bar is at rest, as well as the localization of the co-rotation radius ($\sim$ 6.5 kpc), see §5.

In §4 we employ an axisymmetric model dominated by a spherically symmetric bulge (see Eqn. 3.3), which is employed to grow adiabatically the "boxy/peanut" bar structure into the bulge, to allow particles to reach a reasonable state of statistical equilibrium.

In the following subsections, the methodology employed to determining the Milky Way's potential for multiple disks, the interstellar matter, the stellar halo, the boxy/peanut bar, and the dark matter are presented.

3.3 Axisymmetric approach

3.3.1 The thin disk

In Robin et al. (2003) the global mass density distribution of the thin disk is well modeled from the superposition of oblate spheroid of parametrized surfaces $a_i^2 = r_{gal}^2 + (z/\epsilon_i)^2$, where ϵ_i span range of reasonable values for the ratio of scale-height to scale-length and depend on the age of the sub-component, see Appendix A. While the mass is well constrained from the observed rotation curve, wich gives adjusted values for ϵ_i from the so-called method of "dynamical self-consistency" at the solar Galactic radius position, as presented in Bienaymé et al. (1987), the gravitational potential in the current versions describing the thin disk of the Besançon Galaxy model (e.g., Robin et al., 2003, 2012,

2014; Czekaj et al., 2014) is not computed everywhere in space to allow computation of stellar orbits.

Some improvements have been recently examined by Bienaymé et al. (2015) using Stäckel potentials fitting, which adopt simple expressions for the integral of motions. This method provides a good local approximation of axisymmetric potentials in disk galaxies as has been pointed out in Bienaymé et al. (2015). However, such a Stäckel potential fit fails at low galactic radius closer to the Galactic bulge, and beyond when non-axisymmetric structures are considered, where the integrals of motions are not straightforwardly conserved. In this work we therefore improve this picture, and we employ an axisymmetric plus non-axisymmetric gravitational model, which is valid everywhere in the Milky Way.

A point to be emphasized is that here we employ the gravitational potential associated to each thin disk component as the sum of "homogeneous oblate spheroid" where the functional expressions are numerically solved (see Schmidt, 1956), and whose density laws approximate the density model of Robin et al. (2003) with a step-stair function. Each stair-step function represents a homogeneous spheroid component (see, for example, the Fig. 10 in Pichardo et al., 2004). The basic idea to compute the three-dimensional potential of the thin disk consists in considering that the mass density distribution can be approximated locally in a linear form, i.e, by a succession of linear segments.

In our study, we fixed $N = 200$ components, which approximates well enough the density profiles of the thin disk. We note that a larger value of N improves rapidly the density approximation, but produces practically the same orbits. It is important to note, that this part of the GravPot16 code was developed by Edmundo Moreno, and form part of a more general axisymmetric model, where a new approach and new methodology to solve 3D axisymmetric potentials will be presented in a forthcoming paper (Moreno, Fernández-Trincado, et al., in preparation).

Figure 3.2 illustrates an example of the orbital projection onto the r_{gal} - Z plane for the globular cluster NGC 6712 derived from our potential model, when $N = 200$ and $N = 500$ is employed. Note that while the orbital structure is very similar in both cases, leading to practically the same orbital parameters (eccentricity, apo-, and peri-galactocentric distances, etc), the variation of the orbital Jacobi constant, varies in an order of magnitude, i.e., $|(E_J - E_J^{initial})/E_J^{initial}| \sim 10^{-9}$ to $|E_J - E_J^{initial}/E_J^{initial}| \sim 10^{-11}$. It is a relatively small error and accurate enough for orbital analysis, we have favored $N = 200$ to decrease the computing time.

3.3.2 The thick disk and ISM

Robin et al. (2014) found that the superposition of a young and old thick disk was better to adjust the 2MASS data, and two functional forms were used by the authors, a radially exponential disk with a exponentially decaying vertical distribution "shape-A", and a radially exponential disk with a vertical density of the form $sech^2$ "shape-B". For the computations in this work, we have adopted the second shape, the so-called *shape B*, which consists of a simple hyperbolic secant squared with three parameters, i.e., the local normalisation C_{thick}, the scale height h_z, and the scale length $h_{r_{gal}}$. Appendix A summarises such structural parameters for the two components of the thick disk and

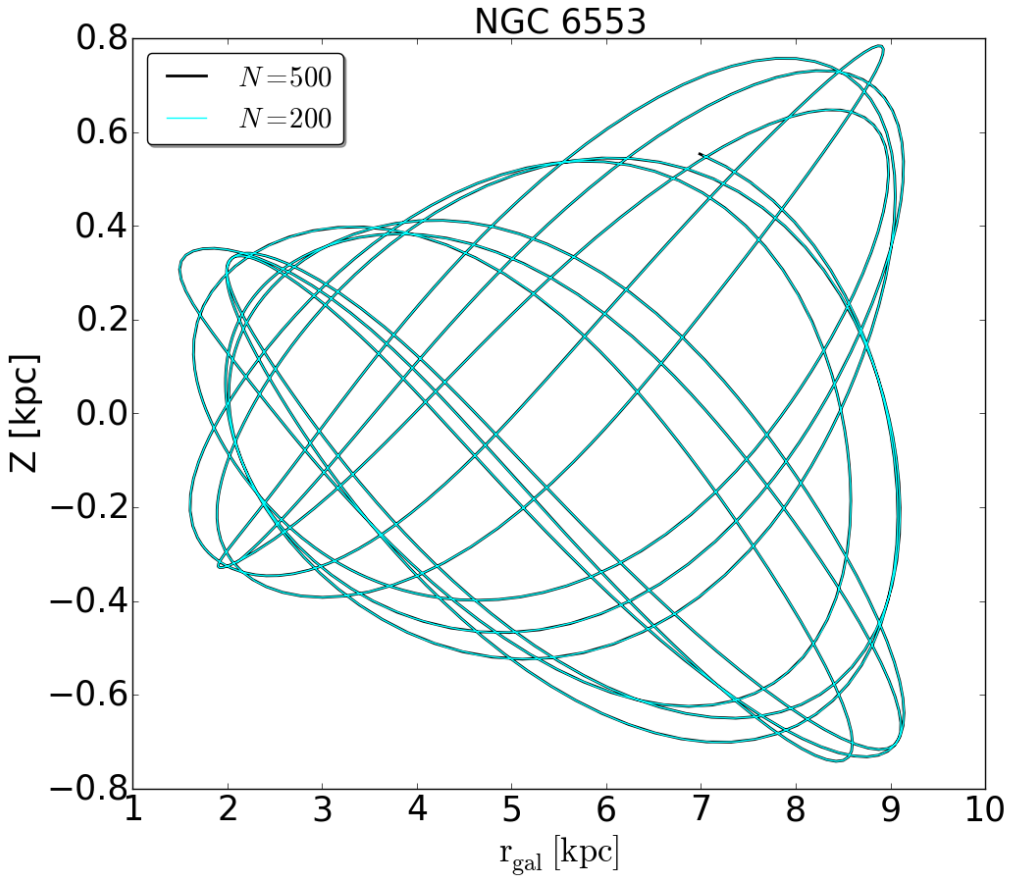

Figure 3.2: Projection of the orbit of the globular cluster NGC 6553 onto the $r_{gal}-$Z plane. The cyan line is the orbital projection from the adopted thin disk potential model with $N = 200$ components, and black line for $N = 500$ components (see text for the definition of N).

interstellar matter employed in this work.

The gravitational potential is built following the same approach recently developed by Smith et al. (2015), which consists in the superposition of three Miyamoto-Nagai disks (3MN models), with different mass (M_d), radial scalelengths (a), and common vertical scaleheight (b), giving a good approximation to the radially exponential stellar thick disk of the Milky Way, i.e., $< 1.5\%$ within 10 kpc, as compared with those calculated using the expressions in Bienaymé et al. (1987); Kuijken & Gilmore (1989) widely used in previous versions of the Besançon Galaxy model (see Robin et al., 2003). The gravitational potential of the thick disk and ISM becomes

Young thick disk,

$$\Phi_{young}(r_{gal}, z_{gal}) \equiv -\sum_{i=1}^{3} \frac{f_i(M_{total})}{\sqrt{r_{gal}^2 + (a_i + \sqrt{z^2 + b^2})^2}} \tag{3.4}$$

where $M_{total} = 7.38 \times 10^9$ $M_\odot$ is the total mass, the radial scalelengths $a_1 = 0.927$ kpc, $a_2 = 4.984$ kpc, and $a_3 = 4.374$ kpc, and the vertical scaleheight $b = 0.513$ kpc.

Old thick disk,

$$\Phi_{old}(r_{gal}, z_{gal}) \equiv -\sum_{j=1}^{3} \frac{f_j(M_{total})}{\sqrt{r_{gal}^2 + (a_j + \sqrt{z^2 + b^2})^2}} \tag{3.5}$$

where $M_{total} = 1.33 \times 10^9$ $M_\odot$ is the total mass, the radial scalelengths $a_1 = 0.898$ kpc, $a_2 = 6.622$ kpc, and $a_3 = 5.85$ kpc, and the vertical scaleheight $b = 1.259$ kpc.

ISM,

$$\Phi_{ISM}(r_{gal}, z_{gal}) \equiv -\sum_{k=1}^{3} \frac{f_k(M_{total})}{\sqrt{r_{gal}^2 + (a_k + \sqrt{z^2 + b^2})^2}} \tag{3.6}$$

where $M_{total} = 4.95 \times 10^9$ $M_\odot$ is the total mass, the radial scalelengths $a_1 = 2.79$ kpc, $a_2 = 11.93$ kpc, and $a_3 = 10.34$ kpc, and the vertical scaleheight $b^{ISM} = 0.16$ kpc.

$f_i(M_{total})$, $f_j(M_{total})$, and $f_k(M_{total})$, in Eqns. 3.4, 3.5, and 3.6 are the 4th-order fit to the total mass, calculated using the eqn. 7 and Table 2 in (Smith et al., 2015). In the same manner the parameters a1-a3 are obtained, while b is the solution of the 3th order polynomial fit as illustrated in Figure 5 in (Smith et al., 2015).

So far, we have compared the rotation curves derived using Eqs. 3.4, 3.5, and 3.6 with the one obtained using the expressions in Kuijken & Gilmore (1989). In our study both methods (e.g., Kuijken & Gilmore, 1989; Smith et al., 2015) give practically the same results (see Figure 3.3) within a 5 kpc sphere around the Milky Way bulge, which is enough to derive the kinematics in this region from test particle simulations. Due to the complicated behavior of our gravitational potential models we decide to adopt the 3MN models from Smith et al. (2015) in order to minimize the computing time in test particle simulations (see §5).

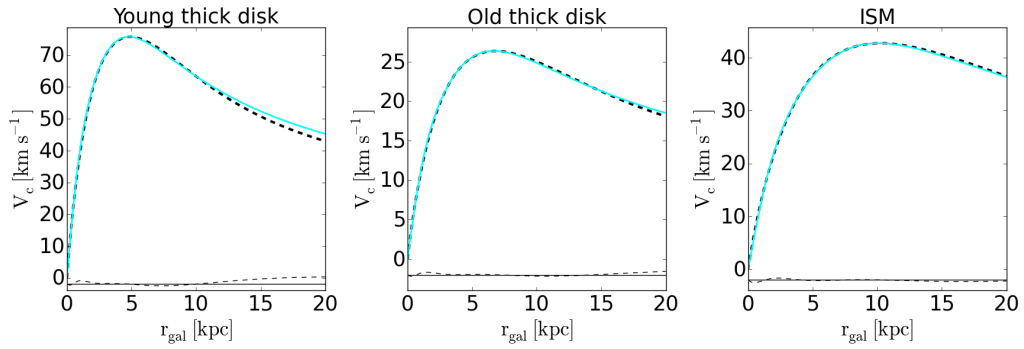

Figure 3.3: Rotation curve of the young-thick disk (left panel), old-thick disk (middle panel), and the ISM (right panel). The rotation curve of the 3MN models (e.g., Smith et al., 2015) is shown (cyan line), and the rotation curve of an exponential disk (black dashed line) as derived from expressions in Appendix A of Kuijken & Gilmore (1989) is shown. The black dashed horizontal lines shows the difference in velocity between both methods, and the black solid line is referred to the zero level.

3.3.3 The stellar halo

The stellar halo is the least massive structure in our fiducial model, and its contribution to the total mass of the model is assumed to be $< 1\%$. We model the stellar halo as the sum of homogeneous oblate spheroids, following the step-stair method introduced by Pichardo et al. (2004) in order to construct an inhomogeneous oblate spheroid. The density profile has the form given in eqn. 6 in Robin et al. (2014), which we repeat in Appendix A for completeness. The potential and forces are calculated using the expressions in subsection 3.1.1 in Pichardo (2003) based in Schmidt (1956), which we repeat here for completeness

$$-\frac{\partial \Phi}{\partial r_{gal}} = -4\pi e^{-3}(1-e^2)^{1/2} r_{gal} \int_0^{\beta} \rho sin^2\beta d\beta \tag{3.7}$$

$$-\frac{\partial \Phi}{\partial z} = -4\pi e^{-3}(1-e^2)^{1/2} z \int_0^{\beta} \rho tan^2\beta d\beta \tag{3.8}$$

$$\Phi = -4\pi e^{-1}\sqrt{1-e^2}\left[\int_0^{r_p} \rho a\beta da + sin^{-1}e \int_{r_p}^{r_N} \rho a da\right] \tag{3.9}$$

where ρ is the constant density of the spheroid (e.g., Pichardo et al., 2003), $sin\beta = e$ if r=(x,y,z) is internal to the inhomogeneous oblate spheroid, and r_p is the effective boundary radius of the spheroid, where the density is equal to zero, and $N = 200$ is number of partitions of the spheroid (shells). If r=(x,y,z) is external point to r_p, then the solution to β is given by $r_{gal}^2 sin^2\beta + z^2 tan^2\beta = a^2e^2$, and the right hand term in Eq. 3.9 is zero.

3.3.4 The dark halo

We maintained the isothermal sphere employed by Robin et al. (2003), and their potential is calculated using the functional form as in Appendix A of Caldwell & Ostriker (1981), repeated here to guide to the reader:

$$\Phi_{DM}(r_{gal}, z_{gal}) = -C_{DM} \times \left[1 + ln\left(\frac{1 + (R_{100}/r_{dm})^2}{1 + ((r_{gal}^2 + z^2)^{1/2}/r_{dm})^2}\right)\right] + C_{DM} \times \left(\frac{tan^{-1}((r_{gal}^2 + z^2)^{1/2}/r_{dm})}{((r_{gal}^2 + z^2)^{1/2}/r_{dm})}\right) \tag{3.10}$$

where C_{DM} is a constant in Galactic units, related to the physical parameters tabulated in A, i.e., the core radius (r_{dm}) and the local density, both of them fitted to the observed rotation curve as described in subsection 2.2.1 in Bienaymé et al. (1987). In this work, the dark matter halo is truncated at $R_{100} = 100$ kpc (e.g., Bienaymé et al., 1987, we keep the original configuration of the dark matter halo truncation radius adopted in the BGM; see).

3.4 Non-axisymmetric approach

In Pichardo et al. (2004) three different techniques to produce a three-dimensional Galactic bar structure were introduced (the ellipsoidal model, the prolate model, and the model of superposition of ellipsoids). These models consist in the sum of concentric homogeneous prolate spheroids ($a > b = c$) and homogeneous ellipsoids ($a > b > c$) where the functional expressions of the potential and force are analytically solved. To calculate the best combination of homogeneous spheroids and homogeneous ellipsoids a step-stair function is employed to approximate the density law of a given bar density (e.g., see Appendix A in Pichardo et al., 2004). Figure 3.4 taken from Figure 4.7 and Figure 4.8 in Pichardo (2003) illustrates an example of the arrangement of homogeneous prolate spheroids (bottom panel) to construct a prolate bar (or inhomogeneous prolate spheroid) which approximate the density model of Freudenreich (1998). The same figure (top panel) shows estimates of the density profile following a step-stair function, where each spheroidal shell have a constant density within a relative variation along the semi-major axis of similar spheroidal surface.

In order to construct a comprehensive orbital study of particles in the Milky Way bulge, we choose to employ the model of superposition of ellipsoids of Pichardo et al. (2004) well-suited to approximate the observed profile of the "boxy/peanut" bar of Robin et al. (2012). We build our triaxial potential by adopting the model of the triaxial boxy bar presented in Pichardo et al. (2004), we search for the new set of parameters $\{k_1, k_2, k_3, k_4, k_5, k_6, k_7, k_8, \theta_1, \theta_2\}$={ 1.1409, 1.4702, 1.0962, 0.237, 0.9980, 1.3424, 1.1802, 0.2537, 0.7669, 0.2609 } that approximates our density law. To generate these parameters, we use a similar procedure as described in (Appendix C; Pichardo et al., 2004), i.e., we generate a fine mesh of radial directions, and find the distances to the orgin of the corresponding points on the surfaces (e.g., Pichardo et al., 2004) of the ellipsoidal model ($\rho_{model}(r)$) and

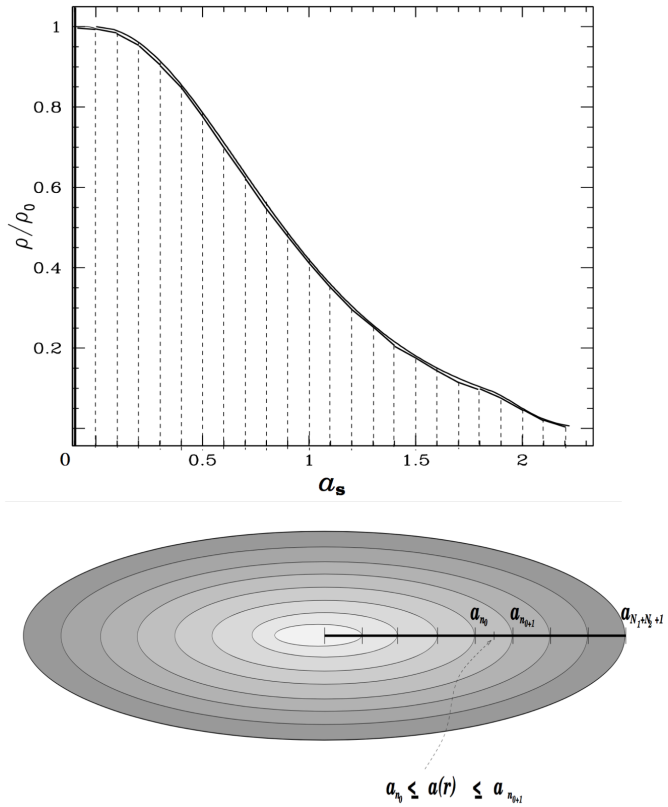

Figure 3.4: These figures have been taken in its original form from Pichardo (2003). Top panel illustrates the step-stair function, where the density of each spheroidal surface approximates the density model of Freudenreich (1998) as a function of the semi-major axis (a_s). The bottom panel illustrates the superposition of concentric homogeneous prolate spheroid, where $a(r)$ is the surface of an arbitrary point inside the region of superposition.

the density profile ($\rho_{bar-BGM}(r)$) of Robin et al. (2012), and determining the goodness of fit from a χ^2 measure between both profiles, we obtain the set scaled ellipsoidal surfaces that approximate of the surface in Robin et al. (2012).

For the Galactic potential we use the same codes developed in Pichardo (2003), which we modified to match the required density law. The main mathematical forms of the gravitational potential of this model are extensively described in Pichardo et al. (2004). The main adopted observational structural parameters of the bar fitted to 2MASS dataset in Robin et al. (2012), the scale lengths are: a = 1.46 kpc, b = 0.49 kpc, c = 0.39 kpc, and the exponents $C_{||} = 3.007$, and $C_{\perp} = 3.329$. They point out that the main parameters of the bar are statistically better fitted with a angle orientation of the bar respect to the Sun-Galactic center line of $\sim 13°$, with a mass of about 0.63×10^{10} $M_{\odot}$. However, these last values (angle orientation and mass), seems in disagreement with the dynamical approach in the present study. The pattern speed of the bar, the new mass estimation and angle orientation will be extensively analysed in §5.

3.5 The overall rotation profile

Figure 3.5 display the resulting overall rotation profile as predicted by our Milky Way model obtained by averaging the azimuthal radial force within the plane ($\langle \nabla \mathbf{\Phi}(\mathbf{x}, \mathbf{y}, \mathbf{z} = \mathbf{0}, \phi) \rangle$) along $\mathbf{r_{gal}}(\mathbf{x}, \mathbf{y}, \mathbf{z} = \mathbf{0})$ as defined in Eq. 3.11, i.e., for a given galactocentric radius ($\mathbf{r_{gal}}$) we compute the mean azimuthal radial force in a non-inertial reference frame to generates the overall rotation profile compatible with that obtained by Sofue (2015).

$$V_c^2 = -\mathbf{r_{gal}}(\mathbf{x}, \mathbf{y}, \mathbf{z} = \mathbf{0}) \cdot \langle \nabla \Phi(x, y, z = 0, \phi) \rangle \tag{3.11}$$

The mean rotation profile is scaled to the composite data (terminal velocity measurement of CO and H_I gas) from Sofue (2015), which gives a circular rotation speed of 244.5 km $^{-1}$ at an assumed Galactocentric distance of the Sun in 8 kpc. Note that the rotation profile is fitted beyond 4.5 kpc from the Galactic centre, and internal measurements from the Sofue (2015) dataset were excluded, i.e., we do not consider any fit in the inner regions (pink shadow region in Figure 3.5), for the following reasons:

1.) Stellar orbits and/or particle simulations (see §4, §5, §6, §7) in the inner regions of the Milky Way do not draw perfect circular motion given the complex geometry of the gravitational potential in these regions, or at least stellar circular motion seems to be quite implausible. In other words, the observations does not provide proof/detection for such orbital configurations.

2.) Chemin et al. (2015) claim that the Galactic velocity profile is very likely flawed and does not represent the true Galactic rotation profile for inner galactocentric radius.

3.6 Setting the local dynamic self-consistency

In the previous sections, the axisymmetric and non-axisymmetric approaches employed to assemble the entire gravitational potential model was briefly introduced. The rotation

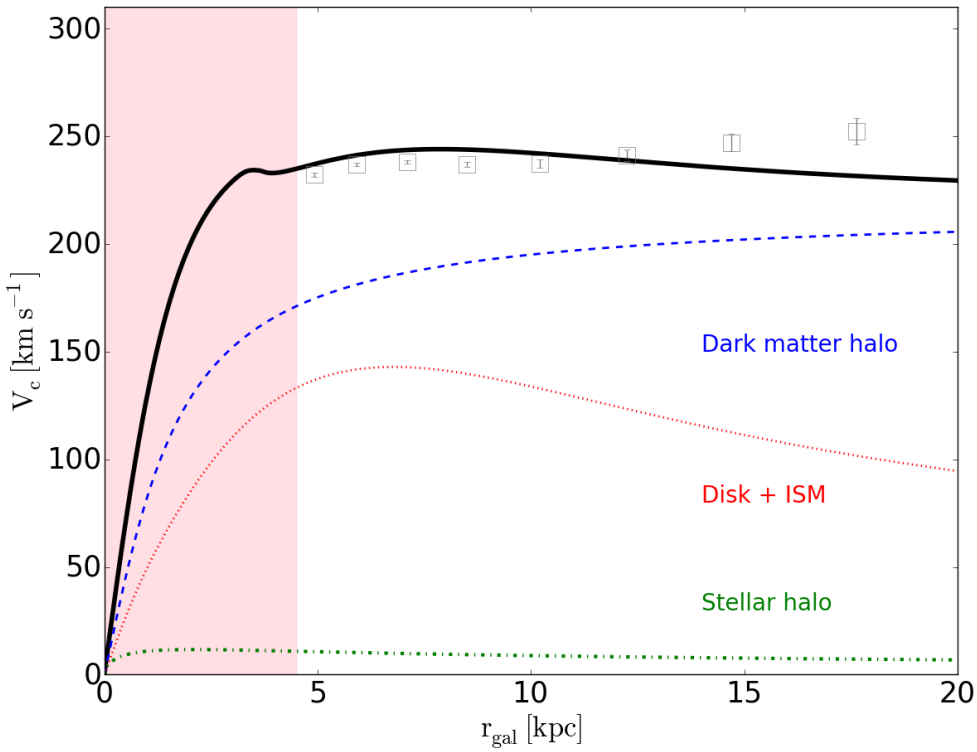

Figure 3.5: The overall rotation profile as predicted in this thesis. We determine the rotation profile as Eq. 3.11, where $\nabla\mathbf{\Phi}(x, y, z = 0, \phi)$ is the azimuthal average of the radial force. The inferred rotation profile does not take into account the super massive black hole and the central mass as described in the text. For comparison, the red and blue dashed lines show the rotation curve as inferred for the stellar disk plus ISM and the dark matter halo, respectively. The green line shows the rotation profile of the stellar halo, and the gray symbols show the inferred rotation profile ($r_{gal} > 4.5$ kpc) from observations from the compilation of Sofue (2015). The overall rotation profile is slightly different from previous versions of the Besançon Galaxy model. In other words, our model has been built to take into account the contribution of the "boxy/peanut" bar towards the inner regions of the Milky Way. It is important to note that the Gravitational potential in the inner region can be relatively uncertain.

Table 3.1: Variation of ratio of scale-height to scale-length (ϵ) for six stellar components of the thin disk, and variations of the core radius and local mass density of the dark matter component as function of the bar angle orientation.

Sub-population	**Age (Gyr)**	$\sim$ **13°**	**20°**	**30°**	**40°**	**50°**
1	0-0.15	0.01400	0.01400	0.01400	0.01400	0.01400
2	0.15-1	0.02245	0.02109	0.01850	0.01542	0.01218
3	1-2	0.03338	0.03150	0.02788	0.02351	0.01883
4	2-3	0.04331	0.04100	0.03653	0.03107	0.02516
5	3-5	0.05527	0.05248	0.04704	0.04036	0.03303
6	5-7	0.06865	0.06534	0.05889	0.05092	0.04209
7	7-10	0.08865	0.08462	0.07672	0.06691	0.05595
-	r_{dm} (kpc)	1.298	1.147	1.006	0.892	0.769
-	$\rho_0(M_\odot/pc^{-3})$	0.5174	0.6543	0.8439	1.070	1.419

profile generated by the model is reasonably compatible with the observed rotation profile as inferred from CO and H_I gas, see §3.5. The next step is to implement and evaluate the non-axisymmetric approach within the "dynamical self-consistency" introduced by Bienaymé et al. (1987), aims to impose constraints upon the main parameters of the thin disk and the dark matter component. The classical scheme of *dynamical self-consistency* has been preserved in all versions of the Besançon synthetic model (e.g., Robin et al., 2003, 2014; Czekaj et al., 2014), in this work, we also keep this approach. It is important to note that the axisymmetric model is "locally" self-consistent but is not guaranteed to be "globally" self-consistent. The effects of the bar in connection with the *dynamical self-consistency* approach will be analysed.

It is important to note that the key point of the Besançon synthetic model to generate the mass density distributions of each component (particularly the thin disk and dark halo) is based on the so-called "dynamical self-consistency" employed in Bienaymé et al. (1987). The method consists in adjusting the axis ratios of each of the thin disk subcomponent, assumed isothermal because it corresponds to a given age, using an age−vertical velocity dispersion (σ_w) at the Solar position, and the Galactic potential, through the Boltzmann equation (Bienaymé et al., 1987). The potential is computed from the Poisson equation. We iterate the process until convergence. We start up with a first guess of the gravitational potential which is dynamically adjusted to the observed rotation profile, searching for the best set of parameters, i.e., the axis ratios (ϵ) of the thin disk, the core radius and local mass density distribution of the dark matter structure, in order to produce a reasonable potential model able to match the rotation profile on the Galactic plane. Thus, the main contribution of this work has been to add non-axisymmetries to the gravitational potential of the Besançon Galaxy model, in order to derive the kinematics of the bulge in presence of a boxy/peanut bar. In the §5, we will further interpret and show the dynamical constraints of the bar, and the 3D kinematics maps of the model. It allows us to determine the velocity field consistenly with the Galactic potential.

In the following, results are given for the axis ratios of the thin disk and the main parameters of the dark matter for the non-axisymmetric potential. Table 3.1 lists the

derived values for the axis ratios and for the dark matter parameters derived from the Boltzmann plus Poisson approach, corresponding to five values of the bar orientation in steps of $\sim 10°$, starting from the present-day bar orientation (e.g., Robin et al., 2012). Note that small variations are found in the parameters as function of the angle orientation, producing small variations (<5 %) in the resulting gravitational potential beyond 4.5 kpc from the Galactic centre. The axis ratio of the younger population of the thin disk is fixed to 0.01399 following Robin et al. (2003), because it is too young to be a relaxed population.

Figure 3.6 shows the vertical force at 1.1 kpc as function of the Galactocentric radius built up with observational data (∼16,269 G-type dwarfs from SEGUE) described in Bovy & Rix (2013) compared with the predicted vertical force from our models. Small values of angles (<30°) are in perfect agreement with the range of values found by Bovy & Rix (2013). These results allow us to be slightly more confident of the quantities predicted by our Milky Way model, for at least, an acceptable range of Galactocentric radii. We see that the impact of changing the orientation of the Galactic bar give practically the same results for angles less than 30° and in all cases the shift is much higher than the observational uncertainties. It is important to note that even when Bovy & Rix (2013) fit an exponential function to the data, our model predicts a trend slightly different, and similar predictions have also been observed with other set of Galactic models (see figure 7 in Pouliasis et al., 2017).

Figure 3.7 shows the rotation velocity profiles for three assumed bar mass models, 0.63×10^{10} $M_\odot$, 1.1×10^{10} $M_\odot$, and 1.6×10^{10} $M_\odot$. These are the respective mass that are entirely transferred from the the spherically symmetric component to the bar structure (see §4). The resulting rotation velocity profiles give practically the same results and shapes beyond 4.5 kpc, while that in the inner regions the peaks are very sensitive to the mass of the model. Clearly the "inner rotation profile" produced by the bar is far to fit the observed data which remain uncertain to date (see review by Chemin et al., 2015).

Figure 3.8 shows the vertical force at 1.1 kpc produced by our bar model when three values of mass for the Galactic bar are used §5. Within the errors, the vertical force produces practically the same results beyond 5 kpc from the bulge regions, which is consistent with measurements from SEGUE G dwarf stars (Bovy & Rix, 2013). Figure 3.9 display the significative variations of the vertical force in the region of inner galactocentric radius as a function of the strength of the Galactic bar.

3.7 The GravPot16 package

As a by product of this work, I provide the GravPot16 package to the community by running it on a public server at https://fernandez-trincado.github.io/GravPot16/pages/simulator.html.

The acronym GravPot16 means: The **Gra**vitational **Pot**ential of the Milky Way version 20**16**. It performs a variety of dynamical analysis in the Milky Way, including orbit integration.

The GravPot16 package has also been widely used in the literature since 2016 for orbit computations (see Fernández-Trincado et al., 2014, 2015a, 2016a, Anders. F in prepara-

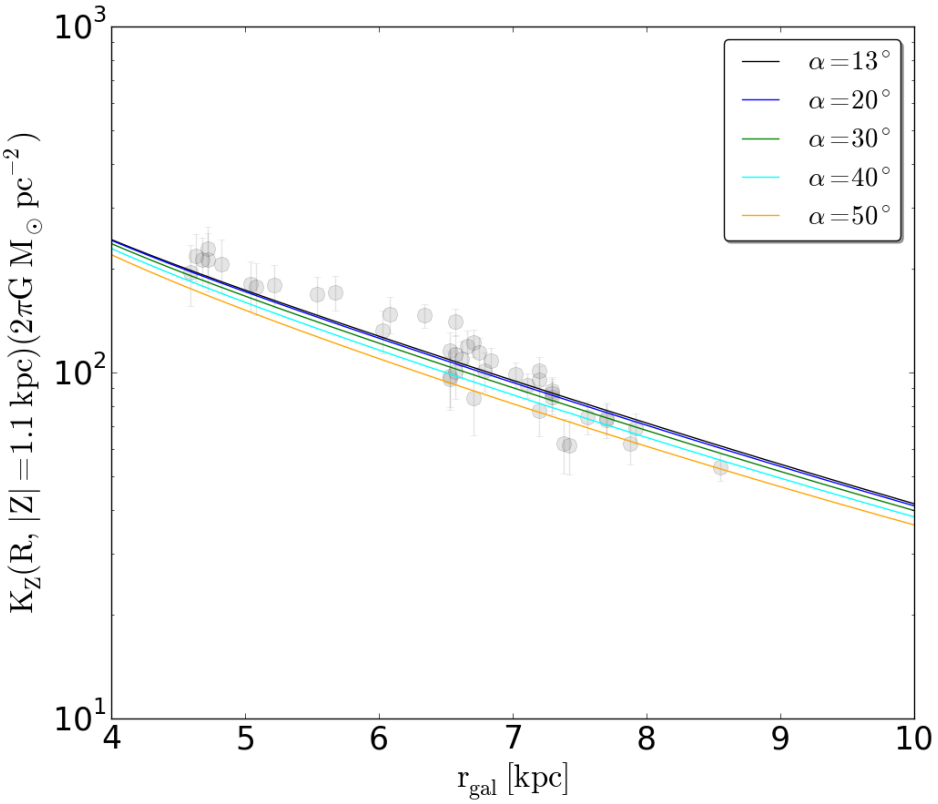

Figure 3.6: The vertical force at 1.1 kpc as function of the Galactocentric radius as measured by SEGUE G dwarf (grey dots) by Bovy & Rix (2013) compared with five toy models with increasing angle of orientation of the Galactic bar.

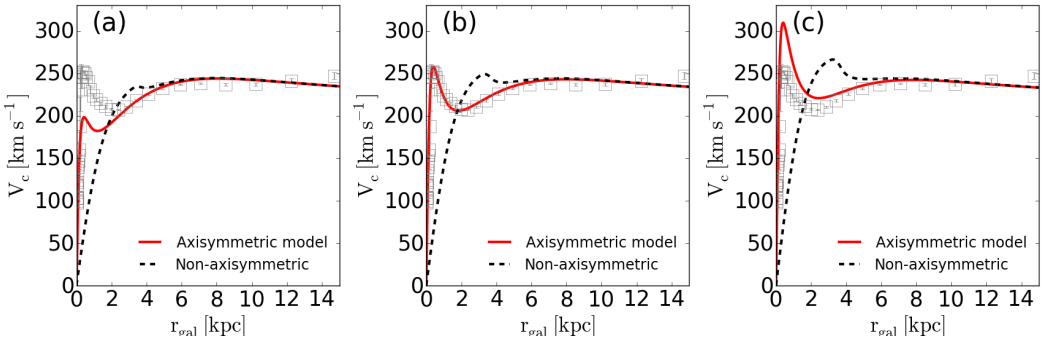

Figure 3.7: Rotation velocity profile for three models with different bar mass (Non-axisymmetric model) and different mass for the spherically symmetric component (Axisymmetric model): 0.63×10^{10} $M_\odot$ (panel a), 1.1×10^{10} $M_\odot$ (panel b), and 1.6×10^{10} $M_\odot$ (panel c). Grey symbols to guide the eye based on the observations of H_I and CO from Sofue (2015).

tion, Fernández-Trincado et al. 2017, submitted). It is also used to set the kinematics of the Besançon synthetic model from 3D test particle simulations, and to constraint the physical parameters of the Galactic bar (see §5).

Parts of this chapter have been previously published as conference proceedings at "Potential of the Galaxy from the Besançon galaxy model including non-axisymmetric components: Preliminary results" (Fernández-Trincado et al., 2014); "Mapping the inner stellar halo of the Milky Way from 2MASS and SDSS-III/APOGEE survey" (Fernández-Trincado et al., 2015a). The whole model, will be presented in a forthcoming paper as "The Besançon Galaxy model for Galactic dynamics: I. A new approach of the stellar population synthesis model for orbit computations" (Fernández-Trincado et al., in preparation).

3.8 Assemble the Milky Way gravitational potential models

Through this thesis we chose the following ensemble of potentials to describe the dynamical properties of the Milky Way:

1.) **Model 1:** We assume an axisymmetric Galactic model to be made up of the superposion of seven disk components (where the potential has been built from homogeneous oblate spheroids), two thick disk components (Eqns. 3.4 and 3.5), the potential associated to the interstellar matter (Eqn. 3.6), the stellar halo contribution (Eqns. 3.7, 3.8, and 3.9), a spherically symmetric potential to model the

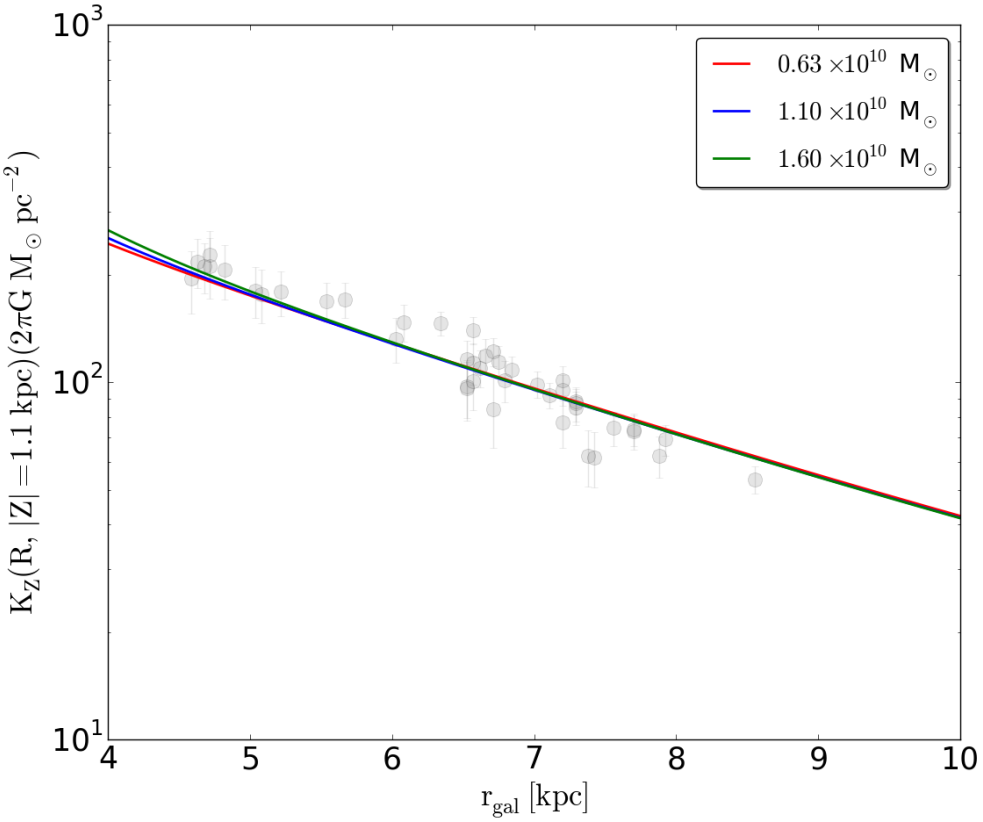

Figure 3.8: This Figure represents the same measurements as in Figure 3.6 compared to three revised ranges of mass of the Galactic bar.

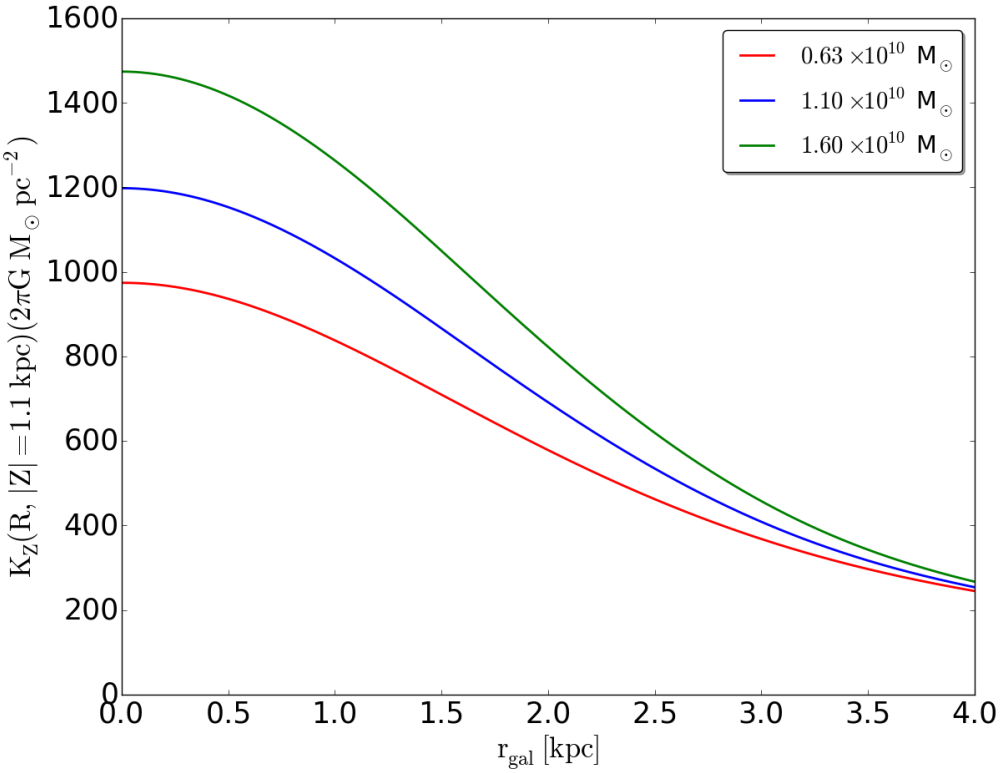

Figure 3.9: This Figure is similar to Figure 3.8 compared to three revised ranges of mass of the Galactic bar, but showing the trends of the vertical force at 1.1 kpc in the inner Milky Way.

Galactic bulge (given by Eqn. 3.3), surrounded by a component of dark matter (Eqn. 3.10).

2.) **Model 2:** We assume a non-axisymmetric Galactic model to be made up of the Galactic components of the Model 1, but now the spherically symmetric bulge potential is replaced by a "boxy/peanut" potential model as described in section 3.4.

To the best of our knowledge, the dynamical effects of a boxy bar has not been considered before in the Besançon stellar populations synthesis model. Thus, in next chapters we have implemented the above mentioned GravPot16 model to compute stellar orbits (applications of the model) and test particles simulations to study the effects of the boxy bar in the structure of the inner Milky Way.

Chapter 4

Test particle simulations: Initial conditions

This chapter describes the construction of controlled massless particles through a fixed Milky Way potential and their response after that a bar structure is created. In connection with the results presented in the next sections (see §5), we aim to establish constraints of the important dynamical parameters of the Galactic bar, i.e., its pattern speed, mass, and angle orientation. In general, the number of particles in our simulations are sufficient for reliable values of the mean and the velocity dispersion toward the bulge fields. Here we present some kinematics behaviour beyond of bulge region.

The gravitational potential that we use to represent the Milky Way model is composed of different mass components developed in §3 which is a sum of the potentials belonging to seven thin disks components, two thick disks components, the interstellar matter (ISM), a Hernquist stellar halo, surrounded by a dark matter halo component truncated at 100 kpc. Also a spherically symmetric potential of the form Miyamoto is employed to progressively creates a bar structure in the inner regions of the Milky Way model, allows us to obtain a smooth distribution of particles and stays stable afterwards.

4.1 What has been called the "bar structure" in the Besançon Galaxy model?

Before we describe our approach to studying the kinematics of particles simulations in the bulge, it is important to understand what means the so-called bar structure in the Besançon synthetic model. As already mentioned, the bar component suggested by Robin et al. (2012) is a dominant structure in the inner Milky Way mapped from photometry in J and K_s bands from the 2MASS dataset, adopting a density law similar to that of Picaud & Robin (2004). Adopting a Monte Carlo approach, the authors were able to measure a boxy/peanut distribution in the Milky Way bulge, finding a boxy/peanut morphology similar to that of measures from the VVV survey (see Wegg & Gerhard, 2013), and the WISE survey (see Ness & Lang, 2016). However, the origin and nature of this structure is still to be understood, and its existence is still under debate (see Lee et al., 2015; Joo et al., 2017, for an alternative interpretation based on multiple stellar populations).

Besides,it is important to note, that in Robin et al. (2012) a single burst population of age ∼8 Gyr has been favoured to represent the stellar population of a boxy/peanut bar in the current picture of the Besançon synthetic model (e.g., Robin et al., 2014). However, in the same work, Robin et al. (2012) cautioned the reader about complementary data to achieve a proper estimation of the age range in the bulge.

Several groups in the past claimed that the bulge is mainly old (Zoccali et al., 2003; Clarkson et al., 2008; Schultheis et al., 2017), however, there are a few studies that provide evidence that at least some stars in the bulge are young (as young as 5 Gyr) (e.g., Bensby et al., 2011; Clarkson et al., 2011; Bensby et al., 2013; Gesicki et al., 2016; Schultheis et al., 2017). Haywood et al. (e.g., 2016), provided a best fitting of the CMD in the SWEEPS field, and claimed that there is no evidence that the bulge is exclusively old, it leads to the interpretation of a bulge formed through dynamical instabilities in the disk (see also Gesicki et al., 2016). Assuming this hypothesis is correct, we examine the kinematics prediction of kinematically cold and warmer stellar disks acting simultaneously, induced mainly by a steady-state boxy bar potential model, in order to place constraints on the physical parameters of the bar. This procedure is shown in next sections.

4.2 Generating the spatial distribution of particles

In the following we explore eight different types of initial conditions for our simulations, designed to mimic the typical density distribution of five thin disk populations (Robin et al., 2003), two thick disk populations and an initially "oblate" distribution of particles assumed to follow a Hernquist stellar halo (Robin et al., 2014), all of them corresponding to the potentials described in §3. We emphasize that these components are part of global Galaxy model chosen in Robin et al. (2003, 2014) to characterise the stellar disk and the stellar halo of the Milky Way from the population synthesis approach (Crézé & Robin, 1983) of the Besançon synthetic model. As was pointed out by Romero-Gómez et al. (2015), the fact that the parameters of the Galactic components defining the initial conditions are the same facilitates the relaxation of the particles.

Both, disks and stellar halo are represented by $N_{total} \sim 10^6$ particles respectively. Notice that each particle system generates low resolution realizations, where the density is $\sim$ 1000 to 3000 particles in boxes of 100 pc wide in Cartesian coordinates. This is sufficient for our general purposes but for the moment they are not sufficient enough ($<$ 3000 particles per kpc^3) in the solar ring ($\sim$ 8 kpc) to study the imprints of the Galactic bar on velocity distribution beyond the bulge regions (this is the matter of a future work where we expect to improve the resolution). Important considerations carried out in this study are:

1) The two younger stellar disks component of the Besançon synthetic model, with stellar ages ranging from less than 1 Gyr, were excluded in our test particle simulations. Assuming an isothermal state and/or achieve relaxation in the system for a youngest population is still uncertain, and a resulting system of particles associated with this population could lead to transient effects due to the bar, producing unreliable results.

2) We set initial conditions for five cold thin disk populations, with stellar ages ranging from 1 Gyr up to $\sim$ 10 Gyr. Hence, in the nomenclature of Robin et al. (2003), our kinematically cold disk components are classified as: Pop 3 (populations with ages between 1 Gyr up to 2 Gyr), Pop 4 (populations with ages between 2 Gyr up to 3 Gyr), Pop 5 (populations with ages between 3 Gyr up to 5 Gyr), Pop 6 (populations with ages between 5 Gyr up to 7 Gyr), Pop 7 (populations with ages between 7 Gyr up to 10 Gyr), and the two warmer thick disk components with ages according Robin et al. (2014), i.e., Pop 8 (population with ages $\sim$ 10 Gyr) and Pop 11 (population with ages $\sim$ 12 Gyr).

3) We also explore the results of an initially "non-rotating" Hernquist stellar halo.

To generate the initial spatial distribution of particles, we employ the Von Neumann accept/reject technique (Press et al., 1992) to make discrete realizations of the density profiles of the thin-, thick- disk and stellar halo presented in Robin et al. (2003, 2014). For instance, Pop 8, assigned to be a warmer thick disk, follows exactly the spatial distribution according to a density profile of the form $\sim sech^2(\frac{|Z-Z_{\odot}|}{2h_Z}) \times exp(-\frac{R-R_{\odot}}{h_R})$ (see e.g., Robin et al., 2014). Other Galactic components (Pop 3, Pop 4, Pop 5, Pop 6, Pop 7, Pop 9, Pop 11) are setup by following the density profiles presented in Appendix A. Figure 4.1 illustrates the initial (t = 0 Gyr) spatial distribution of the particles in the X - Z projection. The plot shows the different scale lengths that initialize the distribution of each stellar component.

4.3 Initializing the particle velocities

Finally, here we initialize the particle velocities to the positions generated above. The Besançon Galaxy model is well-suited for this purpose. The basic idea is that the Besançon Galaxy model computes a first guess of velocities (U, V, W) time-independent for each stellar population observationally restricted (e.g., Bienaymé et al., 1987; Robin et al., 2003). It is important to note that our initial conditions are based on locally self-consistent recipes, but not fully self-consistent globally, and will thus be slightly relaxed before turning on the non-axisymmetric potential. The exact procedure used in this work to set up the initial velocity vectors is the following:

1.) The *age*-velocity vertical dispersion relation (σ_W).

2.) The tangential velocity dispersion, σ_V, and the radial velocity dispersion, σ_U both are defined relatively to σ_W by the ratios σ_U/σ_V and σ_U/σ_W, taken into account the variations of the asymmetric drift (V_{ad}) at the Galactocentric positions (r_{gal}, Z), and vertical dispersion gradient ($\frac{d\sigma_U}{dR}$), as pointed out in Robin et al. (2003). Where V_{ad} has been computed as: $V_{\rm ad} = \frac{\sigma_U^2}{2V_{\rm LSR}}\{\frac{R}{\rho}\frac{d\rho}{dR} + 2 \times \frac{R}{\sigma_U}\frac{d\sigma_U}{dR} + (1 - \frac{\sigma_V^2}{\sigma_U^2}) + (1 - \frac{\sigma_W^2}{\sigma_U^2})\}$ where $\frac{d\rho}{dR}$ is the density gradient (see Robin et al., 2003).

Through this thesis the velocity dispersions $(\sigma_U, \sigma_V, \sigma_W)$ are defined at the Solar positions, while the galactocentric velocity dispersions $(\sigma_R, \sigma_\phi, \sigma_Z)$ are given in a cylindrical reference frame with center in the Milky Way.

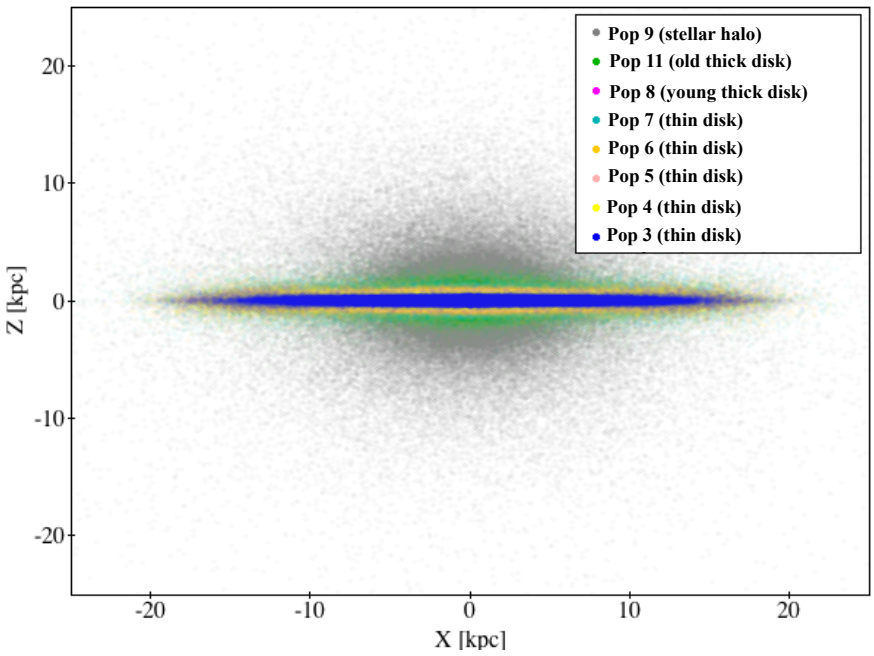

Figure 4.1: X-Z projection illustrating the initial spatial distribution of the particles.

It is important also to note that we make use of V_{ad} as a function of distance from the Galactic plane, as recently has been proposed from the Stäckel approximation introduced by Bienaymé et al. (2015).

In this thesis we have chosen to use the *age*-velocity dispersion relations as derived from the Hipparcos and RAVE datasets, as listed in Table 4.1. These velocity dispersions were obtained following the method described in Robin et al. (2017) using a MCMC method to fit the kinematics of each population, but using only RAVE data as a preliminary study. These values are not published because supersided by the new analysis using RAVE plus TGAS data. Then, for each particle drawn in Figure 4.1, we apply velocities (U, V, W) from the kinematics predicted by the Besançon synthetic model, computed from the expression in Eqn. 4.1 and Enq. 4.2,

$$\sigma_z(r_{gal}) = \sigma_z^{pop} \times \exp^{-(R-R_\odot)\times\frac{d\sigma_Z}{dR}} \tag{4.1}$$

$$\sigma_{plane} = \sigma_{plane}^{pop} \times \exp^{-(R-R_\odot)\times\frac{d\sigma_{plane}}{dR}} \tag{4.2}$$

where $R_\odot = 8000$ pc (the Solar radius), σ_z^{pop} is the vertical velocity dispersion, and $\sigma_{plane} = \sigma_U = \sigma_V$ the components of velocity dispersions (U, V) at the Solar position, as listed in Table 4.1, with $\frac{d\sigma_Z}{dR}$ and $\frac{d\sigma_{plane}}{dR}$ the radial gradients of the velocity components (U, V, W), assumed in the Besançon synthetic model (axisymmetric model) to be equal to -0.1×10^{-03} km s^{-1} pc^{-1}, and $R = r_{gal}$ if $R > 2$ kpc, otherwise $R = 2$ kpc. In this work, we provide new predictions for $\frac{d\sigma_Z}{dR}$ and its response to a "boxy/peanut" bar, while the adopted value of $\frac{d\sigma_{plane}}{dR}$ in the Besançon synthetic model gives practically the same results (see results below).

It is important to note that the kinematics of the Besançon synthetic model (Bienaymé et al., 1987; Robin et al., 2003, 2012, 2014; Bienaymé et al., 2015) is based on several assumptions and approximations, observationally constrained. However, we must emphasise that the kinematical model in the inner regions is still very uncertain in all the versions of the BGM, and sometimes is arbitrarily taken from scaled Milky Way-like N-body models from Fux (1999); Debattista et al. (2005), which do not follow the mass density distribution and gravitational potential of the BGM itself. Having said that, we emphasise that this thesis provides for the first time, a consistent way to predict the kinematics of the whole Galaxy, where the velocity field information is inherited according from the density and gravitational potential of the Besançon Galaxy model.

4.4 Adding the bar potential to the system

First, we now design control simulations with the gravitational potential model described in §3. The starting point consists in integrating the initial conditions forward in time in the axisymmetric case, **Model 1** as described in §3. The particles evolve in an axisymmetric potential during a period of time long enough (5 Gyr) to ensure that the particle system is relaxed within that potential. Once the system has been relaxed the bar is introduced slowly to the potential in order to avoid transient structures. We employ the

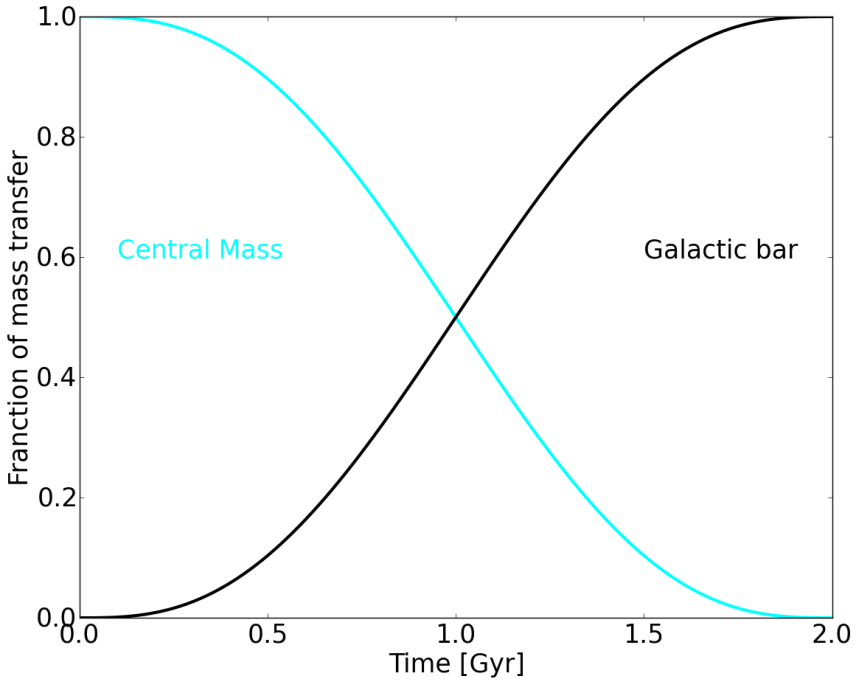

Figure 4.2: Adiabatic growth of the boxy bar (see text).

Table 4.1: Velocity dispersions (σ_U, σ_V, σ_W) as derived from the RAVE-Tycho dataset.

Population Gyr	σ_U km s^{-1}	σ_V km s^{-1}	σ_W km s^{-1}	ϵ
(0 - 0.15)	11.993	8.515	5.757	0.01400
(0.15-1)	15.969	11.338	7.665	0.02109
(1-2)	21.462	15.238	10.302	0.03150
(2-3)	26.133	18.555	12.544	0.04100
(3-5)	31.881	22.636	15.303	0.05248
(5-7)	38.223	27.139	18.347	0.06534
(7-10)	44.909	31.885	21.556	0.08462
(10)	50.000	35.000	25.000	-
(stellar halo)	131.000	106.000	85.000	-
(12)	61.590	49.272	40.033	-

same technique widely used in the literature to grow adiabatically the bar into the simulations (see Monari et al., 2013; Romero-Gómez et al., 2015; Martinez-Medina et al., 2016). In our case it consists in transferring mass from the central mass (spherically symmetric bulge) to the bar structure progressively during a time ($0 < t < t_{growth}$). We arbitrarily take the value $t_{growth} = 2$ Gyr long enough to avoid transient effects, afterwards the bar is stably involved with the background potential. Then, in a similar way as described in (Romero-Gómez et al., 2015), when $t = t_{growth}$ we have an entire bulge dominated by a boxy/bar potential in the inner Milky Way, with physical parameters that will be constrained later. Once the "boxy/bar" potential stays stable in the system, we integrate the particles in the potential during another 3 Gyr (t_{add}), to reach a state of statistical equilibrium (e.g., Romero-Gómez et al., 2015). The mathematical expression employed to grow adiabatically the bar in our system, is the same as described in Dehnen (2000), which we repeat here as

$$M_{bar} = M_{CM}\left(\frac{3}{16}\zeta^5 - \frac{5}{8}\zeta^3 + \frac{15}{16}\zeta + \frac{1}{2}\right); \zeta \equiv 2\frac{t}{t_{growth}} - 1 \tag{4.3}$$

where M_{CM} is the mass of the central mass, and M_{bar} is the mass of the boxy/peanut bar. Figure 4.2 illustrates the process of mass transfer between the central mass to the Galactic bar. An animated illustration of the adiabatic growth of the bar in our model can be found at the official website of the GravPot16 model (https://fernandez-trincado.github.io/GravPot16/).

Secondly, the integration of the motion equations is done with the Runge-Kutta algorithm of seventh-eight order of Fehlberg (1968). This integrator uses a constant stepsize that is set at the initial condition, and produces a relative error smaller, i.e., Jacobi's integral is conserved within a relative variation of $\sim 10^{-11}$. It is important to note that the results presented in this thesis consider only the "last stages" in Milky Way evolution, i.e., this last stages is thought-out to be affected by non stationay processes as has been pointed out by Antoja (2010).

4.5 Velocity dispersions and azimuthal velocities

In this section, we compare different states of the particle system before and after the adiabatic growth of the Galactic bar within the potential. Figure 4.4 shows the mean azimuthal velocity (V_ϕ) as a function of Galactocentric distance (r_{gal}) for the initial conditions (IC, $t = 0$ Gyr), and for the final positions of the set of particles after 5 Gyr (labeled as Axi) forward integration in an axisymmetric potential, and for the last stages ($t_{growth} + t_{add} = 5$ Gyr) of the particle system in statistical equilibrium with the final non-axisymmetric potential model. It is important to note that because of the asymmetric drift, this is not a "rotation curve".

From the final result of the simulations in the non-axisymmetric potential, we have chosen arbitrarily ten azimuthal angles or bands with orientations of 10±8 degree, 20±8 degree, 40±8 degree, 60±8 degree, 80±8 degree, add the particles in the symmetric bands 190±8 degree, 200±8 degree, 220±8 degree, 240±8 degree, 260±8 degree, with respect of the major semiaxis of the Galactic bar, and the Galactocentric radius in bins of 0.6 kpc. These bands are illustrated in Figure 4.3. As expected, beyond the bulge regions, the predicted azimuthal velocity from the axisymmetic and non-axisymmetric potential (see Figure 4.4) follow similar behaviour to the initial conditions, and differs notably in the inner Galaxy, we can also see how the inner peak disappears leading to the smooth azimuthal velocity, except for the component of the stellar halo and the warmer disk at larger r_{gal}.

In the case of the axisymmetric model (black line), the Galactic bulge is a spherically symmetric distribution of mass of the form Miyamoto & Nagai (1975) as already mentioned with a core radius with dimension similar to the major semiaxis of the bar. Given the symmetry of a fully axisymmetric potential model, one would expect to find a Galactic bulge marginally dominated by very eccentric orbits, while several resonant family of orbits appear due to the bar, thus changing the phase-space of the initially symmetric particle system, as can be seen from the trends in differents bands associated with the differents orientation of the bar translate also as the relative strength of the bar through azimuthal angle variations. In other words, perturbations due to the bar can oust particles where they migrate to the disk, halo and/or rearrange particles in the bar itself. This is clear and particularly interesting that the bar induces more easily kinematic features to particle systems kinematically warmer, as can be seen in Pop 8 (young thick disk), Pop 11 (old thick disk) and Pop 9 (stellar halo). In particular the bar produces significant kinematic variations notably in hotter populations, as can seen in the Pop 9 (stellar halo), i.e., the initial conditions and the axisymmetric approach keep consistent results, a stellar halo initially non-rotating stays in the same state and statistically in equilibrium after 5 Gyr forward integration. The initially non-rotating stellar halo tends to form a "transient halo" as a consequence of the presence of the Galactic bar, with particles in "prograde" motion towards the inner Galaxy, and in "retrograde" motions beyond of the bulge regions. This is not surprising at all, because, from the observational point of view, some claims has been made in the literature, for instance, Carollo et al. (2007) found that the inner stellar halo exhibit a small (or zero) prograde rotation towards the inner Milky Way. In §5 and §6 we will analyze the noticeable influence of the Galactic bar on the structure and kinematics of the disk and stellar halo.

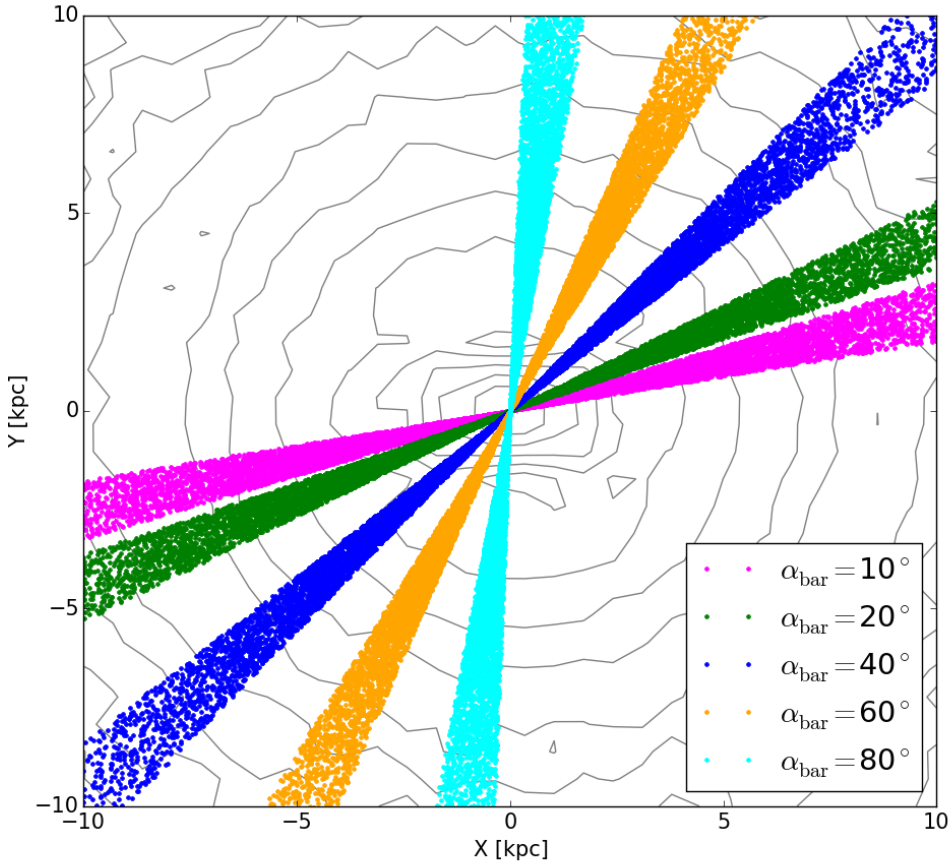

Figure 4.3: Illustration of the particles bands analyzed in this work as a function of the azimuthal angle (see text). As example, the grey lines represents to the logarithmic surface density contours of the disk particle (Pop 3) as seen face-on in the non-inertial reference frame where the bar is at rest.

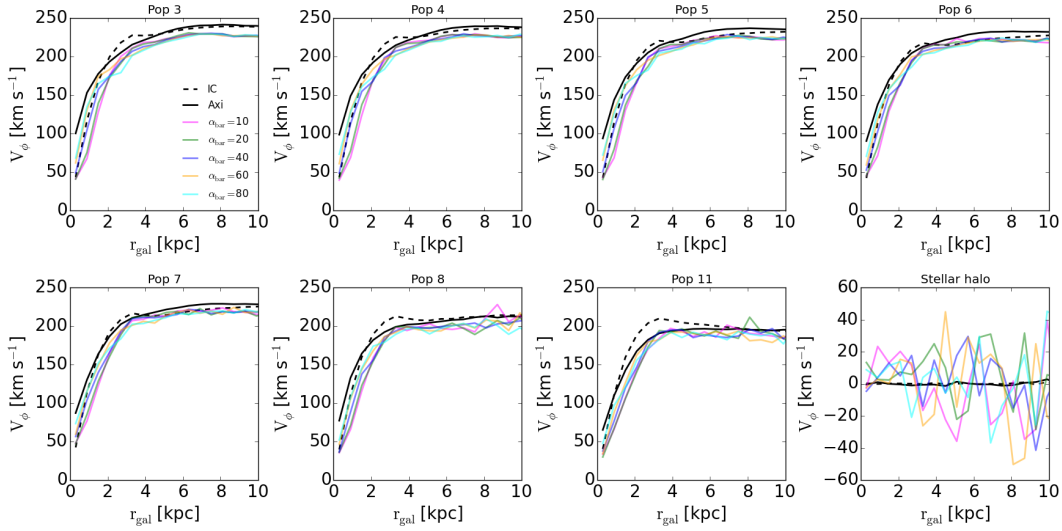

Figure 4.4: Radial distribution of the mean azimuthal velocity V_ϕ as a function of Galactocentric distance (r_{gal} at relatively smaller heights from the plane ($|Z| < 0.3$ kpc). The black dashed line refers to the initial conditions ($t = 0$ Gyr), the black line is the resulting V_ϕ from the axisymmetric model after 5 Gyr forward integration, and the colored lines are the resulting V_ϕ along different azimuthal angles labeled here as α_{bar}, and after 5 Gyr forward integration in the non-axisymmetric potentital which includes a boxy/peanut bar (see text).

Figure 4.5 shows how the radial velocity dispersion (σ_R) and vertical velocity dispersion (σ_Z) respond to the Galactic bar, along of r_{gal} and different bar orientations. We see a similar trend between the axisymmetric and non-axisymmetric models at large Galactocentric radii, i.e., the velocity dispersions decays exponentially with r_{gal}. However in the bulge regions, σ_R and σ_Z, increase in the axisymmetric case, while decrease when the Galactic bar is added. The results of these simulations are very similar to that of the initial conditions near the solar position, with similar trend for the imposed radial velocity dispersion at the beginning and the resultanting (σ_R).

Concerning to σ_Z, we find that the vertical velocity dispersion in the current version of the BGM could be not properly a good representation of the imposed density laws, here the need to invoke test particle simulations, where a steady-state gravitational potential is capable to predicts the properties of the phase-space under perturbations (produced by the so-called bar). For the stellar halo, a process of radial migration of particles is triggered becoming apparent in the formation of transient components in the inner Galaxy. It will be discussed in §6. We note that our initial conditions are not perfectly self-consistent on a global scale, this can immediately be seen from the fact that the mean velocities and velocity dispersions evolve in the axisymmetric case in Figure 4.4 and Figure 4.5. For our initial stellar velocities of the stellar halo, this has not been thought through in depth, and there is thus no reason for this stellar halo to be in true equilibrium. In general, our idealised initial conditions turns out to be pretty much stable for the time-scales over which we integrated it, but this does not mean it is truly in equilibrium. With our method, we find that the initial conditions are not perfect and not fully self-consistent globally. Although it is out of the scope of the present study to making the axisymmetric Besançon Galaxy model fully self-consistent, we do not exclude the use of these techniques in the near future.

4.6 Predicted Vertical velocity dispersion

Here, we provide predictions of the vertical velocity dispersions (σ_Z) for each disk component, when a boxy/peanut bar is added to the Milky Way model (see text above), and we give the best set of parameters that should be used to set the kinematics of the Besançon Galaxy model.

Figure 4.5 shows clearly that the stellar halo is significantly sensitive to the Galactic bar, and the smooth kinematic trends in the axisymmetric model disappears in the non-axisymmetric model, as a consequence of the bar. Some tests using additional integration time (+2 Gyr, +3 Gyr) discard the possibility that the particle system does not remain stable, i.e., an increment of the integration time gives practically the same results. We will employ in the near future the results from particle simulations to set the kinematics (using the mean and dispersion of the particle velocities in smaller boxes) of this Galactic component within the Besançon Galaxy model.

Figure 4.6 in the same fashion as Figure 4.5 shows the final fits to Eqn. 4.4 and Eqn. 4.5, where $\sigma_z^{\odot}$, $\sigma_R^{\odot}$, $\frac{d\sigma_Z}{dR}$, and $\frac{d\sigma_R}{dR}$ now are free parameters. In Table 4.2 we list the best values of these parameters. Each data point and error bar in Figure 4.6 is referred to $\langle\sigma_Z\rangle \pm \sigma$ and $\langle\sigma_R\rangle \pm \sigma$ per radial bins (see text above), from the distributions in the

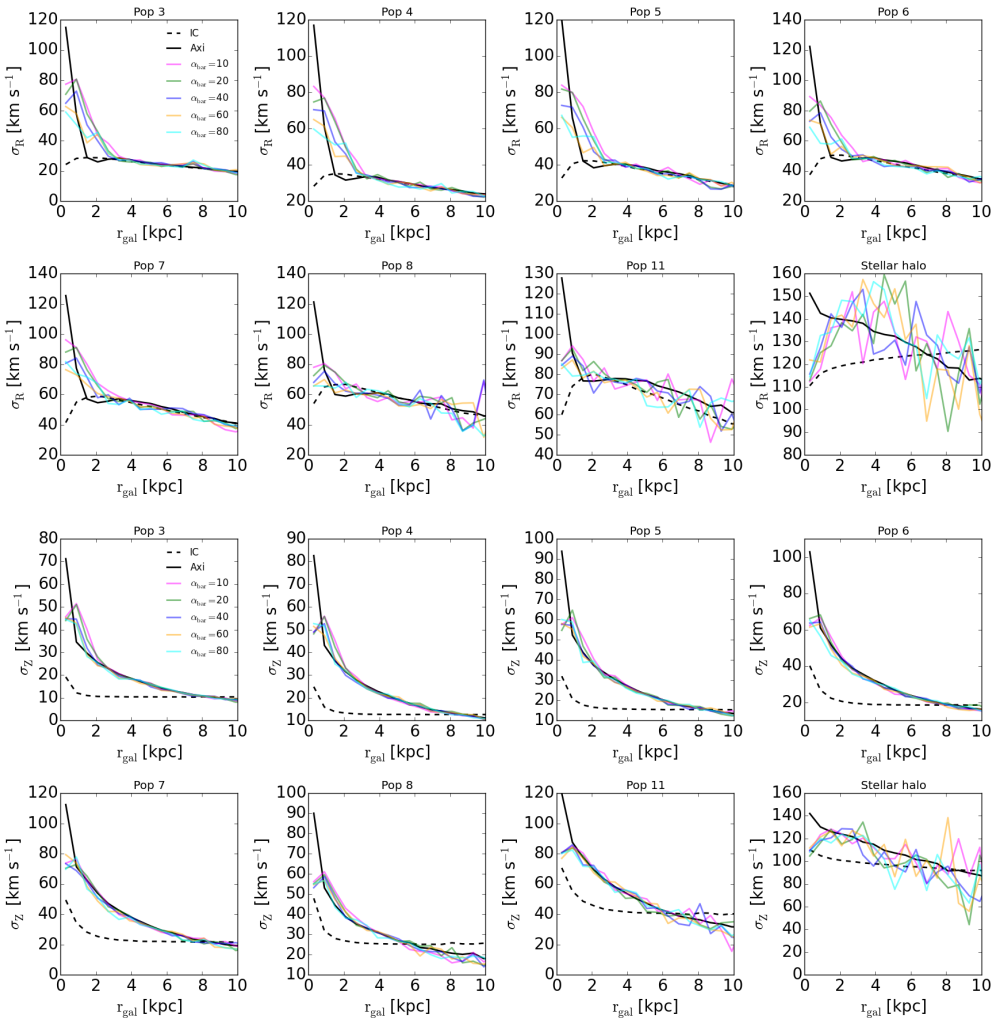

Figure 4.5: Top panel (first and second row): Radial velocity dispersion ($\sigma_{\rm R}$) as a function of Galactocentric distance ($r_{\rm gal}$) with the same lines as in Figure 4.4. Bottom panel (third and fourth row): Vertical velocity dispersion (σ_Z).

non-axisymmetric model as illustrated in Figure 4.5.

Note that the predictions (values listed in Table 4.2) are comparable to observations at the Solar positions for $\sigma_z^{\odot}$ as listed in Table 4.1. However, we find some discrepancy ($\sim$7 km s^{-1}) for the particles belonging to the thick disk components (Pop 8 and Pop 11). We run tests with different values of the integration time (+0.5 Gyr, +1 Gyr, +1.5 Gyr, +2.0 Gyr, +2.5 Gyr) to verify that our results are not affected by possible system instabilities. Figure 4.7 shows that the particles stay stable after this test, and gives practically the same results as shown in bottom panels in Figure 4.6. This suggests that the particles in the disks stay stable with the background potential.

We ran additional tests for the particles in the thick disk components. We changed the initial conditions to new measurements from the TGAS-RAVE datasets by Robin et al. (2017)[1] The results are illustrated in Figure 4.8. We do not find agreements between observations and models for the thick disk, these values are significantly deviated ($\sim$24 km s^{-1}) for the old thick disk (Pop 11) when the TGAS-RAVE datasets is considered, and ($\sim$5-7 km s^{-1}) for the young thick disk (Pop 8) for the combination Hipparcos-RAVE and TGAS-RAVE, and ($\sim$7 km s^{-1}) old thick (Pop 8) disk for the Hipparcos-RAVE datasets. However, note that these differences are comparable to the illustrated error bars at the Solar position. *Conclusion: These additional tests allow us to be slightly more confident on the stability of the system and to know the range of uncertainties of our predictions.*

$$\sigma_z(r_{gal}) = \sigma_z^{\odot} \times \exp^{-(r_{gal}-R_{\odot})\times\frac{d\sigma_Z}{dr_{gal}}} \tag{4.4}$$

$$\sigma_R(r_{gal}) = \sigma_R^{\odot} \times \exp^{-(r_{gal}-R_{\odot})\times\frac{d\sigma_R}{dr_{gal}}} \tag{4.5}$$

where $R_{\odot} = 8000$ pc is the Solar position.

Table 4.2: Velocity dispersions as derived from test particle simulations.

Population Pop	$\sigma_R^{\odot}$ km s^{-1}	$\frac{d\sigma_R}{dR}$ km s^{-1} pc^{-1}	$\sigma_Z^{\odot}$ km s^{-1}	$\frac{d\sigma_Z}{dR}$ km s^{-1} pc^{-1}
3	21.88	-0.000110	10.76	-0.000253
4	25.84	-0.000111	13.48	-0.000231
5	32.23	-0.000098	15.84	-0.000257
6	37.86	-0.000112	18.88	-0.000251
7	44.53	-0.000107	22.11	-0.000254
8	49.25	-0.000087	19.13	-0.000239
11	66.29	-0.000062	33.14	-0.000241

[1]During the preparation of this thesis book, Robin et al. derived new values for σ_U, σ_V, and σ_W at the Solar positions from the TGAS-RAVE datasets. Those values are very similar to the ones used in this work for the thin disk components, while significant variations were found for the thick disk: $\sigma_U^{pop-8} = 40.01$ km s^{-1}, $\sigma_V^{pop-8} = 31.86$ km s^{-1}, and $\sigma_W^{pop-8} = 27.9$ km s^{-1}, and $\sigma_U^{pop-11} = 75.6$ km s^{-1}, $\sigma_V^{pop-11} = 55.40$ km s^{-1}, $\sigma_W^{pop-11} = 66.4$ km s^{-1}. The results for the TGAS-RAVE dataset are shown in Figure 4.8.

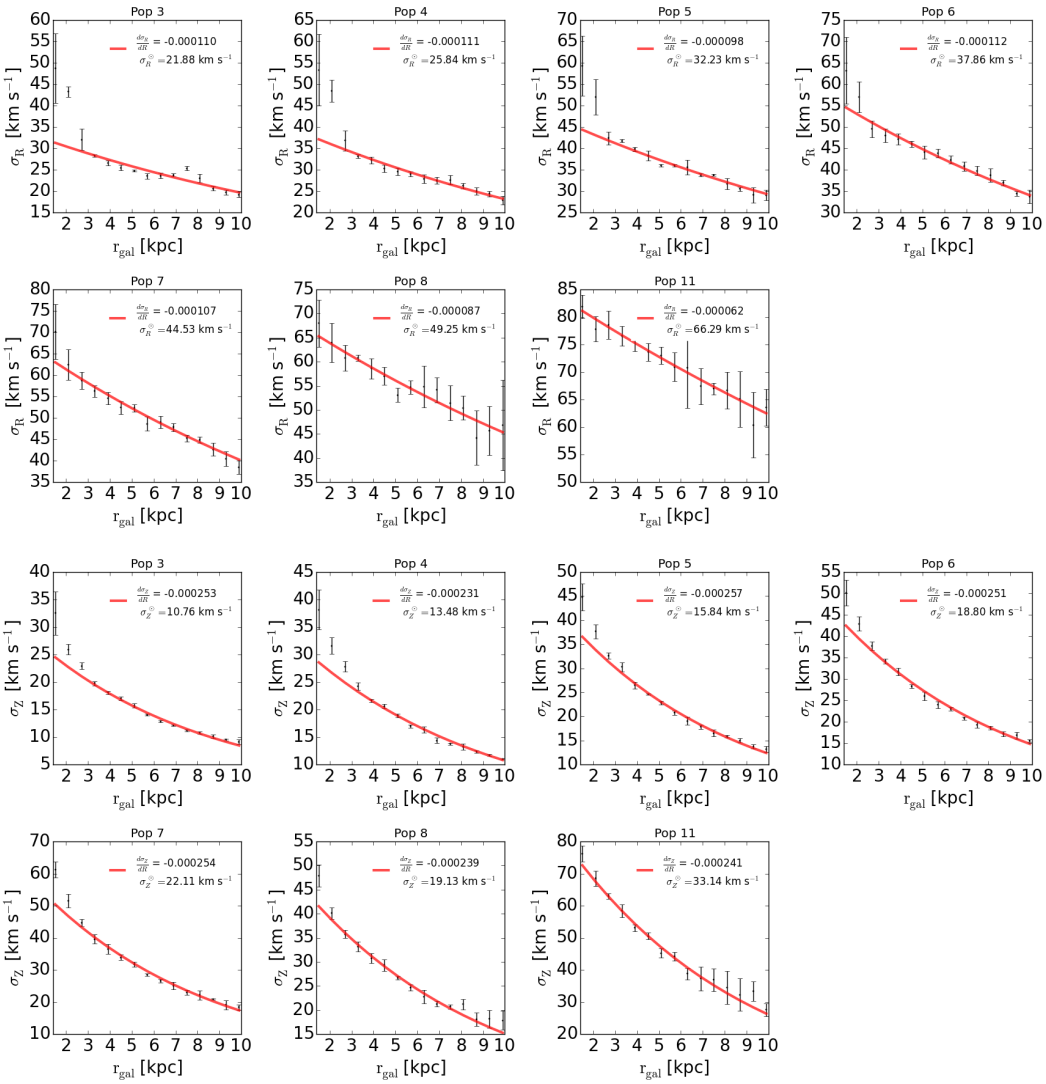

Figure 4.6: Top panel (first and second row): Radial velocity dispersion (σ_R) as a function of Galactocentric distance (r_{gal}). Bottom panel (third and fourth row): Vertical velocity dispersion (σ_Z). The red lines indicate the best-fit velocity dispersion (see text). The error bars indicate the standard deviations obtained by combining the trends among different azimuthal angles (see Figure 4.3).

Table 4.3: Velocity dispersions as derived from test particle simulations.

Population Pop	σ_U km s^{-1}	σ_V km s^{-1}	σ_Z km s^{-1}	$\sigma_R^{\odot}$ km s^{-1}	$\frac{d\sigma_R}{dR}$ km s^{-1} pc^{-1}	$\sigma_Z^{\odot}$ km s^{-1}	$\frac{d\sigma_Z}{dR}$ km s^{-1} pc^{-1}
(1 - 2) Gyr	21.462	15.238	10.302	21.88	-0.000110	10.76	-0.000253
(2 - 3) Gyr	26.133	18.555	12.544	25.84	-0.000111	13.48	-0.000231
(3 - 5) Gyr	31.881	22.636	15.303	32.23	-0.000098	15.84	-0.000257
(5 - 7) Gyr	38.223	27.139	18.347	37.86	-0.000112	18.88	-0.000251
(7 - 10) Gyr	44.909	31.885	21.556	44.53	-0.000107	22.11	-0.000254
(10) Gyr	50.000	35.000	25.000	49.25	-0.000087	19.13	-0.000239
(12) Gyr	61.590	49.272	40.033	66.29	-0.000062	33.14	-0.000241

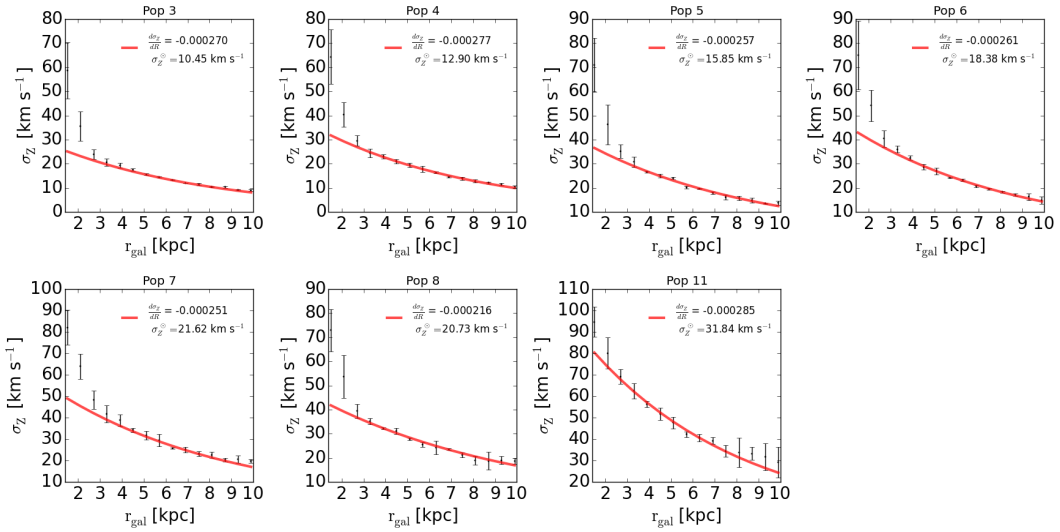

Figure 4.7: This plot represents the same measurements as in Figure 4.6, but now increasing by 2 Gyr the time of integration in the *non-axisymmetric* potential.

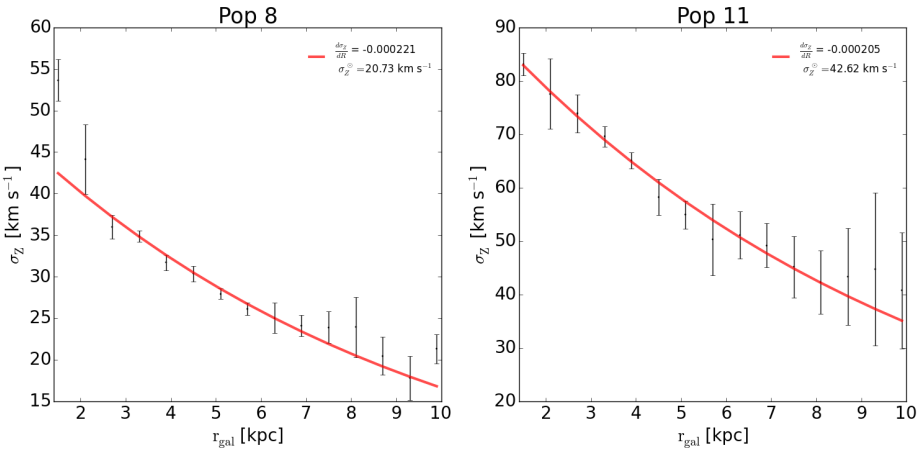

Figure 4.8: This plot represents results for the particles in the thick disk components, adopting initial conditions from new measurements based on the TGAS+RAVE datasets (Robin et al., 2017).

Anticipating the results presented in §4.9, all our analysis above has been presented employing a non-axisymmetric potential that includes a "boxy/peanut" bar with the following physical parameters: bar pattern speed of 35 km s^{-1} kpc^{-1}, bar angle orientation of $\sim 20°$, and bar mass of $\sim 1.2 \times 10^{10}$ M$_\odot$ as listed in Model 22 listed in Table 5.1. This is seen that these parameters produces smaller values of χ^2 than others, however, a visual examination indicates that Model 36 listed in the same table produces also a best-fitting model, with the following bar parameters, $\Omega_{bar} = 55$ km s^{-1} kpc^{-1}, mass of 1.6×10^{10} M$_\odot$, and $\alpha_{bar} = 20°$ (see §5). We also run tests with these values to examinate the sensitivity of the results when the main bar parameters change. The results are presented in Figure 4.9. This figure shows similar measurements as in Figure 4.6, but now adopting the **Model 36** as presented in Table 5.1. As can been seen, the vertical and radial velocity dispersion gives practically the same results at the Solar position, however, towards the Galactic centre larger values appears as a consequence of the strength of the Galactic bar as expected. In other word, a massive bar induces higher velocity dispersion that a less massive one, but beyond this region similar kinematics behaviour is observed to our previous results. We are aware that there are more sophisticated method to discriminate between bar models, however, this thesis is based on the Besançon Galaxy model, which is limited to inclusion of other important Galactic components like spiral arms, that up to this point it is out of the scope of the present work.

On the other hand, the inclusion of other non-axisymmetric structures requires to re-examine the veracity of the process of *Self-consistency dynamical*.

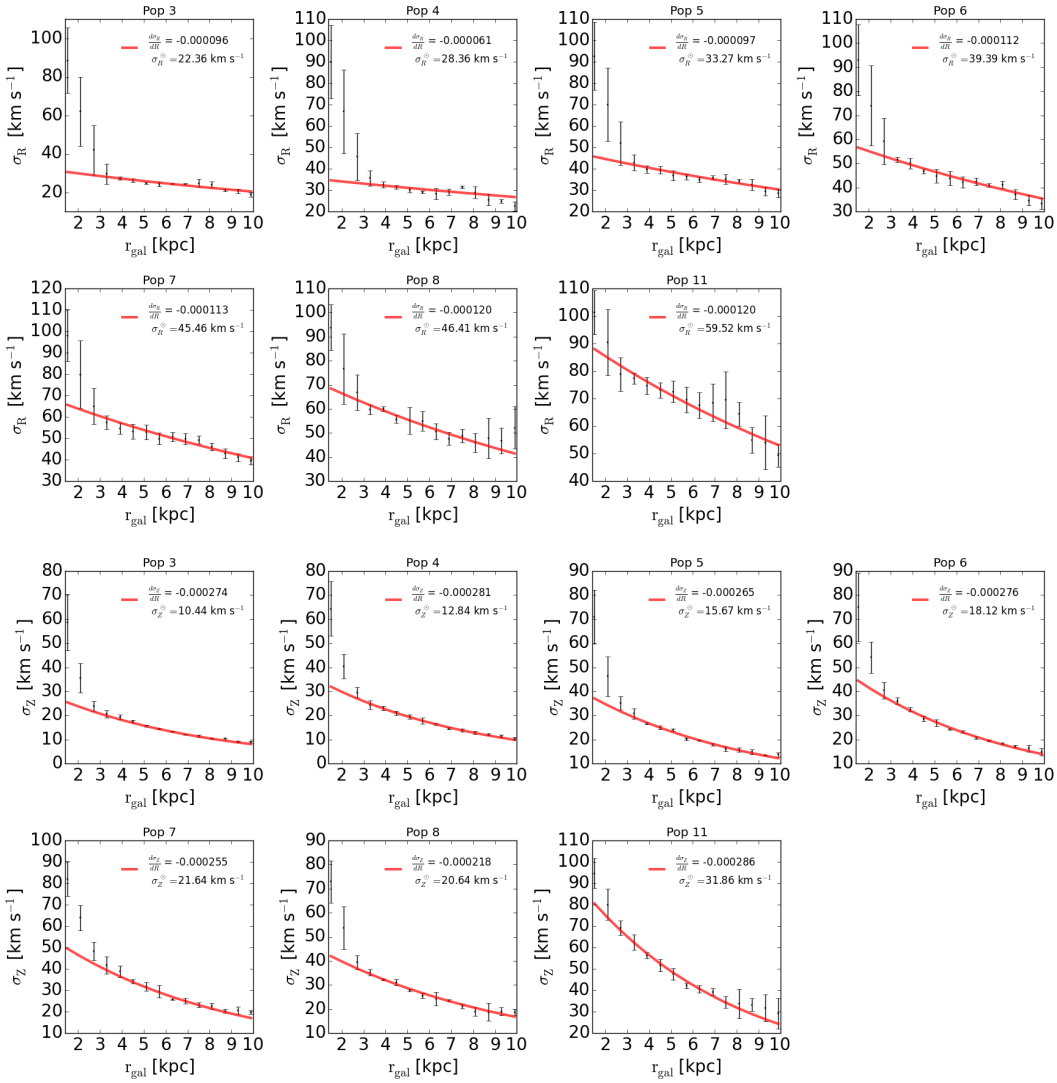

Figure 4.9: This Figure represents similar measurements as in Figure 4.6, but now adopting the following bar parameters: $\Omega_{bar} = 55$ km s^{-1} kpc^{-1}, mass of 1.6×10^{10} M$_\odot$, and angle orientation of $\alpha_{bar} = 20^\circ$ (see §5).

4.7 Qualitative comparison of the BGM with test particle simulations

Figure 4.10 provides a visual comparison of line-of-sight velocity (V_{los}) as a function of the distance as predicted by the Besançon Galaxy model (Robin et al., 2014) taking into consideration similar magnitude range, and spatial distribution that APOGEE observations, and test particle simulations (this thesis), and observations from Data Release 13 (DR13; SDSS Collaboration et al., 2016) of the Sloan Digital Sky Survey III (SDSS-III; Eisenstein et al., 2011). We consider particles and observations covering Galactic longitudes from $-5^{\circ} < l < 20^{\circ}$ and Galactic latitudes $|b| < 20^{\circ}$, and line-of-sight distances < 14 kpc.

We selected 15,216 sources towards the bulge fields from Data Release 13 APOGEE catalogue with estimated spectro-photometric distances computed based on a Bayesian approach (see e.g., Allende Prieto et al., 2006; Santiago et al., 2016, for detailed description of the method). It is important to note that we ignored any quality control cuts in the data, as we are interested in a qualitative exploration of the effects of the bar structure in the inner Milky Way. The motivation is to examine how internal perturbations affect the kinematics in the bulge regions.

In a recent paper, Y. Zhou et al. (submitted) used the effective temperature (T_{eff}) as a distance proxy (where cool stars with Teff < 4000 K, implies that the majority of these stars belongs to the Galactic bulge, in good agreement with the few available spectrophotometric distances available), and claimed that the observed larger velocity distribution observed towards the Galactic bulge field is dominated primarly by cool giant stars suggesting that the vast majority of them belongs to the Galactic bulge, while giant stars in higher temperatures are likely foreground contaminants. Unfortunately our simulations (this work) do not predict stellar parameters, but our results will be combined with the Besançon Galaxy model to provide parts of the parameter space (i.e., T_{eff}, *log g*, luminosity, metallicity, etc.), although it is out of the scope of this thesis.

Comparison between our simulations and APOGEE sample confirms the recent claim by Y. Zhou et al. (in preparation), finding that the majority of the sample belonging to the inner bulge, produces larger velocity distribution due to the induced dynamical effects of the Galactic bar and clearly decreases for foreground particles/stars, as illustrated in the middle and bottom panel of Figure 4.10. Thus, one might expect that any sample dominated by bulge stars shows a particularly larger velocity distribution as consequence of the Galactic bar. Note also that the Besançon Galaxy model[2] (Robin et al., 2014) (top panel in Figure 4.10) predicts a more symmetric velocity distribution in the inner Galaxy. In general our simulations produce a mild tilt as consequence of non-axisymmetries in the Galactic bulge. Such kinematic behaviour seems to be revealed also in the observations, even when the distances are uncertain. In the same figure (middle panel) a lack of particles is observed at distances less than 2 kpc from the Sun, and ~ -100 to ~ 100 km s^{-1}, due to the low resolution of the simulations in the foreground of the bulge region.

[2]We do not apply any relevant selection function, as we are interested in a visual comparison between our simulations with what is expected by the BGM in the same bulge fields.

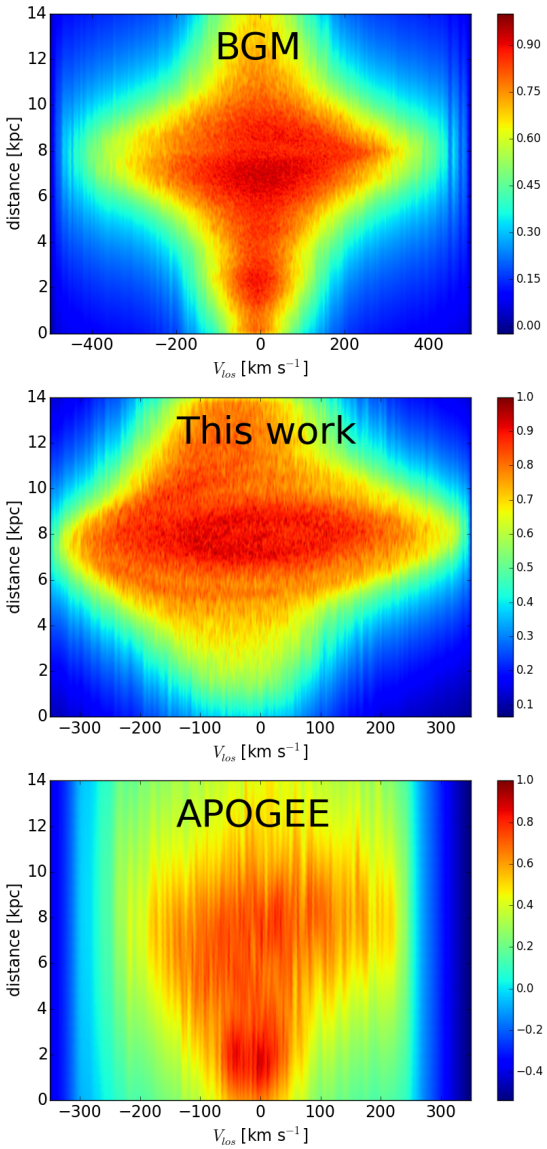

Figure 4.10: Line-of-sight velocity (V_{los}) as a function of the distance, predicted by the Besançon Galaxy model (top panel), test particle simulations carried out in this thesis (middle panel), and Data Release 13 APOGEE datasets (bottom panel). The colours indicate the kernel density estimate, normalized to the maximum number per bin.

Chapter 5

Constraining the physical parameters of the Galactic bar

In the following, we attempt to constrain the physical parameters of the Galactic bar inside the Besançon population synthesis model, aiming to reconstruct the 3D velocity field toward the inner regions of the Milky Way. We have taken advantage of the Milky Way potential model built for this purpose and presented in §3. Our choice of initial conditions was presented in §4 and is based on the density disk profiles and stellar halo of the BGM (Robin et al., 2003, 2014). We perform controlled test particle simulations in an imposed gravitational potential, where the particles reach progressively a state statistically in equilibrium with the potential, and at the same time they inherit information of the density distribution and kinematics of the system (e.g., Romero-Gómez et al., 2015).

We choose 36 configurations for the Galactic bar model, with varying the main parameters of the bar structure (mass, angle orientation, and pattern speeds), and we search for the better set of physical parameters that fit fairly well the global kinematic trends of the Galactic bulge. We employ the following values for the mass of the Galactic bar:

1.) $M_{bar} = 0.63 \times 10^{10}$ M$_\odot$ from Robin et al. (2012), these authors estimate the mass of the Galactic bar based on the integrated luminosity function, taking into account the contribution of white dwarf stars.

2.) $M_{bar} = 1.10 \times 10^{10}$ M$_\odot$, a medium value, similar mass has been widely used by Fernández-Trincado et al. (2015c,b, 2016b).

3.) $M_{bar} = 1.60 \times 10^{10}$ M$_\odot$, this is the value of mass recently employed by Moreno et al. (2015).

Note that these values in mass are within the range suggested in the literature (e.g., Kent, 1992; Dwek et al., 1995; Blum, 1995; Stanek et al., 1997; Portail et al., 2017). The considered bar angle (α_{bar}) for the present-day orientation of the bar (angle between the major axis and the Sun-center line of sight, at positive longitudes), spans from 13° (value found by Robin et al., 2012), 16.5° (intermediate choice), and 20°.

Following Portail et al. (2017), we choose four values for the bar pattern speed in the range 25-55 km s^{-1} kpc^{-1} in steps of 10 km s^{-1} kpc^{-1}. The combination of these

parameters produce 36 models listed in Table 5.1. Finally, each model is compared to the mean and dispersion of the radial velocity distribution as a function of longitude and latitude in the Galactic bulge according to the BRAVA datasets (Kunder et al., 2012).

With the set of parameters above mentioned, we create controlled test particle simulations that can be compared to data. These simulations are considered only in the *last stages* of the Milky Way evolution, as has already been mentioned. We focus on the following two steps to produce these simulations in statistical equilibrium with the background potential:

1.) **Forward orbit integration in an entirely axisymmetric model:** We run forward orbit integration in the **Model 1** (see §3), where the Galactic bulge is assumed to follow a spherically symmetric potential of the form Miyamoto & Nagai (1975). Then, the particles are integrated during $t = 5$ Gyr, time in which the particle system reaches a state stable (statistical equilibrium) with the background potential. Here, we adopt for the bulge the set of masses 0.63×10^{10} $M_\odot$, 1.1×10^{10} $M_\odot$, and 1.6×10^{10} $M_\odot$. Once the particles reach an equilibrium state with the background potential, the Galactic bar is adiabatically added to the axysimmetric potential during a certain number of revolutions, see next step.

2.) **Forward orbit integration in a non-axisymmetric model:** Velocities and positions at the end state of step (1), are now the initial conditions of a system dominated by perturbations of the gravitational potential. The particles moving forward in time during 5 Gyr, and during the first 2 Gyr the bar grows slowly, time in which the mass of the spherically symmetric bulge (step 1) is entirely transfered to the bar structure (see 4). The initial bar parameters are then: $\alpha_{bar} = 13°$, $16.5°$, and $20°$, mass of 0.63×10^{10} $M_\odot$, 1.1×10^{10} $M_\odot$, and 1.6×10^{10} $M_\odot$, and pattern speeds $\Omega_{bar} = 25$ km s^{-1} kpc^{-1}, 35 km s^{-1} kpc^{-1}, 45 km s^{-1} kpc^{-1}, and 55 km s^{-1} kpc^{-1}. In the next section, we analyze the particle system in the final state, i.e., the state of the particles in statistical equilibrium with the bar potential plus the axisymmetric potential. We point out that our non-axisymmetric procedure is not self-consistent at all, and this should be contrasted in the future (postponed for a future study) whether giving mass to our test-particles could allow to close the loop and reproduce the bar potential that we have used in the first place. The same for the densities of the disks in general, where this would need to regenerate the potential if the disks thicken (which apparently does happen).

5.1 Simulating the BRAVA datasets from the BGM

We used our test particles to compare the kinematic predictions towards the Galactic bulge fields to measurements (with typical uncertainties of ~ 5 km s^{-1}) from the Bulge Radial Velocity Assay (BRAVA) survey (Kunder et al., 2012).

We have taken advantage of the Besançon population synthesis model to simulate the BRAVA datasets. We generate synthetic M-giant stars towards the bulge BRAVA fields in the apparent magnitude range $8.2 < K_s < 9.25$ (Kunder et al., 2012; Gardner et al., 2014), adopting the Marshall et al. (2006) 3D map extinction.

For each bulge field, the BGM predicts the distribution of M-giant stars per stellar population, including the thick disk, the seven components of thin disk, the stellar halo, and a boxy/peanut "bar" distribution. Note that the BGM predicts synthetic M-giant stars along the bar structure according to its density profile, and *does not necessarily made consistent predictions between its kinematic and density profile*. We then used a simple selection function to choose all particle disks along a given line-of-sight and more or less covering the same spatial distribution as expected from the BGM to ensure that we are comparing simulations to data in the same volume. To define the selection function, we estimated for each BRAVA field the expected distribution in distances from the luminosity function of M giants in a similar way as Gardner et al. (2014). Figure 5.1 shows the predicted heliocentric distance of the synthetic sample of M-giant stars from the Besançon population synthesis model compared with the selected distribution of disk particles. As already pointed out by Gardner et al. (2014), a detailed selection function is more complex and this implies considering other parameters as: T_{eff}, $log\ g$, which are not available from the test particle simulations. However, for our general purposes the distance and kinematics are relatively enough to compare simulations to data.

On the other hand, kinematic studies of the Galactic bulge as Shen et al. (2010); Ness et al. (2013b); Gardner et al. (2014); Zasowski et al. (2016), etc, are based on simulations of a bulge formed via a simple bar instability mechanism (Martinez-Valpuesta & Gerhard, 2011; Di Matteo et al., 2015), and even when these simulations fit fairly well the kinematic trends of the Milky Way bulge, they fail to reproduce the complex kinematic trends of each stellar population individualy, when separated per metallicity bins (see discussion in Di Matteo et al., 2015). In the following sections, we examine the kinematic behaviour from test particle simulations.

5.2 Comparing test particle simulations to real observational data

Table 5.1 provides the 36 simulations run in this thesis using the potentials of the **Model 2** as described in §3, varying the bar mass, the bar pattern speed and the bar angle. In each parameter configuration, we applied a χ^2 test between simulations and real observational data to select the best-fitting parameters. The χ^2 has been defined as

$$\chi^2_{BRAVA} = \sum_{i=1}^{N_{BRAVA}} \left(\frac{V_{BRAVA_i} - V_{model_i}}{\sigma_{BRAVA_i}} \right)^2 \tag{5.1}$$

where the subscript i stands for each BRAVA data point, $N_{BRAVA} = 74$ is the number of data points also associated to the number of BRAVA fields used in this work, covering Galactic longitude from -10° to 10° and Galactic latitudes $-4°$, $-6°$, and $-8°$, each BRAVA fields consists of ∼100 stars distributed in a field of view of ∼3 square degree. V_{BRAVA_i} and σ_{BRAVA_i} are mean velocities and velocity dispersions for each BRAVA field, and V_{model_i} is the mean velocities as predicted by the model along each BRAVA field. The results are presented in Table 5.1. Note that models 1, 5, 9, 22, 36 have smaller values of

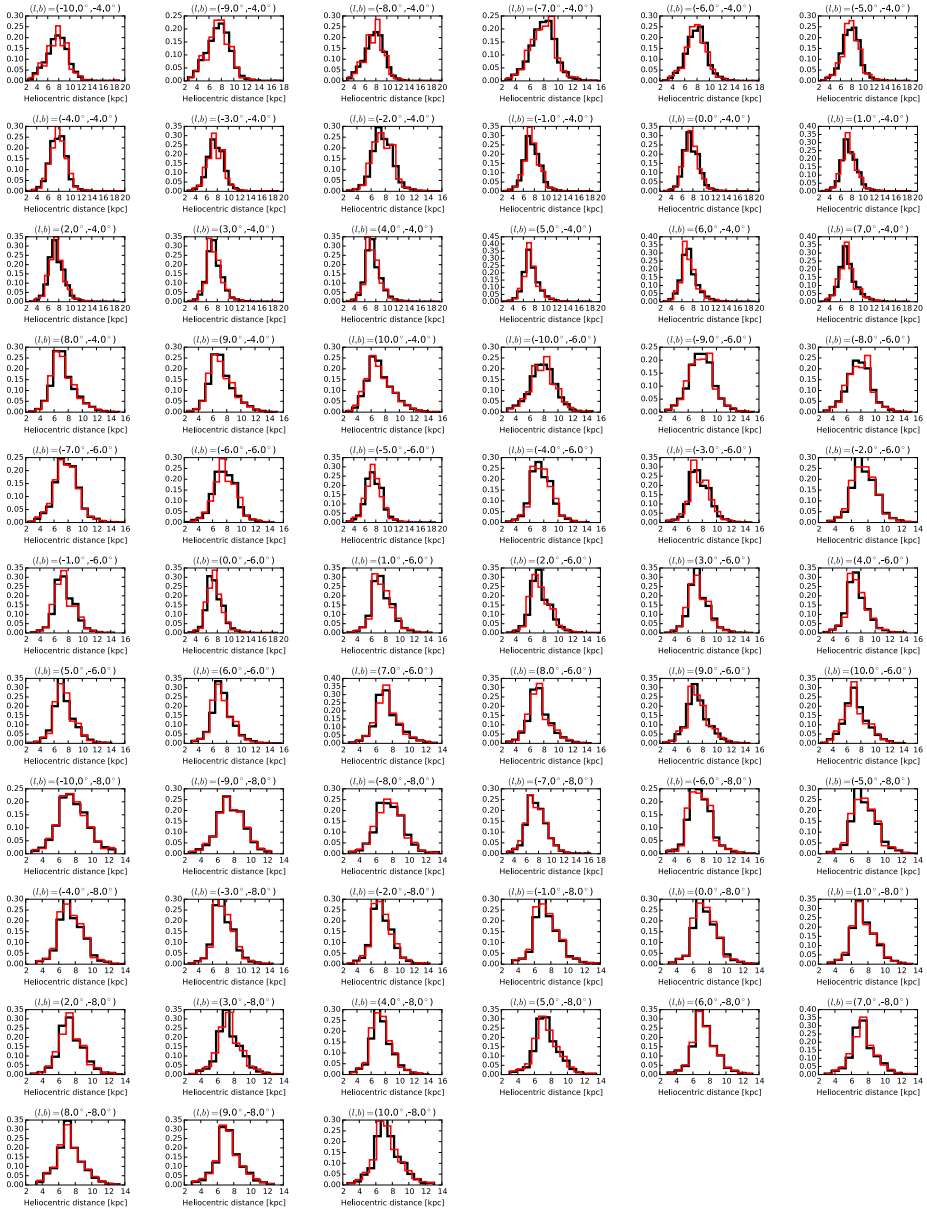

Figure 5.1: This plot shows the heliocentric distance distributions of M-giant stars predicted by the Besançon populations synthesis model (black histograms) along 66 BRAVA fields, and the distributions of the selected disk particles (red histograms).

Table 5.1: Primary sample of disk particle simulations in this thesis

Model	Mass $M_\odot \times 10^{10}$	$\alpha_{\rm bar}$ degree	$\Omega_{\rm bar}$ km s^{-1} kpc^{-1}	χ^2_{BRAVA}
1	0.63	13.0	25	2.52
2	0.63	13.0	35	4.13
3	0.63	13.0	45	5.05
4	0.63	13.0	55	5.66
5	0.63	16.5	25	2.53
6	0.63	16.5	35	4.08
7	0.63	16.5	45	5.24
8	0.63	16.5	55	5.58
9	0.63	20.0	25	2.55
10	0.63	20.0	35	4.19
11	0.63	20.0	45	5.14
12	0.63	20.0	55	5.66
13	1.1	13.0	25	3.24
14	1.1	13.0	35	2.39
15	1.1	13.0	45	2.41
16	1.1	13.0	55	2.94
17	1.1	16.5	25	3.12
18	1.1	16.5	35	2.29
19	1.1	16.5	45	2.26
20	1.1	16.5	55	2.98
21	1.1	20.0	25	3.12
22	**1.1**	**20.0**	**35**	**2.05**
23	1.1	20.0	45	2.26
24	1.1	20.0	55	2.69
25	1.6	13.0	25	8.96
26	1.6	13.0	35	4.07
27	1.6	13.0	45	2.83
28	1.6	13.0	55	2.43
29	1.6	16.5	25	8.84
30	1.6	16.5	35	4.19
31	1.6	16.5	45	2.88
32	1.6	16.5	55	2.54
33	1.6	20.0	25	8.90
34	1.6	20.0	35	3.99
35	1.6	20.0	45	2.73
36	1.6	20.0	55	2.37

χ^2 than others, while visual examination indicates that models 1, 5, and 9 give practically the same results, with similar χ^2. However, for our analysis we have favored the model 22, with a bar mass of $\sim 1.1 \times 10^{10}$ $M_\odot$, a bar pattern speed of 35 km s^{-1} kpc^{-1}, and bar orientation of 20°, wich produces the smaller value of χ^2.

Although this procedure gives the best value in terms of a goodness of fit parameters to the data, a visual examination indicates that other models fit fairly well the overall kinematic trends in the bulge, therefore we cannot rule out other set of bar parameters, such as Model 36 listed in Table 5.1, this would correspond to $\chi^2 = 2.37$, with a bar mass of $\sim 1.6 \times 10^{10}$ $M_\odot$, a bar pattern speed of 55 km s^{-1} kpc^{-1}, and a bar orientation of 20°. Hence, we have seen that there is a clear degeneracy inherent in the parameter space (Ω_{bar}, α_{bar}, and mass). There is a clear tension between models and observations. For instance, Monari et al. (2017a,b) showed that *the existence of the Hercules stream in the local velocity space favours a fast bar*, while bulge dynamical models reproducing the stellar kinematics from BRAVA datasets favours a slow bar (e.g., Portail et al., 2017), as also seen in this thesis based on the best χ^2. To alleviate this tension other elements should be taken into account in our test particles simulations, for example considering the contribution of spiral arms plus bar, allows to examine simultaneously the local velocity space and kinematics behaviour in terms of stellar populations synthesis. However given the limitations of the Besançon Galaxy model to take into account other non-axisymmetric structures like the spiral arms, any new conclusion is beyond the scope of this thesis. Finally, we caution the reader that through this thesis we have favored a slow bar, i.e., our **Model 22** that produces the best fit to the BRAVA datasets with $\chi^2 = 2.05$. It is important to note that the main goal of this work is to set the kinematics of synthetic stellar populations from barred test particle simulations, therefore in §4 we have discussed the main impact in the kinematics when a fast and massive bar is employed.

5.3 Relevant result from this chapter

Our first result leads to a "slow bar", with a bar pattern speed of $\Omega_{bar} = 35$ km s^{-1} kpc^{-1}, a mass of $\sim 1.2 \times 10^{10}$ $M_\odot$, and the present angle between the semi-major axis of the bar and the Sun-Galactic center line of $\sim 20°$. As we have already mentioned these parameters fit fairly well the global kinematic trends observed from the BRAVA datasets, placing the bar corotation radius around $r_{corotation} \sim 7$ kpc (very near to the Solar radius) as shown in Figure 5.2. These values are consistent with the recent dynamical studies towards the Galactic bulge (Portail et al., 2017), but in disagreement with the results from Monari et al. (2017a,b), however, the Besançon Galaxy model do not consider other additional perturbations like the spiral arms which play an important role in the local velocity space (e.g., Antoja et al., 2009; Antoja, 2010). Hence, given the very low resolution of particles in the solar position (8 kpc) any new conclusion concerning the effects of the bar at the Solar position is beyond the scope of this thesis.

The mean velocity and velocity dispersions of the models listed in Table 5.1 are illustrated in Figures 5.3, 5.4, 5.5, 5.6, 5.7, 5.9, 5.10, 5.11. Note that the models 1 - 12 with a bar mass of the order of 0.63×10^{10} $M_\odot$, even if they fit the rotation curve, do not reproduce the velocity dispersions as observed in the real data. This bar mass seems

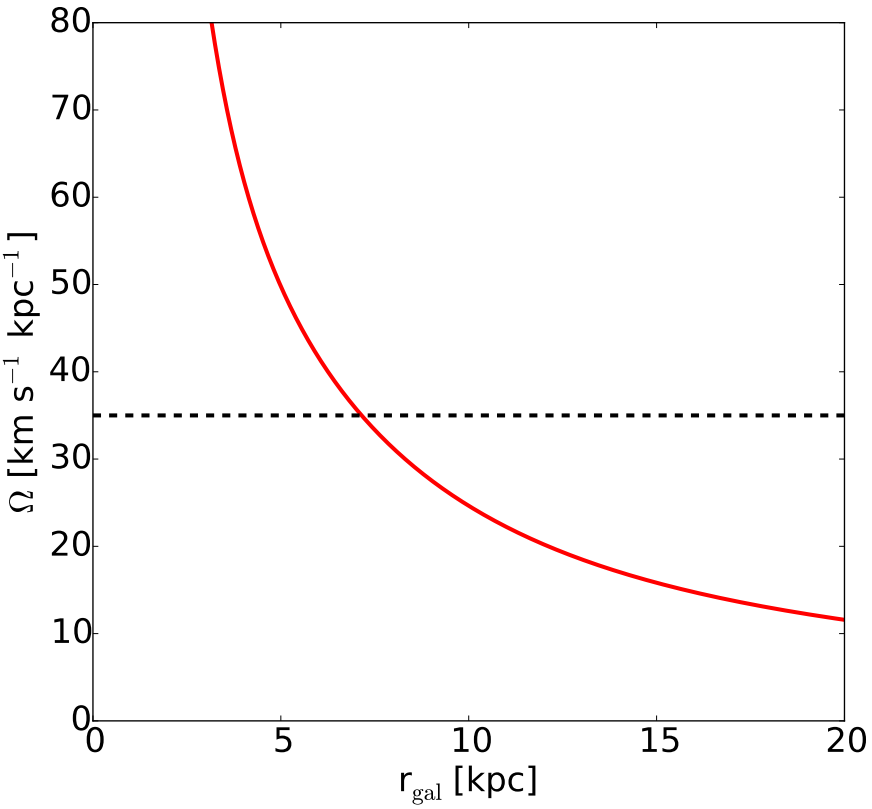

Figure 5.2: Resonance curve in our barred Milky Way model for corotation Ω, this plot shows the localization of the bar resonance. The black dashed line indicates the best fit of the pattern speed found in this thesis, to be $\Omega_{bar} = 35$ km s^{-1} kpc^{-1} (see text).

to be insufficient to gives a bar strength able to produce the velocity field, see the underestimated velocity dispersions profiles Figures 5.3, 5.4, and 5.5, except when a value of the bar pattern speeds of ~ 25 km s^{-1} kpc^{-1} is adopted, giving an acceptable fit only at latitude $-8°$.

We show in Figures 5.9, 5.10, and 5.11 that for a bar mass 2.5 times bigger (1.6×10^{10} M$_\odot$) the velocity dispersion profiles are overestimated, except when a value of the bar pattern speeds of ~ 55 km s^{-1} kpc^{-1} is adopted, in agreement with data. Figure 5.6, 5.7, 5.8 show that a bar mass $\sim 1.1 \times 10^{10}$ M$_\odot$ and a bar pattern speeds ~ 35 km s^{-1} kpc^{-1} provides a very good fit to the velocity and velocity dispersions profiles.

Figure 5.12 illustrates the global kinematic trends toward the Galactic bulge as predicted by our best model that fits fairly well the observed BRAVA data. For comparison, we plot the rotation curve and velocity dispersion profiles of our best model to different Galactic latitudes towards the Galactic bulge (see Figure 5.13). We can see from 5.13 that our best model predicts the expected kinematic trends towards the Galactic bulge, i.e., the velocity dispersion profile increases with decreasing Galactic latitude, in very good agreement with observations.

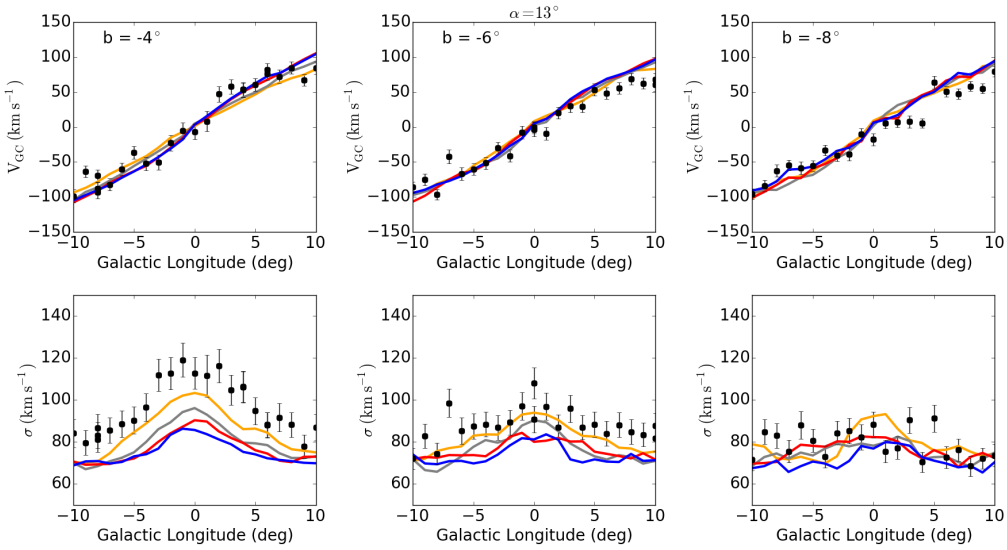

Figure 5.3: Rotation curve (top panel) and velocity dispersions (bottom panel) along three different Galactic latitudes ($-4°$, $-6°$, $-8°$) compared to BRAVA data (black symbols) with the sampling error. For each plot, three physical parameters of the bar are illustrated: $\Omega_{bar} = 25$ km s^{-1} kpc^{-1} (yellow line), $\Omega_{bar} = 35$ km s^{-1} kpc^{-1} (grey line), $\Omega_{bar} = 45$ km s^{-1} kpc^{-1} (red line), $\Omega_{bar} = 55$ km s^{-1} kpc^{-1} (blue line), for an assumed bar orientation to be $\alpha_{bar} = 13°$ with the Sun-GC line of sight, and a total mass for the bar assumed to be 0.63×10^{10} M$_\odot$.

Figure 5.14 shows the mean motion of particles in each disk sub-component for the

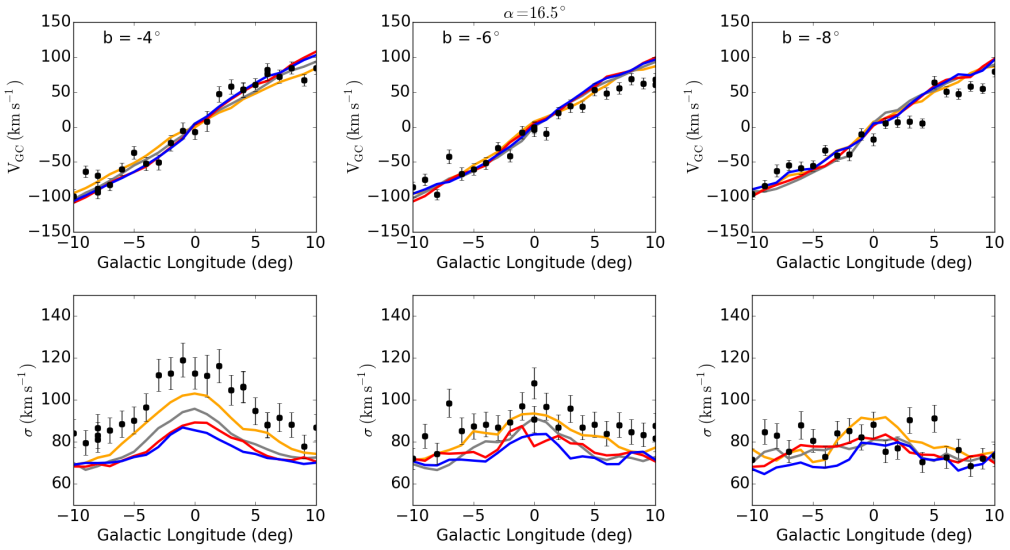

Figure 5.4: This Figure represents the same measurements as in Figure 5.3, but now adopting a bar orientation of $\alpha_{bar} = 16.5°$.

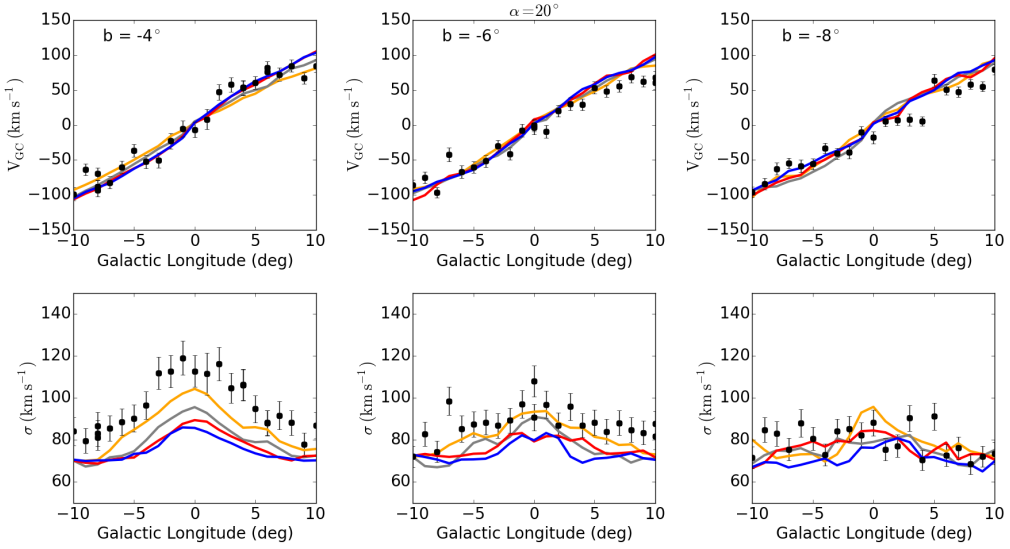

Figure 5.5: This Figure represents the same measurements as in Figure 5.3, but now adopting a bar orientation of $\alpha_{bar} = 20°$.

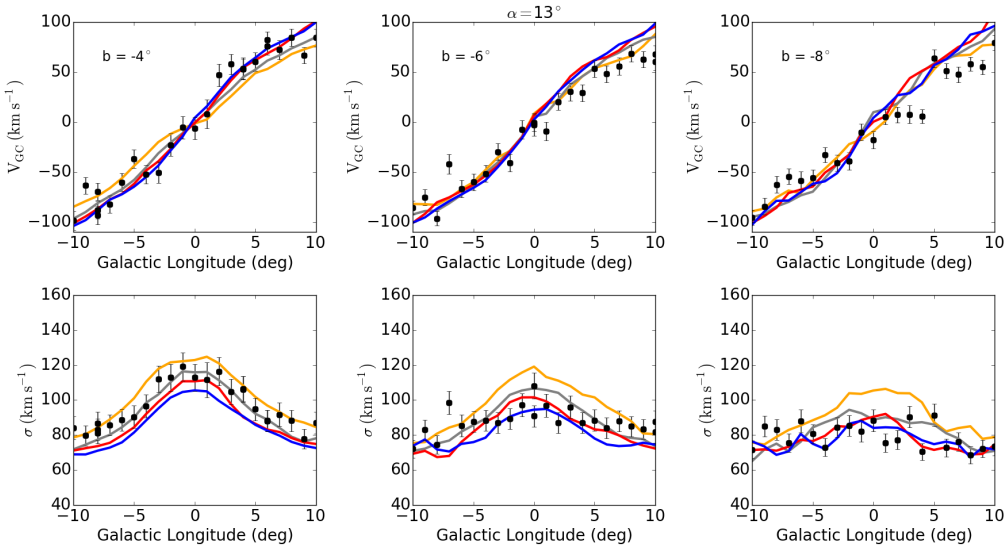

Figure 5.6: This Figure represents the same measurements as in Figure 5.3, but now adopting a bar orientation of $\alpha_{bar} = 13°$ and a bar mass of 1.1×10^{10} $M_{\odot}$.

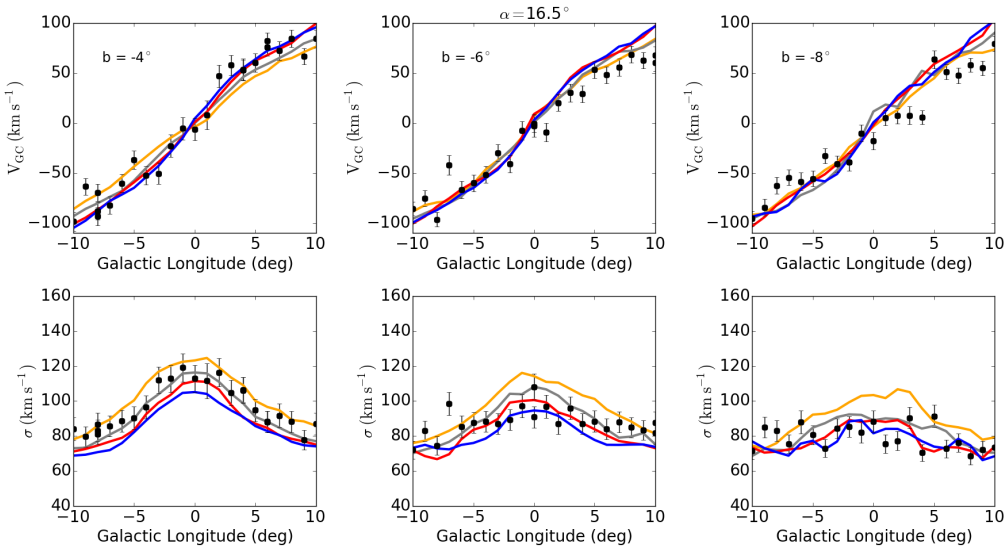

Figure 5.7: This Figure represents the same measurements as in Figure 5.6, but now adopting a bar orientation of $\alpha_{bar} = 16.5°$.

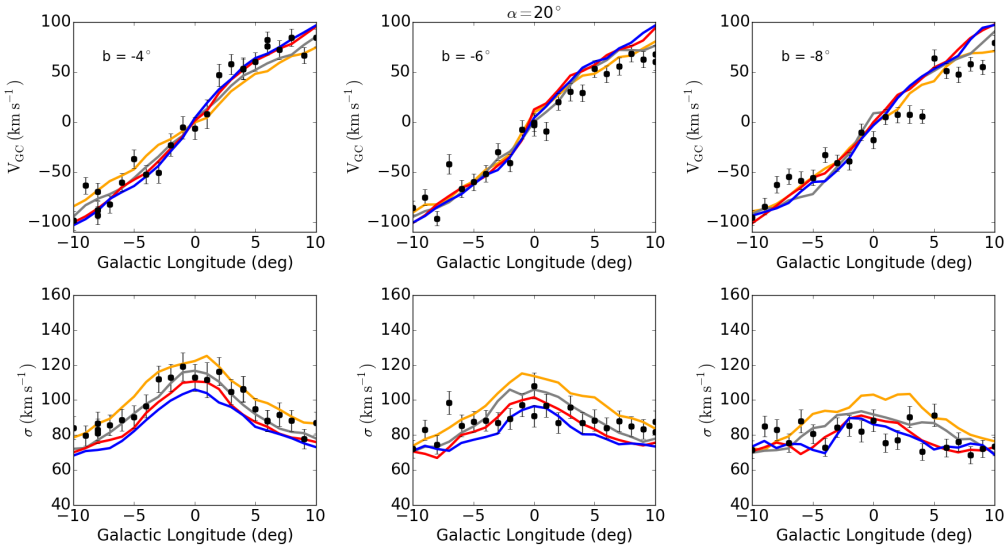

Figure 5.8: This Figure represents the same measurements as in Figure 5.6, but now adopting a bar orientation of $\alpha_{bar} = 20°$.

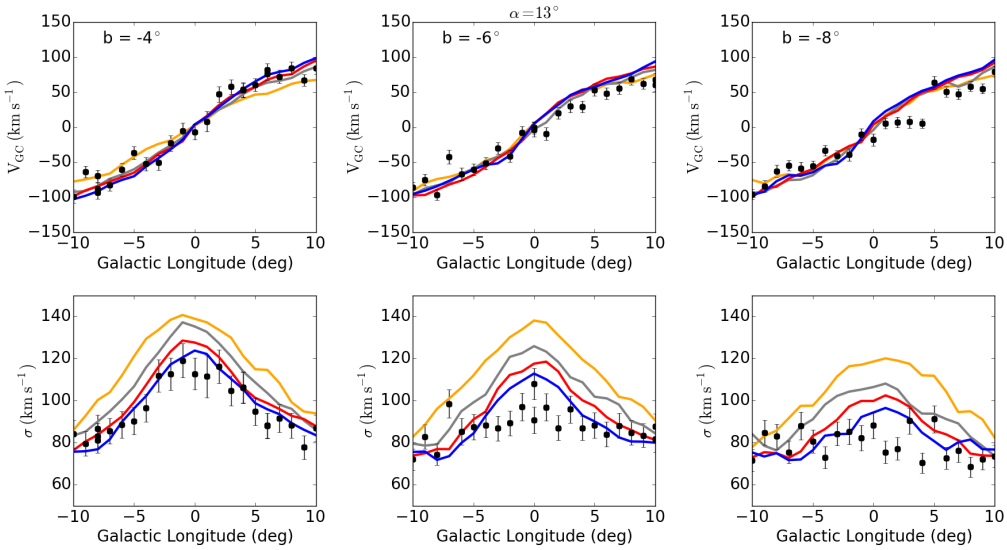

Figure 5.9: This Figure represents the same measurements as in Figure 5.3, but now adopting a bar orientation of $\alpha_{bar} = 13°$ and a bar mass of 1.6×10^{10} $M_{\odot}$.

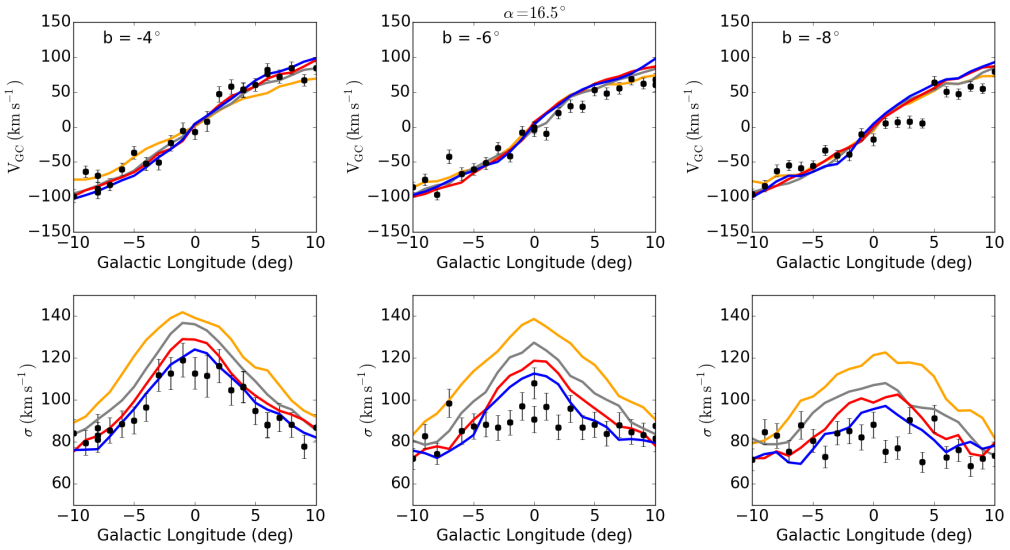

Figure 5.10: This Figure represents the same measurements as in Figure 5.9, but now adopting a bar orientation of $\alpha_{bar} = 16.5°$.

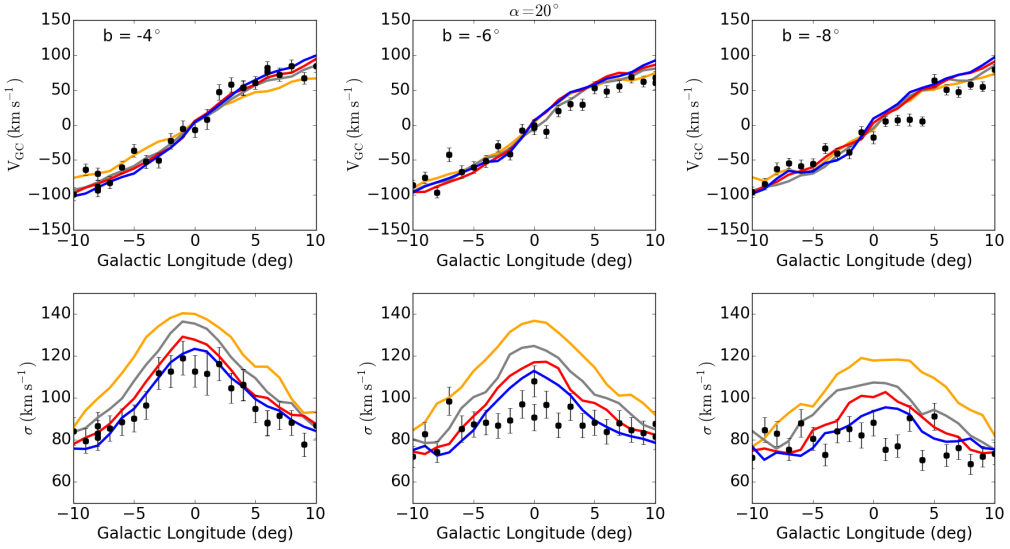

Figure 5.11: This Figure represents the same measurements as in Figure 5.9, but now adopting a bar orientation of $\alpha_{bar} = 20°$.

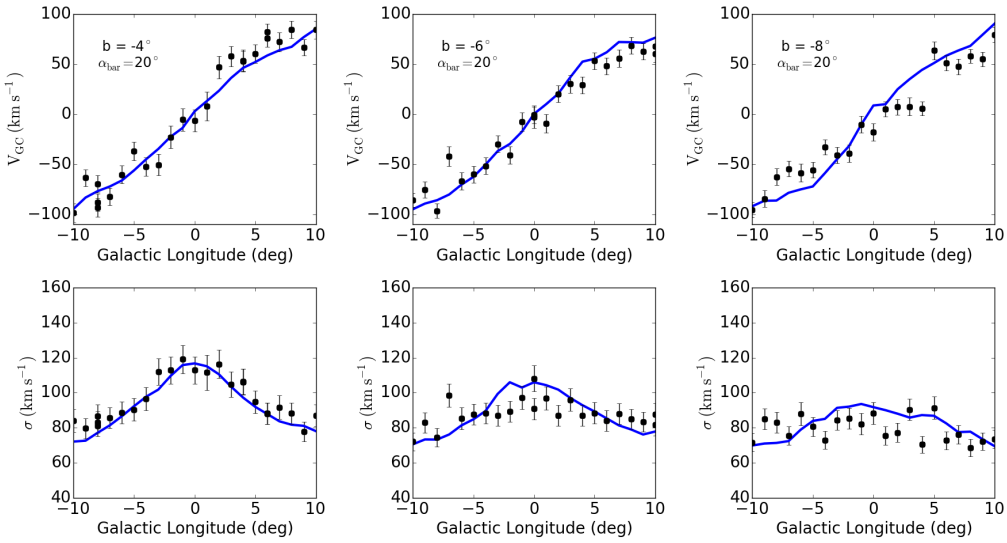

Figure 5.12: Rotation curve and velocity dispersion profiles for our best-fitting model for the BRAVA data. The blue line shows the predicted global kinematic trends towards the Milky Way using the set of bar parameters of the model 22 listed in Table 5.1.

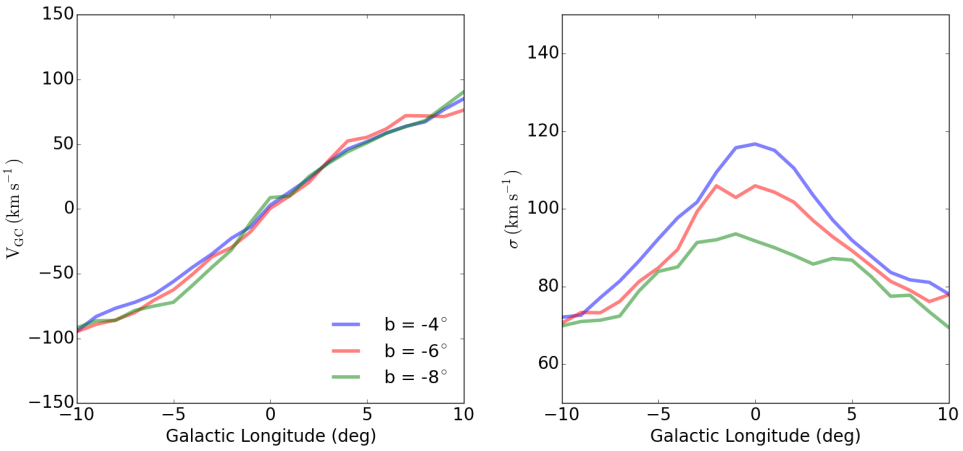

Figure 5.13: Rotation curve (left panel) and velocity dispersion profiles (right panel) from our best model. For comparison, three different Galactic latitudes are shown.

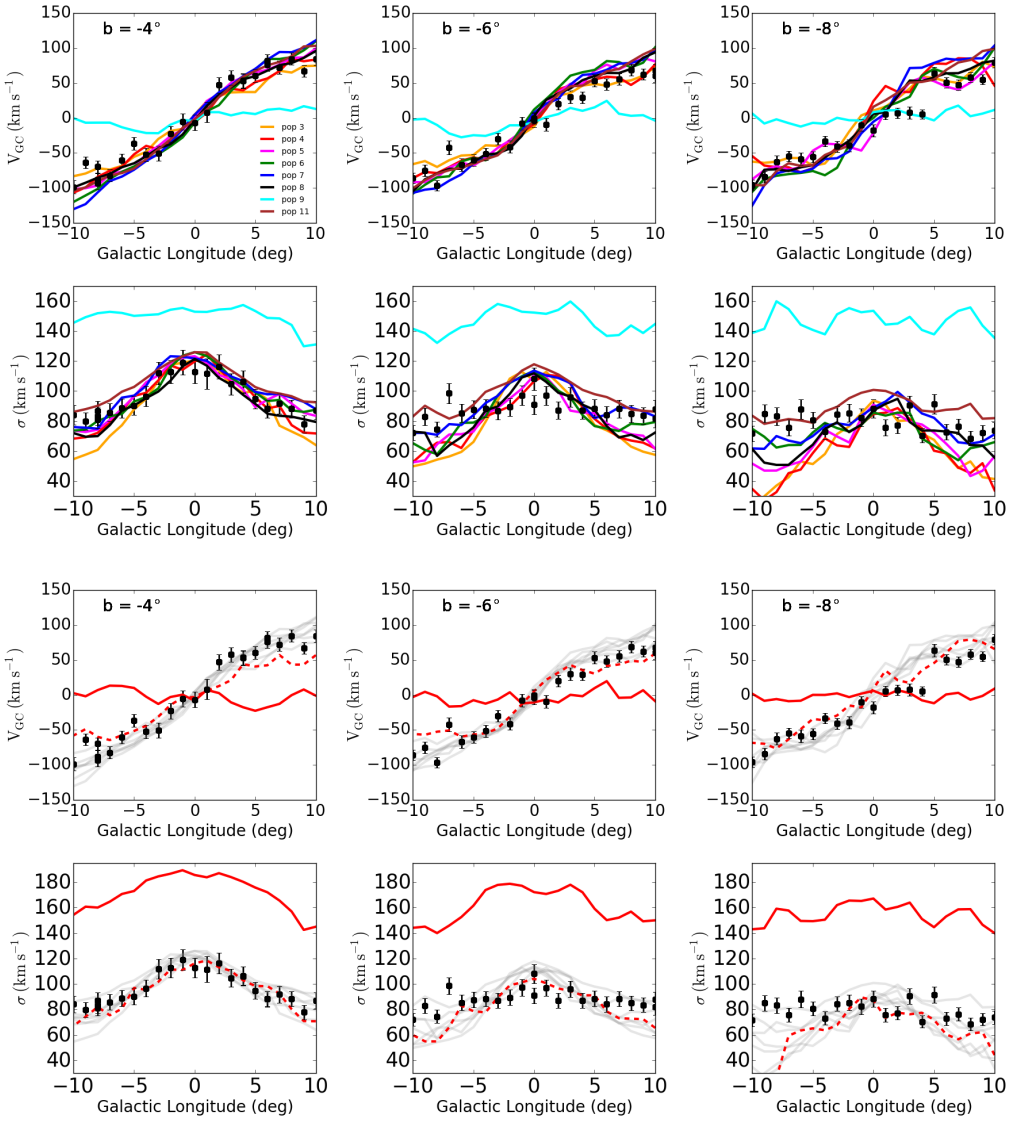

Figure 5.14: Top panel: This Figure represents the same measurements as in Figure 5.13, but for disk sub-components particles and the stellar halo particles. Bottom panel: This Figure represents the same measurements and models (grey lines) as in top panel. Here, we shows two interesting kinematic features of the stellar halo particles, the rotation curve and velocity dispersion profiles for stellar halo particles following the bar structure are illustrated in red dashed lines compared with the stellar halo particles not following the bar structure (red solid line).

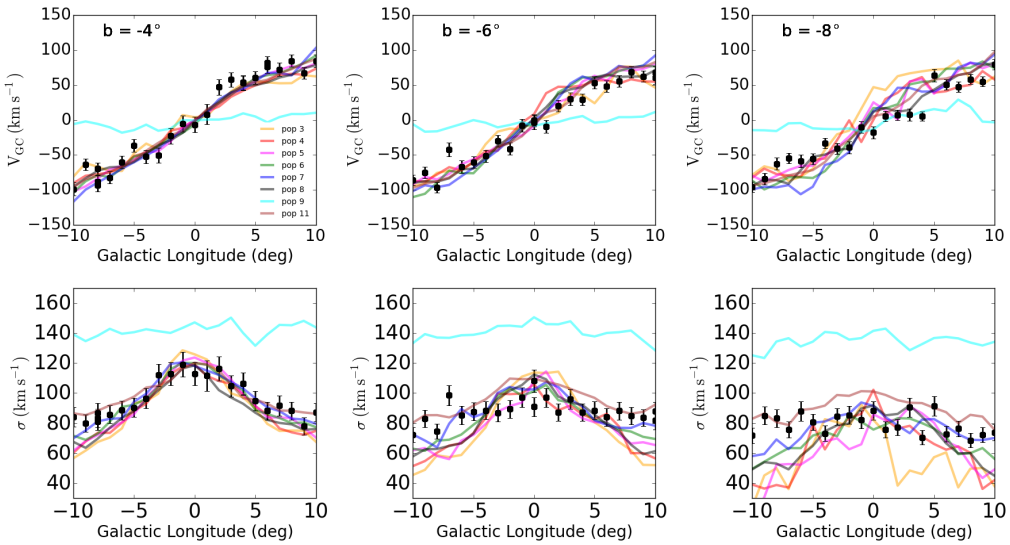

Figure 5.15: This Figure represents the same measurements as in Figure 5.14, but now adopting the Model 36, with a bar orientation of $\alpha_{bar} = 20°$, pattern speed of $\Omega_{bar} = 55$ km s^{-1} kpc^{-1}, and bar mass of 1.6×10^{10} M$_\odot$.

model 22 shown in 5.12, the predicted rotation curve and velocity dispersion profiles for each stellar population (as it has been traditionally called in the BGM), associated to particles in the disk and stellar halo are illustrated in the same. The plot is a comparison between the different stellar populations and the real data towards the Galactic bulge. Note that Figure 5.12 reproduces well the global kinematical trend, despite the fact that the data represent a mix of different populations having different kinematics. The comparison of each sub-population is interesting because it allows to show what is the influence of each population on the global fit, and as a function of latitude and longitude. In Figure 5.14, we clearly identified that different initial conditions produce different kinematic trends towards the Galactic bulge, i.e., in high Galactic latitudes where only the warmer and older disk particles (brown line) seems to explain the velocity dispersion profiles, while in low latitudes ($-4°$) the younger components (thin disks and young thick diks) seems to be successful to explain relatively well the observations. This result supports the vision of a bulge composite nature (e.g., Recio-Blanco et al., 2017). The need to call upon a hotter disk component (e.g., Di Matteo et al., 2015) is not confirmed by our predicted velocity dispersion profiles, at least at low Galactic latitudes ($-4°$ and $-6°$). In other word, it is clear that kinematics colder disk particles are able to explain the observations, however, note that this may be sensitive to the imposed initial conditions, which do not follow the real evolution scenario of the Milky Way, and the initial conditions imposed in this work are the ones inferred from the present-day observations in the solar neighbourhood. A confirmation from N-body simulations adopting multiple disk populations, with

differents length scales, and different kinematics may help to shed some light or confirm our results and the recent discussion in the literature (Di Matteo et al., 2015). We run tests with the values of the **Model 36** to verify that our analysis are not strongly affected by possible variations in the main physical parameters of the Galactic bar. Figure 5.15 shows similar results as 5.14, and confirms that small variations in these parameters do not lead to substantial difference in the overall results presented in this work.

Concerning stellar halo particles, Figure 5.14 displays the predicted kinematic trends for this component (cyan solid line). It shows a small rotation with a high and flat velocity dispersion profiles at all the Galactic latitudes. Anticipating the results presented in §6 and §7, bottom panel in Figure 5.14 illustrates the same measurements as in the top panel of the same Figure, but we now see two marked kinematic trends for the stellar halo. Such models lead to an inner stellar halo with negligible or zero rotation compatible with those particles not following the bar morphology (red solid line), while that stellar halo particles that participate in the bar (∼20% of particles towards the bulge region, see §7) structure are able to produce a marked rotation strikingly similar to those observed in the real data as expected for a system showing cylindrical rotation, but these halo particles following the bar do not participate in the "boxy/peanut" morphology. These results reinforce the vision that a small fraction of the inner stellar halo shows cylindrical rotation with low velocity dispersion profiles in comparison to its not rotating counterpart.

Main conclusion: Our results support the recently discovered population of RR Lyrae which shows negligible rotation (Kunder et al., 2016) towards the Galactic bulge. Hence the majority of the halo stars does not participate to the bar structure (∼ 77%, see §7) and have no rotation, but a minority follows the bar (∼ 22%). It is in good agreement with recent conclusions from N-body simulations (Pérez-Villegas et al., 2017a)..

5.4 Velocity maps and predicted shape of the inner disk

Figure 5.16 and Figure 5.17 illustrate the predicted line-of-sight velocities and dispersions of disk subcomponent particles and the stellar halo particles of our best model, where the logarithmic surface density contours show that the bar dominates the particles distribution of the system in the inner ∼ 4 kpc. In our frame a negative velocity corresponds to a motion away from the Sun, and the peak velocities near the Galactic centre exhibit the characteristic *winged* patterns of the velocity field first noted in N-body simulations by Debattista et al. (2015) as a consequence of the boxy/peanut bar. Note that the stellar halo particles exhibit small rotation in the inner Milky Way, this component will be discussed in §6 and §7. It is important to note that Figure 5.17 shows two significant peaks distributed around the end of the semi-major axis of the bar which we can associate with the boxy/peanut morphology of the bulge, and the velocity dispersion decreases near the minor axis. We will discuss this limitation in the next subsection.

The bottom panel in Figure 5.18 shows the predicted velocity dispersion maps toward the regions of the bulge (< 4.5 kpc) in Galactic coordinates. Two significant peaks are manifested at high latitudes, that can be due to a nuclear and/or extra component not considered in the Besançon Galaxy model. The top panel in Figure 5.18 shows the

velocity maps in Galactocentric coordinates, again negative velocity $\langle V_{los} \rangle$ corresponding to a motion away from the Sun. The eighth panel in the same figure displays the kinematic feature of the stellar halo which exhibit null or negligible rotation due to the influence of the bar (e.g., Saha et al., 2012; Pérez-Villegas et al., 2017a), and the stellar halo particles following the bar produce cylindrical rotation as was illustrated in the bottom panel in Figure 5.14.

Figure 5.19 displays the predicted shape of disk sub-components particles in the region delimited by $|X| < 10$ kpc and $|Y| < 10$ kpc (left panels) and $|X| < 5$ kpc, $|Y| < 5$ kpc and $|Z| < 2.5$ kpc (right panels), in presence of the "boxy/peanut" bar potential. The rows 1 to 5 correspond the thin and cooler disk particles with different scale lengths and axis ratios. In our model the thin disk populations exhibit a prominent "boxy/peanut" morphology, thin at short radii, thicker at intermediate radii around 1 kpc, and thin again at r_{gal} >2 kpc. However, the two thick disk populations (Pop 8 and Pop 11) are puffed up at large radii as consequence of the bar. The old, hotter, and concentrate thick disk does not underline a significant boxy/peanut bar, while the young, warmer, and the young thick disk (Pop 8) seems to underline a noticeable "boxy/peanut" morphology similar to that in the thin disk. Even when our simulations predict a "boxy/peanut" bulge for a young, and concentrate thick disk, this is a consequence of imposed initial conditions. The nature of a younger and concentrate thick disk in the central part is not well understood yet, and remains elusive.

5.5 Concluding remarks

1.) **The thin disk:** Our test particles simulations show that disk particles participate in the "boxy/peanut" morphology of the bulge. This model reproduces well the kinematics of BRAVA data at various latitudes and longitudes. More observational constraints at latitudes around 10° in the bulge region are needed to validate this model.

2.) **The young thick disk:** Note that our young thick disk particles produce a notable "boxy/peanut" structure due to the effects produced by the boxy bar potential. In other words, the imposed initial conditions observationally constrained at the solar position produce such morphology towards the inner Milky Way. It cannot be interpreted as a probability that a dominant "boxy/bulge" is formed from a young thick disk. Our simulations are not able to follow such scenario because the fact that we are setting the initial conditions from present-day kinematics. N-body simulations with an alive potential would be necessary to follow the evolution in time of this component. There may be a possibility that this structure is associated with the component B (metal-poor populations, $\langle$[Fe/H]$\rangle = -0.25$ dex) or the so-called thick boxy/peanut-bulge observed in the ARGOS survey (Ness et al., 2013a,b). Accurate proper motions at the extremity of the bar obtained by the Gaia mission will help to shed some light on these findings.

3.) The old thick and hotter thick disk is puffed up by the Galactic bar, and only a not significant fraction of particles streaming into the boxy/peanut morphology.

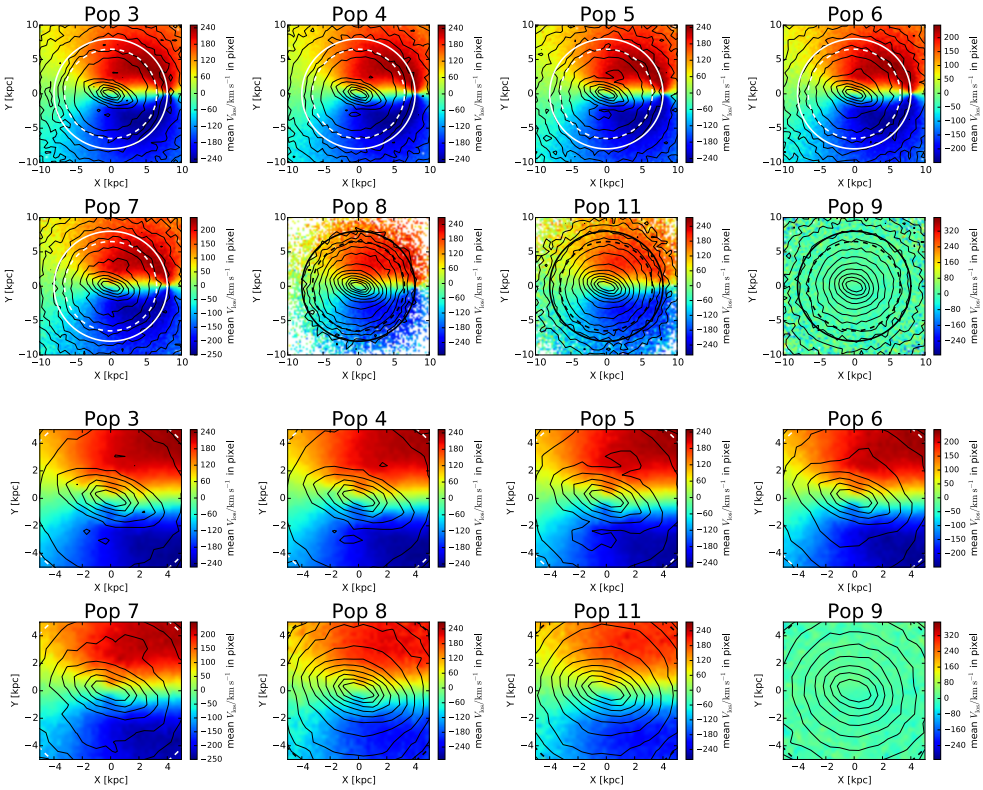

Figure 5.16: Predicted line-of-sight velocity maps of our best model (see text) in the region delimited by $|X| < 10$ kpc and $|Y| < 10$ kpc (firt and second row), and a zoomed-in view of the same region delimited by $|X| < 5$ kpc and $|Y| < 5$ (third and fourth row). Corotation radius is shown in white and black dashed line, and the Solar radius is shown in white and black solid line. The thin black lines shows the logarithmic surface density contours of the disk and halo particles. Colors indicate $\langle V_{los} \rangle$ in units of km s^{-1}.

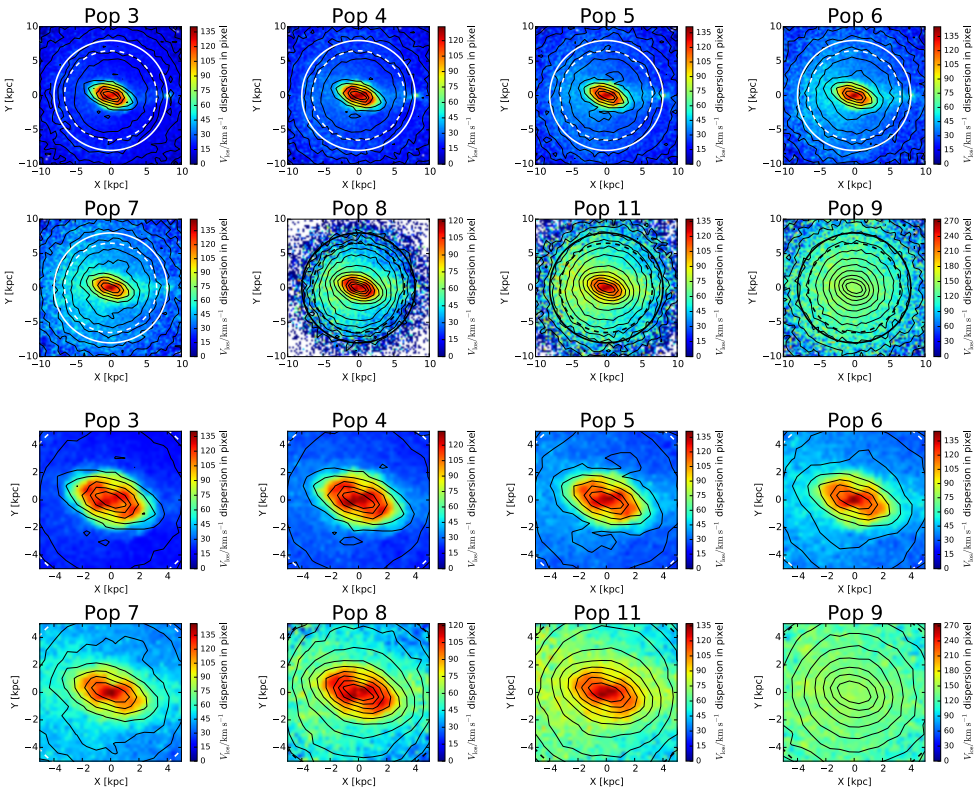

Figure 5.17: This Figure represents the X, Y maps of the velocity dispersion for each stellar population. Colors indicate σV_{los} in units of km s^{-1}.

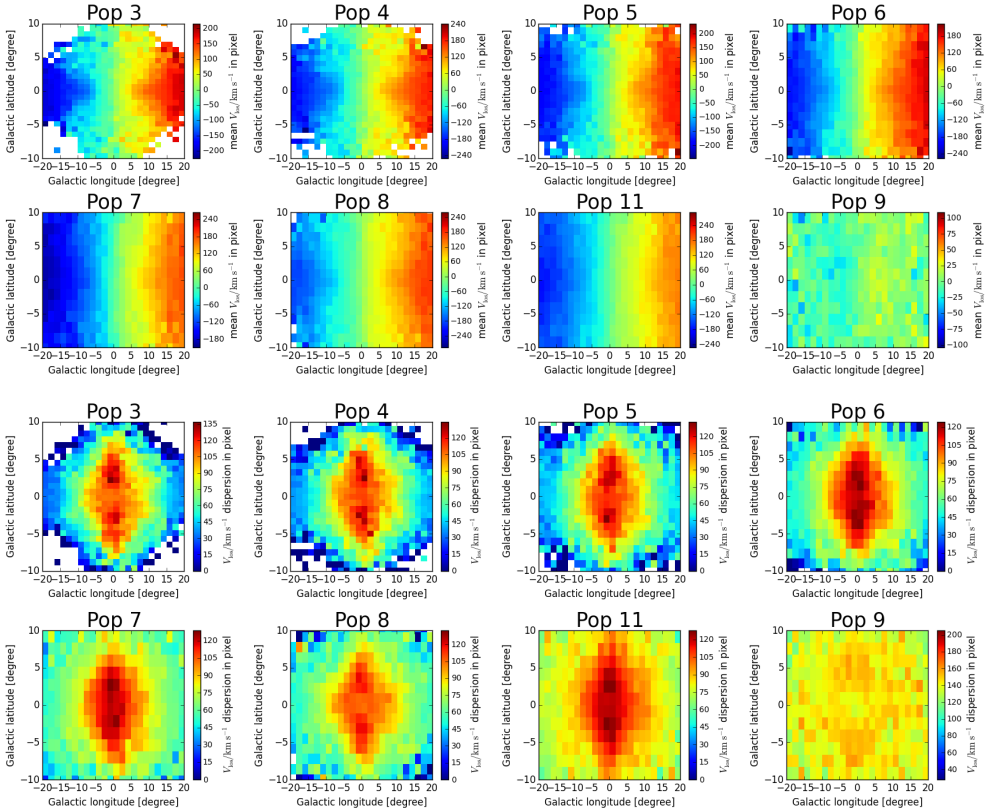

Figure 5.18: The predicted mean line-of-sight velocity (first and second row) and velocity dispersion maps (third and fourth row) in longitude-latitude of our best model for each disk sub-component and the stellar halo particles. In these panels, only particles with $|X| < 3.5$ kpc, $|Y| < 3.5$ and $|Z| < 3.5$ kpc around the bulge regions have been selected.

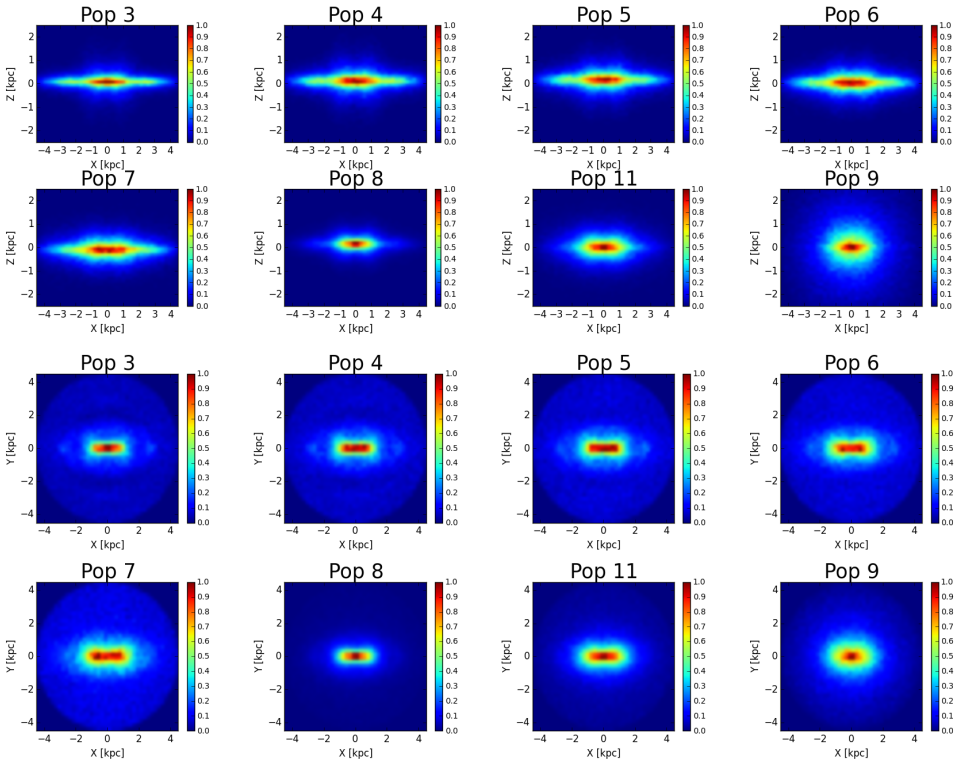

Figure 5.19: Density maps projected on the X, Y and X, Z planes for seven disk models (the legend within each plot indicates the stellar population, see text) in the non-inertial reference frame where the bar is at rest. The colours indicate the kernel density estimate within < 4.5 kpc.

4.) A small fraction of the stellar halo particles participates in the bar structure as shown in Figure 5.14. In §7 we shall show that this small fraction does not participate in the "boxy/peanut" bar.

Here, we want to emphasise that even though our simulations reproduces the overall kinematic trends towards the Milky Way bulge, our variety of initial conditions and our potential model fail in representing the observed velocity dispersion towards the inner part of the Milky Way. Figure 5.20 shows the rotation curve and velocity dispersion profiles of our best model. This plot represents the same measurements as in Figure 5.12, for comparison we add the kinematic trends as function of the Galactic latitude. We note that even though our model reproduces fairly well the rotation curve along Galactic latitude, it appears to generate a dip in the velocity dispersion profile at latitudes below 2°. In other words, our approach to generate a Galactic bulge dominated by a boxy/bar morphology (see §4) is insufficient to match kinematic trends (velocity dispersion profile) in the central part.

We concluded that we need an additional mass in the inner Milky Way in order to reproduce the BRAVA velocity dispersions at low Galactic latitudes, these results seems to support the existence of an extra population in the nuclear region (see e.g., Robin et al., 2012). The morphology of this additional mass is beyond the scope of this thesis but coud be addressed in the near future using kinematic constraints from infrared data (APOGEE).

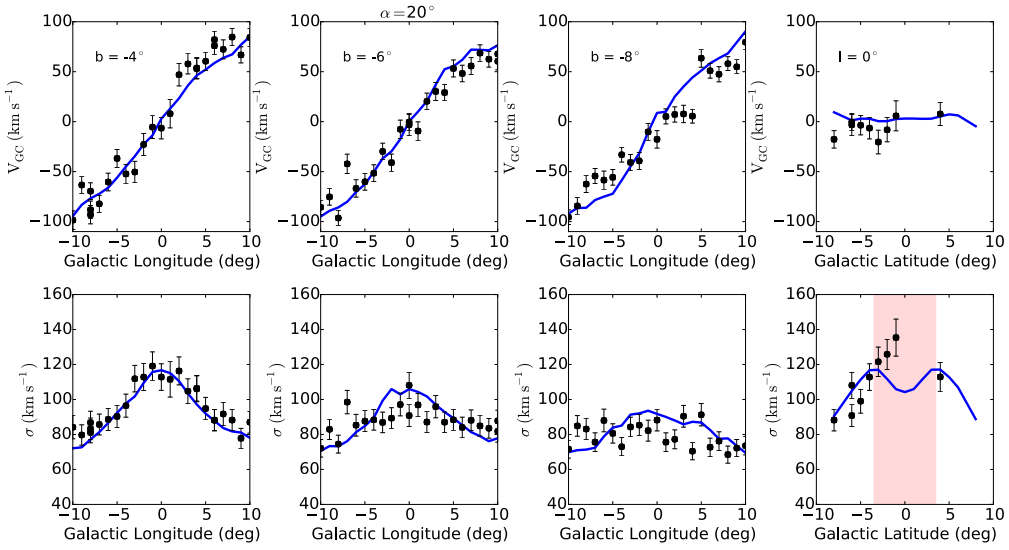

Figure 5.20: Rotation curve and velocity dispersion profiles as function of the Galactic longitude (panels in column 1, 2, and 3), and the kinematic trends as a function of the Galactic latitude is illustrated in the column 4.

Chapter 6

The Stellar Halo

In this chapter we discuss the characteristics of the so-called "stellar halo", thought-out to be the old structure with small net prograde rotation (Carollo et al., 2007, 2010; Hawkins et al., 2015) surrounding the inner primary Galactic components (disk and bulge). From the "theoretical" point of view we perform 3D test particle simulations, in order to review the spatial distribution and kinematics inherited from non-axisymmetric potentials.

6.1 The stellar halo as seen from test particles simulations

The discovery of a significant metal-rich ($\langle$[Fe/H]$\rangle \sim$ -1 dex) population of RR Lyrae stars with a very peculiar kinematic distribution in the Milky Way bulge (see Kunder et al., 2016), has consequently challenged our understanding of the formation of the Milky Way bulge.

Kunder et al. (2016) claimed to have found evidence for a distinctive population, kinematically hotter (high velocity dispersion) observed within the BRAVA-RR[1] stars, with negligible rotation toward the Galactic bulge. The authors interpreted these results as an early population formed before the Galactic bar (e.g., Kunder et al., 2016). The authors also cautioned the reader that if the BRAVA-RR stars had an *halo-bulge* origin, then this component would be the most "metal-rich" stellar halo population identified in the Milky Way (see e.g., Kunder et al., 2016, and reference therein). Most recently, Pérez-Villegas et al. (2017a) claimed to have found similar kinematics behavior ("slow rotation") in the stellar halo component, based on the interpretation of N-body simulations of a bulge formed via bar instabilities, in the same work it have been hypothesised to be associated to angular momentum transfer during the bar evolution (see e.g., Pérez-Villegas et al., 2017a).

In this chapter, we have used test particle simulations designed to match the Milky Way (see §3), to examine such properties of the stellar halo from a different approach. It is important to note that variations present in our test particle simulations are consequence of non stationary effects.

[1]BRAVA-RR: Bulge RR Lyrae Radial Velocity Assay

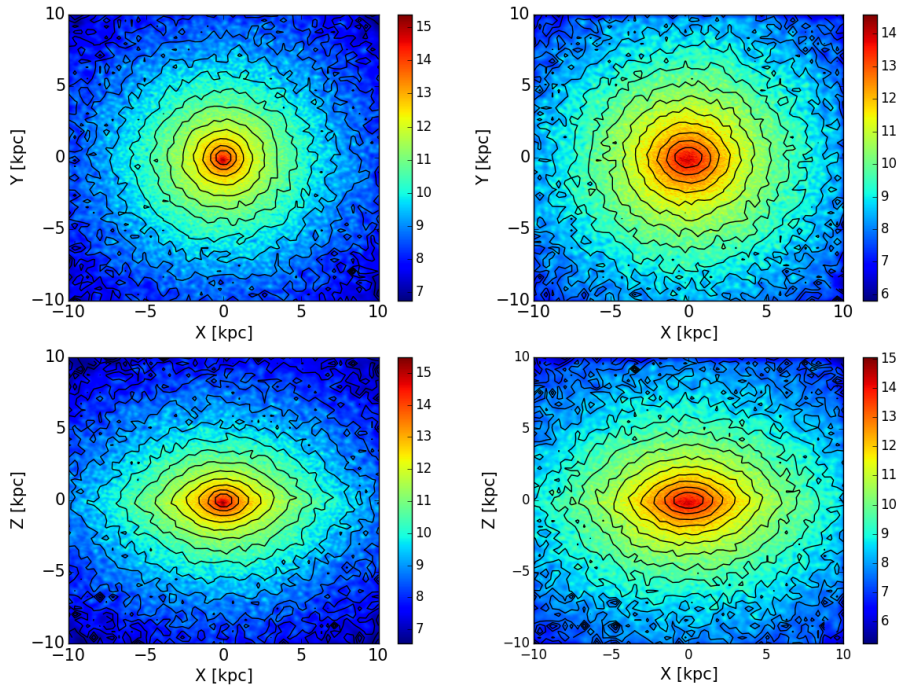

Figure 6.1: Density maps (black contour levels) viewed along different axes for the stellar halo. The colours indicate the logarithm of the surface density. Simulations shows the distribution of particles before bar formation (left), and after adding the bar to the system (right).

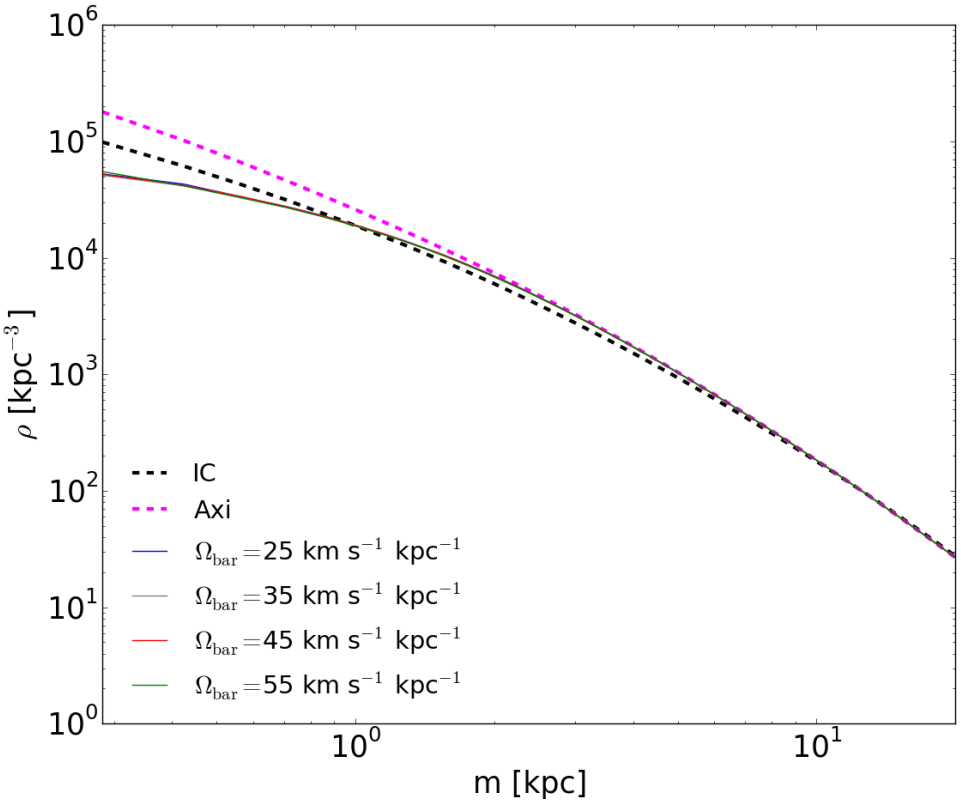

Figure 6.2: Density profiles as a function of $m = \sqrt{{r_{gal}}^2 + (Z/q)^2}$, before (magenta dashed line) and after bar formation for four different patterns speed of the bar (blue, grey, red, and green dashed lines), see text. The density profile of the initial conditions is drawed with as a black dashed line.

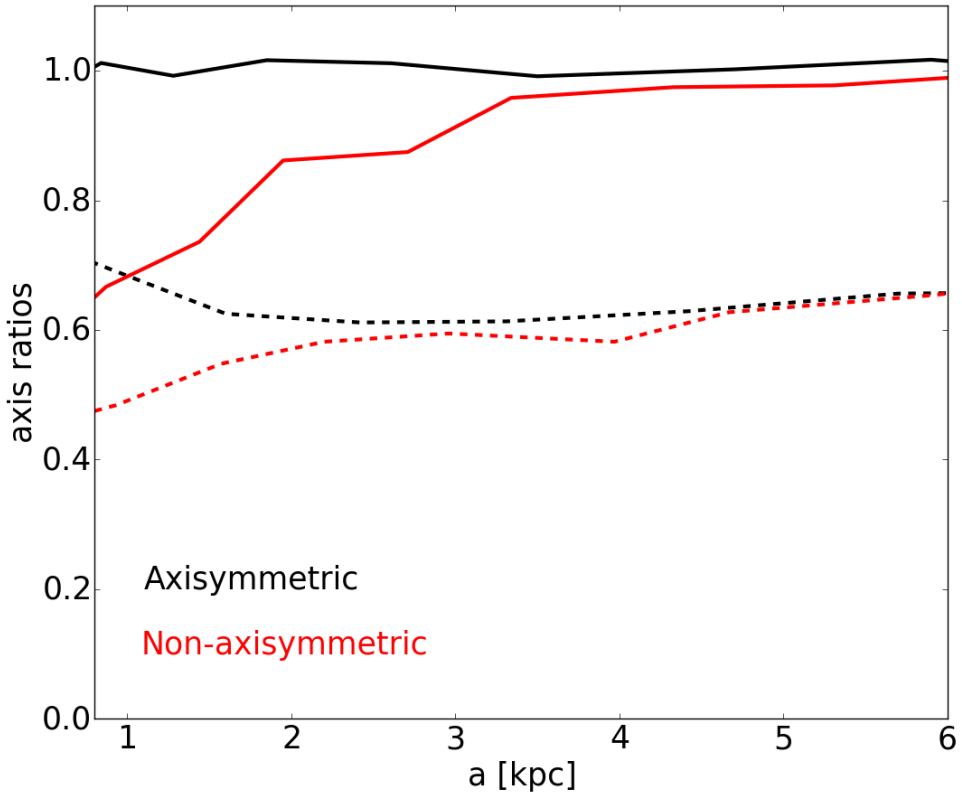

Figure 6.3: Axis ratios variations as a function of the semi-major axis a. The red and black dashed lines refers to c/a, and the continuous lines shows the axis ratios b/a as function of the semi-major axis. Here, we show results to the non-axisymmetric model with $\Omega_{bar} = 35$ km s^{-1} kpc^{-1} (see §5).

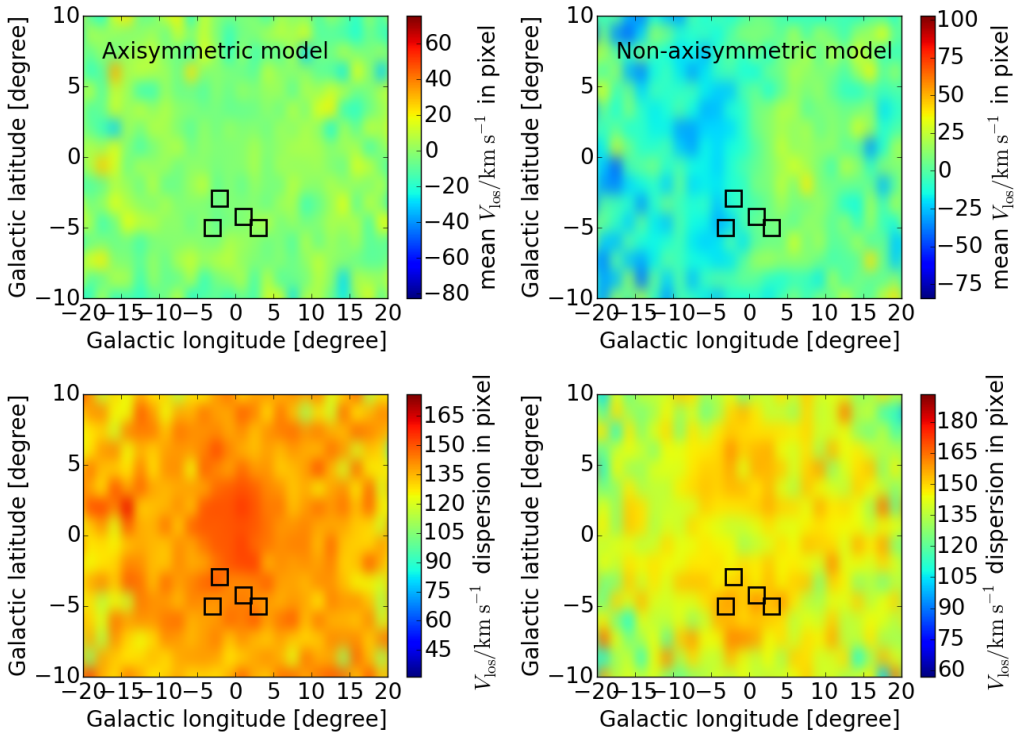

Figure 6.4: Kinematics maps toward the bulge regions as predicted for our halo particle simulations, before and after bar formation. Left for the axisymmetric model and right the non-axisymmetric model or after bar model is added. The black squares shows the Galactic localization of the BRAVA-RR stars studied by Kunder et al. (2016).

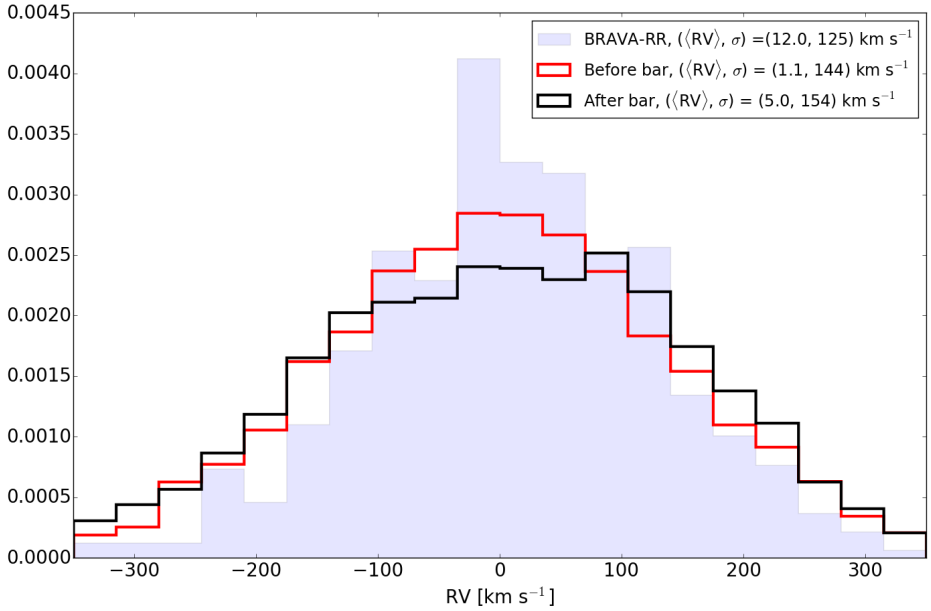

Figure 6.5: Radial velocity distribution of the BRAVA-RR stars (blue histogram) from Kunder et al. (2016) compared with the velocity prediction of our model before (red histogram) and after (black histogram) bar formation. The mean velocity and velocity for each distribution are shown in the top corner.

6.2 The inner structure of the stellar halo

In this thesis, we have employed a Hernsquist model to represent the stellar halo of the Milky Way following the reviewed version of the Besançon Galaxy model (see Robin et al., 2014). The stellar halo has been modeled as an oblate spheroid with a double power-law, its mass distribution has a density of the form $\sim \frac{1}{R_a \times (R_{core}+m)^n}$, where $m = \sqrt{{r_{gal}}^2 + (Z/q)^2}$, and a flattening $q = 0.77$ (e.g., Robin et al., 2014).

It is important to note that the initial spatial distribution of the particles does not follow exactly the same density law than in that study, i.e., the particles have been generated randomly using the Von Neumann accept/reject technique (Press et al., 1992), and the resulting flattening of the system is slightly different, $q \sim 0.6$ Robin et al. (e.g., 2014), this was eventually determined to be due to stochastic effects, and to the purpose of this analysis, we only consider the particle system in a state of statistical equilibrium with the background potential, i.e., the last stages afterwards integration in the axisymmetric and non-axisymmetric approach.

Figure 6.1 shows the predictions of stellar halo particles, before and after that the bar potential model is added to the system. In the same figure we see that a stellar halo initially oblate everywhere has changed its geometry after that the bar has been added. In other words, the Galactic bar has distorted or changed the initially symmetric distribution of particles in the central parts of the Milky Way. Hence the density law has been modified as a consequence of the presence of the bar. This was first noted by Pérez-Villegas et al. (2017a) adopting a single power-law density profile in N-body simulations. Our work from a different approach, confirms the validity of this finding.

Figure 6.2 displays the relative density profiles changes between the initial conditions, before and after bar formation, for four different values of bar pattern speed (see preceding chapter). Notice that after bar formation the density profile comes to be ellipsoidal significantly near the centre of bulge region, and stays stable or relatively similar to the axisymmetric model at large Galactocentric radii.

Figure 6.1 and Figure 6.2 clearly reveals that the inner stellar halo has formed an ellipsoidal structure as consequence of the bar potential, and where before $a = b \neq c$, now it is $a \neq b \neq c$, with a, b, and c the semi axis of a spheroid oblate and an ellipsoid, respectively. To illustrate these variations, Figure 6.3 display the axis ratios, c/a, and b/a as a function of the semi-major axis a, we can see as $b/a \sim 1$ goes to $b/a < 0.65$ in the inner Galaxy, $a < 1$, and $c/a \sim 0.6$ tends to $c/a \sim 0.45$, while that at large radii remain similar.

The conclusion to this experience is that a small fraction of particles (∼22%, see §7) are trapped by the "boxy/peanut" structure during "bar formation"[2], and cause orbital variations that can disperse particles or assemble the bar geometry in the inner Milky Way but the effect is marginally significant at large r_{gal}. Then, those particles of the stellar halo that participate in the bar structure produce small rotation in the system. For instance, Pérez-Villegas et al. (2017a) has quantified this effect, and find that $\sim 12\%$ of their orbital particles follow the bar. We get a value relatively higher $\sim 20-30\%$ as we

[2]In this thesis bar formation refers to the adiabatic growth of the "boxy/peanut" structure towards the Galactic bulge, as already described in §4

will see in §7. We note that changes in the bar pattern speed does not produce significant changes in the density profiles in Figure 6.2. However we have determined in §5 that a bar pattern speed of 35 km s^{-1} kpc^{-1} fits the global kinematics of the Milky Way bulge fairly well, thus we choose this value for the rest of our interpretations. In next section we study the effects of the bar in the velocity distribution of these halo particles.

6.3 Predicted kinematics of the inner stellar halo

Figure 6.4 shows the kinematics maps of our predictions for the halo particles, before and after bar formation, and the localization of the BRAVA-RR stars. We find that our simulations predict a kinematics towards the Milky Way bulge in agreement with previous results (Kunder et al., 2016). Note that the mean V_{los} before bar formation is close to zero, with a relative velocity dispersion of ∼120 km s^{-1} around the BRAVA-RR fields. After bar formation, the velocity field changes as consequence of the bar, and the initially non-rotating halo particles acquire a slow mean rotation, the relative mean variation of $V_{los} \sim 35$ km s^{-1} at high Galactic longitude (|b|>5°), with a velocity dispersion relatively high ∼ 135-150 km s^{-1} around the BRAVA-RR fields, and ∼105 km s^{-1} towards the nuclear part. So far, our results confirm the claims of Pérez-Villegas et al. (2017a), i.e., the rotating halo particles is due to the influence of the Galactic bar.

Main conclusion: In connection with the results presented in §7 we confirm that a small fraction of particles (∼20%) in the stellar halo are able to participate in the bar structure producing a small rotation in the system and variations in the density profile as has been pointed out by Pérez-Villegas et al. (2017a). It is noteworthy that the dependence of the conclusions on different possible initial conditions has not been explored. The initial conditions consist of very idealised stellar halo particles that do not pretend to be strict models of the Milky Way and were not set to be in equilibrium for the stellar halo.

In the following section, some additional orbital properties are presented related with the trapping the particles into the bar potential.

Chapter 7

Particles captured by the bar potential and its relation with the Jacobi energy

In this chapter we deal with the Jacobi energy distribution in the inner regions (< 4.5 kpc) of the Milky Way. Our aim with this analysis is to investigate the properties of the orbital elements of disk particles and stellar halo particles in presence of a boxy/peanut bar. Note also that very little attention has been paid in the literature to explore the properties of the orbital elements of stellar populations towards the Galactic bulge, due to the lack of accurate distance and proper motions available in the literature which makes it difficult to fully resolve the three dimensional velocity vector of each star.

Another major limitation is that the regions of the bulge are dominated by high extinction and crowding, making it difficult to estimate accurately distances. However, many of these restrictions will be reduced in the near future when we are able to derive 3D velocity measures and distances accurately, with the help of large scale near infrared spectroscopic surveys as APOGEE (for details, see Gunn et al., 2006; Eisenstein et al., 2011; Zasowski et al., 2013; Majewski et al., 2015; SDSS Collaboration et al., 2016), in combination with early observations of the Gaia data release (Gaia Collaboration et al., 2016a,b) which will provide proper motions and parallaxes for stars in the end of the bar region (Romero-Gomez et al., 2016), i.e., within ∼ 5 kpc from the solar position, allowing us to study quantities such as the orbital Jacobi energy in the Galactic bulge, etc.

7.1 Maps of the Jacobi energy towards the Galactic bulge

In this chapter we compute the orbital Jacobi energy (E_J) per unit mass as defined in Eqn. B.19, aiming at examining the structure and kinematic behaviour of particles into the Galactic bulge. We make use of the Jacobi energy (E_J) as an orbital proxy, which may split each disk sub-component and stellar halo in two sub-groups, one with particles following the bar structure and one with particles that do not participate in the Galactic bar.

For our computations, we employ the value of $\alpha_{bar} = 20°$, bar pattern speed of $\Omega_{bar} = 35$ km s^{-1} kpc^{-1}, and a bar mass of 1.1×10^{10} M$_\odot$ as listed in Table 5.1 (**Model 22**), see

discussion in §5. It is important to note that E_J is model-dependent, therefore, if the bar paramters of the **Model 36** are employed, the values of the Jacobi energy are shifted by $\sim$-10^3 km^2 s^{-2}, however we note here it does not affect our interpretations.

The maps of the mean Jacobi energy $\langle E_J \rangle$ in boxes 200 pc wide in Cartesian (X, Y, Z) coordinates for each disk sub-component and the stellar halo are shown in Figure 7.1. These maps illustrate the orbital Jacobi energy view of the inner region of the Milky Way. On the other hand, particles in the disk sub-components and/or stellar halo component located inside the corotation radius ($<$ 6.5 kpc) with an orbital Jacobi energy below -2.7×10^5 km^2 s^{-2} can be captured easily by the bar structure due to the influence of the Galactic bar, forming agglomerations of particles in the Galactic bulge, which show the "boxy/peanut" structure for particles into the disk sub-components, and/or "ellipsoidal" morphology for the particles in the stellar halo, as seen in Figure 7.2. Table 7.1 lists the percentage of particles in our simulations that are trapped into the bar potential for each sub-component of the disk and halo.

Table 7.1: Percentage of particles captured by the bar potential.

Population	bar-following particles %	not bar-following particles %	flag
3	41.6	58.4	thin disk
4	40.3	59.7	thin disk
5	38.7	61.3	thin disk
6	36.9	63.1	thin disk
7	33.8	66.2	thin disk
8	68.3	31.7	young thick disk
11	52.3	47.7	old thick disk
9	22.4	77.6	stellar halo

Consequently, in our test particle simulations the Galactic bulge contains several families of resonant orbits, made up of several stable periodic orbits, including orbits type $x1v1$ the so-called "bananas" orbits and other high resonant families, which show the "boxy/peanut" features of the bulge. In other words, particles with typical Jacobi energies below -2.7×10^5 km^2 s^{-2} can travel through the bar structure and becomes vertically unstable in certain regions, while higher values of $E_J > -2.7\times10^5$ km^2 s^{-2}, can move away of the "boxy/peanut" regions of the bar, which provide a significant part of the in-plane density as illustrated in Figure 7.3. These particles do not participate into the bar structure. *This experience provided us with an important result regarding the orbital structure of the bulge. We find a clear correlation between the shape of the bulge, the orbital Jacobi energy, but the real initial conditions are unknown.*

Figure 7.2 reveals the particle density distributions for $E_J < -2.7\times10^5$ km^2 s^{-2}. Note that the "boxy/peanut" structure (*bar-following particles*) is mainly sensitive to the initial conditions, because populations with lower velocity dispersion in the initial conditions have also lower velocity dispersion after the bar potential is included. This plot shows how particles in the thin disk (Pop 3, Pop 4, Pop 5, Pop 6, and Pop 7) are clearly grouped together in the regions dominated by the "boxy/peanut" bulge, as seen

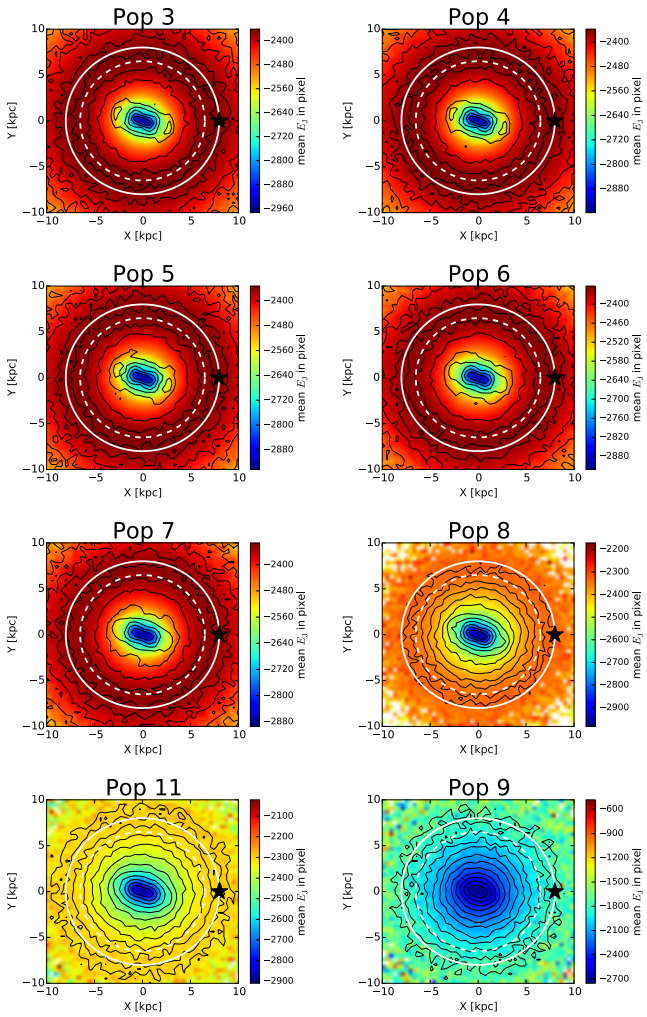

Figure 7.1: Mean Jacobi energy, $\langle E_J \rangle$ maps for all the particles using our model 22 as listed in Table 5.1. The black star symbol correspond to the Solar position ($X = 8$ kpc, $Y = 0$ kpc, and $Z = 0$ kpc), the white continuum line refers to the solar radius, and the white dashed line corresponds to the corotation radius (see §5). Colors indicate $\langle E_J \rangle$ in units of 100 km^2 s^{-2}. The black thin lines corresponds to the logarithmic surface density contours of the model disk particles and stellar halo particles seen face-on.

from side-on (boxy-like structure), and face-on (peanut-like structure) in the same figure. The same figure shows how particles in a cold thin disk (Pop 3) trace a dominant thin "peanut" bulge towards the midplane, and have shorter radial extent, while that particles in a warmer thin disk form a thicker "boxy/peanut" structure seen mainly at higher height above the plane (see Figure 7.2), depending significantly on the initial conditions.

We claim from these results, even when we are not able to follow the formation of the bar from disk instabilities as would be the case in N-body simulations (which can even suffer several buckling events) (see e.g., Martinez-Valpuesta & Shlosman, 2004; Martinez-Valpuesta et al., 2006; Martinez-Valpuesta & Gerhard, 2011; Portail et al., 2015a), our Galactic bar itself leads to different bar shapes, depending mainly on the initial conditions, where the kinematically coldest particles in the disk trapped in the bar become vertical unstable near the mid-plane, and kinematically hotter particles forming a pronounced and vertically extended "boxy/peanut" morphology, except the stellar halo, which have higher velocity dispersion. This could explain why López-Corredoira (2016) did not identified young stars (with ages < 5 Gyr) following the "boxy/peanut" morphology at high latitudes ($|b| > 6°$).

The thick disk particles (Pop 8 and Pop 11) have neither a clearly defined "boxy/peanut" morphology. In Figure 7.2 we plot the distribution of particles in the thick disk taking $E_J < -2.7 \times 10^5$ km^2 s^{-2}. Again, agglomerations of particles are seen in the inner Milky Way, with particles into bar-following orbits. The young thick disk (Pop 8) forms a shorter and thin ellipsoidal component centrally concentrated, while the old thick disk (Pop 11) is puffed up into a thicker ellipsoidal component given its higher velocity dispersion. In the same figure, note that the halo bar-following orbits do not show any prominent "boxy/peanut" morphology as we have discussed in §6, and an ellipsoidal distribution of particles dominates the inner regions of the stellar halo, a small fraction of halo particles rotate with the bar due to the influence of the bar.

Figure 7.3 plots the distributions of particles that do not participate in the Galactic bar, i.e., particles with orbital Jacobi energy $E_J > -2.7 \times 10^5$ km^2 s^{-2} forming a structure surrounding the Galactic bar. We note that a significant fraction of particles seems to move away of the inner part of the Galactic bar, producing a significant ring-shaped region surrounding the Galactic bar with a larger radial extent. The fraction of these particles becomes marginally significant for kinematically hotter components. In other words, this effect is more remarkable for particles distributed on the cold disk, producing a midplane structure (particles moves mainly on the plane) toward the inner region of the Milky Way, and dominated by eccentricities lower that 0.8 as illustrated in Figure 7.4.

The particles in the Galactic disk which streaming into the bar structure have higher eccentricity[1] (see Figure 7.4), moving to higher altitudes. The old thick disk with $E_J > -2.7 \times 10^5$ km^2 s^{-2} moves away from the midplane due to its kinematically warmer nature, while the particles in the stellar halo are scattered to large distances above the midplane traveling around the bulge in an erratic manner and lie on more eccentric orbits. The bottom panel of Figure 7.4 shows how our particles in the disk sub-components and the stellar halo are divided by the orbital Jacobi energy, $E_J \sim -2.7 \times 10^5$ km^2 s^{-2}, and how they are distributed in the Milky Way.

[1]The eccentricity is defined as $e = \frac{R_{max} - R_{min}}{R_{max} + R_{min}}$

Figure 7.5 shows the characteristic orbital energy versus the orbital Jacobi energy, E_J, as defined in Moreno et al. (2015), for each disk sub-component and the stellar halo. We computed the same orbital elements for 63 Galactic globular clusters (see Appendix C) studied by Moreno et al. (2014). These diagrams shows that conservatively a value of $\sim -2.7 \times 10^5$ km^2 s^{-2} for the orbital Jacobi energy excludes the Galactic globular clusters from the bar potential. This allows us to be slightly more confident on the adopted value to split the particles into the two already mentioned groups (bar-following particles, and bar-not following particles), because there is not evidence of globular clusters trapped into the bar structure.

Figure 7.6 and Figure 7.7 illustrates some families of orbits supporting the "boxy/peanut" morphology and the "ring-like" structure as a function of the orbital Jacobi energy and their eccentricity. Note that the meridional orbits for $E_J > -2.7 \times 10^5$ km^2 s^{-2} support the existence for such "ring-like" structure surrounding the Galactic bar, and some few particles with $E_J \sim -2.6 \times 10^5$ km^2 s^{-2} and high orbital eccentricities > 0.8 may participate into the bar structure as higher order resonances.

Main results: *Such a selection $E_J < -2.7 \times 10^5$ km^2 s^{-2} would preferentially select particles streaming along the Galactic bar, causing the main peak in shorter radii, and are therefore the main contribution to our high eccentricities, with particles that participate in the "boxy/peanut" shaped of the Galactic bulge, while a ring-like distribution at larger radial extent is revealed when particles with orbital Jacobi energy $E_J > -2.7 \times 10^5$ km^2 s^{-2} are selected, with particles streaming at near circular orbits (or less excentric orbits).*

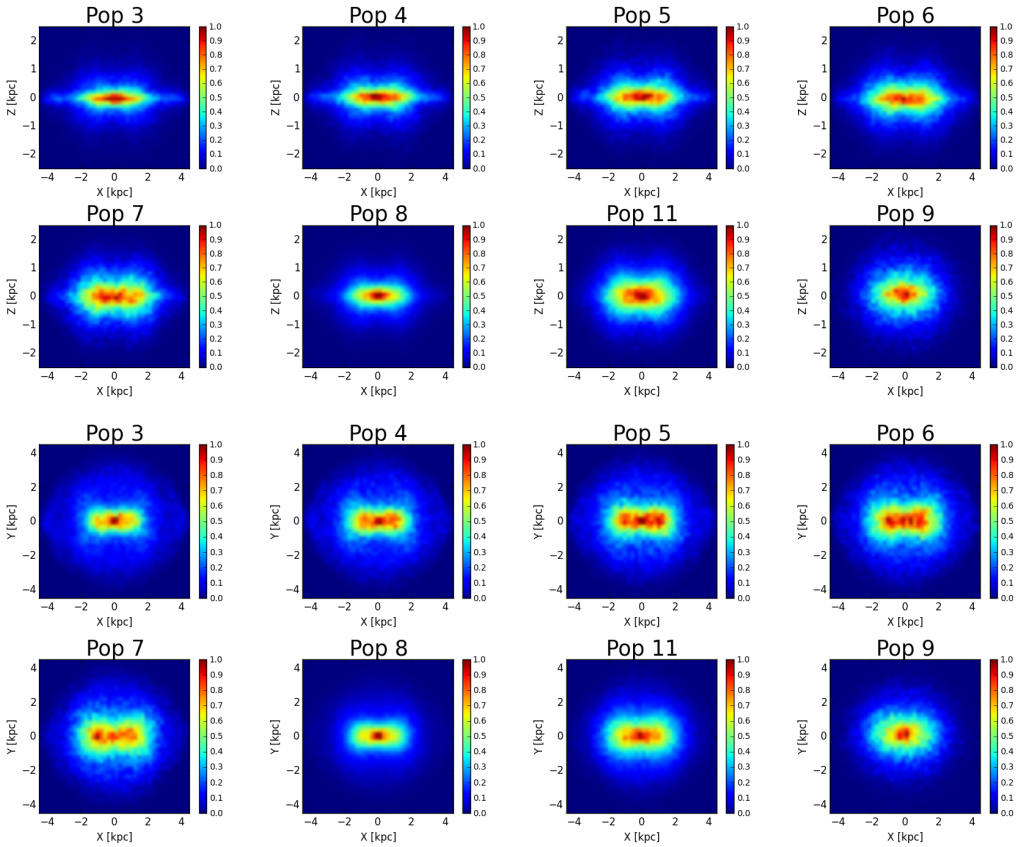

Figure 7.2: Density distribution of particles in the disks and stellar halo with orbital Jacobi energy $E_J < -2.7 \times 10^5$ km^2 s^{-2}.

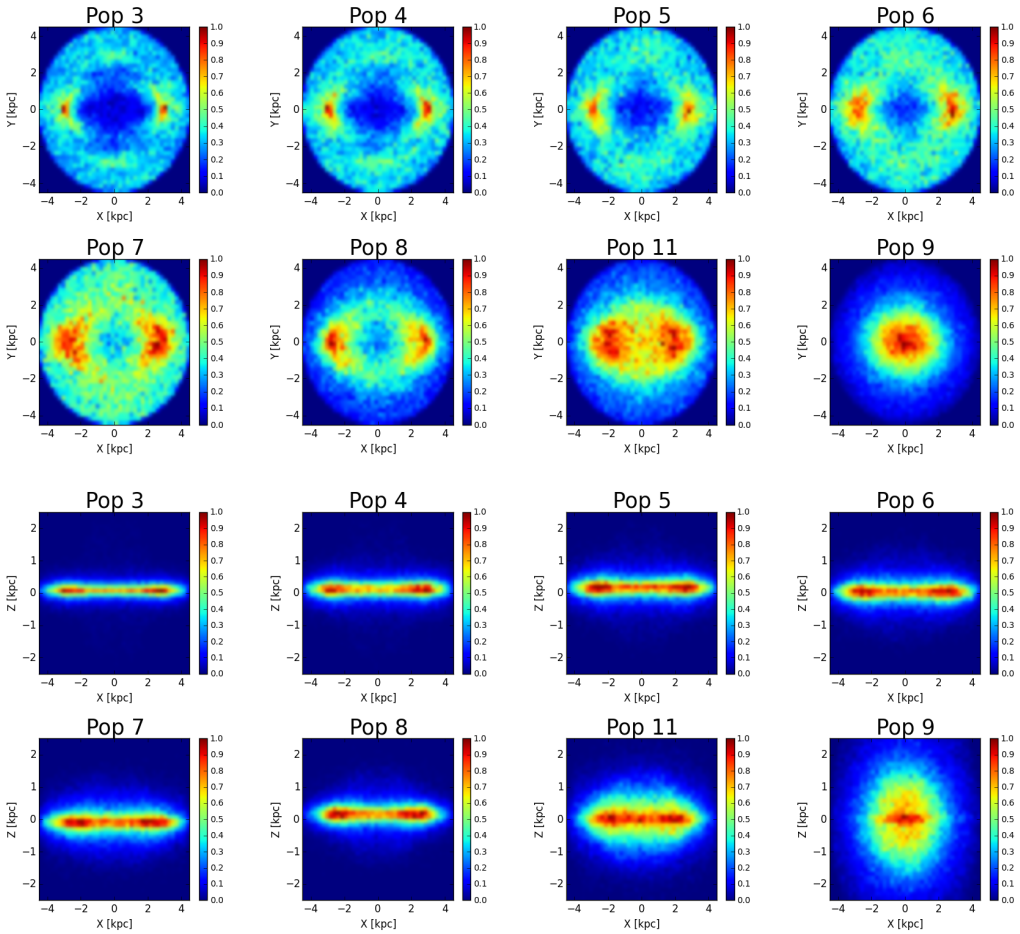

Figure 7.3: Density distribution of particles in the different disks and the stellar halo with orbital Jacobi energy $E_J > -2.7 \times 10^5$ km^2 s^{-2}.

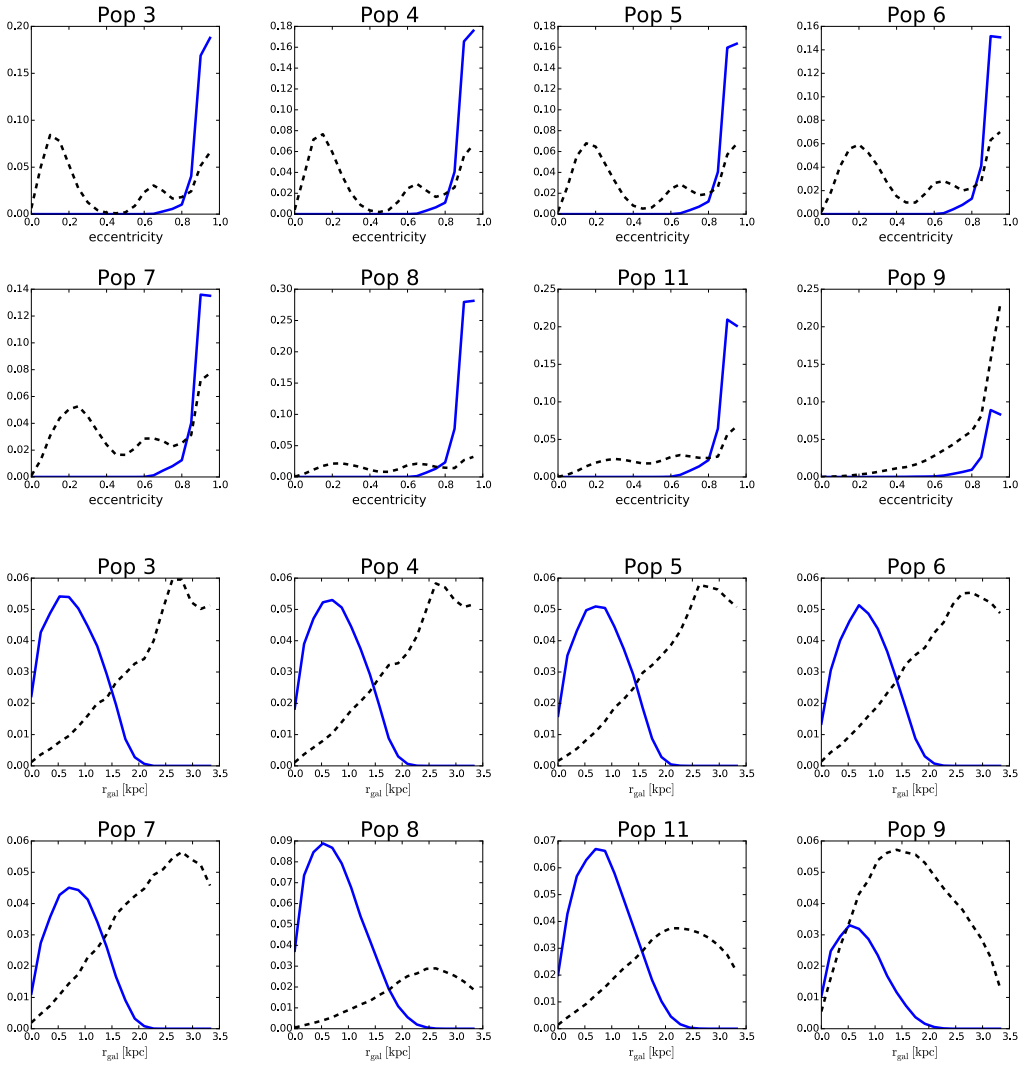

Figure 7.4: Top panel: histograms of the corresponding eccentricities, showing the properties of particles with orbital Jacobi energy $E_J < -2.7 \times 10^5$ km^2 s^{-2} (blue histograms) and orbital Jacobi energy $E_J > -2.7 \times 10^5$ km^2 s^{-2} (black histograms). Bottom panel: histograms of the corresponding Galactocentric radius (r_{gal}).

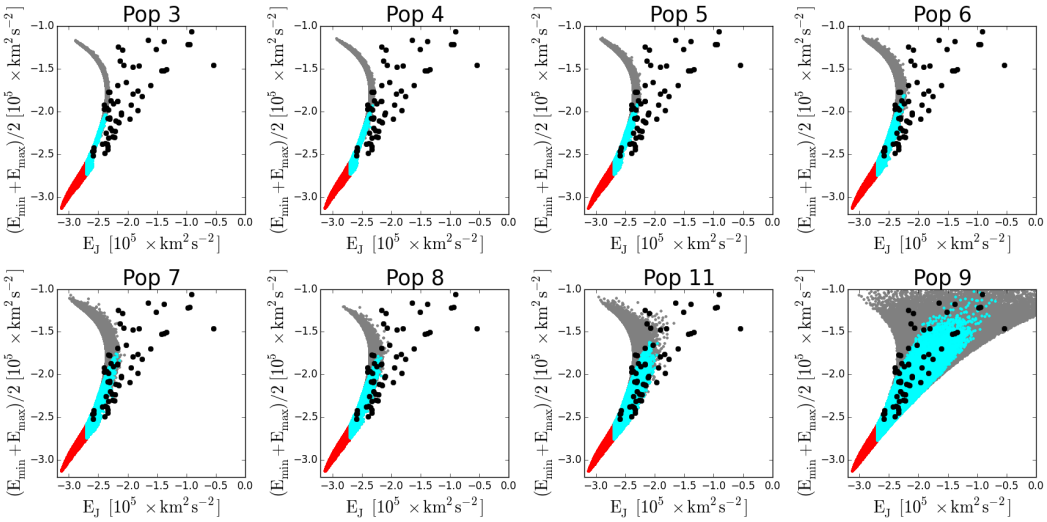

Figure 7.5: Characteristic orbital energy versus the orbital Jacobi energy (E_J) as derived from our best barred Milky Way model. The grey dots are the test particle simulations (see text), the red regions are the particles in our simulations that participate in the bar structure (< 4.5 kpc), the cyan regions are the particles that does not participate in the bar structure (< 4.5 kpc), and the black dots are the globular clusters plotted in Figure 8.8.

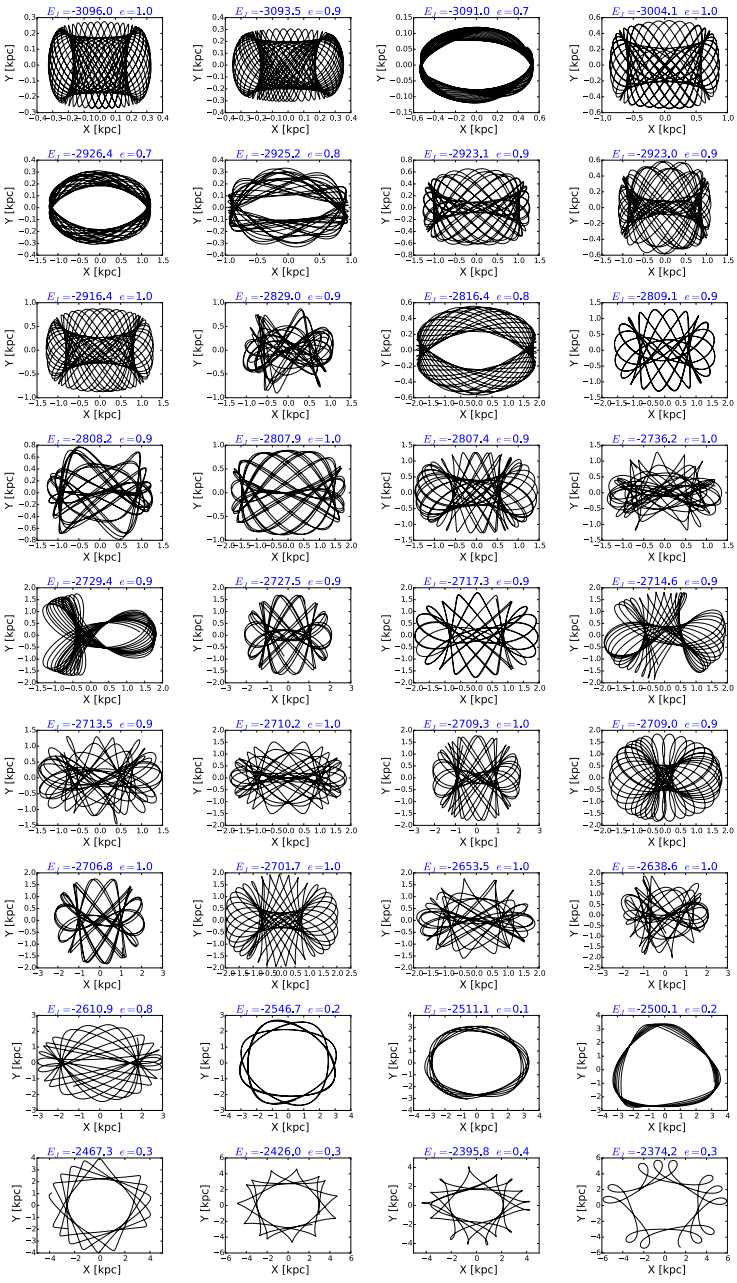

Figure 7.6: This figure shows the orbital projection on the Galactic plane X, Y in the non-inertial reference frame where the bar is at rest, for a sample of particles in the disk associated with population 5, see text. E_J is the orbital Jacoby energy per unit mass in unit of 100 km^2 s^{-2}.

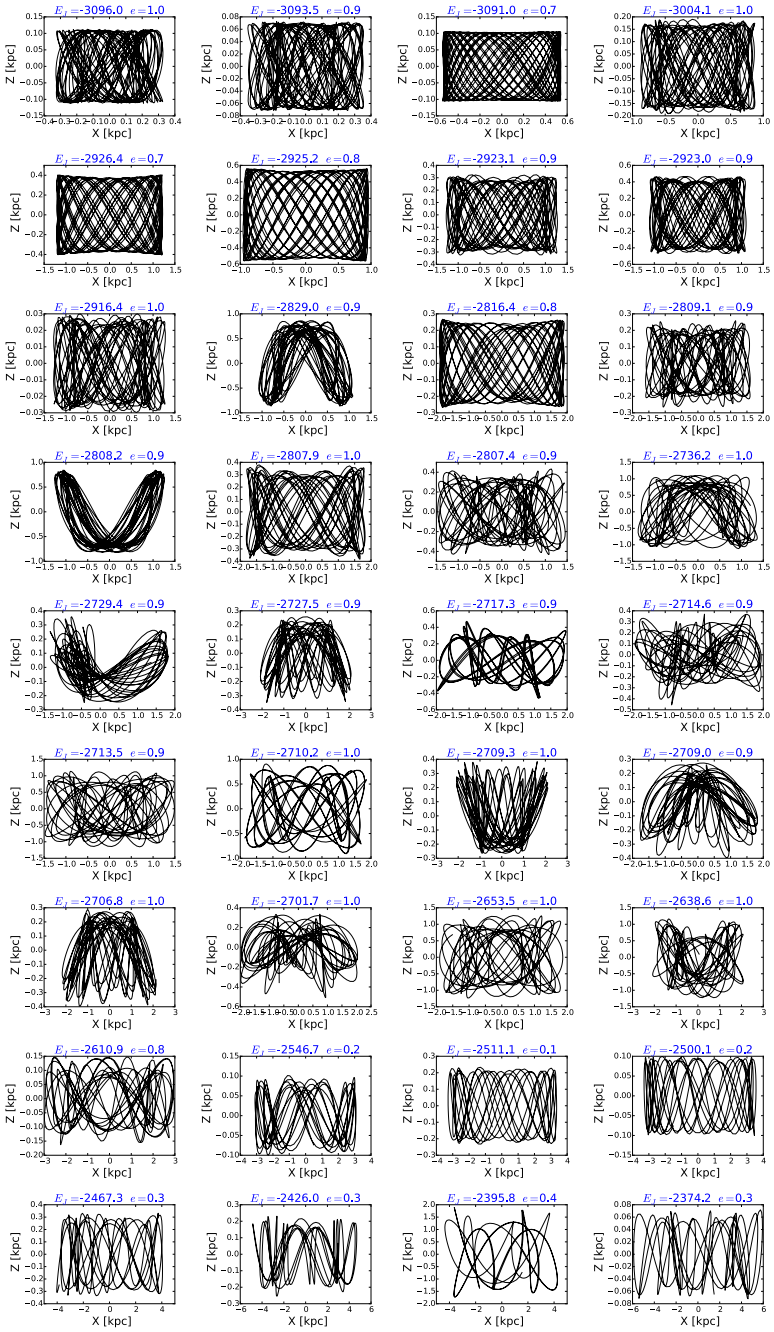

Figure 7.7: This figure shows the orbital projection on the Galactic plane X, Z, for the same sample as in Figure 7.6.

7.2 Non-stationary effects towards the Galactic bulge

We look for non-stationary effects toward the Galactic bulge and its relation with the orbital Jacobi energy.

Figure 7.8 illustrates the V_{los} distributions for particles streaming in the Galactic bar, for the corresponding orbital Jacobi energy $E_J < -2.7 \times 10^5$ km^2 s^{-2} (hereafter bar-following particles), and particles with orbital Jacobi energy $E_J > -2.7 \times 10^5$ km^2 s^{-2} (hereafter not bar-following particles). We note that bar-following particles can produce a main V_{los} peak, a broad distribution centered on zero dominated by particles streaming along the bar structure, while particles which do not follow the bar clearly split into two symmetric peaks at $|V_{los}| \sim 200$ km s^{-1} of particles streaming in the ring-shaped structure surrounding the bar. These distributions are much narrower for the younger disks indicating that these components/structures are cooler. The kinematically warmer component (Pop 11) shows a less pronounced peak with a quite broad distribution dominated by particles moving away from the Galactic plane, while the stellar halo (Pop 9) dominated by not bar-following particles produces a kinematically hotter distribution in a random motion dominated by particles around the Galactic bar, that travel in an erratic manner.

Figure 7.9 shows the predicted kinematic maps corresponding to bar-following particles (top panels) and not bar-following particles (bottom panels). A slow prograde rotation is seen in the disk sub-components for particles trapped in the Galactic bar, with low values of E_J, while a fast prograde rotation is seen in the disk sub-components made up of particles with higher values of E_J. The halo component, shows clearly a prograde rotation for low values of E_J due to influence of the bar, which is dominated by bar-following particles, while the halo particles that do not participate in the Galactic bar and have negligible rotation.

Figure 7.10 shows the corresponding velocity dispersion profiles. This plot compares different observed behaviors, showing a higher dispersion at higher latitude due to instability generated by the "boxy/peanut" shaped of the gravitational potential, and break down near the Galactic center, specially due to missing central mass in our model, as already noted in §5.

Figure 7.11 shows the same as Figure 5.12 but now the rotation curve and velocity dispersion profiles are divided into two groups, bar-following particles and not bar-following particles. The not bar-following particles show a higher rotational velocity with higher velocity dispersion profiles compared with bar-following particles. We see that the particles not trapped in the bar follow similiar behaviour to the overall kinematic trends as observed from the BRAVA datasets, as well as the velocity dispersion profiles. The particles that participate in the bar structure show a slow rotational velocity with similar behaviour to the observed rotation curve, but their velocity dispersion profiles does not match the observations towards higher Galactic longitude ($|l| > 5°$). *This result would imply that what we observe towards the Galactic bulge region from the BRAVA datasets cannot be explained essentially on the basis of particles trapped into the bar structure, without the need to add any significant kinematics from particles with higher orbital Jacobi energy* $E_J > -2.7 \times 10^5$ *km*^{2} *s*$^{-2}$.

In Table 7.1 we list the percentage of particles that parcipates in the bar structure. We find that an important fraction ($\sim 30 - 70\%$) of particle orbits on the inner disk and

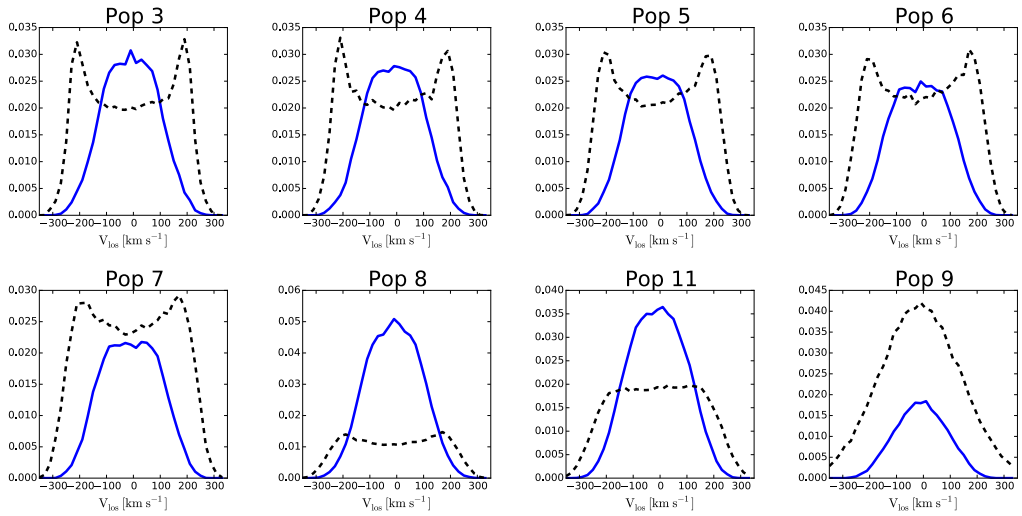

Figure 7.8: V_{los} distributions of particles streaming in the Galactic bar (blue histogram) compared to not bar-following particles (black histogram).

contributes to the bar structure. The fraction of particles on the stellar halo that follows the bar is estimated to be $\sim$ 20% in good agreement with recent measurements(e.g., Pérez-Villegas et al., 2017a).

7.3 The high V_{los} feature in the Milky Way Bulge is not due to the Bar

Nidever et al. (2012) claimed to have found several cold and high velocity peaks in the inner Milky Way from the APOGEE survey. The authors suggest that such peaks can be explained by stars streaming in the Galactic bar. Most recently, Aumer & Schönrich (2015); Molloy et al. (2015a) based on interpretation of N-body simulations find that the high-V_{los} peaks detection firstly reported from the commissioning data of APOGEE (Nidever et al., 2012) can be explained by stars travelling alongside the bar. Contrary to these works, Debattista et al. (2015) claimed to have found evidence for a nuclear disk from N-body simulations, which produces the high-velocity feature observed by Nidever et al. (2012). Here we show that particles captured into the bar potential do not produce significative cold high velocity peaks in the bulge region as has been recently claimed by Nidever et al. (2012); Aumer & Schönrich (2015); Molloy et al. (2015a). We find that significant ($\sim$ 30$-$70%) high-V_{los} peaks are a natural consequence of a midplane structure which is not associated with the Galactic bar.

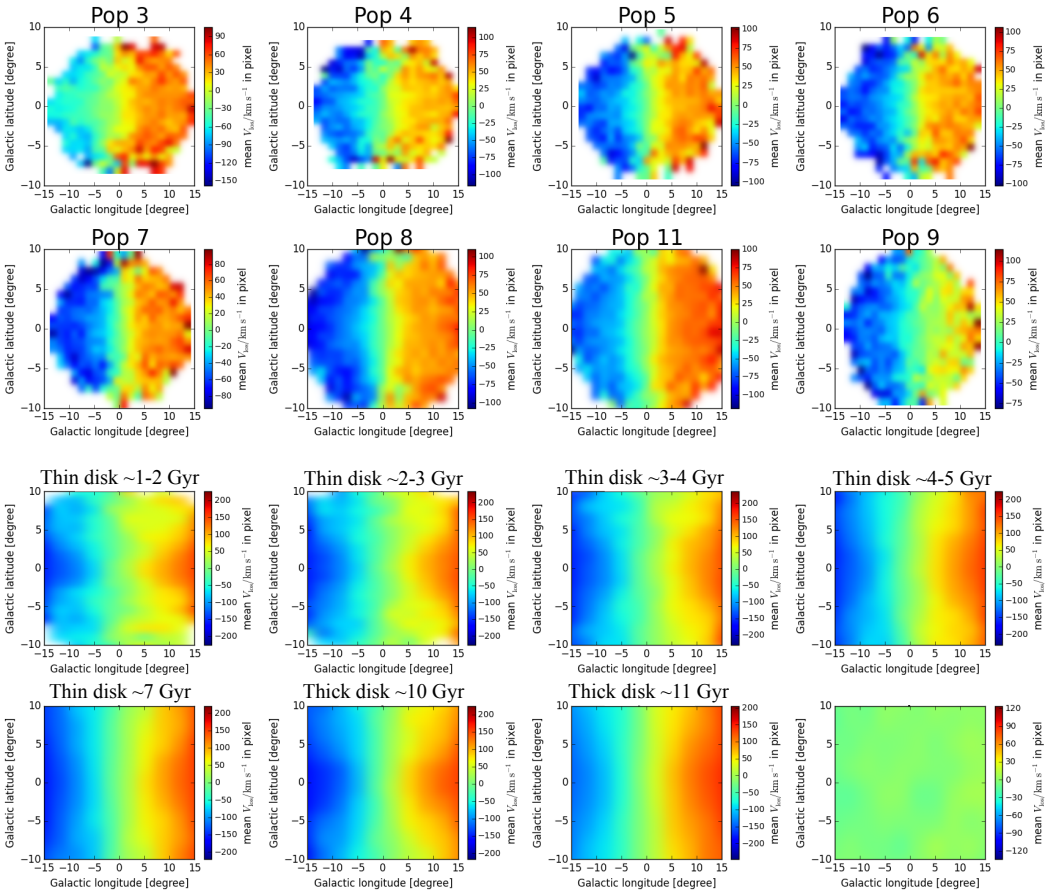

Figure 7.9: Predicted velocity maps corresponding to bar-following particles (first and second row) and not bar-following particles (third and fourth row) in the disk and halo components.

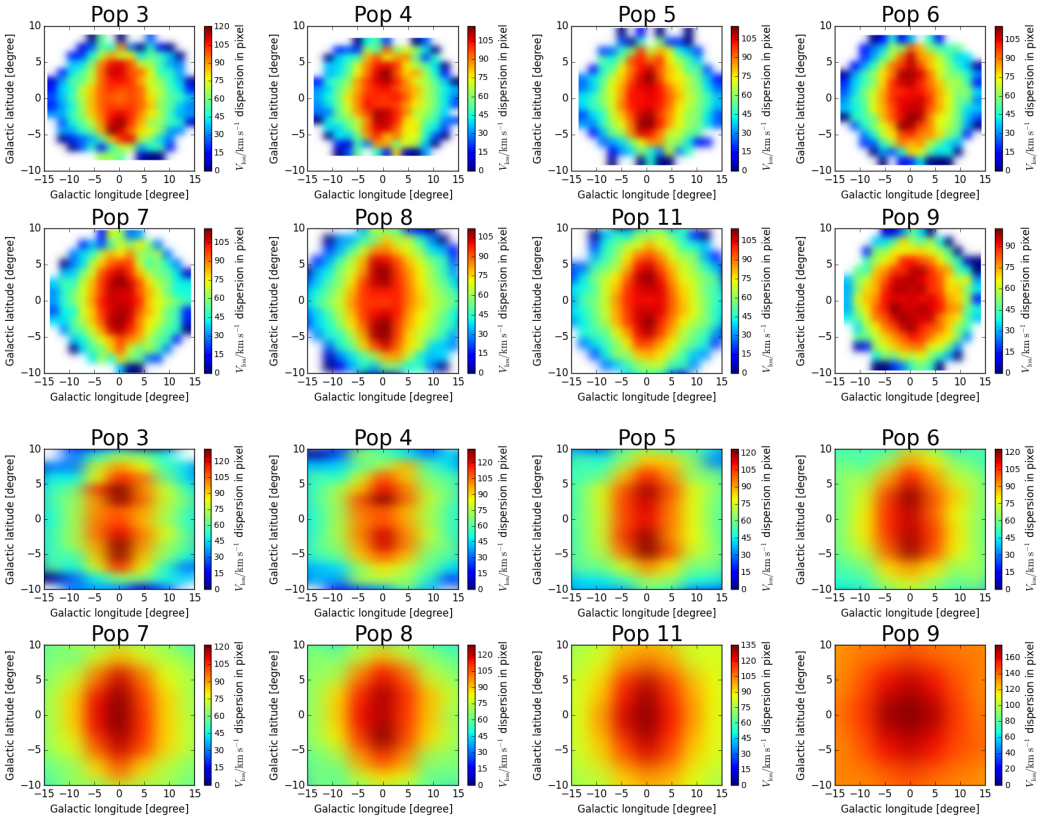

Figure 7.10: Predicted velocity dispersion maps corresponding to bar-following particles (first and second row) and not bar-following particles (third and fourth row) in the disk and halo components.

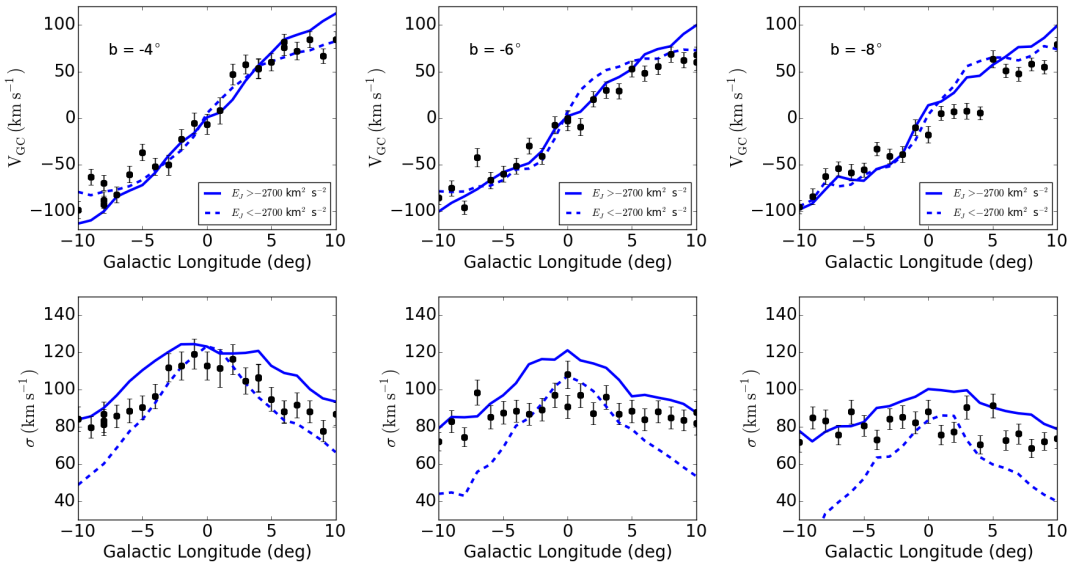

Figure 7.11: Rotation curve and velocity dispersion profiles for bar-following particles (blue dashed line) and not bar-following particles (blue line), compared to the BRAVA datasets.

Chapter 8

Qualitative comparison of eccentricities to models

In this chapter we present a first application of the use of the Galactic potential described in §3. From the Galactic potential, if position and velocities of stars are known with a sufficient accuracy, it is possible to integrate the orbit of the stars. We apply this method to compare orbit integrations with data in the literature. First we compare the distribution of eccentricities that was observed from SDSS DR7 data by (Dierickx et al., 2010). Then we consider TGAS (Gaia first data release) which contain accurate positions on the sky, parallaxes and proper motions. These data, when combined with radial velocities from the APOGEE survey (Zasowski et al., 2013; Majewski et al., 2015), allow to integrate orbits for stars in the solar neighbourhood. The third application is done using field stars with globular cluster-like second-generation abundance patterns identified in the APOGEE survey as tracers of the cluster disruptions and possible accretion origins. We compute the orbital elements of these stars in the Milky Way potential presented in §3.

8.1 Eccentricities from the SDSS DR7 datasets

In order to assess that our model is able to produce consistent outcomes, we compare eccentricities computed from our potential with other integrations of orbits available in the literature. In particular, we focus in this section in the eccentricity distributions of a local sample of ∼31,535 G-dwarfs stars (from the SDSS DR7), which is made predominantly of "thick disk" stars (Dierickx et al., 2010), covering the height range $1 < |Z_{max}| < 3$ kpc. The authors claimed that the observed eccentricity distributions fit fairly well *a "gas-rich merger" scenario, where most thick disk stars were born in situ* as expected from numerical simulations carried out by Sales et al. (e.g., 2009).

In Figure 8.1 we compare the eccentricity distributions of these stars as computed from axisymmetric potentials (e.g., Dierickx et al., 2010), with these ones from our barred Milky Way model (through this chaper, we employ the bar parameters of the *Model 22* as listed in Table 5.1). We find that our barred Milky Way model predicts more low-eccentricity stars than predicted by Dierickx et al. (2010) using a simple potential model. Also our comparison shows that our predictions are reasonable in an absolute sense.

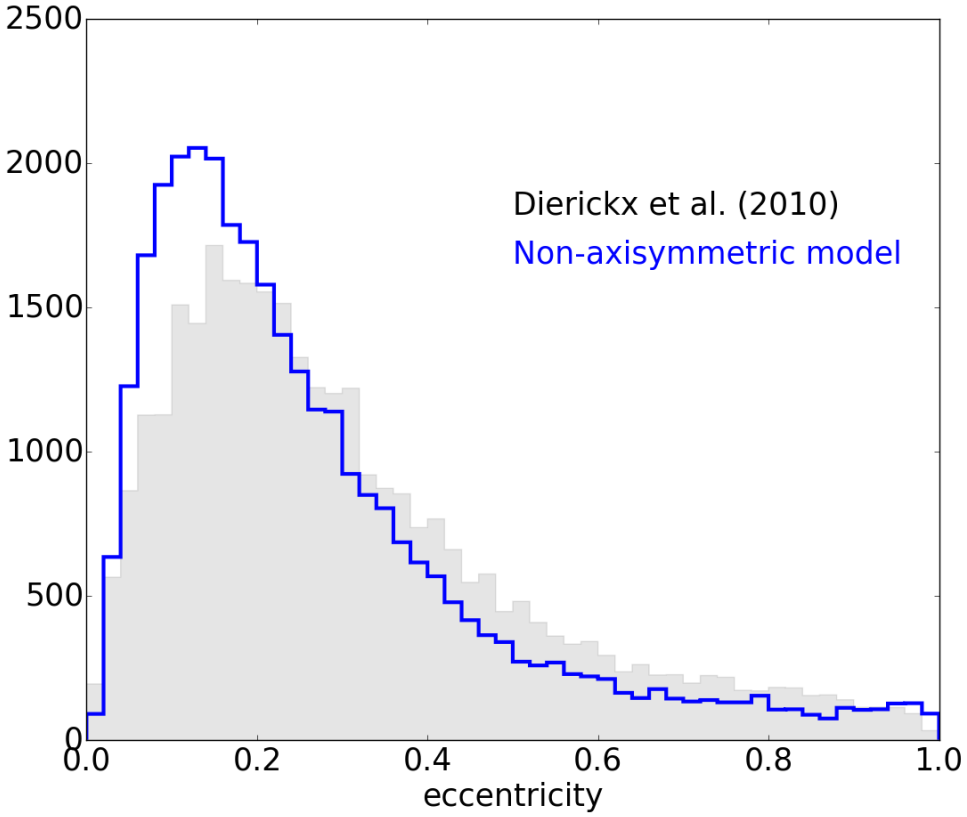

Figure 8.1: Eccentricity distributions of ∼31,535 G-dwarfs stars (grey histogram) from Dierickx et al. (2010) compared with eccentricity distribution (blue histogram) as predicted from the corresponding Galactic model presented in this work.

We now make use of the eccentricity distributions from the same sample as computed from our model, and qualitatively compare them with our predictions using test particle simulations (as presented in §4 and §5) confined to a sphere of radius 5 kpc around the Sun (covering the height range $1 < |Z_{max}| < 3$ kpc). The results are given in Figure 8.2. The observed eccentricity distribution does not coincides with the expected positions of the young (Pop 8) and old (Pop 11) thick disk, while the sub-components of the old thin disk are qualitatively similar to the locally observed distributions. *On the basis that our simulations are observationally and dynamically constrained, we suggest that the distribution of eccentricities cannot validate the scenario proposed by Dierickx et al. (2010), since we obtain the same distribution from thin disc particles. Our claim is based on a qualitative comparison, and an adequate selection function in combination with our eccentricity predictions could rule out the proposed scenario by Dierickx et al. (2010).*

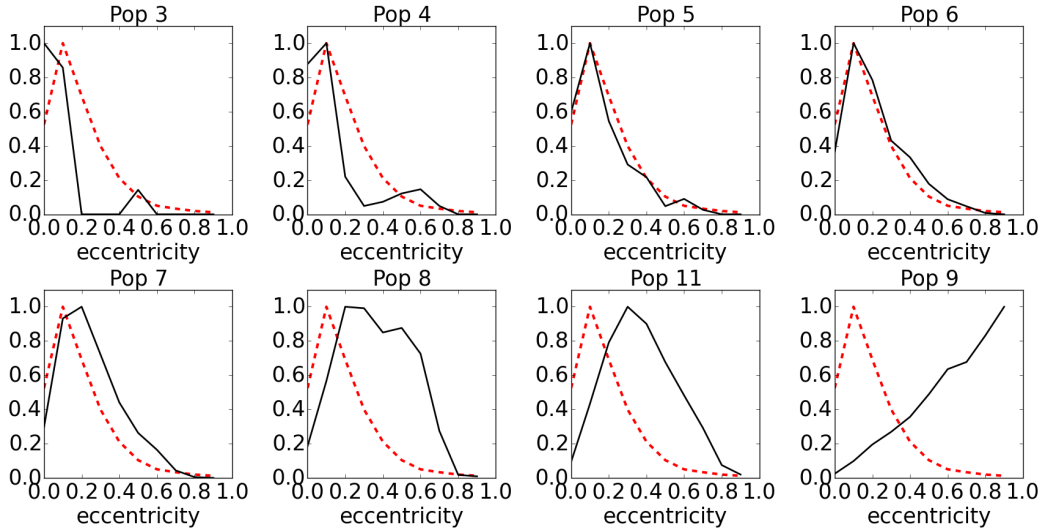

Figure 8.2: Predicted eccentricity distributions from test particle simulations (black line), see §4 and §5, compared to the observed eccentricity distribution (red dashed line) from the SDSS DR7 datasets (Dierickx et al., 2010), and re-computed in this thesis using a barred Milky Way model (see §3).

8.2 Eccentricities from the *TGAS* and APOGEE datasets

Recently, Allende Prieto et al. (2016) have analyzed the main orbital elements in the Milky Way for a few giant stars in the solar neighborhood, for which high quality astrometric information is available from the first Gaia Data Release published as part of the Tycho-Gaia Astrometric Solution (*TGAS*) catalogue (see e.g., Gaia Collaboration et al., 2016b).

A sample of 3,621 nearby giant stars with uncertainties in the parallaxes <30%, and

uncertainty in the radial velocity better than 1 km s^{-1} from the APOGEE survey, has been selected in the same work, combining astrometric measurements from the *TGAS* catalog with accurate radial velocity and chemistry from the SDSS-III Data Release 12 (Holtzman et al., 2015; Alam et al., 2015). They aimed to infer the main orbital elements (Z_{max}, e, and the mean orbital radius R_m) under an axisymmetric Milky Way potential, making use of the *galpy* software[1] (Bovy, 2015). The authors interpreted their results as: *Stars formed farther away from the solar circle tend to be near their orbital peri center, showing larger velocities and on average lower metallicities, while those closer to the Galactic center are usually closer to their orbital apocenter, therefore moving slower and with higher metallicities* (exact copy from conclusions in Allende Prieto et al., 2016).

We complement this work by adapting our barred Milky Way model, and our test particles simulations (see §4 and §5) to the same sample, to enable a qualitative comparison between predicted orbital elements to observed data.

Using the same datasets, we computed the eccentricity distributions as inferred from our barred Milky Way model (using the bar parameters of the **Model 22** as listed in Table 5.1), we then compare the observed eccentricity with the predicted eccentricity distributions from eight snapshots of test particle simulations (five thin disk particles: Pop 3, Pop 4, Pop 5, Pop 6, Pop 7, two thick disk particles: Pop 8, Pop 11, and one stellar halo particles: Pop 9) confined to a sphere of radius 1.5 kpc around the Sun (the test particle simulations used in this section are the same ones built in this thesis). Figure 8.3 and Figure 8.4 show the results.

Figure 8.5 shows the [Fe/H] vs. [α/Fe] distributions for the selected sample (similar to Figure 1 in Allende Prieto et al., 2016). We establish the local thick and thin disk component by splitting the data into $\alpha-$rich and $\alpha-$poor, respectively, adopting an arbitrary cut around [α/Fe] $\sim$ 1.12 dex. In Allende Prieto et al. (2016) extreme values were adopted to define these components, i.e., [α/Fe]<0.1 to define the thin disk component and 0.17 <[α/Fe]< 0.3 to the thick disk component, excluding thus the intermediate population from the *TGAS*-APOGEE datasets.

In Figure 8.3 we find that the thin disk component (hereafter $\alpha-$poor population) shows a significant peak (towards low eccentricity, < 0.2) present at $e \approx 0.1$, and share common eccentricities to the eccentricity distributions of particles in the cold thin disk as illustrated in Figure 8.3 (Pop 3, Pop 4, Pop 5, and Pop 6, with stellar ages ranging from 1 to 7 Gyr, see Robin et al., 2003) of the Milky Way as predicted from our test particle simulations (see Figure 8.3). There is also a significative peak beyond $e > 0.2$ that has thick disk-like eccentricities (see Figure 8.3). Most of these stars chemically ressemble the so-called "thick disk" ($\alpha-$enhanced). The two significative peaks show a clear separation between both components of the disk. Note also that an intermediate population observed in the TGAS-APOGEE datasets (0.1 <[α/Fe]< 0.17 dex) fit fairly well the eccentricity distribution as predicted for the Pop 7 of particles in a cold thin disk, with stellar ages ranging from 7 - 10 Gyr (see Robin et al., 2003). In other words, an intermediate population as observed in the TGAS-APOGEE sample, is kinematically consistent with the thin disk but shows intermediate chemistry. This could indicate that these stars could have formed in a differente manner (see Jofré et al., 2017).

[1] Phttp://github.com/jobovy/galpy

The $\alpha-$enhanced stars show a central peak which is stronger at $e \approx 0.3$ (see Figure 8.3), this peak coincides with the expected positions of the thick disk as seen from test particles simulations in Figure 8.3. There is also one significative tail with higher eccentricity ($e > 0.2$) on the $\alpha-$rich population, this presumes additional *thick disk* contamination exists in the thin disk sample. In other words, $\alpha-$rich stars that have likely been dynamically ejected into the thin disk due to dynamical process (perturbations from the Galactic bar and/or spiral arms), and more likely associated with "heating" (which is a change in the eccentricity conserving the angular momentum) (see e.g., Sellwood & Binney, 2002; Minchev & Famaey, 2010; Jofré et al., 2017). *We note from the results in Figure 8.3, that the eccentricity distributions from $\alpha-$poor stars fit fairly well with that predicted from particles in cold disks, without the need to invoke any additional dynamical process, while the $\alpha-$rich stars seem to show signatures to be affected by internal dynamical process.* Again, a suitable selection function can help to see whether or not the observed eccentricity distribution is inconsistent with that predicted by our models.

In Figure 8.4, an alternate form to the results presented in Figure 2 in Allende Prieto et al. (2016), and represent mainly thin and thick disk stars. In similar manner as in Figure 2 in Allende Prieto et al. (2016), the bins represent the average values of the characteristic orbital energy as defined in Moreno et al. (2015), the orbital Jacobi energy E_J (see §B), the maximum height above the plane Z_{max}, and the eccentricity e, on finer bins in [Fe/H] vs. [α/Fe] plane.

The main orbital elements have been computed using our barred Milky Way model introduced in §3, and the bar parameters of the **Model 22** as listed in Table 5.1. This plot shows how the main orbital elements change from one population to another, i.e., $\alpha-$rich stars tend to high eccentricity and height above the plane, and $\alpha-$poor stars tend to relatively low eccentricity within the Galactic plane, which is kinematically consistent with thin disk population, while intermediate populations with [α/Fe]$\sim$ 0.12 dex tend to have intermediate orbital elements, with intermediate kinematics behaviour as illustrated in Figure 8.3. This has also been pointed out in Jofré et al. (2017); Allende Prieto et al. (2016).

Note that we have introduced two new orbital elements, the so-called "characteristic" orbital energy and the orbital Jacobi energy, extensively studied in Moreno et al. (2015) as proxies to perturbations by resonances[2] with the Galactic bar in the Galactic disk and Galactic halo. It is interesting to note that $\alpha-$rich stars and on average lower metallicities appear at lower characteristic orbital energy and higher orbital Jacobi energy closer to the Galactic center, in good agreement with the orbital Jacobi maps presented in Figure 7.1, $\alpha-$poor stars and on average higher metallicities appear at high characteristic orbital energy and lower orbital Jacobi energy displaced away from the solar circle. Even more interesting result, the intermediate population (0.1<[α/Fe]< 0.17 dex) and on average lower metallicities ([Fe/H]< -0.2 dex) tends to be in intermediate values for the orbital Jacobi energy, and characteristic orbital energy, while the intermediate population (0.1<[α/Fe]< 0.17 dex) and on average higher metallicities ([Fe/H]> -0.2 dex) nearly covered by resonant families which lie in the Galactic plane. The typical orbits found in

[2]In Moreno et al. (2015) was introduced for the first time the characteristic diagrams of energy to delineate the trapping of stars by resonances on the Galactic disk and Galactic halo produced by *nonaxisymmetric* components.

this region are illustred in top panel of Figure 8.6. Similar orbits are extensively analyzed in Moreno et al. (2015), with a characteristic orbital energy ranging between ~ -1750 and -1715×10^2 km^2 s^{-2}, also populated by α-rich stars, where resonant family of orbits seems to delineate a trapping region (see Moreno et al., 2015) on the Galactic plane due to perturbations produced by the Galactic bar. This is illustrated in the diagram shown in Figure 8.6 (red shaded region) made mainly of disk stars (the *TGAS*-APOGE datasets).

In other words, a scenario where the intermediate population is brought into the solar neighbourhood by dynamical process (Jofré et al., 2017) seems plausible, and could be supported by the resonant trapping regions. A second possibility is that many of these stars are likely bulge interlopers, suggesting that contamination from the Galactic bulge is relevant to trace intermediate populations at the Solar position (*alpha*−intermediate). If our claim is correct, the intermediate population could had a distinct origin[3] at the Solar position, probably associated to *resonant trapping* regions, and might be the result of dynamical process dominated by perturbations from the Galactic bar, and/or stars ejected from the bulge. **Future work:** *Chemical abundances from the SDSS-IV (Sloan Digital Sky Survey-IV) DR14 (Data Release 14) combined with TGAS data will be combined to produce a more complete and statistically significant sample, to disentangle the nature of the intermediate population and its relation with moving groups.*

8.3 Tracking stellar orbits of field giant stars with globular cluster second-generation abundance patterns

Recently, Schiavon et al. (2017b) claimed to have found evidence for a new population present in the inner Milky Way, made up of *nitrogen-rich* stars, which shows chemical abundances patterns clearly distinguishable from the bulge itself, and strikingly similar to those observed in globular cluster stars.

The *nitrogen-rich* bulge population is also significantly more metal-rich ($\langle$[Fe/H]$\rangle \sim$ -1 dex) than the halo, and homogeneously distributed along the Galactic bulge, and kinematically indistinguishable from the rest of the bulge population (e.g., Schiavon et al., 2017b), i.e., they are not systematically different in terms of kinematics of the rest of the population of bulge. The authors interpreted these results in several ways, and two possibilities are associated with an inner halo population origins, and/or fossil relics of dissolved globular clusters. More recently, Martell et al. (2016) claimed to have found evidence of such chemical anomalies in *nitrogen-rich* stars similar to that of the *nitrogen-rich* bulge population, in metal-poor stars along the outer halo (e.g., Martell et al., 2016), which suggests that dissolved metal-poor globular clusters seems to be responsible of such chemical patterns beyond of the Galactic bulge. They in general are rare among bulge and outer-halo populations. Identify such chemistry behaviour in the field, could provide crucial observational support to a "merging" scenario for bulge and/or thick disk formation (see discussion in Sales et al., 2009; Ferraro et al., 2016). Observational evidence to such scenario seems to be supported by number of recent discoveries in bulge globular

[3]Intermediate population showing intermediate dynamical behaviour have also been discussed in Allende Prieto et al. (2016); Jofré et al. (2017), however its origin remains elusive to date

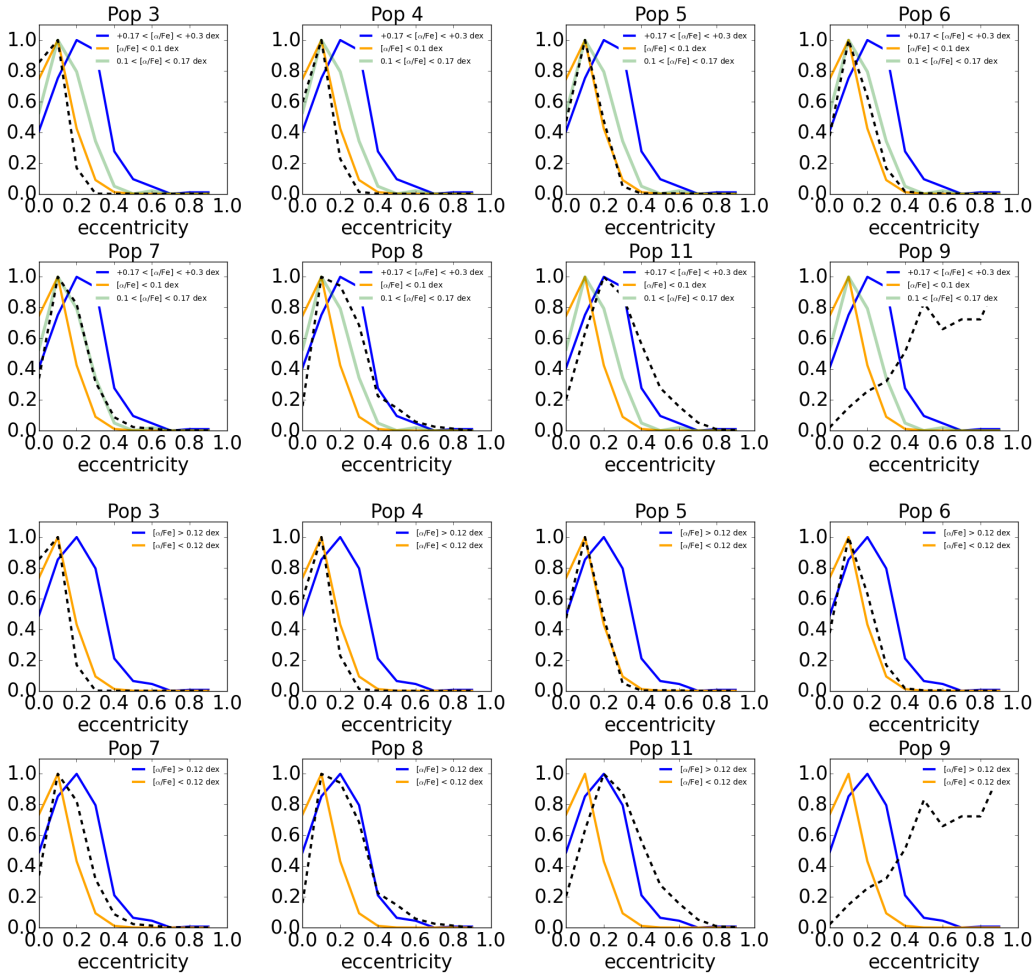

Figure 8.3: Predicted eccentricity distributions (bins are of equal size, 0.1) from test particles simulations (black dashed line), compared to the observed eccentricity distributions from the Gaia DR1 *TGAS* and APOGEE datasets. Histograms in blue and orange show respectively the eccentricity distribution for a $\alpha-$rich disk, and $\alpha-$poor disk using the same cuts as employed in Allende Prieto et al. (2016) (first and second row), and our arbitray cut (third and fourth row). Green histograms shows the eccentricity distribution for $\alpha-$intermediate ($+0.1<[\alpha/\mathrm{Fe}]< +0.17$ dex).

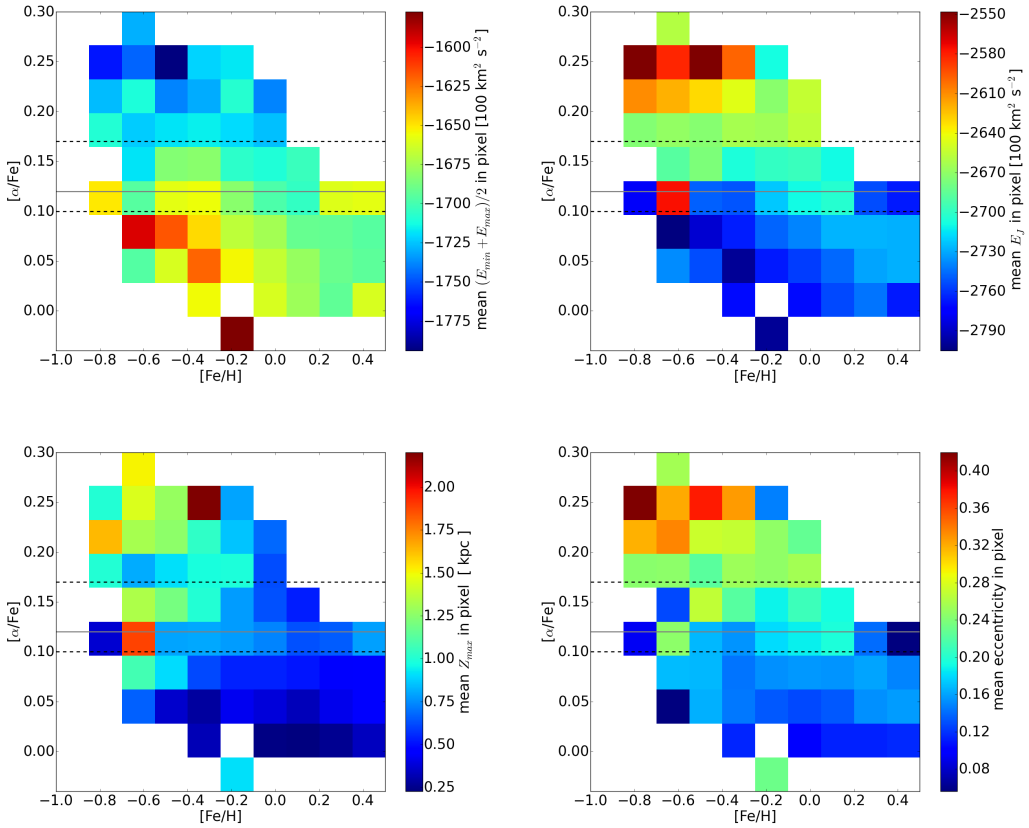

Figure 8.4: [Fe/H] vs. [α/Fe] distribution showing the mean orbital elements per bin: the characteristic orbital energy ($\frac{E_{max}+E_{min}}{2}$) as defined in Moreno et al. (2015), the orbital Jacobi energy E_J, maximum height above the plane Z_{max}, and the eccentricity e. The black dashed lines show the cuts employed by Allende Prieto et al. (2016) to split the sample into thin disk and thick disk component, while the grey line show our arbitrary cut to divide the sample into a $\alpha-$rich disk and a $\alpha-$poor disk.

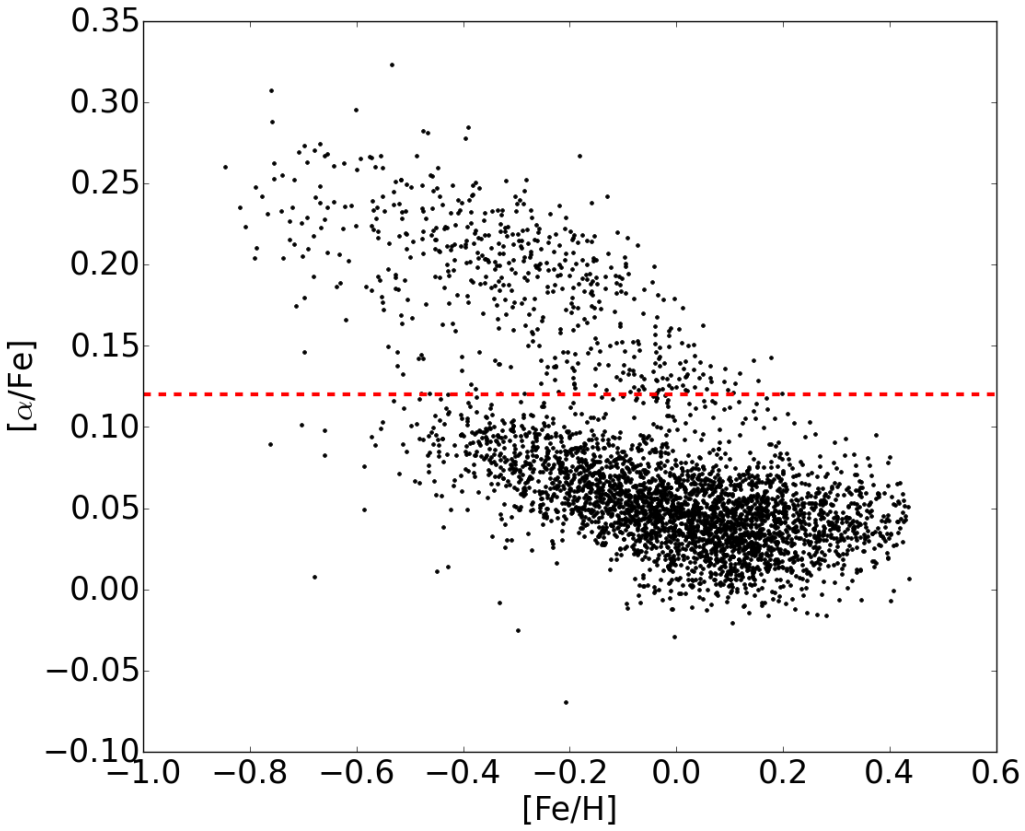

Figure 8.5: [Fe/H] vs. [α/Fe] distribution taken from the compilation of the *TGAS* plus APOGEE datasets from Allende Prieto et al. (2016). The red dashed line show our arbitray cut to split the sample into a thin disk and thick disk component.

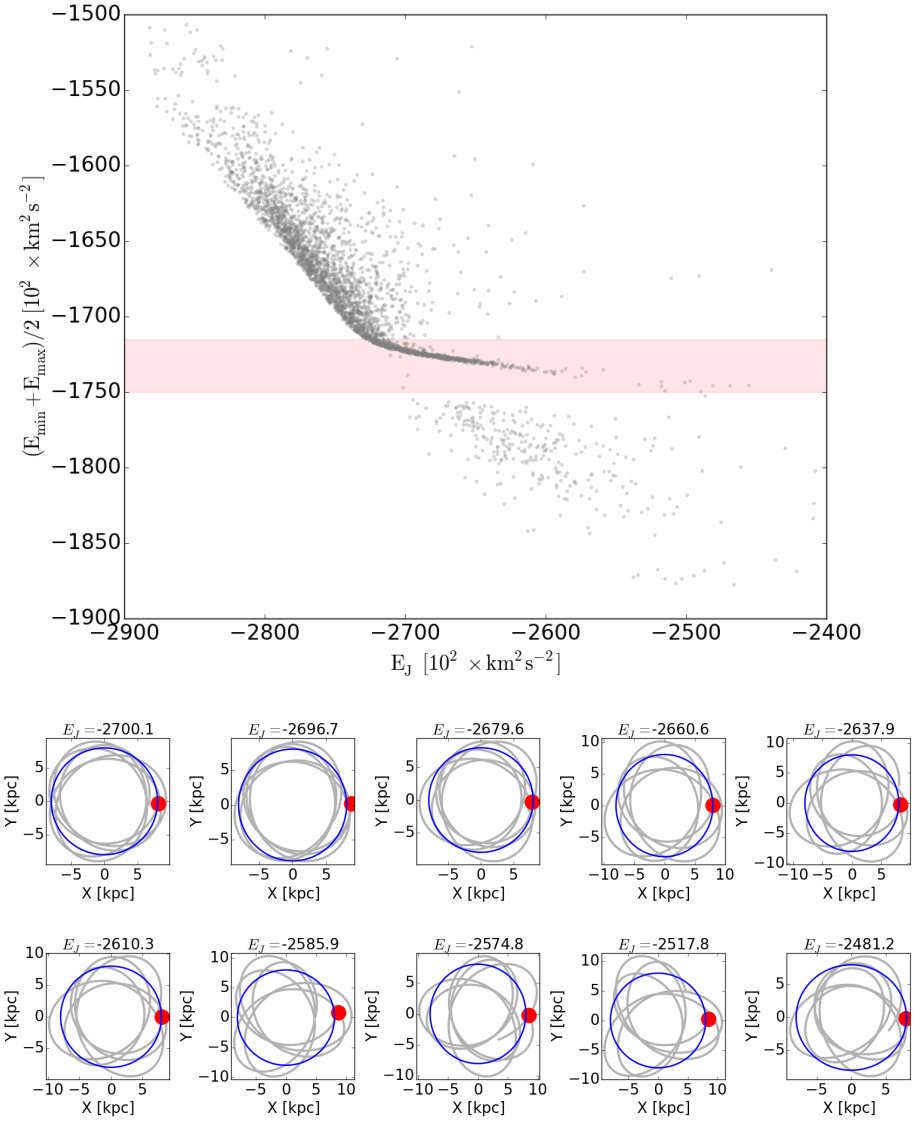

Figure 8.6: Top panel: Characteristic orbital energy $(E_{min} + E_{max})/2$ vs. the orbital Jacobi energy E_J in the non-inertial reference frame as defined in Moreno et al. (2015). The red shadow regions shows the formation of agglomerations of stars associated with periodic orbits in the Galactic disk (see e.g., Moreno et al., 2015), and dominated mainly by α-rich and $\alpha-$intermediate populations. Bottom panel: This panel displays the typical meridional orbits (at the non-inertial reference frame, where the bar is at rest) found along of the formation of the agglomeration of stars seen in the top panel, from high to low orbital Jacobi energy. The red symbol indicate the initial position of the star before integration, and the blue circle refers to the Solar radius.

cluster stars, sites that harbor the signatures of multiple bursts of star formation (e.g., Ferraro et al., 2016; Schiavon et al., 2017a; Rojas-Arriagada et al., 2016; Tang et al., 2017).

Recently, we have started an extensive search of globular cluster like abundance patterns in the Milky Way field, in order to investigate whether chemical variations within the Galactic bulge and outer halo are exclusively found in that regions. We found evidence for such chemical anomalies at low galactic latitudes. In Fernández-Trincado et al. (2016a) we claimed to have identified a giant star in the field with nitrogen and aluminium over-abundances, and low ratios of other light elements like magnesium, oxygen, and carbon (chemical patterns only observed in globular cluster populations) kinematically consistent with the Milky disk but chemically consistent with globular cluster populations. These results are extensively described in subsection 8.3.1.

On the other hand, Schiavon et al. (2017b) have estimated that at least 25 *N-rich* stars could be found in the disk field, based on a scenario of binary mass-transfer, and claims textually: *One might argue that, because the disk has a higher overall metallicity than the N-rich sample, the production of N-rich stars is inhibited, because models suggest that intermediate- mass AGB stars produce less nitrogen at higher metallicity (Ventura et al., 2013).* However, prior to our recent new finding Fernández-Trincado et al. (2016a), the *N-rich* stars had not been identified in the disk. *They seems to be more common in the disk of the Milky Way than previously thought, and many other candidates (* 11 *new N-rich stars in the disk) have been collected from the SDSS-III (DR13) (Fernández-Trincado et al. 2017, in preparation) plus recent work in progress in the SDSS-IV (DR14).* Here, we move forward to provide the orbital elements for the vast majority of that stars (Martell et al., 2016; Fernández-Trincado et al., 2016a) with kinematic data available, we employ in this work the barred model (**Model 2**) that is described in §3.

Figure 8.7 shows [Mg/Fe] versus [Fe/H] for all *migrant* stars (e.g., Fernández-Trincado et al., 2016a; Martell et al., 2016) and Galactic field stars within intermediate metallicity (-1.8 <[Fe/H]< -0.7 dex). Note that most of the *migrant* stars from Martell et al. (2016) show similar Galactic abundances trend as other halo field stars (see e.g., Hawkins et al., 2015, and references therein), while the *N-rich* star from Fernández-Trincado et al. (2016a) fall within the regions dominated by the accreted halo stars (or $\alpha-$rich stars) (e.g., Hawkins et al., 2015), making it a good candidate to be a remnant of globular cluster disruption in the Galactic plane.

Figure 8.8 provides the orbital energy distribution of these stars (when astrometric data is available) compared to that expected for Galactic globular clusters. The main orbital elements for 63 globular clusters (taken from the recent compilation by Moreno et al., 2014) illustrated in the same figure are listed in Appendix C. Their orbits were calculated using the barred Milky Way model presented in §3. This plot shows that the vast majority of the globular clusters appear as agglomerations at higher values of E_J (left part of the diagram) towards the region where the inner disk are situated (see e.g., Moreno et al., 2015), while a handful are situated around lower values of E_J (right part of the diagram), and contain mainly the halo globular clusters. Within the errors, the position of the *migrant* stars (field stars with globular cluster abundance patterns) in this diagram is consistent with the few metal-poor globular clusters present in the same region. The *N-rich* star identified by Fernández-Trincado et al. (2016a) trace similar

trend in orbital energy that a few globular clusters in the disk. These results support the idea that the chemical anomalies observed in the disk can result in stars born in globular clusters being brought into the field, through disrupted clusters (e.g., Carretta et al., 2010; Carretta, 2013; Carollo et al., 2013; Fernández Trincado et al., 2013; Fernández-Trincado et al., 2015a,c,b, 2016b,a; Anguiano et al., 2016, Fernández-Trincado et al. 2017a, in preparation). In some cases these stars can be trapped by different resonances on the Galactic plane produced by the Galactic bar, as it seems to be the case for 2M16011638-1201525 (Fernández-Trincado et al., 2016a) as illustrated by its meridional orbit in Figure 8.9.

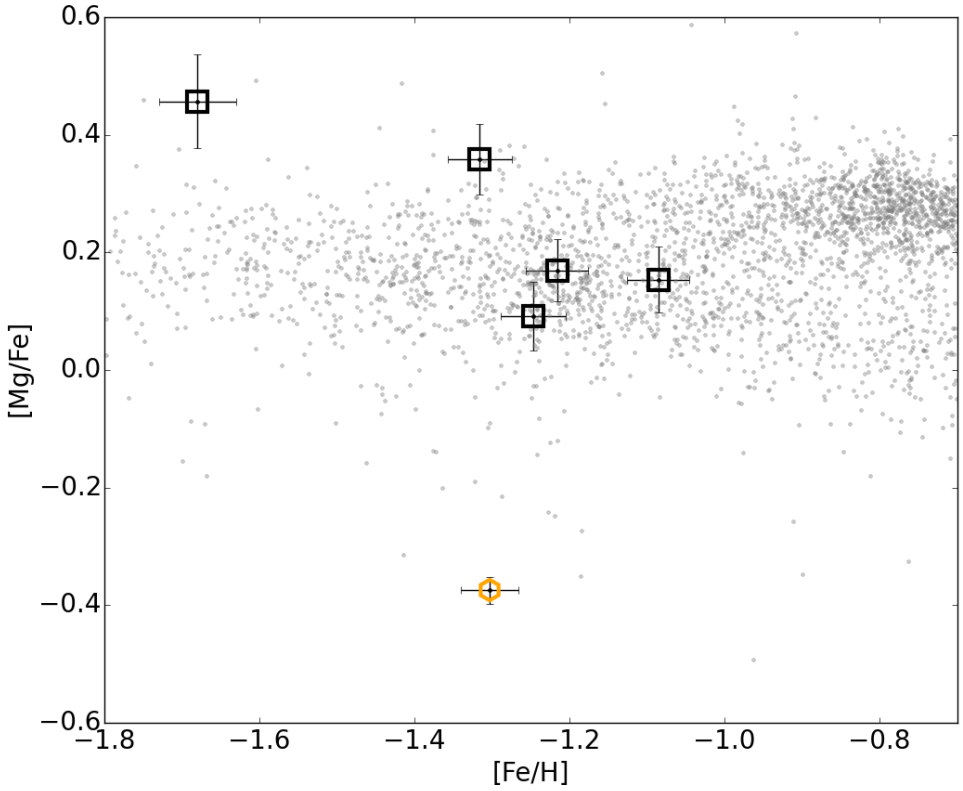

Figure 8.7: The [Mg/Fe] as a function of metallicity for a metal poor sample ($-1.8 <$[Fe/H]< -0.7) from the APOGEE datasets (black dots). The orange hexagon symbols is represent one giant star from Fernández-Trincado et al. (2016a), and the five black squares symbols are the five *migrant* stars from (Martell et al., 2016). All the chemical abundances in this plot have been taken from the APOGEE DR13 catalogue (SDSS Collaboration et al., 2016).

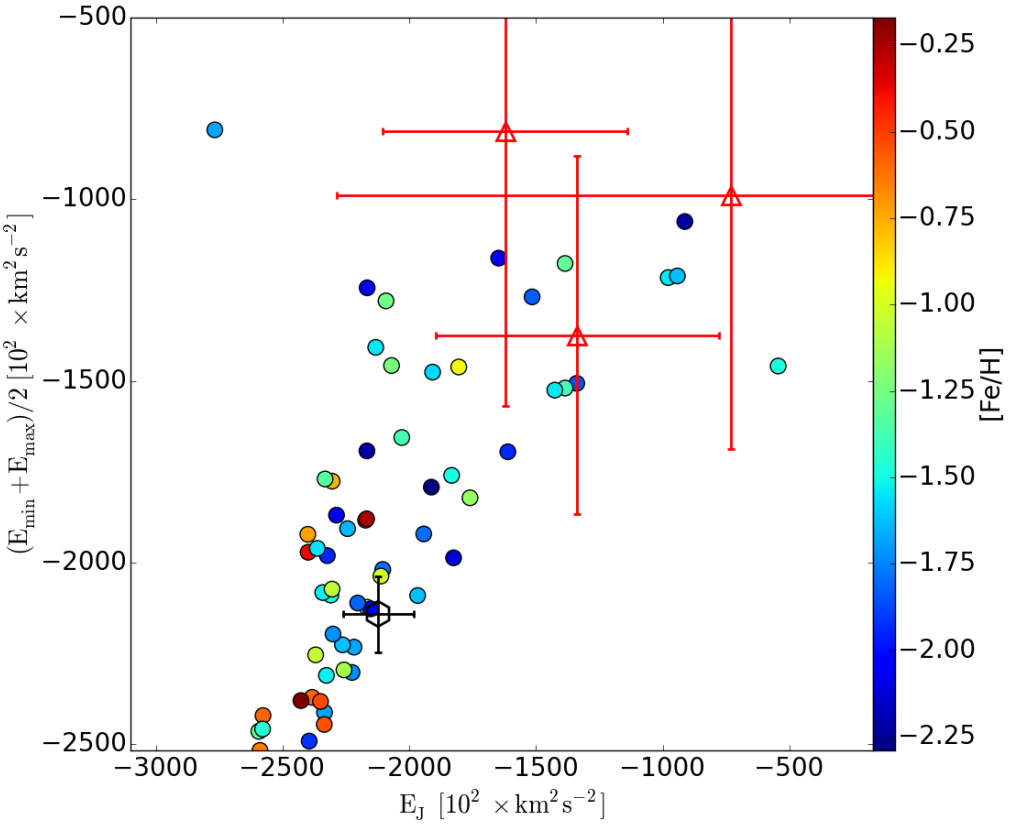

Figure 8.8: The characteristic orbital energy $(E_{min} + E_{max})/2$ versus the orbital Jacobi energy E_J as defined in Eq. B.19. This plot shows the energy distribution for 63 globular clusters listed in Table C.2, one giant star from Fernández-Trincado et al. (2016a), and three *migrant* stars (red triangle symbols) from Martell et al. (2016). Colours represent the metallicity of each globular cluster from Harris (2010).

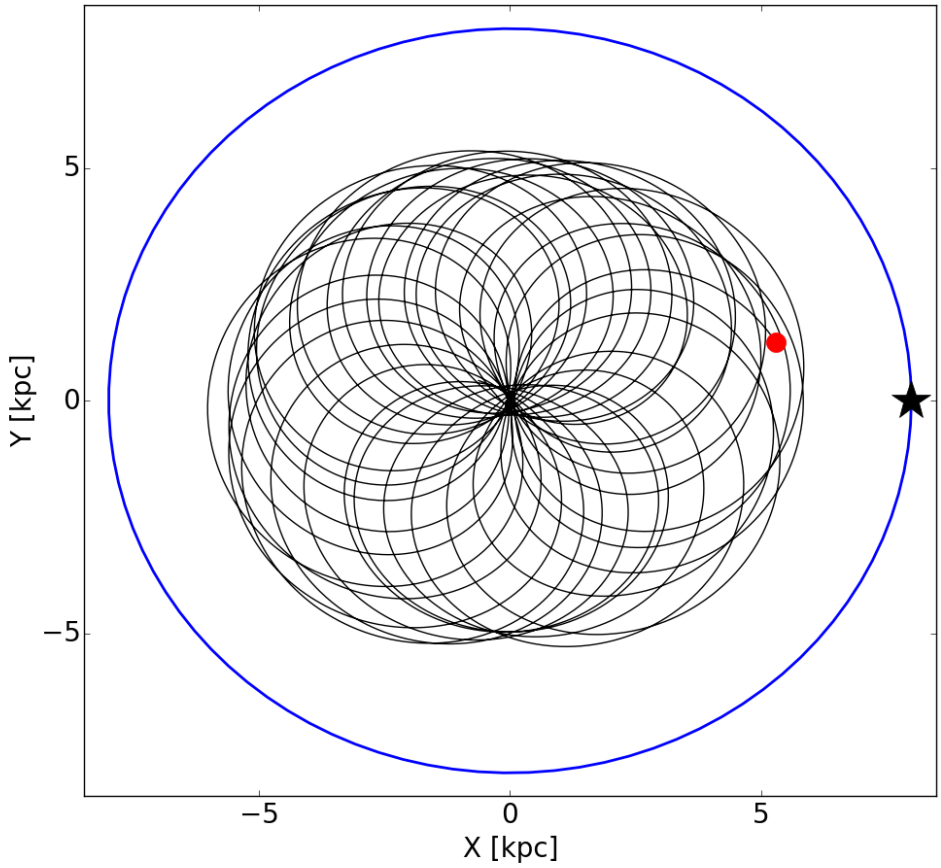

Figure 8.9: Meridional orbit of 2M16011638-1201525 (Fernández-Trincado et al., 2016a) at the non-inertial reference frame, where the bar is at rest. The red symbol indicate the initial position of the star before integration, the blue circle refers to the Solar radius, and the star symbols the positions of the Sun.

8.3.1 Results from the SDSS-III/APOGEE survey

The paper attached to this thesis is the first of a serie, and presents the analysis of chemical abundances in a very peculiar giant star identified from the manual analysis carried out for $\sim$ 100,000 spectra available in the APOGEE data release 12. The revelant findings identified from the APOGEE spectrum are:

1.) In Fernández-Trincado et al. (2016a) we have measured significant variations for some light-elements like aluminium (Al), nitrogen (N), carbon (C), and magnesium (Mg) in a field giant star, 2M16011638-1201525, showing significant differences from the field. Fernández-Trincado et al. (2016a) claimed that 2M16011638-1201525 becomes enriched in nitrogen (N-rich), and the Mg-Al cycle is activated, where Al production happens (see Schiavon et al., 2017b), and high variations in these elements appear to originate only in globular clusters (Lind et al., 2015; Martell et al., 2016). Identify these stars in the field may provide important clues to the origin of such stars, called *migrant* by Martell et al. (2016).

2.) Hasselquist et al. (2016) has measured in the same star (2M16011638-1201525) significant variations of ionized Neodymium (Nd II), which provides strong signature for neutron-capture element in this star.

3.) Cunha (2017) has measured recently significant variations of Cerium (Ce II) in the same star, revealing that 2M16011638-1201525 is also enhanced in *s*-process elements (synthesized in AGB stars) (see e.g., Hasselquist et al., 2016, and references therein).

The Astrophysical Journal, 833:132 (7pp), 2016 December 20 doi:10.3847/1538-4357/833/2/132

DISCOVERY OF A METAL-POOR FIELD GIANT WITH A GLOBULAR CLUSTER SECOND-GENERATION ABUNDANCE PATTERN

J. G. Fernández-Trincado[1], A. C. Robin[1], E. Moreno[2], R. P. Schiavon[3], A. E. García Pérez[4,5], K. Vieira[6], K. Cunha[7], O. Zamora[4,5], C. Sneden[8], Diogo Souto[9], R. Carrera[4,5], J. A. Johnson[10], M. Shetrone[11], G. Zasowski[12], D. A. García-Hernández[4,5], S. R. Majewski[13], C. Reylé[1], S. Blanco-Cuaresma[14], L. A. Martinez-Medina[2], A. Pérez-Villegas[15], O. Valenzuela[2], B. Pichardo[2], A. Meza[16], Sz. Mészáros[17], J. Sobeck[13], D. Geisler[18], F. Anders[19,20], M. Schultheis[21], B. Tang[18], A. Roman-Lopes[22], R. E. Mennickent[18], K. Pan[23], C. Nitschelm[24], and F. Allard[25]
[1] Institut Utinam, CNRS UMR 6213, Université de Franche-Comté, OSU THETA Franche-Comté-Bourgogne, Observatoire de Besançon, BP 1615, F-25010 Besançon Cedex, France; jfernandez@obs-besancon.fr, jfernandezt87@gmail.com
[2] Instituto de Astronomía, Universidad Nacional Autónoma de México, Apdo. Postal 70264, México D.F., 04510, Mexico
[3] Astrophysics Research Institute, Liverpool John Moores University, 146 Brownlow Hill, Liverpool, L3 5RF, UK
[4] Instituto de Astrofísica de Canarias, E-38205 La Laguna, Tenerife, Spain
[5] Departamento de Astrofísica, Universidad de La Laguna, E-38206 La Laguna, Tenerife, Spain
[6] Centro de Investigaciones de Astronomía, AP 264, Mérida 5101-A, Venezuela
[7] Dept. of Physics and Astronomy, Johns Hopkins University, Baltimore, MD 21210, USA
[8] Department of Astronomy and McDonald Observatory, The University of Texas, Austin, TX 78712, USA
[9] Observatório Nacional, Rua General José Cristino, 77, 20921-400 São Cristóvão, Rio de Janeiro, RJ, Brazil
[10] Department of Astronomy, The Ohio State University, Columbus, OH 43210, USA
[11] Department of Astronomy, University of Texas at Austin, Austin, TX 78712, USA
[12] Department of Physics and Astronomy, Johns Hopkins University, Baltimore, MD 21218, USA
[13] Department of Astronomy, University of Virginia, P.O. Box 400325, Charlottesville, VA 22904-4325, USA
[14] Observatoire de Genève, Université de Genève, CH-1290 Versoix, Switzerland
[15] Max-Planck-Institüt für Extraterrestrische Physik, Gießenbachstraße, D-85748 Garching, Germany
[16] Departamento de Ciencias Fisicas, Universidad Andres Bello, Sazie 2212, Santiago, Chile
[17] ELTE Gothard Astrophysical Observatory, H-9704 Szombathely, Szent Imre Herceg st. 112, Hungary
[18] Departamento de Astronomía, Universidad de Concepción, Casilla 160-C, Concepción, Chile
[19] Leibniz-Institut für Astrophysik Potsdam (AIP), An der Sternwarte 16, D-14482, Potsdam, Germany
[20] Laboratório Interinstitucional de e-Astronomia—LIneA, Rua Gal. José Cristino 77, Rio de Janeiro, RJ—20921-400, Brazil
[21] Laboratoire Lagrange (UMR7293), Université de Nice Sophia Antipolis, CNRS, Observatoire de la Côte d'Azur, BP 4229, F-06304 Nice Cedex 4, France
[22] Departamento de Física y Astronomía, Universidad de la Serena, Av. Juan Cisternas 1200 Norte, La Serena, Chile
[23] Apache Point Observatory and New Mexico State University, P.O. Box 59, sunspot, NM, 88349-0059, USA
[24] Unidad de Astronomía, Facultad de Ciencias Básicas, Universidad de Antofagasta, 601 Avenida Angamos, Antofagasta, Chile
[25] Univ Lyon, Ens de Lyon, Univ Lyon1, CNRS, Centre de Recherche Astrophysique de Lyon UMR5574, F-69007, Lyon, France
Received 2016 April 5; revised 2016 October 5; accepted 2016 October 6; published 2016 December 13

ABSTRACT

We report on the detection, from observations obtained with the Apache Point Observatory Galactic Evolution Experiment spectroscopic survey, of a metal-poor ([Fe/H] = −1.3 dex) field giant star with an extreme Mg–Al abundance ratio ([Mg/Fe] = −0.31 dex; [Al/Fe] = 1.49 dex). Such low Mg/Al ratios are seen only among the second-generation population of globular clusters (GCs) and are not present among Galactic disk field stars. The light-element abundances of this star, 2M16011638-1201525, suggest that it could have been born in a GC. We explore several origin scenarios, studying the orbit of the star in particular to check the probability of its being kinematically related to known GCs. We performed simple orbital integrations assuming the estimated distance of 2M16011638-1201525 and the available six-dimensional phase-space coordinates of 63 GCs, looking for close encounters in the past with a minimum distance approach within the tidal radius of each cluster. We found a very low probability that 2M16011638-1201525 was ejected from most GCs; however, we note that the best progenitor candidate to host this star is GC ω Centauri (NGC 5139). Our dynamical investigation demonstrates that 2M16011638-1201525 reaches a distance $|Z_{\rm max}| < 3$ kpc from the Galactic plane and minimum and maximum approaches to the Galactic center of $R_{\rm min} < 0.62$ kpc and $R_{\rm max} < 7.26$ kpc in an eccentric ($e \sim 0.53$) and retrograde orbit. Since the extreme chemical anomaly of 2M16011638-1201525 has also been observed in halo field stars, this object could also be considered a halo contaminant, likely to have been ejected into the Milky Way disk from the halo. We conclude that 2M16011638-20152 is also kinematically consistent with the disk but chemically consistent with halo field stars.

Key words: globular clusters: general – stars: abundances – stars: Population II

1. INTRODUCTION

It is a commonly accepted observational fact that second-generation stars make up a significant fraction of the population of most Galactic globular clusters (GCs; Carretta et al. 2009a, 2009b; Bastian & Lardo 2015), and they display unique inhomogeneities in their abundance of light elements involved in proton-capture processes. The elements C, N, O, F, Na, Al, Mg, and perhaps Si (e.g., Gratton et al. 2012; Mészáros et al. 2015 and references therein) provide useful information about the environment in which they were formed. A fraction of GC populations show a pronounced [Al/Fe] and [Mg/Fe] anti-correlation (e.g., Sneden et al. 2004; Johnson et al. 2005; Marino et al. 2008; Carretta et al. 2009a, 2012; Mészáros et al. 2015), a remarkable characteristic (i.e., a *chemical*

fingerprint) of some second-generation stars, which are not typically observed in the field, except in some peculiar cases, as described below.

Interestingly, it has been suggested that ∼3% of field stars in the Galaxy show atypical light-element patterns similar to those seen only among the secondary population of Galactic GCs (e.g., Carretta et al. 2010; Martell & Grebel 2010; Martell et al. 2011; Ramírez et al. 2012). They could be explained by the escape of individual stars from those systems (Carretta et al. 2010; Carollo et al. 2013; Carretta 2013; Fernández-Trincado et al. 2013, 2015b, 2015c, 2016; Anguiano et al. 2016).

Only a few studies confirm the existence of such stars in the Galactic field. For example, (i) some Aquarius stream stars appear to originate from a GC (e.g., Wylie-de Boer et al. 2012); (ii) the Carretta (2013) study on NGC 6752 identifies a few field star candidates with clear chemical patterns of GCs; (iii) Ramírez et al. (2012) found an elevated Na/O ratio abundance in two field halo dwarf stars; (iv) Lind et al. (2015) recently discovered a metal-poor field halo star with a high Al–Mg ratio; (v) Martell et al. (2016) recently identified five stars in the Galactic halo with GC-like abundance patterns, and these stars are thought to be migrants from GCs; (vi) Schiavon et al. (2016) analyzed the chemical composition of 5,175 stars in fields centered on the Galactic bulge, and found 59 giant stars with elevated nitrogen abundances, anti-correlated with [C/Fe] and correlated with [Al/Fe] abundance; and several scenarios have been put forward to explain such anomalies in the Galactic bulge, i.e., the authors proposed that these stars may likely come from disrupting GCs, though an alternative scenario being considered is that N-rich stars could be formed in environments similar to GCs (for more details, see Schiavon et al. 2016). Detection of such light-element abundance inhomogeneities in non-GC stars is particularly important for understanding how many Galactic field stars could have been deposited by GCs.

In this work, we report the first discovery in Apache Point Observatory Galactic Evolution Experiment (APOGEE) data of a peculiar giant star in the Milky Way field that stands out due to its very low magnesium and high aluminum abundance as well as other very significant light-element abundance anomalies, such as a greatly enhanced nitrogen-to-iron ratio ([N/Fe] > 1.0). This star could be the most convincing evidence yet for a Galactic field star stripped from a GC.

2. A PECULIAR GIANT STAR OBSERVED BY APOGEE

The star of interest, 2M16011638-1201525, was found in APOGEE (Zasowski et al. 2013; Majewski et al. 2016), a near-infrared spectroscopic survey (part of the Sloan Digital Sky Survey III, SDSS-III; Eisenstein et al. 2011) targeting primarily Milky Way red giants, at a resolution of $R \approx 22{,}500$, acquired with the APOGEE multi-object spectrograph mounted at the SDSS 2.5 m telescope (Gunn et al. 2006). We refer the reader to Holtzman et al. (2015) and Nidever et al. (2015) for detailed information on the data and for the data reduction pipeline.

We turn our attention to the giant star 2M16011638-1201525, which has high [Al/Fe] = 1.49 and a strongly depleted [Mg/Fe] = −0.31 (manually confirmed using MOOG[26]). 2M16011638-1201525 has been identified as part of a sample of ∼265 giant stars originally surveyed

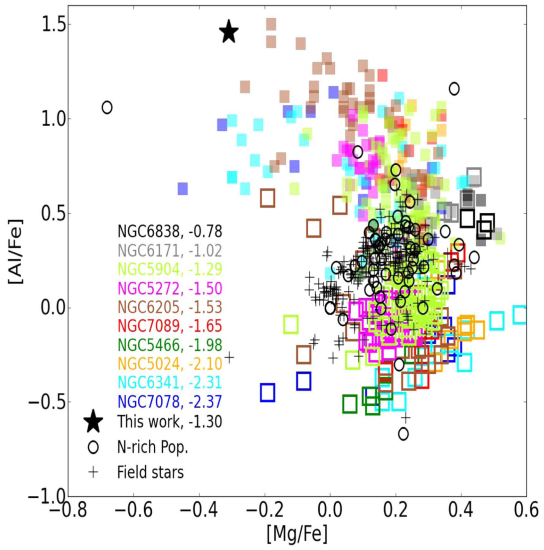

Figure 1. Al and Mg abundances of 393 red giant stars in 10 GCs from Mészáros et al. (2015). The first generation is marked as open square symbols, and the second generation as filled square symbols. The average metallicity ([Fe/H]) is listed after the cluster name. The black star symbol represents the star analyzed in this work, the black open circles the Schiavon et al. (2016) sample, and the plus symbols 211 stars with available ASPCAP abundances in the same field of 2M16011638-1201525.

spectroscopically by APOGEE in a field centered on (l, b) = (0, +30), showing unusual chemical abundances and a high-quality stellar radial velocity. Figure 1 shows a comparison of our results with those derived from 393 giants in 10 GC stars (see Mészáros et al. 2015) and 59 bona fide field nitrogen-rich stars giants in the bulge from Schiavon et al. (2016). In particular we show that 2M16011638-1201525 has one of the most extreme combinations of abundances. 2M16011638-1201525 shows a radial velocity (with typical uncertainties of less than 1 km s^{-1}) dispersion (*vscatter*) less than 1 km s^{-1} over 4 visits, which makes it unlikely to be a variable star or a binary star. We also examine variations between 2MASS and DENIS magnitudes and USNO-B catalogs and find no evidence for photometric variations between those catalogs, i.e., ($K_{2MASS} - K_{DENIS}$) = −0.016 mag and ($R1 - R2$) = 0.07 mag.

Figure 1 shows the light-element anomalies of 2M16011638-1201525, in this case for Al and Mg abundances. Such extreme values of Al enhancements and Mg depletions are only observed in second-generation GC population, as seen in Figure 1.

The main atmospheric parameters (T_{eff}, log g, and [Fe/H]) of 2M16011638-1201525 were checked using an extended and updated version of iSpec[27] (Blanco-Cuaresma et al. 2014) to work in the spectral regime of APOGEE (∼1.51–1.7 μm). For a set of atmospheric parameters and atomic data, iSpec generates synthetic spectra, computed from the ATLAS atmosphere model (Kurucz 2005), and minimizes the difference with the observed spectrum using a least-squares algorithm.

We adopt the iSpec-recommended stellar parameters: T_{eff} = 4572 ± 100 K, log g = 1.66 ± 0.1, and [Fe/H]

[26] http://www.as.utexas.edu/~chris/moog.html

[27] http://www.blancocuaresma.com/s/iSpec/

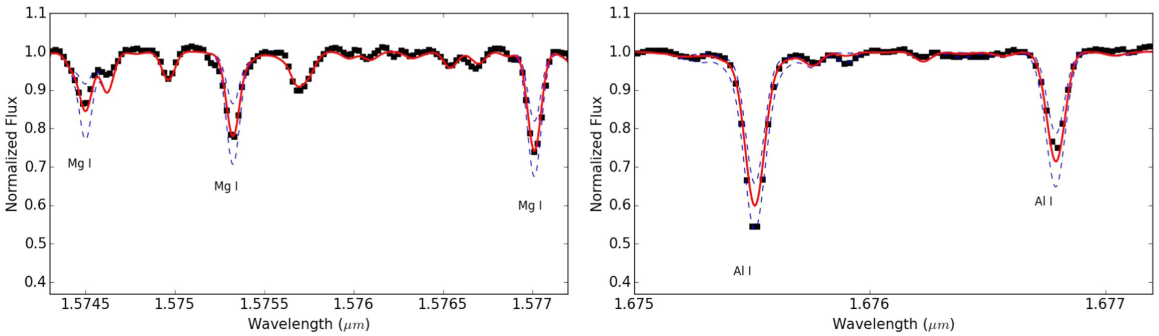

Figure 2. Best-fit for the Mg I and Al I lines (red curve) in the observed infrared spectrum (black filled squares) of 2M16011638-1201525 with S/N > 700. The two blue dashed curves correspond to synthetic spectrum abundance choices that are offset from the best fit by ±0.5 dex.

$= -1.30 \pm 0.1$), which are entirely consistent with those obtained by the ASPCAP pipeline (García Pérez et al. 2016), and $T_{\rm eff} = 4575 \pm 92$ K, $\log g = 1.61 \pm 0.11$, and [Fe/H] $= -1.31 \pm 0.05$. Both sets of model parameters computed with the ATLAS model grid are consistent with those we found using MARCS stellar atmosphere models (Gustafsson et al. 2008; Zamora et al. 2015).

In this work,[28] we focus on the abundances of Al, Mg, C, N, and O, which are typical chemical signatures of GCs (Gratton et al. 2012). We did not include sodium, a typical species to separate GC populations, in our analysis as its lines in our APOGEE spectra (1.6373 and 1.6388 μm) are weak in the typical $T_{\rm eff}$ and metallicity for the star studied in this work, which would lead to unreliable abundance results.

APOGEE spectra have three main windows to determine aluminum abundances: 1.6718, 1.6750, and 1.6763 μm. We did not analyze the line at 1.6718 μm because it is poorly fitted in the core and this may be an indicator of NLTE or saturation effects (Hawkins et al. 2016). The selected lines at 1.6750 and 1.6763 μm show an offset of ±0.5 dex (see Figure 2) between the two best-fit abundances, i.e., the derived line-to-line abundance is A(1.6750 μm) = 6.81 and A (1.6763 μm) = 6.31. It is important to note that this discrepancy does not affect the discussion and conclusions of this work, i.e., the line-to-line and relative abundance indicates that the star is Al-rich. For 2M16011638-1201525 we have done a manual inspection of the best MOOG (v. Jan2016, Sneden 1973) fitted synthesis of Al, Mg, C, N, and O lines using atomic and molecular species, the most recent OH line list by Brooke et al. (2016), and Solar abundance values from Asplund et al. (2005). The best MOOG fitted synthesis of Al and Mg lines for 2M16011638-1201525 is shown in Figure 2. For our manual analysis, we adopted the best fit of the atmospheric stellar parameters recommended by iSpec, in good agreement with other independent analyses and methods. This step was necessary to provide a consistent comparison of the results from a manual abundance analysis with the values determined from the ASPCAP pipeline. Table 1 gives these abundances and those derived by the ASPCAP pipeline using a different line list of atomic and molecular species. For comparison the abundances derived from the photometric effective temperatures are given in the same table.

Table 1
Chemical Abundances of 2M16011638-1201525

	APOGEE DR12 $T_{\rm eff}$ 4575 K	This work $T_{\rm eff}$ 4572 K	Photometric $T_{\rm eff}$ 4340 K
[Fe/H]	−1.31	−1.30	−1.30
[C/Fe]	0.09	−0.15	−0.06
[N/Fe]	1.08	1.46	1.05
[O/Fe]	0.21	−0.06	0.03
[Mg/Fe]	−0.04	−0.31	−0.43
[Al/Fe]	1.06	1.49	1.28

Note. The solar reference abundances are from Asplund et al. (2005).

We additionally computed abundances assuming the effective temperature from photometry to check for any significant deviation in our results, i.e., a photometric effective temperature was calculated from the $J-K$ color relation using the methodology presented in González Hernández & Bonifacio (2009). Photometry is extinction-corrected using the Rayleigh–Jeans color excess method (see Majewski et al. 2011), which leads to an extinction value $\langle A_{\rm K}^{\rm WISE} \rangle \sim 0.157$ mag. For comparison, Table 1 shows the values obtained in each procedure. The observed small discrepancies do not affect the main result of our work about the extreme abundances of Mg, Al, and N.

Furthermore, our abundances were compared with those in the literature, i.e., chemical abundances from the DR12 data (García Pérez et al. 2016) and GC stars (Mészáros et al. 2015) —see Figure 1. Those values are quite different from ours, as also seen in the online[29] version from the best ASPCAP fit. This is due to the fact that we used the same wavelength windows as Mészáros et al. (2015; see their Table 3), which are significantly different from the ASPCAP DR12 windows. Also we did not use any of the weak Mg lines, which in these metal-poor stars mostly disappear from the spectra. These differences in [Mg/Fe], [Al/Fe], [N/Fe], [C/Fe], [N/Fe], and [O/Fe] abundances are also likely to be due to the updated line list which includes both atomic and molecular species used by MOOG in our procedure. The chemical abundances relevant to this work are not affected by the analysis methods used.

[28] To facilitate the reproducibility and reuse of our results, we have made all the simulations available in a public repository at https://github.com/Fernandez-Trincado/SDSS-IV-Project0184/blob/master/README.md.

[29] DR12 Science Archive Server: http://dr12.sdss3.org/irSpectrumDetail?commiss=0&locid=4520&show_aspcap=True&apogeeid=2M16011638-1201525.

Table 2
Phase-space Data

Coordinates	(J2000)
(α, δ)	$(240.^{\circ}31825, -12.^{\circ}03127)$
(l, b)	$(358.^{\circ}87794, 29.^{\circ}5692)$
Heliocentric Distance	[kpc]
	(2.67 ± 0.68)[a]
	(2.94 ± 0.62)[b]
$V_{\rm los}$	[km s^{-1}]
	(82.23 ± 0.84)[a]
	(84.68 ± 0.79)[c]
Proper Motions	$(\mu_{\alpha} \cos\delta,\ \mu_{\delta})$
	(mas yr^{-1})
	$(-11.5 \pm 1.7,\ -16.9 \pm 1.7)$[d]
	$(-12.3 \pm 2.1,\ -16.0 \pm 2.1)$[e]
	$(-15.7 \pm 2.7,\ -17.2 \pm 2.4)$[f]

Notes.
[a] Kordopatis et al. (2013).
[b] Hayden et al. (2014).
[c] SDSS-III/APOGEE.
[d] UCAC4.
[e] PPMXL.
[f] Tycho-2 (unfortunately, improvements in distance and proper motions are not available from the TGAS (Gaia Collaboration et al. 2016) catalog for this star).

3. GALACTIC MODEL AND SIMULATIONS

We performed a series of orbital[30] integrations using a semi-analytical, multicomponent model of the Milky Way potential to predict the orbital parameters of 2M16011638-1201525 in the Galaxy, based on the reliable (Table 2) six-dimensional phase-space coordinates (3D position and 3D velocity).

We consider axisymmetric and non-axisymmetric Galactic models, including a prolate bar and spiral-arms structures. The relevant parameters employed in the bar and the spiral arms are the same as those explained in Moreno et al. (2014) and Robin et al. (2012).

We employed the kinematical parameters of 2M16011638-1201525 and those associated with the Galactic model and consider their corresponding uncertainties as 1σ variations in a Gaussian Monte Carlo sampling. The adopted Solar motion with its uncertainties is $(U,\ V,\ W)_{\odot} = (-11.1 \pm 1.2,\ 12.24 \pm 2.1,\ 7.25 \pm 0.6)$ km s^{-1} (e.g., Schönrich et al. 2010; Brunthaler et al. 2011). In each computed orbit, we obtain the following orbital parameters: the maximum distance from the Galactic plane, $Z_{\rm max}$; the maximum and minimum Galactocentric radii, $r_{\rm max}$ and $r_{\rm min}$; and the orbital eccentricity, defined as $e = (r_{\rm max} - r_{\rm min})/(r_{\rm max} + r_{\rm min})$.

To estimate the effect of axisymmetric and non-axisymmetric components of the Galactic potential in the computed orbital parameters, we considered the following four configurations of the Galactic potential:

(i) Model 1: the axisymmetric model, which is the direct scaling of the Allen & Santillan (1991) model
(ii) Model 2: the non-axisymmetric model mentioned above, using the prolate bar with the spiral arms (see Pichardo et al. 2003, 2004)
(iii) Model 3: the non-axisymmetric model using the boxy bar with the spiral arms (see Pichardo et al. 2003, 2004)
(iv) Model 4: We also performed orbit integration of 2M16011638-1201525 using the *GravPot16*[31] code. We have assumed a Milky Way gravitational potential model using the mass distribution of the last version of the Besançon Galaxy model (see Fernández-Trincado et al. 2014; Robin et al. 2014) based on the superposition of many composite stellar populations belonging to the thin disk, dark matter halo component, and interstellar matter (ISM; e.g., Robin et al. 2003); the thick disk (shape B; see Robin et al. 2014) and stellar halo (Robin et al. 2014; Fernández-Trincado et al. 2015a); and a standard triaxial boxy-shape bar (Robin et al. 2012). The results are shown in Figure 4. We refer the reader to these papers for further details of the density profiles.

In these models the orbits of the star are integrated over 2 Gyr, with 10^4 orbits in Model 1 and 10^3 orbits in both Model 2 and Model 3. We have found that in Models 2, 3, and 4 the computed orbital parameters of 2M16011638-1201525 are very similar and thus do not depend sensitively on the assumed model of the Galactic bar.

For the orbital computation of 2M16011638-1201525, we also tested the set of distances and proper motions given in Table 2; small variations in these observables do not lead to substantial difference in the orbital parameters and do not affect the overall conclusions of this work.

We chose to use the accurate (<1 km s^{-1}) radial velocity from APOGEE. We adopted the spectro-photometric estimated distance from Hayden et al. (2014) based on Bayesian methods developed for APOGEE data, which is in good agreement with the distance measurements from the RAVE survey (see Table 2). We have adopted absolute proper motions from the UCAC4 catalog (Fourth U.S. Naval Observatory CCD Astrograph Catalogue; Zacharias et al. 2013), because the error in proper motion (with uncertainties <2 mas yr^{-1}) is smaller than those in other catalogs (see Table 2) and is less affected by potential systematic uncertainties (Vickers et al. 2016). We note that the small uncertainties on the proper motions are good enough to estimate the space-velocity vector accurately,[32] i.e., $(U_{\rm LSR},\ V_{\rm LSR},\ W_{\rm LSR}) = (93.9 \pm 10.9,\ -246.1 \pm 68.9,\ 21.7 \pm 19.9)$ km s^{-1}.

4. POSSIBLE ORIGINS

A possible scenario producing very extreme Mg–Al–N nucleosynthesis could be an association with an intermediate-mass ($\sim$3–6 $M_{\odot}$) AGB star (see Ventura et al. 2011; Schiavon et al. 2016) in a binary companion. A future work will be dedicated to investigating in more detail other mechanisms, including binary stellar mergers or pollution of the ISM by a previous generation of massive stars.

In the following subsections we will analyze other scenarios that could have led this peculiar star to its current phase-space location in the Galaxy.

[30] We have adopted a righthanded coordinate system for (U, V, W), so that they are positive in the directions of the galactic center, galactic rotation, and north galactic pole, respectively.

[31] https://fernandez-trincado.github.io/GravPot16/

[32] The velocities ($U_{\rm LSR}$, $V_{\rm LSR}$, $W_{\rm LSR}$) are estimated relative to the local standard of rest (LSR).

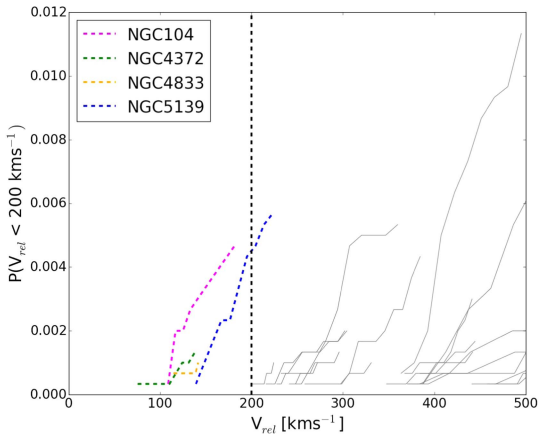

Figure 3. Cumulative probability distribution of the relative velocities ($V_{\rm rel}$) during close encounters between 2M16011638-1201525 and Galactic GCs from Moreno et al. (2014). The vertical dashed line shows the velocity threshold (200 km s^{-1}) adopted in this work.

4.1. A Dwarf Spheroidal (dSph) Galaxy Interloper?

Lind et al. (2015) argue that stars with low [Mg/Fe] ratios are commonly found in dSph galaxies. However, [Al/Fe] enhancement is not expected in these systems (see Koch & McWilliam 2008). Therefore, given the high Al enhancement and strongly depleted Mg observed in 2M16011638-1201525, we conclude that it seems unlikely that a merged and disrupted dSph galaxy could have hosted 2M16011638-1201525.

4.2. A Globular Cluster Escapee?

In order to study the ejection scenario of 2M16011638-1201525 from a not entirely disrupted GC into the Milky Way disk, we performed a kinematical analysis using Model 2 over a 2 Gyr period. It is based on a 3×10^5 Monte Carlo cluster and 2M16011638-1201525 orbits for a sample of 63 Galactic GCs with good proper motion measurements (see Moreno et al. 2014).

We assumed that 2M16011638-1201525 could have been ejected from a given GC, with a relative velocity below a certain threshold ($V_{\rm rel} < 200$ km s^{-1}), which may be possible in the interaction of black holes and/or binary systems (see Fernández-Trincado et al. 2015b). Then, we computed the cumulative probability distribution (see Figure 3) for the relative velocity ($V_{\rm rel}$), which is defined as the relative velocity during each close encounter, occurring at times $t < 2$ Gyr and within a distance less than or equal to the tidal radius of the GC ($\delta\ r < r_t$; Moreno et al. 2014). If a close past encounter is probable, then the GC could be identified as a possible progenitor of 2M16011638-1201525.

Our results suggest that our hypothesis of 2M16011638-1201525 being ejected from a given GC is negligible for 59 of the GCs and very small (<0.5%) for four GCs in our sample (see Figure 2): NGC 5139 (ω Cen), NGC 104 (47 Tucanae), NGC 4372, and NGC 4833.

Other parameters also disfavor the proposed hypothesis: 2M16011638-1201525 is metal-poor, [Fe/H] $= -1.30$ dex, with orbital parameters that reach a distance $|Z_{\rm max}| \sim 3$ kpc from the Galactic plane (see Figure 4), which are not consistent with the metallicity (Harris 1996) and orbital properties (Moreno et al. 2014) of three of the four clusters mentioned above: NGC 104 ([Fe/H] $= -0.72$ dex, $|Z_{\rm max}| \sim 3.13$ kpc), NGC 4372 ([Fe/H] $= -2.17$ dex, $|Z_{\rm max}| \sim 1.57$ kpc), and NGC 4833 ([Fe/H] $= -1.85$ dex, $|Z_{\rm max}| \sim 1.54$ kpc). Both NGC 4372 and NGC 4833 are more metal-poor than 2M16011638-1201525, while NGC 104 is more metal-rich—having a more Mg-rich population in particular (see Carretta et al. 2013)—than 2M16011638-1201525. Therefore, these 3 clusters are an unlikely origin for the star.

Our chemodynamical results show that among the more probable GC candidates associated with 2M16011638-1201525, NGC 5139 could be a possible progenitor system. This cluster is metal-poor, [Fe/H] $= -1.53$ dex (Harris 1996), and has an orbit that reaches a distance $|Z_{\rm max}| \sim 1.69$ kpc from the Galactic plane (Moreno et al. 2014). Additionally, NGC 5139 shows enrichment levels spanning ~ -1.8 dex to ~ -0.5 dex (e.g., Villanova et al. 2014 and references therein) and atypical light-element abundances with a pronounced Mg–Al anti-correlation (e.g., Norris & Da Costa 1995), like that seen in 2M16011638-1201525. From Figure 3, we conclude that this star could have been radially ejected in any direction from NGC 5139 (blue dashed line in Figure 3). 2M16011638-1201525 has a velocity greater than the cluster's escape velocity, i.e., $V_{\rm rel} > 60.4$ km s^{-1} (see Fernández-Trincado et al. 2015b and references therein), reaching a total energy (E) and angular momentum (Lz) from the ejection process slightly similar to those of NGC 5139. We note that 2M16011638-1201525 is moving on a retrograde orbit and has a specific angular momentum, $Lz = -307$ km s^{-1} kpc, similar to that of NGC 5139, i.e., $Lz = -342.5$ km s^{-1} kpc (see Moreno et al. 2014); this result could strengthen the association of this star with NGC 5139.

We emphasize that there is evidence which suggests NGC 5139 as a dominant contributor of retrograde stars and of stars with chemical anomalies generally found only within GCs (Altmann et al. 2005; Majewski et al. 2012; Fernández-Trincado et al. 2015c). These stellar debris and the newly discovered star strongly suggest that NGC 5139 was not formed on its present orbit and has been affected by frequent passages through the disk (e.g., Meza et al. 2005). Hence, much of the stellar debris claimed to be part of NGC 5139 follows orbital properties ($R_{\rm min}$, $R_{\rm max}$, $Z_{\rm max}$) slightly different from those of the host system.

We also highlight that 2M16011638-1201525 has halo-like radial velocity based on the kinematics predicted by the revised version of the Besançon Galaxy model (Robin et al. 2014), implying that this star could also be interpreted as a "halo interloper," especially given a retrograde motion and a peculiar chemical fingerprint that is consistent with the GC halo population.

4.3. A Galactic Bulge Interloper?

Schiavon et al. (2016) have recently discovered a new stellar population in the Galactic bulge (called the N-rich population), which clearly shows atypical light-element patterns, particularly elevated nitrogen abundance [N/Fe] > 1.0 dex. Such abundances are very different from what is seen in the normal stellar population of the Galactic bulge in the same spatial region (i.e., $|b| < 16°$, $-20° < l < 20°$, and 5 kpc $< d_\odot <$ 11 kpc).

We consider a possible scenario where 2M16011638-1201525 could be associated with this new stellar population,

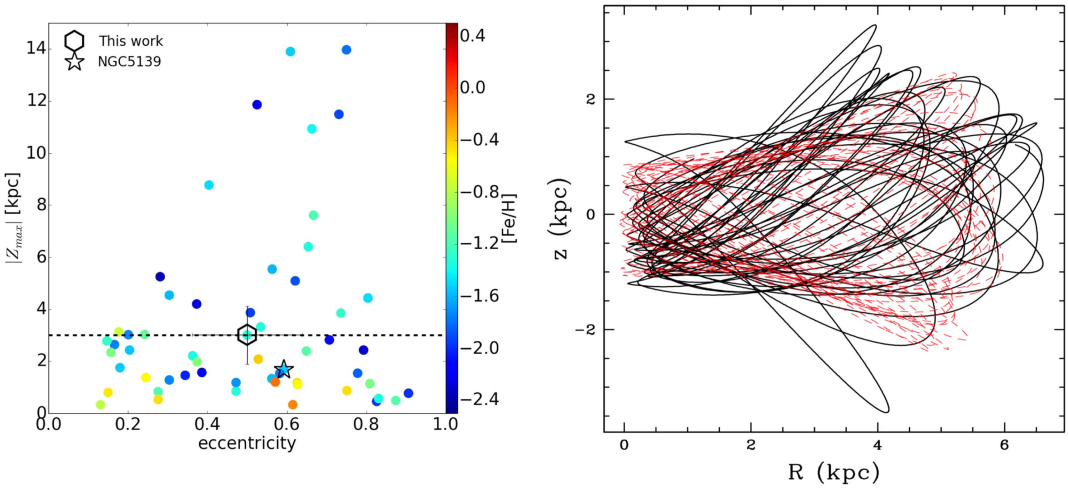

Figure 4. Left: maximum distance $|Z_{max}|$ from the Galactic plane as a function of the orbital eccentricity for 2M16011638-1201525 and 63 GC from Moreno et al. (2014). The open star symbol refers to NGC 5139. The horizontal black dashed line represents 3 kpc, the higher limit for the thick disc proposed by Carollo et al. (2010). Right: meridional orbit of 2M16011638-1201525 computed with Model 3 (black line) and Model 4 (red dashed line).

since this star shows nitrogen enhancement similar to that of Schiavon's sample, i.e., 2M16011638-1201525, like the N-rich population, has elevated nitrogen abundance, [N/Fe] = 1.46 dex (see Table 1). Interestingly, our orbital solutions show that 2M16011638-1201525 passes through the Galactic bulge at its closest approach to the Galactic center $R_{\rm min} \sim 0.62$ kpc and reaches a maximum distance from the Galactic center at $R_{\rm max} < 7.26$ kpc (see the orbit projection in Figure 4) in an eccentric orbit $e = 0.53$. Given its peculiar chemical fingerprint and orbital elements within the Galactic disk, this star could be interpreted as a N-rich bulge interloper. It is interesting to note that there are a handful of N-rich stars from Schiavon's sample with intermediate Al abundance and Mg enhancement (see Figure 1), making it difficult to chemically link this population with 2M16011638-1201525, which falls outside the main group of field stars and within the locus of the second-generation GC population. However, there is also one star from Schiavon's sample that has Al enhancement and a strongly depleted Mg abundance and is likely within the Al–Mg tail of the N-rich population. On the other hand, one might expect N-rich contaminants with extreme Al–Mg abundance ratios. However, given the kinematic and chemical properties of 2M16011638-1201525, a GC-like second-generation identification seems more probable.

5. CONCLUSIONS

We made use of high-resolution, near-IR spectra from the SDSS-III/APOGEE survey, and we discovered the existence of a star within the Milky Way disk with light-element anomalies associated with one of the most extreme combinations of Mg and Al anti-correlation, seen only in second-generation GC populations. Our orbital computations based on reliable six-dimensional phase-space coordinates of this peculiar giant star, 2M16011638-1201525, show that it travels through the Milky Way in a coplanar, eccentric orbit relatively close to the Galactic plane, which suggests that this star has been dynamically ejected into the Milky Way disk from the halo.

A more exotic explanation of such peculiar chemistry in a disk-like orbit star is that it could be chemically linked with the ω Cen progenitor system, from which it might have been ejected. However, ω Cen is a very complex and unusual stellar system in the Milky Way, and its origin is still not well understood (GC or dSph galaxy?). Other GC progenitor candidates might be examined with more detail in the near future, given the upcoming and more accurate six-dimensional phase-space data set that will be produced by the *Gaia* space mission.

The authors wish to thank the referee for their constructive comments, which significantly improved the presentation of this paper.

We thank UNAM-PAPIIT grants IN 105916 and IN 114114. JGF-T is currently supported by Centre National d'Etudes Spatiales through PhD grant 0101973 and Région de Franche-Comté and by the French Programme National de Cosmologie et Galaxies.

E.M., L.A.M.M., B.P., and A.P.V. acknowledge support from UNAM/PAPIIT grant IN 105916. D.A.G.H. was funded by Ramón y Cajal fellowship number RYC-2013-14182.

D.A.G.H. and O.Z. acknowledge support provided by the Spanish Ministry of Economy and Competitiveness under grant AYA-2014-58082-P.

S.R.M. and C.S. acknowledge support from NSF grants AST-1312863 and AST-1211585, respectively.

A.M. acknowledges support from Proyecto Interno UNAB DI-677-15/N.

D.G. and R.M. gratefully acknowledge support from the Chilean BASAL Centro de Excelencia en Astrofísica y Tecnologías Afines grant PFB-06/2007. Szabolcs Mészáros has been supported by the János Bolyai Research Scholarship of the Hungarian Academy of Sciences.

This research made use of *GravPot16* (Fortran version), a community-developed core under the git version-control system on GitHub. Monte Carlo simulations were executed on computers from Instituto de Astronomía-UNAM, México.

Funding for SDSS-III has been provided by the Alfred P. Sloan Foundation, the Participating Institutions, the National Science Foundation, and the U.S. Department of Energy, Office of Science. The SDSS-III web site is http://www.sdss3.org/.

SDSS-III is managed by the Astrophysical Research Consortium for the Participating Institutions of the SDSS-III Collaboration, including the University of Arizona, the Brazilian Participation Group, Brookhaven National Laboratory, Carnegie Mellon University, University of Florida, the French Participation Group, the German Participation Group, Harvard University, Instituto de Astrofisica de Canarias, the Michigan State/Notre Dame/JINA Participation Group, Johns Hopkins University, Lawrence Berkeley National Laboratory, Max Planck Institute for Astrophysics, Max Planck Institute for Extraterrestrial Physics, New Mexico State University, New York University, The Ohio State University, Pennsylvania State University, University of Portsmouth, Princeton University, the Spanish Participation Group, University of Tokyo, University of Utah, Vanderbilt University, University of Virginia, University of Washington, and Yale University.

REFERENCES

Allen, C., & Santillan, A. 1991, RMxAA, 22, 255
Altmann, M., Catelan, M., & Zoccali, M. 2005, A&A, 439, L5
Anguiano, B., De Silva, G. M., Freeman, K., et al. 2016, MNRAS, 457, 2078
Asplund, M., Grevesse, N., & Sauval, A. J. 2005, in ASP Conf. Ser. 336, Cosmic Abundances as Records of Stellar Evolution and Nucleosynthesis, ed. T. G. Barnes, III & F. N. Bash (San Francisco, CA: ASP), 25
Bastian, N., & Lardo, C. 2015, MNRAS, 453, 357
Blanco-Cuaresma, S., Soubiran, C., Heiter, U., & Jofré, P. 2014, A&A, 569, A111
Brooke, J. S. A., Bernath, P. F., Western, C. M., et al. 2016, JQSRT, 168, 142
Brunthaler, A., Reid, M. J., Menten, K. M., et al. 2011, AN, 332, 461
Carollo, D., Beers, T. C., Chiba, M., et al. 2010, ApJ, 712, 692
Carollo, D., Martell, S. L., Beers, T. C., & Freeman, K. C. 2013, ApJ, 769, 87
Carretta, E. 2013, A&A, 557, A128
Carretta, E., Bragaglia, A., Gratton, R., & Lucatello, S. 2009a, A&A, 505, 139
Carretta, E., Bragaglia, A., Gratton, R. G., et al. 2009b, A&A, 505, 117
Carretta, E., Bragaglia, A., Gratton, R. G., et al. 2010, A&A, 516, A55
Carretta, E., Bragaglia, A., Gratton, R. G., Lucatello, S., & D'Orazi, V. 2012, ApJL, 750, L14
Carretta, E., Gratton, R. G., Bragaglia, A., D'Orazi, V., & Lucatello, S. 2013, A&A, 550, A34
Eisenstein, D. J., Weinberg, D. H., Agol, E., et al. 2011, AJ, 142, 72
Fernández-Trincado, J. G., Vivas, A. K., Mateu, C. E., & Zinn, R. 2013, MmSAI, 84, 265
Fernández-Trincado, J. G., Robin, A. C., Bienaymé, O., et al. 2014, in EAS Publications Ser. 67 (Les Ulis: EDP Sciences), 369
Fernández-Trincado, J. G., Robin, A. C., & Reylé, C. 2015a, in Proc. Annual Meeting of the French Society of Astronomy and Astrophysics, SF2a-2015, ed. F. Martins et al. (Les Ulis: EDP Sciences), 15
Fernández-Trincado, J. G., Robin, A. C., Reylé, C., et al. 2016, MNRAS, 461, 1404
Fernández-Trincado, J. G., Robin, A. C., Vieira, K., et al. 2015c, A&A, 583, A76
Fernández-Trincado, J. G., Vivas, A. K., Mateu, C. E., et al. 2015b, A&A, 574, A15
Gaia Collaboration, Prusti, T., de Bruijne, J. H. J., et al. 2016, A&A, 595, A1
García Pérez, A. E., Allende Prieto, C., Holtzman, J. A., et al. 2015, ApJ, 151, 6
González Hernández, J. I., & Bonifacio, P. 2009, A&A, 497, 497
Gratton, R. G., Carretta, E., & Bragaglia, A. 2012, A&ARv, 20, 50
Gunn, J. E., Siegmund, W. A., Mannery, E. J., et al. 2006, AJ, 131, 2332
Gustafsson, B., Edvardsson, B., Eriksson, K., et al. 2008, A&A, 486, 951
Harris, W. E. 1996, AJ, 112, 1487
Hawkins, K., Masseron, T., Jofre, P., et al. 2016, A&A, 594, 43
Hayden, M. R., Holtzman, J. A., Bovy, J., et al. 2014, AJ, 147, 116
Holtzman, J. A., Shetrone, M., Johnson, J. A., et al. 2015, AJ, 150, 148
Johnson, C. I., Kraft, R. P., Pilachowski, C. A., et al. 2005, PASP, 117, 1308
Koch, A., & McWilliam, A. 2008, AJ, 135, 1551
Kordopatis, G., Gilmore, G., Steinmetz, M., et al. 2013, AJ, 146, 134
Kurucz, R. L. 2005, MSAIS, 8, 14
Lind, K., Koposov, S. E., Battistini, C., et al. 2015, A&A, 575, L12
Majewski, S. R., Nidever, D. L., Smith, V. V., et al. 2012, ApJL, 747, L37
Majewski, S. R., Schiavon, R. P., Frinchaboy, P. M., et al. 2016, AN, 337, 863
Majewski, S. R., Zasowski, G., & Nidever, D. L. 2011, ApJ, 739, 25
Marino, A. F., Villanova, S., Piotto, G., et al. 2008, A&A, 490, 625
Martell, S. L., & Grebel, E. K. 2010, A&A, 519, A14
Martell, S. L., Shetrone, M. D., Lucatello, S., et al. 2016, ApJ, 825, 146
Martell, S. L., Smolinski, J. P., Beers, T. C., & Grebel, E. K. 2011, A&A, 534, A136
Mészáros, S., Martell, S. L., Shetrone, M., et al. 2015, AJ, 149, 153
Meza, A., Navarro, J. F., Abadi, M. G., & Steinmetz, M. 2005, MNRAS, 359, 93
Moreno, E., Pichardo, B., & Velázquez, H. 2014, ApJ, 793, 110
Nidever, D. L., Holtzman, J. A., Allende Prieto, C., et al. 2015, AJ, 150, 173
Norris, J. E., & Da Costa, G. S. 1995, ApJL, 441, L81
Pichardo, B., Martos, M., & Moreno, E. 2004, ApJ, 609, 144
Pichardo, B., Martos, M., Moreno, E., & Espresate, J. 2003, ApJ, 582, 230
Ramírez, I., Meléndez, J., & Chanamé, J. 2012, ApJ, 757, 164
Robin, A. C., Marshall, D. J., Schultheis, M., & Reylé, C. 2012, A&A, 538, A106
Robin, A. C., Reylé, C., Derrière, S., & Picaud, S. 2003, A&A, 409, 523
Robin, A. C., Reylé, C., Fliri, J., et al. 2014, A&A, 569, A13
Schiavon, P. R., Zamora, O., Lucatello, S., et al. 2016, MNRAS, submitted (arXiv:1611.03086)
Schönrich, R., Binney, J., & Dehnen, W. 2010, MNRAS, 403, 1829
Sneden, C. 1973, ApJ, 184, 839
Sneden, C., Kraft, R. P., Guhathakurta, P., Peterson, R. C., & Fulbright, J. P. 2004, AJ, 127, 2162
Ventura, P., Carini, R., & D'Antona, F. 2011, MNRAS, 415, 3865
Vickers, J. J., Röser, S., & Grebel, E. K. 2016, AJ, 151, 99
Villanova, S., Geisler, D., Gratton, R. G., & Cassisi, S. 2014, ApJ, 791, 107
Wylie-de Boer, E., Freeman, K., Williams, M., et al. 2012, ApJ, 755, 35
Zacharias, N., Finch, C. T., Girard, T. M., et al. 2013, AJ, 145, 44
Zamora, O., García-Hernández, D. A., Allende Prieto, C., et al. 2015, AJ, 149, 181
Zasowski, G., Johnson, J. A., Frinchaboy, P. M., et al. 2013, AJ, 146, 81

Chapter 9

Conclusions & Perspectives

We have presented a steady-state Milky Way gravitational potential model (the so called *GravPot16* model), observationally and dynamically constrained. We built up the *GravPot16* model based on locally self-consistent dynamical constraints with the density profiles, thanks to the unique combination of Synthetic Stellar Populations (Robin et al., 2003, 2012, 2014) and observational data. The significant constraint that we consider in the determination of our model is the disk scale heights and the physical parameters of the local dark matter component. This work has also provided several successful outcomes to assess that our model is able to give results consistent with the literature. We explore simple test particle simulations for a variety of initial conditions belonging to seven age-bin disk components (e.g., Robin et al., 2003, 2014) and a component associated with a Hernquist stellar halo (see Robin et al., 2014), this set of particles attempt to mimic stars with different kinematic conditions. An important aspect of our method is the use of initial conditions restricted to locally self-consistent recipes, but are not fully consistent globally, which are slightly relaxed before turning on the non-axisymmetric potential, and it turns out to be pretty much stable for the time-scales over which we have integrated it, but this does not mean it is truly in equilibrium. It will be interesting also to check whether giving mass to our test-particles could allow to close the loop and reproduce the bar potential that we have used in the first place. The same for the densities of the disks in general, where this would need to regenerate the potential if the disks thicken that apparently does happen, this has been postponed for a future study. This simple methodology has allowed us to evaluate the role of a realistic non-axisymmetric bulge structure on the kinematics of each stellar sub-component which inherit information of both density-potential pair, with the significant advantage of reproducing several observational kinematic behaviours. Our conclusions can be summarized in the following way:

1. Throughout this study, we have taken advantage of the *GravPot16* model which is a specific model for galactic dynamics that fits fairly well several observational characteristics of the Milky Way, including the perpendicular force (K_Z) at 1.1 kpc as predicted in Bovy & Rix (2013), as well as the overall rotation curve from observations of H_I and CO gas from the compilation of Sofue (2015). However, as it can be noted in the §3, the construction of the overall gravitational potential and the field forces are based in a combination of semi-analytic expressions. Although some mathematical forms can be numerically resolved. This complicated mathematical

approach is very expensive computationally, and does not produce exact solutions which can be important at the scale of <1 **parsec**. Concerning the inner thin disk, given the complicated mathematical expressions of the gravitational potential, we have favored a "spherical hole" following Robin et al. (2003) which is more simple to compute numerically. In Robin et al. (2014) a "cylindrical hole" symmetry was employed towards the inner regions of the Milky Way to fit the density profile of the thin disk using SDSS data, but there was no significant difference in the fit with regards to the "spherical hole". The geometric difference appears only in a specific region of the bulge, at short distances from the Galactic center and out-of the plane. This new geometry could play an important role in the configuration and orbital structure of the inner region (< 0.5 kpc). However, definitive evidence for a "cylindrical" and/or "spherical" hole in the inner thin disk remains elusive to date, and only few studies seem to support the presence of a hole in the inner disk (see Matsunaga et al., 2016).

2. Simple controlled simulations of massless particles were performed under the *GravPot16* model developed in this thesis. With this procedure, we have obtained the final velocity distributions, wich fit fairly well the overall kinematics of the Galactic bulge. Several bar potential models were employed, varing the main physical parameters of the bar (pattern speed, Ω_{bar}, mass, and angle orientation, α_{bar}) in order to produce dynamical constrains of these parameters. All our considerations suggest that at least the mass of the Galactic bar suggested by Robin et al. (2012) and estimated to be of the order of 0.63×10^{10} $M_{\odot}$ is underestimated. Our dynamical approach suggests that a mass of the order of almost twice (1.7 to 2.6 times) can reproduce fairly well the overall global kinematic characteristics of the Milky Way bulge. On the other hands, there is a clear tension between models and interpretations in the literature concerning to the pattern speed of the bar, that suggests that a fast and/or slow rotating bar can reproduce the kinematic behaviour towards the Galactic bulge and/or the local stellar velocity space (e.g., Monari et al., 2017a,b; Portail et al., 2017; Pérez-Villegas et al., 2017b). In this work we find, that a bar pattern speed of 35 km s^{-1} kpc^{-1} (slow rotating bar) with a corotation radius around ∼6.5 kpc may fits fairly well the BRAVA data, with a minimum value of $\chi^2 = 2.05$ for our best fit to data. However, we note also from visual examination that a bar with a pattern speed of 55 km s^{-1} kpc^{-1} (fast rotating bar) with corotation around ∼4.5 kpc gives an acceptable fit to the BRAVA data with a worse χ^2 of 2.37. We conclude that these parameters are clearly degenerated, and more strict constrains are needed to discriminate these parameters. For example, combined interpretation of local stellar velocity space with the bulge kinematic trends and its relation with the spiral arms plus the Galactic bar plus variations of the geometry of dark matter component can help to alleviate this tension, this study is postponed to future work. We also find that the best-fitting model for the orientation of the semi-major axis of the bar for the present-day is no less than 20° in good agreement with the literature (Freudenreich, 1998), this value is ∼ 7° larger that the value found by Robin et al. (2012), however, this result is still controversial. Lastly, through this work we have favored the bar parameters $\omega_{bar} = 35$ km s^{-1} kpc^{-1}, $\alpha_{bar} = 20°$, and $M_{\rm bar} = 1.1 \times 10^{10}$ $M_{\odot}$,

which produces a smaller value of χ^2 fitting the BRAVA dataset than other models. We find that our conclusions are unchanged for the second best-fitting model, with $\omega_{bar} = 55$ km s^{-1} kpc^{-1}, $\alpha_{bar} = 20°$, and $M_{bar} = 1.6 \times 10^{10}$ $M_\odot$.

3. An important result of the study, which will be considered in a future work, is that our simulation methodology predicts that an additional mass component need to be invoked in the inner region of the Milky Way to fit the global trends observed in the nuclear region of the bulge (within ~ 1.5 kpc). Indeed, the Galactic bulge of our model is made up primarily of a massive "boxy/peanut" bar structure plus the contribution of other Galactic components belonging to the disk, stellar halo, interstellar matter, and dark matter, which are essentially the same Galactic components employed by the Besançon Galaxy model (Robin et al., 2003, 2012, 2014). However, we find that these components by themselves are not enough to reproduce the velocity dispersion profile as observed in the BRAVA dataset at low Galactic latitude ($|b| < 4°$).

4. In a first order, the simulations presented in this thesis, predicts the radial velocity dispersion, $\sigma_R(r_{gal})$ as a function of the galactocentric radius before and after the adiabatic growth of the Galactic bar within the potential. We find that the predicted $\sigma_R(r_{gal})$ stays similar to the imposed initial conditions at large Galactocentric distances ($r_{gal} > 4$ kpc) for the five sub-components of the thin disk, which differs in the inner region, given that the Besançon Galaxy model assumes a non realistic kinematics trend toward the Galactic bulge, this have been improved from our dynamical approach, we find the analytical expressions, the best set of parameters that reproduce the kinematic trends $\sigma_R(r_{gal})$ as function of the galactocentric radius (see Eqn. §4.5). Noticeable perturbations of the bar are observed along different galactocentric radius for the two thick disk components, which are kinematically warmer. While the stellar halo being a Galactic component kinematically hotter produces significant trends as consequence of the perturbations of the Galactic bar. In Figure 4.4 we clearly see that a stellar halo initially not rotating, exhibit a rotation not null due to the influence of the bar in the system. This effect produces relevant changes in the geometry of the density profile of the stellar halo as seen in §8. In Eqn. §4.4 we find the best set of parameters (vertical gradient, $\frac{d\sigma_Z}{dR}$, and the local vertical velocity dispersions, $\sigma_Z^{\odot}$) to set the vertical velocity dispersion as a function of the galactocentric radius in the Besançon Galaxy model as predicted from our barred model.

5. In §6 we confirm that the stellar halo is ellipsoidal in the inner region of the Milky Way and becomes oblate in the outer parts, it was first noted by Pérez-Villegas et al. (2017a) from the interpretation of N-body simulations. We find that an important fraction ($\sim 22\%$) of the particles in the inner Milky Way participate in the bar structure, this implies that we could expect some relevant metal poor stars streaming into the bar potential. It is important to note, that the initial conditions associated with the stellar halo has not been thought through in depth, and there is thus no reason for this stellar halo to be in true equilibrium, however, it turns out to be pretty much stable for the time-scales over which we integrated it.

6. In §7 we identify a midplane structure surrounding the Galactic bar with kinematic properties strikingly similar to those observed in the APOGEE commissioning data by Nidever et al. (2012). This indicates that the high V_{los} feature found in the region of the Milky Way bulge are a natural consequence of stars not associated with the Galactic bar.

9.1 Perspectives

In this work we have developed useful tools, methods and techniques that will allow the analysis and interpretations of many spectroscopic and astrometric surveys, including Gaia in the near future. We have also derived new fits to the vertical and radial velocity dispersions from test particle simulations using a barred model. These new parameters are useful to be implemented into the Besançon Galaxy model to set the kinematics of the model (radial velocity, and proper motions), taking into account the density-potential pair (where the non-axisymmetries are implicitly included), and particularly to be used for the interpretation of the Milky Way bulge observations. These implementations are being done in the new versions of the Besançon Galaxy model, and deeper analysis taking into account the appropriate selection function should be done. The comparisons of our kinematic predictions with other large spectroscopic surveys (APOGEE, Gaia-ESO, GIBS, ARGOS, etc) and particularly with APOGEE South (APOGEE-2/SDSS-IV) in the near future, would allow to examine for example the presence/absence of high$-V_{los}$ feature towards the Galactic bulge.

We will investigate and characterize the nature of the additional component needed in the inner region of the Galactic bulge to reproduce the velocity dispersion profiles. Several simulations are in process to get more information about this component.

In the future we plan to investigate more in detail the effect of the bar in the solar neighbourhood, to compare the velocity fields and the known streams (Famaey et al., 2005) with our model. For this aspect it will be necessary to produce test particle simulations with a higher number of particles to get the required spatial resolution. This study could be extended to the wide solar neighbourhood for which Gaia will provide accurate parallaxes and proper motions in 2018 in its next data release.

Appendix A

Density profiles

A.1 Thin disk

A.1.1 Young thin disk, Age $<$ 0.15 Gyr

$$\rho(r_{gal}, z_{gal}) = C_{thin_{Age<0.15}} \times \left[\exp(-(a/h_{R+})^2) - \exp(-(a/h_{R-})^2)\right] \tag{A.1}$$

where $a^2 = \mathrm{r}_{\mathrm{gal}}^2 + \frac{Z^2}{\epsilon^2}$, $\epsilon = \sqrt{1-e^2}$ is the ellipticity and eccentricity of an ellipsoid obtained from dynamics considerations (see §1), $C_{thin_{Age<0.15}}$ is the normalization constant associated with the local density $\rho_{\odot}$, and $h_{R+} = 5$ kpc and $h_{R-} = 3$ kpc, are the scale lengths, and h_{R-} define a spherically symmetric hole in the inner disk. It is important to note that the geometry of such a hole in the inner disk was not studied in detail in this work, it was assumed to be spherically symmetric following Robin et al. (2003). A new parametrization has been recently presented by Robin et al. (2014) for a cylindrical hole. To date it still remains quite very uncertain, and its existence seems to be supported by recent observations, i.e, a recent lack of classical Cepheids in the inner part of the Galactic disk was identify by Matsunaga et al. (2016).

A.1.2 Thin disk, Age $>$ 0.15 Gyr

$$\rho(r_{gal}, z_{gal}) = C_{thin_{Age>0.15}} \times \left[\exp(-(0.5 + a/h_{R+})^2) - \exp(-(0.5 + a/h_{R-})^2)\right] \tag{A.2}$$

a is similar to Eq. A.1, and $h_{R+} = 2.17$ kpc and $h_{R-} = 1.33$ kpc.

A.2 Thick disk

The thick disk parametrization is taken from Robin et al. (2014) and is given by the following density profiles

A.2.1 Young thick disk, Age $\sim$ 10 Gyr

$$\rho(r_{gal}, z_{gal}) \approx C_{thick_{Age\sim10}} \times sech^2(|Z|/2h_Z) \times (-(\mathrm{r_{gal}} - 8)/h_{r_{gal}}) \tag{A.3}$$

where $h_Z = 0.345$ kpc and $h_{r_{gal}} = 2.040$ kpc, are the scale height and scale length, respectively. $C_{thick_{Age\sim10}}$ is the local normalization constant.

A.2.2 Old thick disk, Age $\sim$ 12 Gyr

$$\rho(r_{gal}, z_{gal}) \approx C_{thick_{Age\sim12}} \times sech^2(|Z|/2h_Z) \times (-(\mathrm{r_{gal}} - 8)/h_{r_{gal}}) \tag{A.4}$$

where $h_Z = 0.795$ kpc and $h_{r_{gal}} = 2.919$ kpc, are the scale height and scale length, respectively. $C_{thick_{Age\sim12}}$ is the local normalization constant.

In the computation of the potential the Eqn. A.3 and Eqn. A.4 have been approximated by the sum of three Miyamoto-Nagai disks (see Smith et al., 2015). This approach has been employed in this work due to the complicated forms of the gravitational potential model, in order to reduce the computing time. For the computations in this work, we have adopted the following mass: $M_{Age\sim10} = 7.38 \times 10^9$ $\mathrm{M_\odot}$ and $M_{Age\sim12} = 1.33 \times 10^9$ $\mathrm{M_\odot}$.

A.3 The Interstellar Matter (ISM)

$$\rho(r_{gal}, z_{gal}) \approx C_{ISM} \times \exp\left(-\frac{\mathrm{r_{gal}} - \mathrm{R_\odot}}{h_R}\right) \times \exp\left(-\frac{Z}{h_Z}\right) \tag{A.5}$$

where $h_Z = 0.14$ kpc and $h_{r_{gal}} = 5.0$ kpc, are the scale height and scale length of the ISM, respectively. For the computations in this work, we have adopted the following mass, $M_{ISM} = 4.95 \times 10^9$ $\mathrm{M_\odot}$.

A.4 Stellar halo

The density profiles of the stellar halo follow the Hernquist model presented in (Robin et al., 2014), repeated here to guide the reader

$$\rho(r_{gal}, z_{gal}) = C_{stellarhalo} \times \frac{1}{R_a \times (R_a + R_{core})^n} \tag{A.6}$$

where $R_a^2 = \mathrm{r}_{\mathrm{gal}}^2 + (\frac{\mathrm{Z}}{\mathrm{q}})^2$, $R_{core} = 2.1$ kpc, $n = 2.1$, and $q \sim 0.77$, see discussion about variations of the axis ratio q in presence of the Galactic bar in §6. In the Besançon stellar population model the mass of the stellar halo is estimated to be $M_{stellar-halo} \sim 0.264 \times 10^9$ $\mathrm{M}_{\odot}$.

A.5 The boxy/peanut bar

The Galactic bar is an approximation to the model presented in Robin et al. (2012) and have the following mass density distribution:

$$\rho(X, Y, Z) = C_{bar} \times sech^2(R_s) \tag{A.7}$$

$$R_s^{C_{||}} = \left[\left| \frac{X}{X_0} \right|^{C_\perp} + \left| \frac{Y}{Y_0} \right|^{C_\perp} \right]^{C_{||}/C_\perp} + \left| \frac{Z}{Z_0} \right|^{C_{||}} \tag{A.8}$$

where the exponents $C_{||} = 3.007$, $C_\perp = 3.329$, and $X_0 = 1.46$, $Y_0 = 0.49$, and $Z_0 = 0.39$ are the scale lengths of the Galactic bar as presented by (Robin et al., 2012). The mass, pattern speed and angle orientation are derived in this work from dynamical constraints (see §5). Notice that in this thesis new constraints for the main physical parameters of the Galactic bar were presented in §5.

A.6 The dark matter

The dark matter component is the symmetrically spherical component used in the Besançon Galaxy model. This component is fitted to the observed rotation curve (from measurement of CO and HI gas) from Sofue (2015) at large galacticentric radii. The parameters are sensibly different from Robin et al. (2003) who used different observational

constraints for the rotation curve and did not account for the non-axisymmetric components. These variations are listed in Table A.1 for the three bar models considered in §5.

$$\rho(r_{gal}, z_{gal}) = C_{darkmatter} \times \frac{1}{1 + (r_{gal}^2 + Z^2)/R_{dm}^2} \tag{A.9}$$

where R_{dm} is the core radius, and $C_{darkmatter}$ is the central mass density distribution.

Table A.1: Dark matter parameters after fitting the rotation curve and assuming different bar mass.

Bar mass	$C_{darkmatter}$ $M_\odot/pc^3$	R_{dm} kpc
0.63×10^{10} $M_\odot$	0.5011	1.32
1.10×10^{10} $M_\odot$	0.2974	1.72
1.60×10^{10} $M_\odot$	0.1816	2.20

Appendix B

Reference systems

The particles and stars analyzed in this thesis follow the system of equations presented below. The non-inertial reference frame is defined where the bar is at rest and the bar rotation is in the clockwise direction.

All the computations presented in this thesis were done using the Runge-Kutta algorithm of seventh-eight order of Fehlberg (1968).

B.1 Galactic system

The system of equations B.1 - B.5 are employed in our programs to transfom the observations (α, δ, l, b, μ_l, μ_b, heliocentric distance d_{hel}, line-of-sight velocity V_{los})$\rightarrow$ ($X_{in}, Y_{in}, Z_{in}, Vx_{in}, Vy_{in}, Vz_{in}$) generally given in the inertial reference frame to the non-inertial reference frame, and viceversa (Eqns. B.6 - B.9). V_l, and V_b are computed using the transformation of the equatorial proper motion to the Galactic system from (Poleski, 2013), and X_{in}, Y_{in}, Z_{in} are computed as follow,

$$X_{in} = R_{\odot} - d_{hel} \times \cos(l) \times \cos(b) \tag{B.1}$$

$$Y_{in} = -d_{hel} \times \sin(l) \times \cos(b) \tag{B.2}$$

$$Z_{in} = d_{hel} \times \sin(b) \tag{B.3}$$

where d_{hel} is the heliocentric distance, the Sun is assumed (X, Y, Z)=$(0, 8, 0)$ kpc, l and

b the Galactic latitude and Galactic longitude, respectively.

For $Vx_{in}, Vy_{in}, Vz_{in}$ we employ the following expresions from Bond et al. (2010),

$$Vx_{in} = -V_{los} \times \cos(l) \times \cos(b) + V_b \times \cos(l) \times \sin(b) + V_l \times \sin(l) - U_\odot \tag{B.4}$$

$$Vx_{in} = -V_{los} \times \sin(l) \times \cos(b) + V_b \times \sin(l) \times \sin(b) - V_l \times \cos(l) - V_\odot - V_{lsr} \tag{B.5}$$

$$Vz_{in} = V_{los} \times \sin(b) + V_b \times \cos(b) + W_\odot \tag{B.6}$$

where $(U_\odot), (V_\odot), (W_\odot) = (11.1, 12.24, 7.25)$ km s^{-1} (Brunthaler et al., 2011), and $V_{lsr} = 244.5$ km s^{-1} (this work).

B.2 Inertial to Non-intertial reference system

$$\alpha(t) = \alpha_{bar} - \Omega_{bar} t \tag{B.7}$$

$$X_{non} = X_{in} cos(\alpha(t)) - Y_{in} sin(\alpha(t)) \tag{B.8}$$

$$Y_{non} = X_{in} sin(\alpha(t)) + Y_{in} cos(\alpha(t)) \tag{B.9}$$

$$Vx_{non} = (Vx_{in} + Y_{in}\Omega_{bar}) cos(\alpha(t)) - (Vy_{in} - X_{in}\Omega_{bar}) sin(\alpha(t)) \tag{B.10}$$

$$Vy_{non} = (Vx_{in} + Y_{in}\Omega_{bar}) sin(\alpha(t)) + (Vy_{in} - X_{in}\Omega_{bar}) cos(\alpha(t)) \tag{B.11}$$

where Ω_{bar} is the pattern speed of the Galactic bar.

B.3 Non-inertial to intertial reference system

$$X_{in} = X_{non}cos(\alpha(t)) + Y_{non}sin(\alpha(t)) \tag{B.12}$$

$$Y_{in} = -X_{non}sin(\alpha(t)) + Y_{non}cos(\alpha(t)) \tag{B.13}$$

$$Vx_{in} = (Vx_{non} - Y_{non}\Omega_{bar})cos(\alpha(t)) + (Vy_{non} + X_{non}\Omega_{bar})sin(\alpha(t)) \tag{B.14}$$

$$Vy_{in} = (Vx_{non} - Y_{non}\Omega_{bar})sin(\alpha(t)) + (Vy_{non} + X_{non}\Omega_{bar})cos(\alpha(t)) \tag{B.15}$$

B.4 Motion equations

The corresponding equations of motion (Pichardo, 2003) are:

$$\frac{d^2X}{dt^2} = \frac{\partial\Phi_{axi}}{\partial X} + \frac{\partial\Phi_{non-axi}}{\partial X} + 2\Omega_{bar}\frac{dX}{dt} + \Omega_{bar}^2 X \tag{B.16}$$

$$\frac{d^2Y}{dt^2} = \frac{\partial\Phi_{axi}}{\partial Y} + \frac{\partial\Phi_{non-axi}}{\partial Y} + 2\Omega_{bar}\frac{dY}{dt} + \Omega_{bar}^2 Y \tag{B.17}$$

$$\frac{d^2Z}{dt^2} = \frac{\partial\Phi_{axi}}{\partial Z} + \frac{\partial\Phi_{non-axi}}{\partial Z} \tag{B.18}$$

B.5 Jacobi integral

We calculate the Jacobi integral E_J (Binney & Tremaine, 1994) as:

$$E_J = \frac{1}{2}\vec{v}^2 + \Phi_{axi} + \Phi_{non-axi} - \frac{1}{2}|\vec{\Omega}_{bar} \times \vec{R}|^2 \tag{B.19}$$

Throughout thi work, E_J is given in 10^2 km^2 s^{-2}.

B.6 Orbital energy

We calculate the orbital energy E per unit mass as:

$$E = \frac{1}{2}\vec{v}^2 + \Phi_{axi} + \Phi_{non-axi} \tag{B.20}$$

We call E_{min}, and E_{max} the minimum and maximum values of E, and the characteristic orbital energy $(E_{min} + E_{max})/2$ as defined in (Moreno et al., 2015). The orbital energy is given in 10^2 km^2 s^{-2}.

B.7 The Jacobi constant

The Jacobi constant (see Pichardo et al., 2004) is defined as:

$$C_J \approx |(E_J^{initial} - E_J^{end})/E_J^{initial}| \tag{B.21}$$

Throughout this work, the Jacobi constant is conserved within a relative variation better than $C_J \approx 10^{-12}$.

Appendix C

Globular cluster orbits

Figure C.1 display the meridional orbital projection for 63 Galactic globular clusters listed in Moreno et al. (2014) with high quality information available in the literature. The sample of globular clusters have been selected from the late compilation of cluster properties given by (Harris, 2010). The globular clusters are integrated in time from $t = 0$ to $t = 2$ Gyr (t corresponds to a forward time integration), conserving the Jacobi integral (E_J) within a relative variation $\sim 10^{-11}$. The best set of parameters described in §5 was used by the **Model 2** (see §3) to produce the orbital elements. The main orbital parameters derived from our best barred Milky Way model are listed in Table C.1.

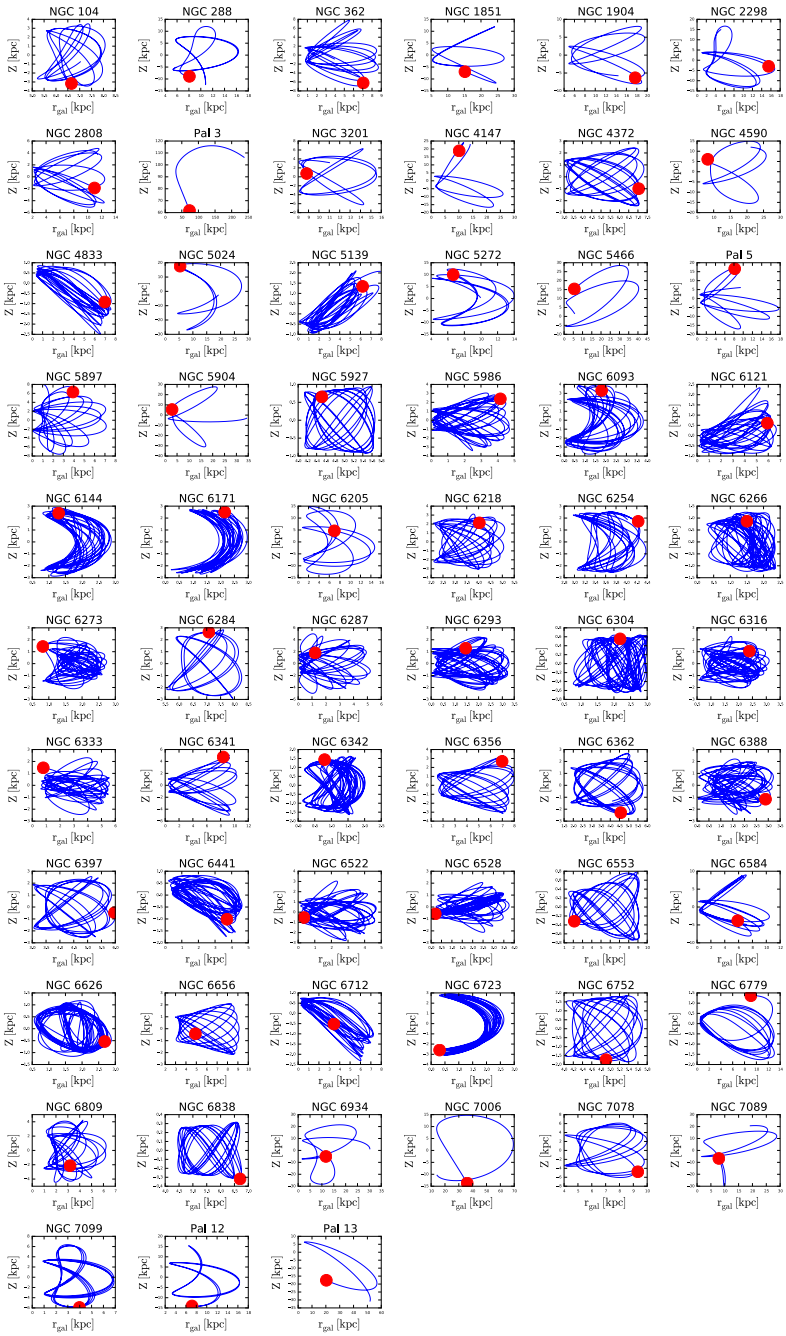

Figure C.1: Orbital projection on the Galactic plane $r_{gal} - Z$ for 63 globular clusters listed in Moreno et al. (2014). The red symbol indicate the initial position of the cluster before integration.

Table C.1: Main orbital parameters for 63 globular clusters orbiting the Milky Way. The integration of the motion equations is done with the GravPot16 model (see text), adopting the best set of bar parameters that fit fairly well the global kinematic trends in the Galactic bulge (see 4). This table lists the main orbital parameters: minimum Galactocentric distance r_{min} (column 2), maximum Galactocentric distance (column 3), maximum height from the plane (column 4), eccentricity defined as $e = (r_{max} - r_{min})/(r_{max} + r_{min})$ (column 5), minimum orbital energy, E_{min} (column 6), maximum orbital energy, E_{max} (column 7), and the orbital Jacobi constant, E_J (column 8).

Ids	r_{min} kpc	r_{max} kpc	Z_{max} kpc	e	E_{min} 100 km^2 s^{-2}	E_{max} 100 km^2 s^{-2}	E_J 100 km^2 s^{-2}
NGC 104	5.171	9.453	3.968	0.292	-1773.61	-1704.04	-2532.68
NGC 288	5.082	16.582	12.632	0.530	-1455.04	-1447.12	-2338.29
NGC 362	0.124	10.298	10.162	0.976	-1991.74	-1749.38	-1721.91
NGC 1851	5.320	27.562	12.257	0.676	-1275.21	-1262.50	-2453.36
NGC 1904	4.877	19.521	8.086	0.600	-1450.76	-1400.75	-2452.22
NGC 2298	1.046	17.795	16.847	0.888	-1509.77	-1478.26	-1264.61
NGC 2808	1.961	12.952	4.163	0.736	-1784.05	-1560.94	-2182.16
Pal 3	32.15	384.432	116.072	0.845	43.28	43.28	-6289.78
NGC 3201	7.957	15.717	6.352	0.327	-1454.62	-1451.82	-129.078
NGC 4147	1.092	24.274	24.147	0.913	-1349.90	-1306.34	-1605.64
NGC 4372	2.696	7.313	2.744	0.461	-2024.95	-1858.96	-2442.22
NGC 4590	6.803	26.817	17.360	0.595	-1249.08	-1237.89	-2573.44
NGC 4833	0.401	8.383	3.670	0.908	-2123.52	-1733.88	-2147.90
NGC 5024	4.376	27.674	27.096	0.726	-1159.61	-1159.35	-1861.40
NGC 5139	0.481	7.098	2.950	0.872	-2225.67	-1891.87	-1907.52
NGC 5272	4.168	14.183	12.799	0.545	-1472.59	-1470.90	-2096.18
NGC 5466	0.868	40.642	42.558	0.958	-1068.88	-1057.28	-842.403
Pal 5	0.665	18.142	18.037	0.929	-1563.60	-1337.05	-1336.55
NGC 5897	0.038	8.283	8.205	0.990	-2002.23	-1689.40	-1953.25
NGC 5904	1.167	34.084	31.162	0.933	-1207.03	-1166.15	-1471.87
NGC 5927	2.532	5.636	0.927	0.379	-2308.82	-1972.21	-2573.85
NGC 5986	0.024	6.275	3.922	0.992	-2459.21	-1942.10	-2208.46
NGC 6093	0.236	5.963	4.750	0.923	-2302.57	-1922.68	-2273.92
NGC 6121	0.036	5.919	2.892	0.987	-2510.13	-2090.51	-2172.97
NGC 6144	0.059	4.680	4.439	0.974	-2445.93	-2030.96	-2189.25
NGC 6171	0.571	3.957	2.662	0.747	-2462.20	-2065.37	-2431.31
NGC 6205	0.803	14.965	15.234	0.898	-1520.72	-1515.96	-1373.82
NGC 6218	0.830	6.075	3.308	0.759	-2399.73	-1934.39	-2411.07
NGC 6254	1.804	5.479	2.913	0.504	-2362.49	-1937.05	-2461.84
NGC 6266	0.406	2.565	1.167	0.726	-2698.10	-2309.36	-2676.24
NGC 6273	0.758	2.469	1.986	0.529	-2599.88	-2299.04	-2327.98
NGC 6284	5.353	9.646	3.238	0.286	-1782.58	-1691.32	-2575.39

Table C.2: Continued

Ids	r_{min} kpc	r_{max} kpc	Z_{max} kpc	e	E_{min} 100 km^2 s^{-2}	E_{max} 100 km^2 s^{-2}	E_J 100 km^2 s^{-2}
NGC 6287	0.089	5.778	5.462	0.969	-2248.03	-1937.25	-2155.89
NGC 6293	0.011	3.381	2.835	0.992	-2553.88	-2272.51	-2408.40
NGC 6304	0.942	2.944	0.603	0.514	-2722.89	-2245.96	-2690.90
NGC 6316	0.224	4.296	1.697	0.900	-2650.31	-2186.87	-2303.95
NGC 6333	0.041	4.138	3.261	0.980	-2484.31	-2057.16	-2358.98
NGC 6341	0.044	9.906	5.066	0.991	-2017.40	-1707.77	-1956.17
NGC 6342	0.004	2.477	1.585	0.995	-2782.36	-2348.23	-2626.44
NGC 6356	1.605	8.646	4.087	0.686	-2087.82	-1780.31	-2272.77
NGC 6362	0.843	7.194	2.465	0.790	-2380.40	-1945.25	-2398.04
NGC 6388	0.144	4.005	1.948	0.930	-2626.89	-2231.35	-2352.98
NGC 6397	3.043	6.802	2.429	0.381	-2013.84	-1914.45	-2473.32
NGC 6441	0.013	4.532	2.445	0.994	-2572.70	-2150.15	-2342.07
NGC 6522	0.052	3.602	2.690	0.971	-2549.91	-2158.30	-2439.76
NGC 6528	0.021	3.715	2.211	0.988	-2660.87	-2109.65	-2531.37
NGC 6553	1.651	8.413	0.766	0.671	-2180.14	-1760.14	-2368.39
NGC 6584	0.465	11.161	10.257	0.919	-1903.50	-1568.07	-1857.04
NGC 6626	0.034	2.681	1.463	0.974	-2734.94	-2309.31	-2641.92
NGC 6656	2.652	8.842	2.134	0.538	-1943.85	-1802.21	-2413.21
NGC 6712	0.019	6.466	2.744	0.993	-2310.47	-2031.29	-2121.13
NGC 6723	0.040	5.139	4.242	0.984	-2444.88	-1958.89	-2248.25
NGC 6752	4.032	6.250	2.003	0.215	-1956.40	-1900.82	-2540.40
NGC 6779	0.482	13.806	3.943	0.932	-1892.06	-1551.32	-1559.66
NGC 6809	0.481	5.659	4.932	0.843	-2349.57	-1968.01	-2247.96
NGC 6838	4.696	7.485	0.340	0.228	-1894.97	-1838.71	-2619.70
NGC 6934	1.612	30.252	28.461	0.898	-1212.76	-1209.40	-867.510
NGC 7006	13.72	69.528	37.955	0.670	-808.59	-808.09	-3642.92
NGC 7078	4.073	10.129	6.205	0.426	-1689.94	-1666.43	-2375.34
NGC 7089	1.690	30.884	30.290	0.896	-1210.55	-1202.64	-815.815
NGC 7099	1.036	6.623	6.521	0.729	-2097.70	-1870.56	-1768.94
Pal 12	2.807	17.019	15.661	0.716	-1457.21	-1449.86	-1955.37
Pal 13	4.482	57.106	49.206	0.854	-900.79	-899.04	222.77

Appendix D

List of contributions

In addition to the work presented in this book, the author has contributed to a number of other research projects listed in next.

Publications in refereed journals

24. ***Atypical Mg-Poor Milky Way field stars with globular cluster second-generation like chemical patterns***
J. G. Fernández-Trincado; et al., 2017, **submitted to ApJL**

23. ***Chemical abundances and ages of the bulge stars in the high velocity peak***
Yingying Zhou; ...; **J. G. Fernández-Trincado**; et al., 2017, **submitted to ApJ**

22. ***APOGEE chemical abundances of the Sagittarius Dwarf galaxy***
Sten Hasselquist; ...; **J. G. Fernández-Trincado**; et al., 2017, submitted to ApJ

21. ***Kinematics of the local disk from the RAVE survey and the Gaia first data release***
A. C. Robin; ...; **J. G. Fernández-Trincado**; et al., 2017, A&A , **accepted**.

20. ***The Gaia-ESO Survey: low-α element stars in the Galactic Bulge***
A. Recio-Blanco; ...; **J. G. Fernández-Trincado**; et al., 2017, A&A , **A&A Letter, accepted**.

19. ***Baade's window with APOGEE - Metallicities, ages and chemical abundances***
M. Schultheis; ...; **J. G. Fernández-Trincado**; et al., 2017, A&A, 600, A14

18. ***SDSS IV MaNGA: Discovery of an H_α blob associated with a dry galaxy pair – ejected gas or a 'dark' galaxy candidate?***
Lihwai Lin; ...; **J. G. Fernández-Trincado**; et al., 2017, ApJ, 837, 32

17. ***Rotation velocity lags in the extraplanar ionized gas from MaNGA observations of edge-on galaxies***
Bizyaev, D; ...; **J. G. Fernández-Trincado**; et al., 2017, ApJ, 839, 87

16. ***Timing the Evolution of the Galactic Disk with NGC 6791: An Open Cluster with Peculiar High-*** *alpha* ***Chemistry as seen by APOGEE***
Sean Linden; ...; **J. G. Fernández-Trincado**; et al., 2017, ApJ, **accepted**.

15. ***Sloan Digital Sky Survey IV: Mapping the Milky Way, Nearby Galaxies and the Distant Universe***.
Blanton, Michael R.; ...; **J. G. Fernández-Trincado**; et al., 2017, ApJ, **accepted**.

14. ***Identification of neodymium in the APOGEE H-band spectra***
Sten Hasselquist; ...; **J. G. Fernández-Trincado**; et al., 2017, ApJ, 833, 81

13. ***Multiple populations in bulge globular clusters through the NIR eyes of APOGEE: NGC 6553***
Baitian Tang; ...; **J. G. Fernández-Trincado**; et al., 2017, MNRAS, 465, 501

12. ***APOGEE Chemical Abundances of Globular Cluster Giants in the Inner Galaxy.***
Ricardo P. Schiavon; ...; **J. G. Fernández-Trincado**; et al., 2017, MNRAS, 466, 1010

11. ***Chemical trends in the Galactic Halo from APOGEE data.***
E. Fernández-Alvar; ...; **J. G. Fernández-Trincado**; et al., 2016, MNRAS, 465, 1586

10. ***Spectral energy distribution of M-subdwarfs : A study of their atmospheric properties.***
A. S. Rajpurohit; ...; **J. G. Fernández-Trincado**, 2016, A&A, 596, A33

9. ***Discovery of a Metal-Poor Field Giant with a Globular Cluster Second-Generation Abundance Pattern***
J. G. Fernández-Trincado; et al., 2016, ApJ, 833, 132, ***Paper highlighted by CNRS, Institut UTINAM - UMR 6213, and UNAM-IA Mexico***

8. ***Close enconters involving RAVE stars at and beyond the 47 Tucanae tidal radius***
J. G. Fernández-Trincado; et al., 2016, MNRAS, 461, 1404

7. ***Clues on the Milky Way disc formation from population synthesis simulations.***
A. C. Robin; ...; **J. G. Fernández-Trincado**; et al., 2016, Astronomische Nachrichten, 337, 884

6. ***The thirteenth data release of the Sloan Digital Sky Survey: First spectroscopic data from the SDSS-IV survey mapping nearby galaxies at Apache Point Observatory***

SDSS Collaboration; ...; **J. G. Fernández-Trincado**; et al., 2016, ApJ, 2016arXiv160802013S, **submitted**.

5. ***Combining Strong Lensing and Dynamics in Galaxy Clusters: integrating MAMPOSSt within LENSTOOL I. Aplication on SL2SJ02140-0535***
T. Verdugo; ...; **J. G. Fernández-Trincado**; et al., 2016, A&A, 595, A30

4. ***RAVE stars tidally stripped or ejected from the ω Centauri globular cluster***
J. G. Fernández-Trincado; et al., 2015, A&A, 583, 76. ***Paper highlighted by the RAVE survey.***

3. ***Searching for tidal tails around ω Centauri using RR Lyrae stars***
J. G. Fernández-Trincado; et al., 2015, A&A, 574, 15

2. ***The Abundance of Bullet Groups in ΛCDM***
J. G. Fernández-Trincado; et al.; 2014, ApJL, 787, 34

1. ***Characterizing SL2S galaxy groups using the Einstein radius***
T. Verdugo; ...; **J. G. Fernández-Trincado**, 2014, A&A, 571, 65

Conference Proceedings

8. ***No evidence for tidal tails from short period pulsating stars on the outskirts of ω Centauri***
J. G. Fernández-Trincado; et al. 2016, to appear in Terceras Jornadas de Astrofísica Estelar, AAA Workshop Series, Vol. 9, 2016 L. P. Bassino, Z. L. López García, L. S. Cidale & F.A. Bareilles, Eds.

7. ***Mapping optically variable QSOs towards the Galactic plane***
J. G. Fernández-Trincado; et al., 2015, SF2A, 13

6. ***Mapping the inner stellar halo of the Milky Way from 2MASS and SDSS-III/APOGEE survey***
J. G. Fernández-Trincado; et al., 2015, SF2A, 15

5. ***Potential of the Galaxy from the Besancon Galaxy Model including non-axisymmetric components: Preliminary results***
J. G. Fernández-Trincado; et al., 2014, EAS Publications Series, 67, 369

4. ***Searching for the Progenitor Galaxy of Omega Centauri Using RR Lyrae Spectra***
Natalia Carignano; ...; **Fernandez Trincado J. G.**, et al. 2017, American Astronomical Society Meeting Abstracts (2017AAS...22934305C), 229, 343.05

3. ***Two Groups of Red Giants with Distinct Chemical Abundances in the Bulge Globular Cluster NGC 6553 Through the Eyes of APOGEE***
Tang B., ..., **Fernandez Trincado J. G.**; et al., 2017, American Astronomical Society Meeting Abstracts (2017AAS...22922103T), 229, 221.03

2. ***Using APOGEE Data to Examine Late-K and Early-M Dwarfs***
Schmidt; Sarah J.; ...; **Gregorio Fernández Trincado; Jose**; et al., 2015, American Astronomical Society Meeting Abstracts (2015AAS...22513810S), 225, 138.10

1. ***Searching for RR Lyrae stars around omega Centauri (NGC5139)***
J. G. Fernández-Trincado; et al., 2013, MemSAI, 84, 265

Press release and media resources

1. ***Découverte d'une étoile géante dont la composition chimique intrigue***
CNRS News (France) - 16 décembre 2016: http://www.insu.cnrs.fr/node/6239

Bibliography

Abazajian, K. N., Adelman-McCarthy, J. K., Agüeros, M. A., et al. 2009, ApJS, 182, 543

Alam, S., Albareti, F. D., Allende Prieto, C., et al. 2015, ApJS, 219, 12

Allen, C. & Santillan, A. 1991, Rev. Mexicana Astron. Astrofis., 22, 255

Allende Prieto, C., Beers, T. C., Wilhelm, R., et al. 2006, ApJ, 636, 804

Allende Prieto, C., Kawata, D., & Cropper, M. 2016, A&A, 596, A98

Anguiano, B., De Silva, G. M., Freeman, K., et al. 2016, MNRAS, 457, 2078

Antoja, T. 2010, UNIVERSITAT DE BARCELONA Phd Thesis, 1, 101,102

Antoja, T., Helmi, A., Dehnen, W., et al. 2014, A&A, 563, A60

Antoja, T., Valenzuela, O., Pichardo, B., et al. 2009, ApJ, 700, L78

Astropy Collaboration, Robitaille, T. P., Tollerud, E. J., et al. 2013, A&A, 558, A33

Athanassoula, E. 2003, MNRAS, 341, 1179

Athanassoula, E. 2005, MNRAS, 358, 1477

Aumer, M. & Schönrich, R. 2015, MNRAS, 454, 3166

Babusiaux, C. 2016, Publ. Astr. Soc. Autralia, 33, 26

Babusiaux, C., Gómez, A., Hill, V., et al. 2010, A&A, 519, A77

Ballero, S. K., Matteucci, F., Origlia, L., & Rich, R. M. 2007, A&A, 467, 123

Benjamin, R. A., Churchwell, E., Babler, B. L., et al. 2005, ApJ, 630, L149

Bensby, T., Adén, D., Meléndez, J., et al. 2011, A&A, 533, A134

Bensby, T., Yee, J. C., Feltzing, S., et al. 2013, A&A, 549, A147

Bienaymé, O., Robin, A. C., & Crézé, M. 1987, A&A, 180, 94

Bienaymé, O., Robin, A. C., & Famaey, B. 2015, A&A, 581, A123

Binney, J. 2012, MNRAS, 426, 1324

Binney, J., Gerhard, O. E., Stark, A. A., Bally, J., & Uchida, K. I. 1991, MNRAS, 252, 210

Binney, J. & Tremaine, S. 1994, (Pricenton University Press), 1

Bland-Hawthorn, J. & Gerhard, O. 2016, ARA&A, 54, 529

Blitz, L. & Spergel, D. N. 1991, ApJ, 379, 631

Blum, R. D. 1995, ApJ, 444, L89

Boeche, C., Siebert, A., & Steinmetz, M. 2008, in American Institute of Physics Conference Series, Vol. 1082, American Institute of Physics Conference Series, ed. C. A. L. Bailer-Jones, 61–65

Bond, N. A., Ivezić, Ž., Sesar, B., et al. 2010, ApJ, 716, 1

Bovy, J. 2015, ApJS, 216, 29

Bovy, J. & Rix, H.-W. 2013, ApJ, 779, 115

Bovy, J., Rix, H.-W., Liu, C., et al. 2012, ApJ, 753, 148

Brunthaler, A., Reid, M. J., Menten, K. M., et al. 2011, Astronomische Nachrichten, 332, 461

Bureau, M. & Freeman, K. C. 1999, AJ, 118, 126

Caldwell, J. A. R. & Ostriker, J. P. 1981, ApJ, 251, 61

Carollo, D., Beers, T. C., Chiba, M., et al. 2010, ApJ, 712, 692

Carollo, D., Beers, T. C., Lee, Y. S., et al. 2007, Nature, 450, 1020

Carollo, D., Martell, S. L., Beers, T. C., & Freeman, K. C. 2013, ApJ, 769, 87

Carretta, E. 2013, A&A, 557, A128

Carretta, E., Bragaglia, A., Gratton, R. G., et al. 2010, A&A, 516, A55

Chemin, L., Renaud, F., & Soubiran, C. 2015, A&A, 578, A14

Churchwell, E., Babler, B. L., Meade, M. R., et al. 2009, pasp, 121, 213

Clarkson, W., Sahu, K., Anderson, J., et al. 2008, ApJ, 684, 1110

Clarkson, W. I., Sahu, K. C., Anderson, J., et al. 2011, ApJ, 735, 37

Combes, F. & Sanders, R. H. 1981, A&A, 96, 164

Crézé, M. & Robin, A. 1983, in IAU Colloq. 76: Nearby Stars and the Stellar Luminosity Function, ed. A. G. D. Philip & A. R. Upgren, Vol. 76, 391

Cunha, K., e. a. 2017, ApJ, 1

Czekaj, M. A., Robin, A. C., Figueras, F., Luri, X., & Haywood, M. 2014, A&A, 564, A102

Debattista, V. P., Carollo, C. M., Mayer, L., & Moore, B. 2005, ApJ, 628, 678

Debattista, V. P., Ness, M., Earp, S. W. F., & Cole, D. R. 2015, ApJ, 812, L16

Dehnen, W. 2000, AJ, 119, 800

Di Matteo, P., Gómez, A., Haywood, M., et al. 2015, A&A, 577, A1

Di Matteo, P., Haywood, M., Gómez, A., et al. 2014, A&A, 567, A122

Dierickx, M., Klement, R., Rix, H.-W., & Liu, C. 2010, ApJ, 725, L186

Dwek, E., Arendt, R. G., Hauser, M. G., et al. 1995, ApJ, 445, 716

Eggen, O. J., Lynden-Bell, D., & Sandage, A. R. 1962, ApJ, 136, 748

Eisenstein, D. J., Weinberg, D. H., Agol, E., et al. 2011, AJ, 142, 72

Elmegreen, B. G., Bournaud, F., & Elmegreen, D. M. 2008, ApJ, 688, 67

Famaey, B., Jorissen, A., Luri, X., et al. 2005, A&A, 430, 165

Fehlberg, E. 1968, NASA TR R-287

Fernández-Alvar, E., Carigi, L., Allende Prieto, C., et al. 2017, MNRAS, 465, 1586

Fernández-Trincado, J. G., Robin, A. C., Bienaymé, O., et al. 2014, in EAS Publications Series, Vol. 67, EAS Publications Series, 369–369

Fernández-Trincado, J. G., Robin, A. C., Moreno, E., et al. 2016a, ApJ, 833, 132

Fernández-Trincado, J. G., Robin, A. C., & Reylé, C. 2015a, in SF2A-2015: Proceedings of the Annual meeting of the French Society of Astronomy and Astrophysics, ed. F. Martins, S. Boissier, V. Buat, L. Cambrésy, & P. Petit, 15–19

Fernández-Trincado, J. G., Robin, A. C., Reylé, C., et al. 2016b, MNRAS, 461, 1404

Fernández-Trincado, J. G., Robin, A. C., Vieira, K., et al. 2015b, A&A, 583, A76

Fernández Trincado, J. G., Vivas, A. K., Mateu, C. E., & Zinn, R. 2013, Mem. Soc. Astron. Italiana, 84, 265

Fernández-Trincado, J. G., Vivas, A. K., Mateu, C. E., et al. 2015c, A&A, 574, A15

Ferraro, F. R., Massari, D., Dalessandro, E., et al. 2016, ApJ, 828, 75

Freeman, K. & Bland-Hawthorn, J. 2002, ARA&A, 40, 487

Freeman, K., Ness, M., Wylie-de-Boer, E., et al. 2013, MNRAS, 428, 3660

Freudenreich, H. T. 1998, ApJ, 492, 495

Fux, R. 1999, A&A, 345, 787

Gaia Collaboration, Brown, A. G. A., Vallenari, A., et al. 2016a, A&A, 595, A2

Gaia Collaboration, Prusti, T., de Bruijne, J. H. J., et al. 2016b, A&A, 595, A1

García Pérez, A. E., Allende Prieto, C., Holtzman, J. A., et al. 2016, AJ, 151, 144

Gardner, E., Debattista, V. P., Robin, A. C., Vásquez, S., & Zoccali, M. 2014, MNRAS, 438, 3275

Gesicki, K., Zijlstra, A. A., & Miller Bertolami, M. M. 2016, ArXiv e-prints

Gillessen, S., Eisenhauer, F., Trippe, S., et al. 2009, ApJ, 692, 1075

Gonzalez, O. A., Rejkuba, M., Zoccali, M., et al. 2013, A&A, 552, A110

Gonzalez, O. A., Rejkuba, M., Zoccali, M., et al. 2012, A&A, 543, A13

Gonzalez, O. A., Zoccali, M., Debattista, V. P., et al. 2015, A&A, 583, L5

Gunn, J. E., Siegmund, W. A., Mannery, E. J., et al. 2006, AJ, 131, 2332

Harris, W. E. 2010, ArXiv e-prints

Hasselquist, S., Shetrone, M., Cunha, K., et al. 2016, ApJ, 833, 81

Hawkins, K., Jofré, P., Masseron, T., & Gilmore, G. 2015, MNRAS, 453, 758

Haywood, M., Di Matteo, P., Snaith, O., & Calamida, A. 2016, A&A, 593, A82

Hill, V., Lecureur, A., Gómez, A., et al. 2011, A&A, 534, A80

Høg, E., Fabricius, C., Makarov, V. V., et al. 2000, A&A, 355, L27

Holtzman, J. A., Shetrone, M., Johnson, J. A., et al. 2015, AJ, 150, 148

Howard, C. D., Rich, R. M., Clarkson, W., et al. 2009, ApJ, 702, L153

Howard, C. D., Rich, R. M., Reitzel, D. B., et al. 2008, ApJ, 688, 1060

Immeli, A., Samland, M., Gerhard, O., & Westera, P. 2004, A&A, 413, 547

Ivezić, Ž., Connolly, A., Vanderplas, J., & Gray, A. 2014, Statistics, Data Mining and Machine Learning in Astronomy (Princeton University Press)

Jofré, P., Das, P., Bertranpetit, J., & Foley, R. 2017, MNRAS, 467, 1140

Joo, S.-J., Lee, Y.-W., & Chung, C. 2017, ApJ, 840, 98

Kawata, D., Grand, R. J. J., & Cropper, M. 2012, in European Physical Journal Web of Conferences, Vol. 19, European Physical Journal Web of Conferences, 07006

Kawata, D., Hunt, J. A. S., Grand, R. J. J., et al. 2014, in EAS Publications Series, Vol. 67, EAS Publications Series, 247–250

Kent, S. M. 1992, ApJ, 387, 181

Kordopatis, G., Gilmore, G., Steinmetz, M., et al. 2013, AJ, 146, 134

Kormendy, J. & Kennicutt, Jr., R. C. 2004, ARA&A, 42, 603

Kuijken, K. & Gilmore, G. 1989, MNRAS, 239, 571

Kunder, A., Koch, A., Rich, R. M., et al. 2012, AJ, 143, 57

Kunder, A., Rich, R. M., Hawkins, K., et al. 2015, ApJ, 808, L12

Kunder, A., Rich, R. M., Koch, A., et al. 2016, ApJ, 821, L25

Laurikainen, E. & Salo, H. 2016, Galactic Bulges, 418, 77

Lee, Y.-W., Joo, S.-J., & Chung, C. 2015, MNRAS, 453, 3906

Lind, K., Koposov, S. E., Battistini, C., et al. 2015, A&A, 575, L12

Lindegren, L., Lammers, U., Bastian, U., et al. 2016, A&A, 595, A4

López-Corredoira, M. 2016, A&A, 593, A66

López-Corredoira, M., Cabrera-Lavers, A., & Gerhard, O. E. 2005, A&A, 439, 107

Majewski, S. R., Schiavon, R. P., Frinchaboy, P. M., et al. 2015, ArXiv e-prints

Marshall, D. J., Robin, A. C., Reylé, C., Schultheis, M., & Picaud, S. 2006, A&A, 453, 635

Martell, S. L., Shetrone, M. D., Lucatello, S., et al. 2016, ApJ, 825, 146

Martinez-Medina, L. A., Pichardo, B., Moreno, E., Peimbert, A., & Velazquez, H. 2016, ApJ, 817, L3

Martinez-Medina, L. A., Pichardo, B., Pérez-Villegas, A., & Moreno, E. 2015, ApJ, 802, 109

Martinez-Valpuesta, I., Aguerri, J. A. L., González-García, A. C., Dalla Vecchia, C., & Stringer, M. 2017, MNRAS, 464, 1502

Martinez-Valpuesta, I. & Gerhard, O. 2011, ApJ, 734, L20

Martinez-Valpuesta, I. & Gerhard, O. 2013, ApJ, 766, L3

Martinez-Valpuesta, I. & Shlosman, I. 2004, ApJ, 613, L29

Martinez-Valpuesta, I., Shlosman, I., & Heller, C. 2006, ApJ, 637, 214

Matsunaga, N., Feast, M. W., Bono, G., et al. 2016, MNRAS, 462, 414

McMillan, P. J. 2017, MNRAS, 465, 76

McWilliam, A. 2016, Publ. Astr. Soc. Autralia, 33, 40

McWilliam, A., Matteucci, F., Ballero, S., et al. 2008, AJ, 136, 367

McWilliam, A. & Zoccali, M. 2010, ApJ, 724, 1491

Michalik, D., Lindegren, L., & Hobbs, D. 2015, A&A, 574, A115

Minchev, I. & Famaey, B. 2010, ApJ, 722, 112

Miyamoto, M. & Nagai, R. 1975, PASJ, 27, 533

Molloy, M., Smith, M. C., Evans, N. W., & Shen, J. 2015a, ApJ, 812, 146

Molloy, M., Smith, M. C., Shen, J., & Evans, N. W. 2015b, ApJ, 804, 80

Monari, G., Antoja, T., & Helmi, A. 2013, ArXiv e-prints

Monari, G., Famaey, B., & Siebert, A. 2015, MNRAS, 452, 747

Monari, G., Famaey, B., & Siebert, A. 2016, MNRAS, 457, 2569

Monari, G., Famaey, B., Siebert, A., et al. 2017a, MNRAS, 465, 1443

Monari, G., Helmi, A., Antoja, T., & Steinmetz, M. 2014, A&A, 569, A69

Monari, G., Kawata, D., Hunt, J. A. S., & Famaey, B. 2017b, MNRAS, 466, L113

Moreno, E., Allen, C., & Pichardo, B. S. 2008, in Revista Mexicana de Astronomia y Astrofisica, vol. 27, Vol. 34, Revista Mexicana de Astronomia y Astrofisica Conference Series, 131–132

Moreno, E., Pichardo, B., & Schuster, W. J. 2015, MNRAS, 451, 705

Moreno, E., Pichardo, B., & Velázquez, H. 2014, ApJ, 793, 110

Muna, D., Alexander, M., Allen, A., et al. 2016, ArXiv e-prints

Nataf, D. M., Udalski, A., Gould, A., Fouqué, P., & Stanek, K. Z. 2010, ApJ, 721, L28

Nataf, D. M., Udalski, A., Skowron, J., et al. 2015, MNRAS, 447, 1535

Ness, M. & Freeman, K. 2016, Publ. Astr. Soc. Autralia, 33, 22

Ness, M., Freeman, K., Athanassoula, E., et al. 2013a, MNRAS, 430, 836

Ness, M., Freeman, K., Athanassoula, E., et al. 2013b, MNRAS, 432, 2092

Ness, M., Freeman, K., Athanassoula, E., et al. 2012, ApJ, 756, 22

Ness, M. & Lang, D. 2016, AJ, 152, 14

Ness, M., Zasowski, G., Johnson, J. A., et al. 2016, ApJ, 819, 2

Nidever, D. L., Holtzman, J. A., Allende Prieto, C., et al. 2015, AJ, 150, 173

Nidever, D. L., Zasowski, G., Majewski, S. R., et al. 2012, ApJ, 755, L25

Pasetto, S., Natale, G., Kawata, D., et al. 2016, MNRAS, 461, 2383

Pérez-Villegas, A., Portail, M., & Gerhard, O. 2017a, MNRAS, 464, L80

Pérez-Villegas, A., Portail, M., Wegg, C., & Gerhard, O. 2017b, ApJ, 840, L2

Picaud, S. & Robin, A. C. 2004, A&A, 428, 891

Pichardo, B. 2003, UNAM Phd Thesis, 1, 192

Pichardo, B., Martos, M., & Moreno, E. 2004, ApJ, 609, 144

Pichardo, B., Martos, M., Moreno, E., & Espresate, J. 2003, ApJ, 582, 230

Pichardo, B., Moreno, E., Allen, C., et al. 2012, AJ, 143, 73

Poleski, R. 2013, ArXiv e-prints

Portail, M., Gerhard, O., Wegg, C., & Ness, M. 2017, MNRAS, 465, 1621

Portail, M., Wegg, C., & Gerhard, O. 2015a, MNRAS, 450, L66

Portail, M., Wegg, C., Gerhard, O., & Martinez-Valpuesta, I. 2015b, MNRAS, 448, 713

Pouliasis, E., Di Matteo, P., & Haywood, M. 2017, A&A, 598, A66

Press, W. H., Teukolsky, S. A., Vetterling, W. T., & Flannery, B. P. 1992, Numerical recipes in FORTRAN. The art of scientific computing

Raha, N., Sellwood, J. A., James, R. A., & Kahn, F. D. 1991, Nature, 352, 411

Recio-Blanco, A., Rojas-Arriagada, A., de Laverny, P., et al. 2017, ArXiv e-prints

Reylé, C., Marshall, D. J., Robin, A. C., & Schultheis, M. 2009, A&A, 495, 819

Rich, R. M. 1992, in IAU Symposium, Vol. 149, The Stellar Populations of Galaxies, ed. B. Barbuy & A. Renzini, 29

Robin, A. & Crézé, M. 1986a, A&A, 157, 71

Robin, A. & Crézé, M. 1986b, A&AS, 64, 53

Robin, A. C., Bienaymé, O., Fernández-Trincado, J. G., & Reylé, C. 2017, ArXiv e-prints

Robin, A. C., Marshall, D. J., Schultheis, M., & Reylé, C. 2012, A&A, 538, A106

Robin, A. C., Reylé, C., Derrière, S., & Picaud, S. 2003, A&A, 409, 523

Robin, A. C., Reylé, C., Fliri, J., et al. 2014, A&A, 569, A13

Rojas-Arriagada, A., Recio-Blanco, A., Hill, V., et al. 2014, A&A, 569, A103

Rojas-Arriagada, A., Zoccali, M., Vásquez, S., et al. 2016, A&A, 587, A95

Rojas-Niño, A., Read, J. I., Aguilar, L., & Delorme, M. 2016, MNRAS, 459, 3349

Romero-Gómez, M., Figueras, F., Antoja, T., Abedi, H., & Aguilar, L. 2015, MNRAS, 447, 218

Romero-Gomez, M., Figueras, F., Antoja, T., et al. 2016, in Astronomical Society of the Pacific Conference Series, Vol. 507, Multi-Object Spectroscopy in the Next Decade: Big Questions, Large Surveys, and Wide Fields, ed. I. Skillen, M. Barcells, & S. Trager, 65

Saha, K. & Gerhard, O. 2013, MNRAS, 430, 2039

Saha, K., Martinez-Valpuesta, I., & Gerhard, O. 2012, MNRAS, 421, 333

Saito, R. K., Zoccali, M., McWilliam, A., et al. 2011, AJ, 142, 76

Sales, L. V., Helmi, A., Abadi, M. G., et al. 2009, MNRAS, 400, L61

Santiago, B. X., Brauer, D. E., Anders, F., et al. 2016, A&A, 585, A42

Scannapieco, C. & Tissera, P. B. 2003, MNRAS, 338, 880

Schiavon, R. P., Johnson, J. A., Frinchaboy, P. M., et al. 2017a, MNRAS, 466, 1010

Schiavon, R. P., Zamora, O., Carrera, R., et al. 2017b, MNRAS, 465, 501

Schmidt, M. 1956, Bull. Astron. Inst. Netherlands, 13, 15

Schultheis, M., Cunha, K., Zasowski, G., et al. 2015, A&A, 584, A45

Schultheis, M., Rojas-Arriagada, A., García Pérez, A. E., et al. 2017, A&A, 600, A14

SDSS Collaboration, Albareti, F. D., Allende Prieto, C., et al. 2016, ArXiv e-prints

Sellwood, J. A. & Binney, J. J. 2002, MNRAS, 336, 785

Shen, J. & Li, Z.-Y. 2016, Galactic Bulges, 418, 233

Shen, J., Rich, R. M., Kormendy, J., et al. 2010, ApJ, 720, L72

Siebert, A., Williams, M. E. K., Siviero, A., et al. 2011, AJ, 141, 187

Smith, R., Flynn, C., Candlish, G. N., Fellhauer, M., & Gibson, B. K. 2015, MNRAS, 448, 2934

Sofue, Y. 2015, PASJ, 67, 75

Soszyński, I., Udalski, A., Szymański, M. K., et al. 2014, actaa, 64, 177

Stanek, K. Z., Udalski, A., SzymaŃski, M., et al. 1997, ApJ, 477, 163

Steinmetz, M., Zwitter, T., Siebert, A., et al. 2006, AJ, 132, 1645

Tang, B., Cohen, R. E., Geisler, D., et al. 2017, MNRAS, 465, 19

Taylor, M. B. 2005, in Astronomical Society of the Pacific Conference Series, Vol. 347, Astronomical Data Analysis Software and Systems XIV, ed. P. Shopbell, M. Britton, & R. Ebert, 29

Ventura, P., Di Criscienzo, M., Carini, R., & D'Antona, F. 2013, MNRAS, 431, 3642

Wegg, C. & Gerhard, O. 2013, MNRAS, 435, 1874

Wegg, C., Gerhard, O., & Portail, M. 2015, MNRAS, 450, 4050

Weiland, J. L., Arendt, R. G., Berriman, G. B., et al. 1994, ApJ, 425, L81

Whitelock, P. 1992, in Astronomical Society of the Pacific Conference Series, Vol. 30, Variable Stars and Galaxies, in honor of M. W. Feast on his retirement, ed. B. Warner, 11

Williams, A. A., Evans, N. W., Molloy, M., et al. 2016, ApJ, 824, L29

Wilson, J. C., Hearty, F., Skrutskie, M. F., et al. 2010, in Proc. SPIE, Vol. 7735, Ground-based and Airborne Instrumentation for Astronomy III, 77351C

Yanny, B., Rockosi, C., Newberg, H. J., et al. 2009, AJ, 137, 4377

Zamora, O., García-Hernández, D. A., Allende Prieto, C., et al. 2015, AJ, 149, 181

Zasowski, G., Johnson, J. A., Frinchaboy, P. M., et al. 2013, AJ, 146, 81

Zasowski, G., Ness, M. K., García Pérez, A. E., et al. 2016, ApJ, 832, 132

Zoccali, M., Renzini, A., Ortolani, S., et al. 2003, A&A, 399, 931

Zoccali, M. & Valenti, E. 2016, Publ. Astr. Soc. Autralia, 33, 25

Zwitter, T., Siebert, A., Munari, U., et al. 2008, AJ, 136, 421